

STABILISING ALLOYS IN NON-EQUILIBRIUM CRYSTAL STRUCTURES BY EPITAXIAL GROWTH

by

THIBAUT DECOSTER

A thesis submitted to the
University of Birmingham
for the degree of
DOCTOR OF PHILOSOPHY

Nanoscale Physics Research Laboratory
School of Physics and Astronomy
University of Birmingham
December 2012

Abstract

Thin film and surface science is an active field with important technological applications as illustrated by the transistor which is produced by the growth of thin layers on semiconductor substrates and by the recording head produced by alternating layers of magnetic and non-magnetic materials. This thesis relates thin film and surface science experiments applied to quasicrystalline and ferromagnetic alloys.

Quasicrystals have a strong potential for technological applications, in catalysis for example. Quasicrystal alloys are stable in a narrow region of the phase diagram. The quasicrystalline phase field consists of different quasicrystalline phases. Depending on the temperature and the chemical composition, the quasicrystal may or may not be stable inducing different surface morphology behaviours. This thesis reports detailed analysis of annealing and phase transition related structures on the (10000), (00001), and (10 $\bar{2}$ $\bar{2}$ 4) surfaces of d -Al_{72.2}Ni_{19.2}Co_{8.6}. We observe rectangular hollow features appearing, growing, and coalescing while cooling the sample from the high temperature phase. We also observe quasicrystalline islands faceting on AlNiCo(10000) and nano-pillars growing on non-sputtered AlNiCo(10 $\bar{2}$ $\bar{2}$ 4). For a better understanding of the quasicrystals' physical properties, one wants to grow quasicrystalline thin films of reduced chemical complexity. Single elements don't form quasicrystalline thin films beyond a monolayer. This thesis reports the successful growth of binary AlNi quasicrystal thin films in the multilayer regime at different compositions using AlNiCo(10000) as a growth template.

The AlNi/AlNiCo system shows how epitaxial deposition is a powerful tool to create structures which are non-stable in the bulk state. This is also a point of interest for the MnSb/GaAs ferromagnetic-semiconductor system. The equilibrium structure of MnSb is of the NiAs type but other structures with theoretical 100% polarisation can be stabilised by epitaxy. We studied MnSb thin films with equilibrium bulk structure grown epitaxially on GaAs(111). The surface magnetism of the MnSb thin film has been imaged for the first time by spin-polarised low-energy electron microscopy revealing the spin direction mapping of magnetic domains at the surface of MnSb.

Atomic resolution is routinely obtained with the current generation of transmission electron microscopes. For three-dimensional atomic resolution, the problem is to obtain suitable samples. In this thesis, we report the development of instruments and a methodology to fabricate atomically flat terraces with nanometre dimension at the tip of etched tungsten wires and the MBE growth of Au clusters on these terraces.

UNIVERSITY OF
BIRMINGHAM

University of Birmingham Research Archive

e-theses repository

This unpublished thesis/dissertation is copyright of the author and/or third parties. The intellectual property rights of the author or third parties in respect of this work are as defined by The Copyright Designs and Patents Act 1988 or as modified by any successor legislation.

Any use made of information contained in this thesis/dissertation must be in accordance with that legislation and must be properly acknowledged. Further distribution or reproduction in any format is prohibited without the permission of the copyright holder.

Contents

Physical Constants	iv
Table of acronyms	v
Introduction	1
Chapter 1 : Quasiperiodicity and Quasiperiodic Alloys	5
1.1 Crystal and crystallography	6
1.1.1 Lattices and terminology of crystals	6
1.1.2 The reciprocal lattice	8
1.1.3 The crystallographic restriction	9
1.2 Quasiperiodicity and long-range order structures	10
1.2.1 Tilings and coverings	10
1.2.2 Fibonacci sequence	11
1.2.3 Quasiperiodicity generated by the projection method	12
1.2.4 Penrose tiling	15
1.3 Incommensurate structures and approximants	17
1.4 The various families of quasicrystals	17
1.4.1 Metastable quasicrystals	18
1.4.2 Stable quasicrystals	18
1.5 Alumnides	19
1.5.1 Stabilisation of quasicrystals	20
1.5.2 <i>d</i> -AlNiCo, a decagonal quasicrystal	22
1.5.3 Icosahedral quasicrystals	29
Chapter 2 : Quasicrystal Thin Films	31
2.1 Oxidised surfaces	31
2.2 Topography and surface preparation	31
2.2.1 Surface science of <i>d</i> -AlNiCo: 10-fold surface	33
2.2.2 Surface science of <i>d</i> -AlNiCo: 2-fold surface	34
2.3 Thin film growth modes	35
2.3.1 Lattice registration	36
2.3.2 Origin and consequences of stress in the heteroepitaxial layer	37
2.3.3 Stranski-Krastanov: a 2D to 3D phase transition	38
2.4 Quasicrystal thin film growth modes	39

2.4.1	Rotational epitaxial growth	40
2.4.2	Epitaxial growth	45
2.4.3	Volmer-Weber growth	45
2.5	Quasicrystal-crystal epitaxy	45
Chapter 3 : MnSb Thin Films for Spintronics		48
3.1	Magnetism and thin film magnetism	51
3.1.1	Involved energies in ferromagnetism	52
3.1.2	Origin of the magnetic domains in ferromagnets	53
3.1.3	From macro- to microscopic systems	55
3.1.4	Magnetism in thin films	56
3.1.5	Magnetic phase transition in bulk and thin films	60
3.2	Growth on MnSb on GaAs(111)B	61
3.2.1	Crystallography of III-V semiconductors	61
3.2.2	Crystallography and surface structure of Manganese Pnictide alloys	62
3.2.3	Heteroepitaxial growth of MnSb on GaAs	62
Chapter 4 : Instruments		65
4.1	The mean free path of electrons	65
4.2	The Ewald sphere construction	67
4.3	Electron sources and analysers	68
4.4	Molecular Beam Epitaxy	69
4.5	Imaging and spectroscopy with SEM	69
4.6	Electron spectroscopy for chemical analysis	71
4.7	SPA-LEED: theory and techniques	72
4.8	LEEM and SPLEEM	76
4.8.1	Very-low-energy-electron/matter interaction	76
4.8.2	LEEM optics	80
4.8.3	Contrast mechanisms	81
4.8.4	Spin-polarised LEEM (SPLEEM)	83
4.8.5	Resolution of the SPLEEM at the NCEM	84
4.8.6	Electron energy determination	85
4.9	TEM and STEM	85
4.9.1	Introduction to electron tomography	87

4.9.2	Electron lenses and apertures	88
4.9.3	Resolution, spherical and chromatic aberrations	89
4.9.4	Electron optics in TEM	90
Chapter 5	Morphology of Various <i>d</i>-AlNiCo Surfaces	95
5.1	Morphology of the <i>d</i> -AlNiCo(10000) surface	95
5.1.1	Island morphology on <i>d</i> -AlNiCo(10000) surface	97
5.1.2	Topography of <i>d</i> -AlNiCo(10000) surface	98
5.1.3	Growth study of the black features	104
5.2	Morphology of the <i>d</i> -AlNiCo(10 $\bar{2}$ $\bar{2}$ 4) surface	111
5.3	Morphology of the <i>d</i> -AlNiCo(00001) surface	114
5.4	Summary	116
Chapter 6	AlNi Thin Film Growth on 2-fold AlNiCo	117
6.1	Calibration	118
6.2	Clean surface of 2-fold <i>d</i> -AlNiCo	121
6.3	Ni deposition on 2-fold <i>d</i> -AlNiCo	125
6.4	Al/Ni co-deposition on 2-fold <i>d</i> -AlNiCo	129
6.5	Al/Ni co-deposition on 2-fold <i>d</i> -AlNiCo at higher Al:Ni ratio	135
6.6	Summary	139
Chapter 7	Surface Magnetism of MnSb/GaAs(111)B	140
7.1	Description of the sample	140
7.2	Morphology change upon annealing	141
7.3	SPLEEM contrast of MnSb/GaAs(111)B at different energies	143
7.4	Direction mapping of MnSb magnetic domains	146
7.5	Magnetisation changes across magnetic domain boundaries	151
7.6	Summary	154
Chapter 8	Etched Tungsten Wires for Tomography	155
8.1	Introduction to the controlled etching device	156
8.2	Results	160
	Conclusion and Perspectives	168
	Bibliography	173

Physical constants

Electron rest mass	m_e	=	$9.109 \times 10^{-31} \text{ kg}$
Avogadro's number	N_0	=	6.02×10^{23}
Electron charge	e	=	$1.6 \times 10^{-19} \text{ C}$
Permeability of free space	μ_0	=	$4\pi \times 10^{-7} \text{ H} \cdot \text{m}^{-1}$
Boltzmann constant	k_B	=	$1.38 \times 10^{-23} \text{ J} \cdot \text{K}^{-1}$
Speed of light	c	=	$3 \times 10^8 \text{ m} \cdot \text{s}^{-1}$
Planck constant	h	=	$6.62 \times 10^{-34} \text{ J} \cdot \text{s}$
Stefan-Boltzmann constant	σ	=	$5.67 \times 10^{-8} \text{ W} \cdot \text{m}^{-2} \cdot \text{K}^{-4}$

Table of acronyms

ADF	Annular Dark-Field
AFM	Atomic Force Microscopy
AL	Attenuation Length
BF	Bright Field
BFP	Back Focal Plane
CCD	Charge-Coupled Device
DOS	Density Of States
DP	Diffraction Pattern
EDS	Energy-Dispersive X-ray Spectroscopy
EELS	Electron Energy Loss Spectroscopy
fcc	Face Centered Cubic
FIB	Focused Ion Beam
FM	Frank-van der Merve
FMR	Ferromagnetic Resonance
HAADF	High Angle Annular Dark Field
hcp	Hexagonal Close-Packed
HDPE	High-Density PolyEthylene
HOPG	Highly Oriented Pyrolite Graphite
HRTEM	High-Resolution Transmission Electron Microscope
IMFP	Inelastic Mean Free Path
LEED	Low Energy Electron Diffraction
LEEM	Low Energy Electron Microscopy
LWF	Local Work Function
MAE	Magneto-Crystalline Anisotropy
MBE	Molecular Beam Epitaxy
ML	Monolayer
PEEM	Photo-Emission Electron Microscopy
PMI	Pseudo-Mackay Icosahedron
QC	Quasicrystal
QSE	Quantum Size Effect
RHEED	Reflection High Energy Electron Diffraction
RT	Room Temperature
SEM	Scanning Electron Microscopy
SADP	Selected-Area Diffraction Pattern
SF	Step Flow
SK	Stranski-Krastanov
SPA-LEED	Spot Profile Analysis - Low Energy Electron Diffraction
SPELEEM	Spectroscopic Photoemission and Low Energy Electron Microscopy
SPLEEM	Spin-Polarized Low Energy Electron Microscopy
STEM	Scanning Transmission Electron Microscopy
STM	Scanning Tunneling Microscopy
STS	Scanning Tunneling Spectroscopy
TEM	Transmission Electron Microscopy
TM	Transition Metal
UHV	Ultra High Vacuum
VW	Volmer-Weber
XAES	X-ray induced Auger Electron Spectroscopy
XPEEM	X-ray Photo-Emission Electron Microscopy
XPS	X-ray Photoelectron Spectroscopy

Introduction

This thesis presents experimental research in the field of condensed matter and more precisely thin film and surface science. For a solid, the surface is less energetically favourable than the bulk material. Surfaces readily rearrange or react, so that the energy is reduced by processes such as passivation or adsorption. A semiconductor has dangling bonds at its surface, the atoms rearrange themselves in order to lower the surface free energy. A well known example of surface reconstruction is the Si(111)-(7×7). Another way to reduce the surface contribution to the overall energy is to minimise the surface area itself. This can be observed in the shape of liquid droplets or solid islands on surfaces. The symmetry breaking induced by a surface also affects the magnetism. At a surface, the magnetic anisotropy term can exceed all other magnetic contributions resulting in a large change in the local polarisation.

Metallic surfaces are very reactive especially with oxygen and water. To study pristine surfaces, one wants to remove the oxide layer and perform measurements in an oxygen and water free environment. Thin film and surface science experiments are thus performed in an ultra-high vacuum (UHV) environment with a pressure below 10^{-12} bar. A native oxide layer can be removed from the sample by hitting the surface with ionised noble gas atoms, a process called sputtering. This treatment is followed by annealing to rebalance the surface topography and stoichiometry. In this environment it is as well possible to anneal specimens to high temperature (750°C) without oxidising the sample. The clean environment of a UHV chamber, crucial for surface preparation, also allows molecular deposition in a controllable way at the atomic scale. This technique known as molecular beam epitaxy (MBE) allows the creation and study of structures that do not exist in nature. Investigations generally focus on the interface between the surface and the deposited film, the creation of low-dimensional systems, or the substrate effect on the deposited material.

In order to perform surface morphology or surface stoichiometry analysis, one needs surface sensitive tools. Because of their intrinsic properties, electrons provide a probe for the study of surfaces. Low energy electrons are used to study the atomic structure of a surface by diffraction (LEED) and are also used to obtain chemical information or to observe atomic steps in the physical space (LEEM). Electrons at higher energy provide microscopic resolution not reachable by conventional optical

microscopes such as sub-angstrom resolution with a transmission electron microscope (TEM). Although high energy electrons generate a large interaction volume when colliding with matter, the secondary electrons generated by ionisation can escape the material only from within the first 2-3 nanometres. This property is exploited in the secondary electron microscope (SEM) to obtain excellent topographic information. To infer the chemical stoichiometry of the sample the energy distribution of photoemission electrons is exploited by X-ray photoelectron spectroscopy (XPS).

The thin film and surface science related experiments presented in this thesis were performed on three systems; namely the quasicrystalline AlNiCo alloy, MnSb thin films and atomically flat tungsten tips as a base for electron tomography.

Quasicrystallinity is a form of matter discovered by Shechtman in 1984 who was awarded in 2011 with a Nobel Prize for his discovery. In contrast to conventional crystals, the atomic structure of quasicrystals does not repeat itself periodically in space but quasiperiodically instead. However, they exhibit long-range ordering. A mathematical description and the physical properties of quasicrystal alloys are discussed in chapter 1. AlNiCo is a complex alloy showing various phases within the quasicrystalline phase field and a strong anisotropy in its value of the surface energy. Using UHV-SEM, electron dispersion spectroscopy (EDS), and atomic force microscopy (AFM), we observed and analysed phase transition related features at Al-NiCo surfaces. These features depend on the surface orientation and on the surface preparation. They are elongated rectangle shaped hollows on the AlNiCo(10000) surface and 35° tilted nano-pillars on AlNiCo($10\bar{2}\bar{2}4$). The results of these experiments are discussed in chapter 5 while the SEM and EDS techniques are succinctly introduced in chapter 4. AlNiCo displays non-conventional physical properties such as low surface free energy and high resistivity even though consisting of metallic elements. It is still not clear how quasiperiodicity affects the alloys' physical properties in detail. UHV-compatible quasicrystals are at least ternary alloys. Using MBE techniques, one can aim to grow thin films of reduced chemical complexity on a quasicrystal substrate to induce a quasiperiodic structure in the thin films. So far, this goal had only been achieved for film thicknesses up to one atomic layer. In this thesis, we present the results of successful growth of quasicrystalline binary AlNi alloy thin films of multilayer thickness at different chemical compositions. The thin films' structures and stoichiometries were analysed by LEED and XPS, respectively. The details and the analysis of these experiments are given in chapter 6 whereas

a comprehensive introduction to the background on quasicrystal thin films is given in chapter 2. LEED, the related SPA-LEED technique, and XPS are introduced in chapter 4.

This thesis also discusses the epitaxial MnSb/GaAs(111)B system which has prominent potential applications for spintronics. Spintronics is a term referring to the field that deals with systems or devices that use the spin of an electron instead of its charge to store or carry information. MnSb/GaAs is an interesting system for spintronics applications. MnSb is a ferromagnetic material with a Curie temperature well above room temperature. The square base of its tetragonal structure matches the GaAs semiconductor in its (111) direction. GaAs is a semiconductor widely used in electronics. MnSb has a spin polarisability of approximately 35% at the Fermi energy. Thus, a flawless interface with GaAs would allow spin injection into a semiconductor. Furthermore, recent theoretical calculations have shown that the spin polarisation effect could be enhanced by growing MnSb alloys in the wurtzite structure. This new system would then be half-metallic. This project is part of a collaboration with Dr. Gavin Bell and Dr. James Aldous who prepared the samples. Details regarding the preparation of this system are given in chapter 3. In this same chapter, we will discuss ferromagnetism in the bulk, in reduced dimensions, and at the surface. The surface morphology of the system was explored by LEEM. The surface magnetism was measured with the same instrument using LEEM with spin-polarised electrons allowing direct morphological and magnetic comparisons. These experiments are detailed in chapter 7. Technical details regarding the acquisition of LEEM images and elements for the understanding of the contrast of LEEM images are presented in chapter 4.

The third and last topic discussed in this thesis is the development of an innovative approach to prepare tomography samples for transmission electron microscopy. Essentially, this method aims to use surface science techniques such as MBE and sputtering for the sample's preparation. Etching was used to reach the nanometre dimensions required for TEM experiments. Tungsten is used for tip etching since it is fairly chemically and thermally stable. The final geometry is an etched tip with an atomically flat surface on the nanometre scale at its apex that will be used for MBE deposition. Chapter 8 presents the first results to obtain the tungsten surface in low dimensions. To obtain this geometry, we have developed devices to crystallise tungsten wires, thin and etch tungsten wires in a controllable way, and to clamp

and anneal the tips to perform MBE experiments. Gold nanoclusters have been successfully grown on an etched tip. Electron tomography and recent breakthroughs in obtaining three dimensional atomic reconstruction are reviewed in chapter 4. The TEM instrument is also succinctly introduced in this same chapter.

This work has been made possible with the support of a number of people who I would like to thank. First of all, my supervisor Dr. Wolfgang Theis with whom I kept learning through the different projects we were involved in. I would like to thank Prof Katharina Franke and Prof José Ignacio Pascual for welcoming me in their groups at the Freie Universität Berlin; Dr. Adrian Quesada, Dr. Andreas Schmidt, and Dr. Peter Ercius for their considerable assistance during our stay at NCEM in Berkeley; Dr. Gavin Bell and Dr. James Aldous for providing the magnetic samples which eventually lead to a successful cooperation. Finally, Prof Richard Palmer for giving me the chance to study at NPRL.

Chapter 1 : Quasiperiodicity and Quasiperiodic Alloys

On the 5 November 1984, D. Shechtman, I. Blech, D. Gratias and J.W. Cahn startled the world of solid state physics with the discovery of quasicrystals in a publication entitled "Metallic Phase with Long-Range Orientational Order and No Translational Symmetry" [1]. The sample was an alloy of aluminium and manganese rapidly quenched. Using a TEM in its diffraction mode, they observed the diffraction pattern of material's grains whose sharp peaks had the symmetry of a three dimensional icosahedron. Furthermore, the intensity of diffraction spots did not decrease with the distance from the center of the diffraction pattern as it does for periodically ordered crystals, and finally the spacing between the reflection spots was related by powers of τ , the golden mean.

Prior to this publication it had not only been axiomatic that the internal structure of a crystal was periodic, but also its corollary; icosahedral symmetry is incompatible with periodicity and is therefore impossible for crystals. However, three days before Shechtman's publication, D. Levine and P.J. Steinhardt submitted a paper to the same journal in which they introduced a structural model of a quasicrystal [2]. This demonstrates that even though quasicrystals came as a surprise, new perspectives and theoretical techniques had been developed earlier.

Initially, Daniel Shechtman encountered the rejection of his manuscript by a leading journal and the opposition of many notable crystallographers (including Linus Pauling, double Nobel prize). Subsequent results verified beyond any doubt the existence of these materials and hundreds of quasicrystalline compounds have been discovered since. Following the discovery of quasicrystals in 1992, the definition of a crystal was revised by the International Union of Crystallography, a crystal since being defined as "any solid with an essentially discrete diffraction pattern". In 2011, Daniel Shechtman was awarded the Nobel prize in Chemistry for his discovery.

In the next sections, the theoretical background on quasicrystals will be introduced. These sections are mainly based on books having either a mathematical [3,4], geometric [5], physics [6], or applied physics [7,8] approach.

1.1 Crystal and crystallography

The physics of condensed matter is to a very great extent the physics of crystals. A crystal exhibits translational symmetry resulting in a finite number of possible structures. A crucial property of ideal, fully ordered crystals is that their diffraction patterns show Bragg reflections (Dirac δ -peak) only, and no structural diffuse scattering. The intensity distribution is related to the Fourier transform of the structure. In this section we will discuss the description of a crystal in real space and in reciprocal space, and the crystallographic restriction.

1.1.1 Lattices and terminology of crystals

Although never perfect, atomic arrangements in condensed matter are described by infinite arrays of geometric points called **lattices**. In a lattice, every point has an identical surrounding, all lattice points are equivalent and the crystal therefore exhibits perfect translational symmetry. The points in the three-dimensional crystal lattice are thus given by the following equation

$$\mathbf{r} = n_1 \mathbf{a} + n_2 \mathbf{b} + n_3 \mathbf{c}, \quad (1.1)$$

where n_1, n_2, n_3 are integers and $\mathbf{a}, \mathbf{b}, \mathbf{c}$ are fundamental unit vectors of the translational symmetry. The volume associated with a single lattice point is called the **primitive cell**.

It can be demonstrated that there are only 14 different periodic ways of arranging identical points in a 3D space determined by the permitted symmetries of a periodic array of points. These 14 arrays are called **Bravais lattices** and are shown in table 1.1. The volume unit depicting the lattice is not always a primitive cell. It is often convenient to use a large volume called the **unit cell**. The unit cell illustrates the symmetry in a more obvious way and favours the use of orthogonal axes. A group of atoms can be associated with each lattice point with the position vector written as follows

$$\mathbf{r}_j = n_1 \mathbf{a} + n_2 \mathbf{b} + n_3 \mathbf{c} + \mathbf{R}_j. \quad (1.2)$$

With \mathbf{R}_j a position vector within the unit cell relative to the lattice point (n_1, n_2, n_3) . The group of atoms associated with every lattice point is called a **basis**, any crystal structure is therefore specified by its Bravais lattice and a basis. If we can perform

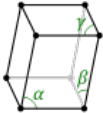
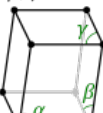
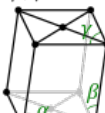
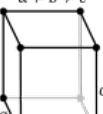
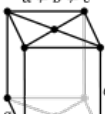
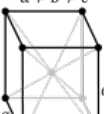
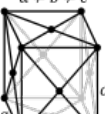
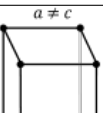
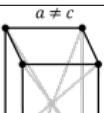
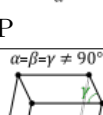
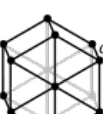
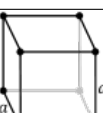
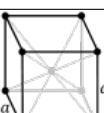
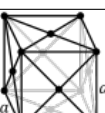
	The 14 Bravais lattices			
triclinic	$\alpha, \beta, \gamma \neq 90^\circ$  P (primitive)			
monoclinic	$\alpha \neq 90^\circ$ $\beta, \gamma = 90^\circ$  P	$\alpha \neq 90^\circ$ $\beta, \gamma = 90^\circ$  C (base-centered)		
orthorombic	$a \neq b \neq c$  P	$a \neq b \neq c$  C	$a \neq b \neq c$  I (body-centered)	$a \neq b \neq c$  F (face-centered)
tetragonal	$a \neq c$  P	$a \neq c$  I		
trigonal	$\alpha = \beta = \gamma \neq 90^\circ$  R (rhombohedral primitive)			
hexagonal	 P			
cubic	 P	 I		 F

Table 1.1: The seven crystal systems and fourteen Bravais lattices.

a symmetry operation on an object we can also reverse it, for each symmetry we also have an inverse symmetry. The set of symmetry operations of a given object forms a **group**. This group is the symmetry group of the object. The introduction of the basis induces new symmetry elements such as rotations or reflections. These elements are the so-called **point-group** symmetry of the basis. Each operation of the point group must turn the atomic arrangement of the crystal into itself. For three-dimensional periodic structures, there are 230 distinct symmetries available. These combinations are called **space-groups** [6].

The **Miller indices** form a notation system in crystallography for planes and directions in Bravais lattices. The Miller indices describe all crystallographic planes within the unit cell. A family of lattice planes is determined by three integers, which are written (hkl) [6]. Directions or rows of atoms in the lattice are specified by the coordinate of the nearest lattice point to the origin in the chosen direction. A direction is written $[uvw]$ and a set of symmetrically equivalent directions $\langle uvw \rangle$. The distance from the origin to the plane (hkl) lying within the unit cell is the interplanar spacing d_{hkl} .

1.1.2 The reciprocal lattice

A family of crystal planes (hkl) is completely characterised by the normal to the planes \mathbf{n}_{hkl} and the interplanar spacing d_{hkl} . To describe a structure, one uses the lattice in reciprocal space formed by the vectors given below [6]

$$\mathbf{G}_{hkl} = 2\pi \times \mathbf{n}_{hkl} / d_{hkl}. \quad (1.3)$$

Equation 1.3 tells that there is only one point in the reciprocal space for each family of planes in the direct lattice. Similarly to equation 1.1, the reciprocal lattice vector \mathbf{G} is written

$$\mathbf{G} = h \mathbf{A} + k \mathbf{B} + l \mathbf{C}, \quad (1.4)$$

with \mathbf{A} , \mathbf{B} , and \mathbf{C} , the unit vectors in the reciprocal space related to the unit vectors in the direct space by

$$\mathbf{A} = 2\pi \frac{\mathbf{b} \times \mathbf{c}}{\mathbf{a} \cdot (\mathbf{b} \times \mathbf{c})}. \quad (1.5)$$

\mathbf{B} and \mathbf{C} are given by the following relations

$$\begin{aligned} \mathbf{A} \cdot \mathbf{a} &= 2\pi \text{ and cyclic permutations,} \\ \mathbf{A} \cdot \mathbf{B} &= \mathbf{A} \cdot \mathbf{C} = \mathbf{B} \cdot \mathbf{C} = 0. \end{aligned} \quad (1.6)$$

1.1.3 The crystallographic restriction

Crystallographers classify lattices into families according to the symmetries which fix their lattice points and on how the symmetry group acts on the lattice. The lattice symmetry is governed by geometrical laws, thus a lattice can have n -fold rotational symmetry if $n=1, 2, 3, 4$ or 6 . This result is known as the crystallographic restriction [3].

As stated previously there are only 230 space groups permitted. Any arbitrarily chosen point group cannot readily be combined with translational symmetry [6]. As shown in figure 1.1, a 2D space can be easily tiled by rectangular, square, triangular or hexagonal tiles. These regular polygons have vertex angles equal to integral fractions of 2π making it possible to arrange lattice points in such a way that each of them is surrounded by six triangular tiles ($2\pi/6$), four square tiles ($2\pi/4$) or three hexagonal tiles ($2\pi/3$). Conversely, 5-fold and rotations of order over 6-fold are

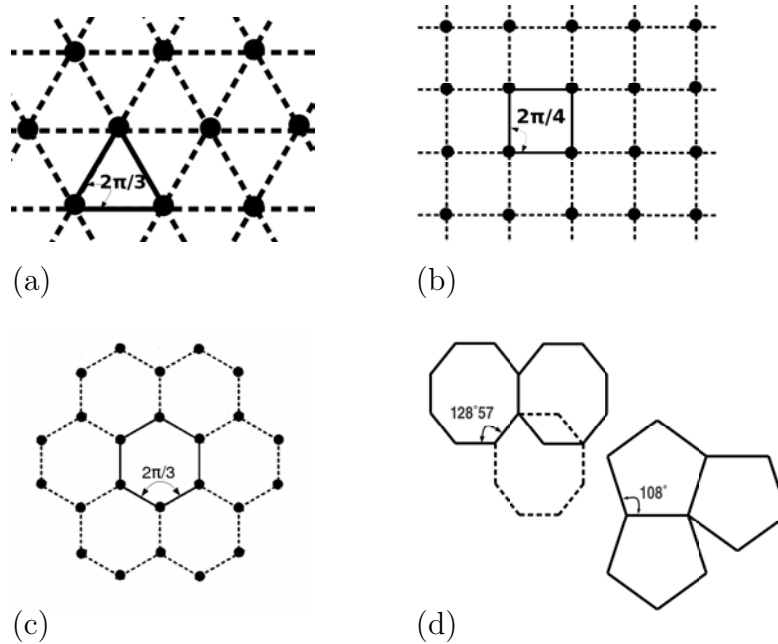


Figure 1.1: (a), (b), (c), permitted tilings (triangle, square, hexagon) and (d) impossible tilings (pentagon, heptagon,...) of the two-dimensional space.

forbidden by periodic space tiling. For a pentagonal tile, figure 1.1.d, the vertex angles are equal to 108° which is contained 3.33 times in 2π that is three pentagons plus an angular gap of 36° . Heptagons are not acceptable either as their vertex angles are equal to $128^\circ 57'$ which is contained 2.8 times in 2π .

As detailed in section 1.2, a crystallographic restriction is dimension dependent

as is the set of possible symmetry operations. Five and twelve fold axes become possible in 4D, and 7-fold in 6D [3].

1.2 Quasiperiodicity and long-range order structures

In this section we will discuss the Penrose tiling which is crucial for the understanding of quasicrystal structure. Beforehand, we will introduce the concepts of tiling and covering then the Fibonacci sequence both mathematically and phenomenologically with the projection method. The latter is an illustrative example of a way to generate quasiperiodic tilings.

1.2.1 Tilings and coverings

Tiling refers to a placement of one or more tiles with no overlaps in such a way that a plane is completely covered. In contrast, a covering is a placement of tiles that covers the plane but overlaps are allowed [9]. The mathematical basis of tilings has been described by Grünbaum and Shephard in the book "Tilings and Patterns" [10] where they outline the advances in the area of aperiodic tiling. This area of research had a major impact with the discovery of the Penrose tiling introduced in details in section 1.2.4.

A periodic tiling can be divided into finite cells. In figure 1.2, the tiles are parallelograms but they are not unit cells of the tiling because they differ in orientation. However, an aperiodic tiling can be of any kind; the deterministic quasiperiodic

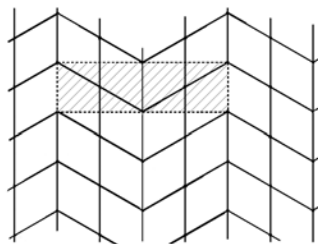


Figure 1.2: (a) The tiles of this parallelogram tiling are not unit cells. The actual unit cell is shown with a dotted line.

Penrose tiling (figure 1.3.a) or a "random" tiling (figure 1.3.b) are both aperiodic. A

quasiperiodic tiling however can be obtained by projecting a section of a tiling that is periodic in a higher dimensional space (section 1.2).

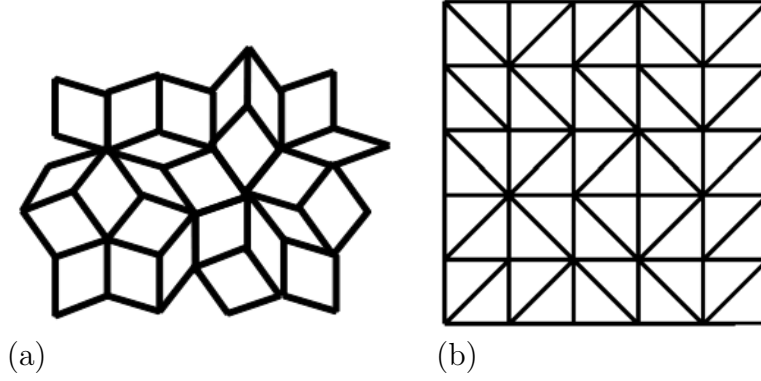


Figure 1.3: Two types of aperiodic tiling, (a) quasiperiodic Penrose tiling and (b) random tiling.

1.2.2 Fibonacci sequence

The Fibonacci sequence is obtained by an iterative application of the substitution rule

$$\sigma : L \rightarrow LS, S \rightarrow L \quad (1.7)$$

The substitution rule can be alternatively written employing the substitution matrix \mathbf{S}

$$\sigma : \begin{pmatrix} L \\ S \end{pmatrix} \rightarrow \underbrace{\begin{pmatrix} 1 & 1 \\ 1 & 0 \end{pmatrix}}_{=\mathbf{S}} \begin{pmatrix} L \\ S \end{pmatrix} = \begin{pmatrix} LS \\ L \end{pmatrix} \quad (1.8)$$

From equation 1.8, one can derive the scaling properties of the Fibonacci sequence from the eigenvalues λ_i of the substitution matrix \mathbf{S} .

$$\det|\mathbf{S} - \lambda\mathbf{I}| = 0, \quad (1.9)$$

where \mathbf{I} is the unit matrix. The evaluation of the determinant yields the characteristic polynomial

$$\lambda^2 - \lambda - 1 = 0 \quad (1.10)$$

with the eigenvalues

$$\lambda_1 = (1 + \sqrt{5})/2 = 2 \cos(\pi/5) = 1.618... = \tau, \quad (1.11)$$

$$\lambda_2 = (1 - \sqrt{5})/2 = -2 \cos(2\pi/5) = -0.618 = 1 - \tau = -1/\tau \quad (1.12)$$

and the eigenvectors

$$\mathbf{v}_1 = \begin{pmatrix} \tau \\ 1 \end{pmatrix}, \mathbf{v}_2 = \begin{pmatrix} -1/\tau \\ 1 \end{pmatrix}. \quad (1.13)$$

The eigenvalue equation $\mathbf{S} \mathbf{v}_i = \lambda_i \mathbf{v}_i$ can now be written explicitly

$$\begin{pmatrix} 1 & 1 \\ 1 & 0 \end{pmatrix} \begin{pmatrix} \tau \\ 1 \end{pmatrix} = \begin{pmatrix} \tau + 1 \\ \tau \end{pmatrix} = \tau \begin{pmatrix} \tau \\ 1 \end{pmatrix}. \quad (1.14)$$

By identification of the above equation with 1.8, we replace the matrix $\begin{pmatrix} L \\ S \end{pmatrix}$ by $\begin{pmatrix} \tau \\ 1 \end{pmatrix}$ to show that an infinite Fibonacci tiling $s(\mathbf{r})$ is invariant under scaling with the eigenvalue τ [4],

$$s(\tau \mathbf{r}) = s(\mathbf{r}). \quad (1.15)$$

1.2.3 Quasiperiodicity generated by the projection method

Quasiperiodic structures can have orientational symmetries not compatible with space groups of periodic structures. However these "forbidden" point group symmetries may be allowed with a periodic tiling of increased dimensionality. For example, 5-fold rotations with a regular pentagon (five vertices) may be completely defined with four vectors. Thus, four space dimensions are required to accommodate periodic tiling made of tiles which have the rotational symmetry of a pentagon.

In a similar way, the 1D Fibonacci chain can be generated from a 2D space. To create this structure, we start with a 2D square lattice that has coordinates $(Ha, H'a)$ on the basis $(\mathbf{e}_1, \mathbf{e}_2)$ with a the lattice parameter of the 2D square lattice and H, H' integers (figure 1.4). Thus the lattice points are defined by

$$\mathbf{R} = H a \mathbf{e}_1 + H' a \mathbf{e}_2. \quad (1.16)$$

The lattice sites are projected into a 1D subspace which is a straight line given by an angle α with the horizontal rows of the square lattice. We call this axis r_{par} . It is viewed as the "physical space" where the quasicrystalline structure lies. r_{perp} is the axis perpendicular to r_{par} and is referred as the "perpendicular space". r_{perp} has no physical meaning but serves for the mathematical description. The lattice points have components in the coordinate system (R_{par}, R_{perp}) defined by the following equation

$$\begin{aligned} R_{par} &= \mathbf{R} \cdot \mathbf{r}_{par}, \\ R_{perp} &= \mathbf{R} \cdot \mathbf{r}_{perp}. \end{aligned} \quad (1.17)$$

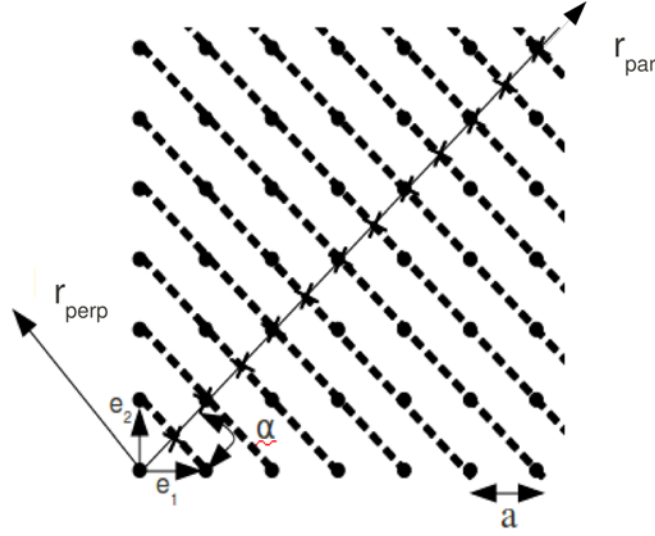


Figure 1.4: 1D illustration of the projection method with \bullet the 2D square lattice and \times the projected 1D periodic structure. The slope of the 1D space (α) is rational with respect to the lattice rows.

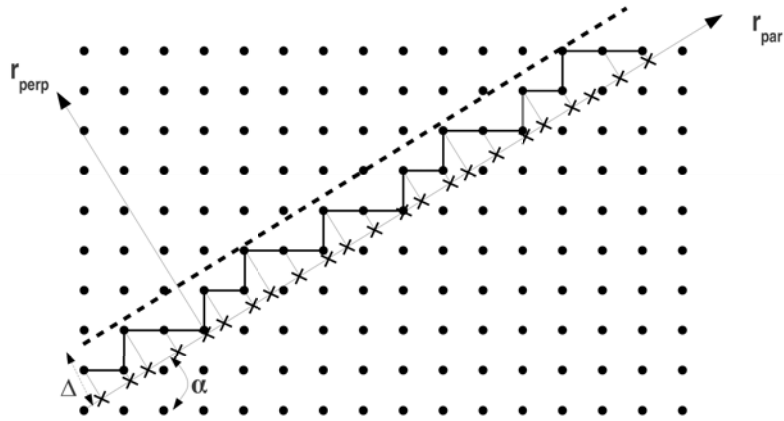


Figure 1.5: 1D illustration of the projection method. The slope is irrational, the projection of the square lattice into R_{par} is a perfect non-periodic structure made of two tiles of incommensurate size. With the slope α equals to τ , one obtains the Fibonacci chain.

If $\tan \alpha$ is a rational number with respect to the rows of the square lattice, the projected 1D structure is a discrete periodic set of sites (figure 1.4). Conversely, if $\tan \alpha$ is irrational, the projected 1D structure is no longer periodic. The projected set of points is dense and for an atomic description, the 1D structure would exhibit non-physically short atomic distances. To relax the density, the projection on r_{par} is restricted to the points confined within a strip parallel to r_{par} which has a cross-section Δ in the perpendicular r_{perp} as shown in figure 1.5. The length of the cross-section is given by the following equation

$$\Delta = a \cos \alpha + a \sin \alpha. \quad (1.18)$$

In the particular case where the slope α of r_{par} with respect to the horizontal rows is given by

$$\tan \alpha = 1/\tau, \quad (1.19)$$

the 1D projected structure is made of two tiles whose lengths are those of a Fibonacci chain as shown in figure 1.5 with

$$\begin{aligned} L &= a \cos \alpha, \\ S &= a \sin \alpha. \end{aligned} \quad (1.20)$$

The coordinates of the lattice points are given by the following relations

$$R_{par} = Ha \cos \alpha + H'a \sin \alpha = (H\tau + H')a \sin \alpha, \quad (1.21)$$

$$R_{perp} = H'a \cos \alpha - Ha \sin \alpha = (H'\tau - H)a \sin \alpha. \quad (1.22)$$

Using $\sin \alpha = (2 + \tau)^{-\frac{1}{2}}$ derived with trigonometric arguments from equation 1.19, R_{par} and R_{perp} can also be written as following

$$R_{par} = \frac{a}{(2 + \tau)^{\frac{1}{2}}} (H\tau + H'), \quad (1.23)$$

$$R_{perp} = \frac{a}{(2 + \tau)^{\frac{1}{2}}} (H\tau - H'). \quad (1.24)$$

The atoms in the Fibonacci chain are at the position

$$x = R_{par} = a(H\tau + H')/(2 + \tau)^{\frac{1}{2}}, \quad (1.25)$$

with $|R_{par}| \leq \Delta/2$ that is to say with (H, H') satisfying the condition

$$|(H'\tau - H)| \leq (1 + \tau)/2 = 1.309 \dots \quad (1.26)$$

as shown in figure 1.5.

In this section we have discussed the projection method that provides an easy way to generate quasiperiodic tiling.

1.2.4 Penrose tiling

This section will introduce the tools to answer the following question of importance for quasicrystals: "How many different types of tiles are needed to tile the 2D space in a purely aperiodic manner without overlapping tiles or empty spaces between them?". The answer to this question came in 1974 as "2 tiles" in Roger Penrose's aperiodic tiling of the plane in his article "The Role of Aesthetics in Pure and Applied Mathematical Research" [11]. He used two rhombs with equal side lengths but different opening angles. The resulting tiling is non-periodic, has long-range orientational order with five-fold symmetry and is self-similar. Penrose says he invented his tiling as a game. However, N.G. de Bruijn in 1981 displayed the mathematical potential of the method with the projection from higher-dimensional space [12] discussed in section 1.2.3 which was later used in connection with quasicrystals. R. Ammann used the corresponding rhombohedra instead of the rhombi to create the first generalisation to Penrose tiling in 3D [13].

Penrose tilings are made of two rhombs. The skinny rhomb has angles of 36° ($\theta = \pi/5$) and 144° (4θ) and the fat rhomb has angles of 72° (2θ) and 108° (3θ). With the edge of the rhomb defined as a unit length, the long diagonal of the fat rhomb is τ and the short diagonal of the skinny rhomb is $1/\tau$. Penrose tiles have arrows on their edges that must be matched in order to complete a tiling. The

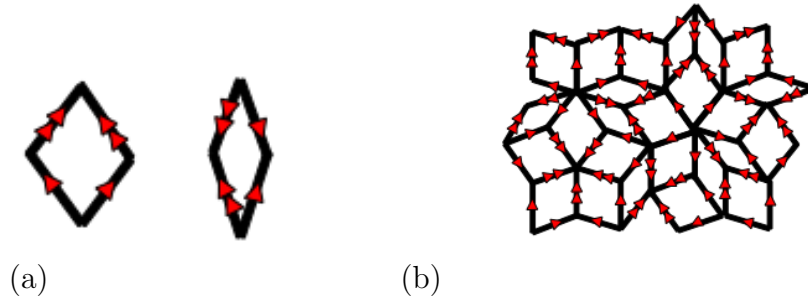


Figure 1.6: (a) the two rhombs used for the penrose tiling with matching rules expressed as arrowed edges. (b) 2D Penrose tiling

matching rules for the rhombs are shown in figure 1.6.a, the edges are marked with single and double arrows making the tiling an oriented graph. Figure 1.6.b shows a Penrose tiling with the arrowed tiles. The matching rules do not generate a tiling automatically. Some local configurations cannot be extended as shown in figure 1.7.

A Penrose tiling can also be generated from another one by an inflation procedure. This tiling is called the inflated tiling. The self-similarity of a 2D Penrose

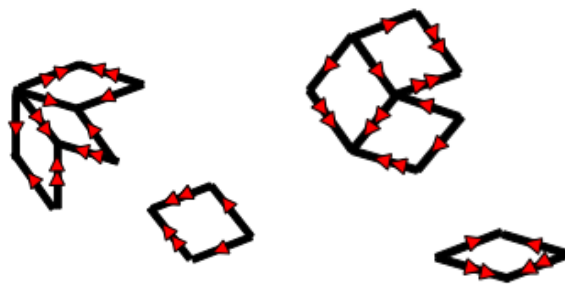


Figure 1.7: two incompletable configurations

lattice is depicted in figure 1.8 with the tiles scaled by τ .

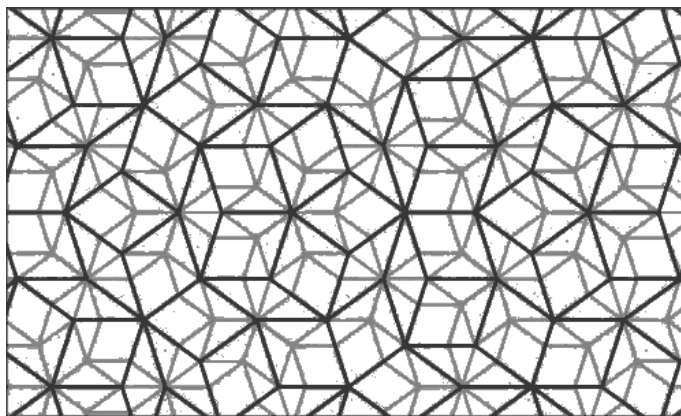


Figure 1.8: Scaling of original penrose tiling by S , the generated Penrose tiling is congruent to the original one, enlarged by a factor τ .

In this section, it was shown that any periodic structure of dimension n can yield a quasicrystalline structure in $n - 1$ dimensions. We introduced the projection method to generate 1D aperiodic structures, including the Fibonacci sequence, from a regular array of points. We also introduced the 2D Penrose tiling emphasising the self-similarity of quasicrystalline structures within rescaling.

In the next section, we will discuss quasicrystallinity in alloys. The first quasicrystals observed were metastables but stable quasicrystals in the decagonal and icosahedral phases were quickly discovered. We will introduce elements to understand their stabilisations in these phases. The discussion will be mainly on the decagonal quasicrystals, atomic clusters which are the building units and on the indexing method of decagonal quasicrystals.

1.3 Incommensurate structures and approximants

Before the discovery of quasicrystals, solid-state physics studied incommensurate modulated phases and composite crystals with a modulated structure. The modulation refers to a distortion or a static perturbation characterised by its own independent periodicity.

Incommensurate structures can be viewed as underlying periodic lattices with actual atom positions displaced with respect to the lattice sites. Although the displacement is periodic, the lattice and displacement are not in a rational ratio. The diffraction patterns of these phases exhibit Bragg maxima arranged with usual crystal symmetry surrounded by satellite reflections. An example of an incommensurate structure can be large atoms deposited on a surface made of smaller atoms as in the system Kr/graphite. When the density of the adlayer's atoms is too high, the atoms rearrange themselves out-of-phase with the supporting surface due to geometric constraints. The 3D structure and its modulation can be presented in 4D space in which the fourth dimension "stores" the phase information as a new degree of freedom. When excited, this new degree of freedom can lead collective excitations called phasons in analogy to phonons.

An approximant is a periodic crystal which has a large unit cell within which the substructure is based on similar cluster types as those found in an aperiodic sample. The chemical composition is also very close to the parent quasicrystal. A crystalline approximant has a composition and structural unit very similar to the quasicrystal ones but is nevertheless a crystal.

1.4 The various families of quasicrystals

Shechtman *et al* reported the observation of an icosahedral symmetry after heat treatment of a rapidly solidified AlMn alloy [1]. Chattopadhyay *et al* studying the same system identified a phase made of a periodic stacking of two-dimensional quasiperiodic planes making the quasicrystal periodic along one direction [14]. Bendersky arrived at the same conclusion and established the symmetry as $10/mmm$ (10-fold) for the 2D quasiperiodic plane by electron diffraction [15]. After the discovery of this decagonal quasicrystal, other two-dimensional quasicrystals were discovered; octagonal [16], dodecagonal [17], and a 2D pentagonal quasicrystal [18]. Furthermore, cubic [19] and hexagonal quasicrystals [20] have also been observed. He *et al* dis-

covered a phase quasiperiodic along a two-fold direction (digonal phase) [21].

Quasicrystals are known to form in metastable or stable phases in more than a hundred alloy systems. Most of these stable quasicrystals are alumnides. We will introduce stable and metastable quasicrystals. Furthermore, we will focus on aluminium rich quasicrystals and especially the decagonal (d) AlNiCo phase that is used for the experiments.

1.4.1 Metastable quasicrystals

Metastable quasicrystals are characterised by a high degree of disorder. These alloys exhibit periodic ordering when heated and adopt a quasicrystalline structure by rapid quenching of the melt. After the discovery of metastable Al₆Mn quasicrystals, a number of attempts were made to find other quasicrystalline phases.

The first icosahedral alloy was discovered in Al₆Mn. Substituting Mn with other transition metals or by adding metalloids, icosahedral (i) phases were found in binary alloys of Al with Fe, Cr, Ru, V, W, and Mo. These alloys were prepared by melt-spinning with typical quenching rates of $\sim 10^6$ K/s [22]. This method yields micron-size grains of quasicrystalline phases in an Al matrix. After this discovery, a decagonal phase was found in the same alloy using a slower cooling or subsequent annealing. Decagonal, icosahedral, and crystalline phases coexist often in the material. However, i -quasicrystals form preferentially in the Al-early transition metal (TM) systems (AlCr, AlV, AlMn, and AlMo) whereas the d phase forms in the Al-late transition metal (TM) systems (AlFe, AlCo, AlNi, and AlRh). Along with the position of the elements in the periodic table, the structure of quasicrystals has been found to be related to their corresponding approximant crystals. The approximant crystals of icosahedral quasicrystal are cubic or orthorhombic, whereas in the decagonal phase they are orthorhombic or monoclinic [8].

Other symmetries have also been observed such as 2D octagonal in rapidly solidified CrNiSi [23] or a dodecagonal in BiNi alloys [24].

1.4.2 Stable quasicrystals

Stable quasicrystals were discovered in ternary and quaternary alloys by substitution of Al with other TM elements. Another class of stable quasicrystals was discovered in the MgAlZn system. The quasicrystalline phase is obtained by conducting rapid solidification from the crystalline approximant. Tsai *et al*, discovered

the stable AlCuFe five-fold quasicrystal being inspired by a paper by Henley and Elser that pointed out the relationship between quasicrystals and certain crystalline compounds [25]. Tsai *et al* looked for structures with large lattice parameters and local units with five-fold symmetry and noticed the existence of the tetragonal crystalline compounds $\text{Al}_7\text{Cu}_2\text{Fe}_1$ ($a = 0.634\text{nm}$, $c = 1.487\text{nm}$). Rapid solidification of this alloy formed a mixture of quasicrystalline matrix and amorphous phases in the grain boundaries. The quasicrystal had a composition close to $\text{Al}_{65}\text{Cu}_{20}\text{Fe}_{15}$. Tsai *et al* then prepared melt-spinning of this alloy to get mostly single quasicrystalline phase with grains of the size of a few tenths of micrometers, which was the biggest reported at the time [26]. This sample turned out to be stable. Further discoveries were made by replacing Fe in AlCuFe by elements located in the same row on the periodic table. This was the discovery of high-strength Al based amorphous alloys as AlCuV, AlCuZr, or a new group of stable quasicrystals such as AlCuRu or AlCuOs [8].

Many other quasicrystal alloys were found by replacing same column elements leading to the discovery of several types of decagonal quasicrystals. Amongst the decagonal quasicrystals, AlNiCo was found to be thermodynamically stable over a wide range of composition and temperature [27]. Stable decagonal quasicrystalline phases were also found in AlNiFe [28] and Al-Ni-Ru [29] alloys but AlNiCo remains the most studied decagonal phase.

1.5 Alumnides

Alumnides can be found in a large variety of forms from solid solutions, disordered alloys and ordered compounds to quasicrystals. These alloys possess high strength, light weight and some of their phases are thermodynamically stable. In the quasicrystal phase they display very high structural quality [30].

The discovery of quasicrystalline phases in the AlMn system has revived the interest for alumnides containing transition metal atoms [31–33]. When the first thermodynamically stable quasicrystals became available, experiments showed unusual electronic [34] and magnetic properties [35]. For example, AlMn quasicrystals are diamagnetic in spite of containing significant contribution of transition metals.

With the discovery of thermodynamically stable quasicrystals [36] with structural perfection as good as in the best periodic alloys [37] it became possible to

understand the influence of the quasicrystalline phase on their physical properties. The first studies of quasicrystals were mostly focused on *i*-alloys. Some striking features include a very high value of the electrical resistivity not expected for an alloy consisting of normal metallic elements (0.01 $\Omega\cdot\text{cm}$ for the *i*-AlPdMn system at room temperature compared with 28 n $\Omega\cdot\text{cm}$ for Al) and their temperature coefficients of resistivity is often negative in disagreement to the behavior of typical metals. [34, 38–40]. Additionally, the resistivity is very sensitive to the sample composition and increases as their structural quality improves. The poor conductance of quasicrystals has stimulated a search for the existence of an energy gap at the Fermi level [41, 42]. Quasicrystals exhibit unusual surface properties which have stimulated numerous experiments: low friction, low adhesion, and good oxidation resistance [8].

Al-rich quasicrystals are unexpected regarding their chemical compositions, they are brittle, hard, and poor conductors of heat and electricity [8]. Their brittleness make them poor candidates for bulk applications but still render them viable for coating and for composites in which interfaces are of prime importance.

The aluminium based quasicrystals can be classified according to their constituents

- "*sp quasicrystals*", containing elements with *s* and *p* valence electrons (Al, Si, Mg, Zn, Au, Li, Ga, Cu). The 3d electrons of Cu atoms are considered as core electrons as they have minor influence at the Fermi energy.
- "*spd quasicrystals*", containing transition metal elements of the 3d, 4d, or 5d series: V, Cr, Mo, Mn, Re, Fe, Ru, Os, Co, Ni, Pd,...

All stable and metastable aluminium based quasicrystals are summarised in table 1.2 in the icosahedral and decagonal phases. The alloys of very high structural quality are printed in bold.

1.5.1 Stabilisation of quasicrystals

An alloy structure is stable if it has the lowest free energy $F = U - TS$ amongst the competing phase. For an ordered phase, the entropy has a minor contribution and the internal energy of a structure is often calculated at 0 K. The factors that influence the free energy F most are therefore the internal energy which depends of the electronegativity difference of the elements, atomic size ratios, and band-structure considerations. In alloys and especially in metals, band-structures are related to the

	sp quasicrystals Frank-Kasper type $e/a \simeq 2.0 - 2.2$	spd quasicrystals Mackay type $e/a \simeq 1.7 - 1.9$
Meta-stable	<i>Icosahedral phases</i> Al-Mg-Zn Al-Mg-(Cu, Ag) Al-Li-(Au, Zn)	<i>Icosahedral phases</i> Al-TM (TM=V, Cr, M, Ru, Re,...) Al-(Mn, Cr)-Si, Ge <i>Decagonal phases</i> Al-TM (TM=Mn, Fe, Co, Pd) Al-(Cu, Ni, Pd)-TM (TM=Fe, Mn, Co, Rh, Ir)
Stable	<i>Icosahedral phases</i> Al-Li-Cu	<i>Icosahedral phases</i> Al-Cu-TM (TM= Fe , Ru , Os) Al-Pd-TM (TM= Mn , Re) Al-Mn-Si <i>Decagonal phases</i> Al-Cu, Ni-TM (TM= Co , Rh, Ir) Al-Pd-TM (TM= Mn , Re)

Table 1.2: Al based quasicrystals from [43]. Alloys printed in bold are quasicrystalline states of very high structural quality. The ratio e/a refers to the number of valence electrons per atom.

overlap of neighbouring atomic wave-functions where conduction electrons are delocalised throughout the structure. For transition metal alumnides, the differences $\Delta\chi$ in electronegativity are small ($\Delta\chi \simeq 0$). The atomic size ratio in these systems is also close to one indicating that band structures must play a major role in the stability of these phases.

To date there is no a general rule which can be used to predict which alloys and at which compositions a quasicrystal may be found. However, the existence of a large unit cell tetrahedrally close-packed phase (Frank-Kasper phase) is a favourable circumstance for the formation of quasicrystals.

The successful replacement of Fe by Ru and Os also suggests a stabilisation by the electronic structure since these three quasicrystals exhibit a value of the electron/atom ratio of 1.75. Gratias *et al* [44] showed that the icosahedric phase in the Al-Cu-Fe phase diagram is located along a line defined by the equation $e/a \simeq 1.86$, e/a being the number of valence electrons per atom. The e/a ratio is a determinant parameter for quasicrystal stability. It allows as well the classification of quasicrystals according to their related phases from their electronic properties and their local atomic order.

1.5.2 d -AlNiCo, a decagonal quasicrystal

Soon after the discovery of icosahedral quasicrystals with quasiperiodic bulk structure in all three dimensions [1], a decagonal phase was identified in the Al-Mn system by Bendersky *et al* [15]. Decagonal AlMn was only metastable, and stable decagonals were discovered later in the ternary AlCuCo [45] and AlNiCo [37]. Sato *et al* made available the first single d -AlNiCo quasicrystal of excellent quality at the centimetre scale [46].

The decagonal phase presents periodicity in one plane and quasiperiodicity with a 10-fold symmetry in the orthogonal plane. In other words, decagonal quasicrystals can be seen as a stacking of quasiperiodic planes. They possess two sets of five equivalent 2-fold symmetry axes rotated by 18° in the quasiperiodic plane as illustrated by figure 1.9. The full periodicity can be recovered in a 5 dimensional space

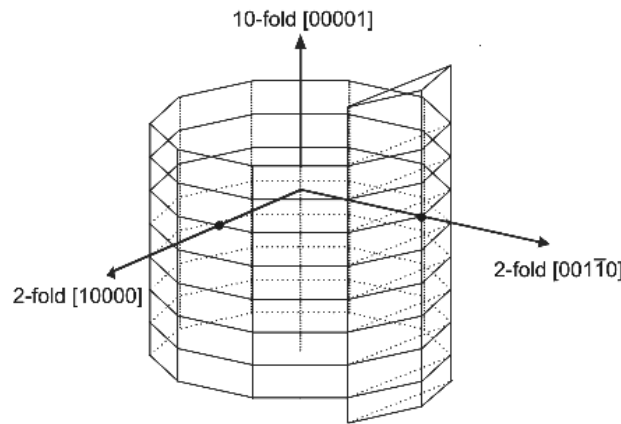


Figure 1.9: Schematic view of a d -quasicrystals showing stacking along the periodic axis and the two inequivalent (10000) and $(101\bar{1}0)$ 2-fold surfaces. Figure reprinted from [47].

using the Miller indices as shown by figure 1.10. (00001) is the plane perpendicular to the vector $[00001]$ (10-fold) and the two inequivalent 2-fold planes perpendicular to the vectors $[10000]$ and $[101\bar{1}0]$ are referred to as the (10000) and $(101\bar{1}0)$ planes, respectively.

Decagonal phases offer a unique opportunity to compare physical properties along the periodic and quasiperiodic direction. For instance, the electrical resistivity in $\text{Al}_{70}\text{Ni}_{15}\text{Co}_{15}$ along these two directions was found to be in a 30 to 1 ratio [49]. As expected, many other properties display a strong anisotropy, Hall effect [50], thermopower [51], thermal conductivity [52], optical conductivity [53] or mechanical [54]. The Hall coefficient R_H of d -quasicrystals is positive ($R_H > 0$) for an applied mag-

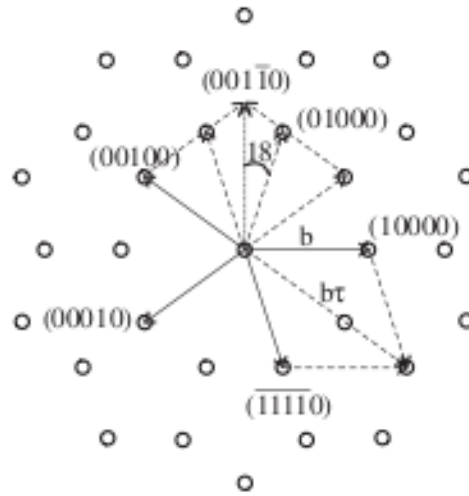


Figure 1.10: Schematic of the indexing of a decagonal quasicrystal. The circles refer to the positions of diffraction spots generated and projected normal to the periodic axis. Figure reprinted from [48].

netic field lying in the quasicrystal plane whereas it changes sign to negative ($R_H < 0$) when the field is applied along the periodic direction.

Gille *et al* observed facets at the surface of Czochralski-grown single crystals namely the decagonal dipyrramids ($\{00\bar{1}\bar{1}1\}$ and $\{10\bar{1}02\}$), the decagonal prisms ($\{10000\}$ and $\{10\bar{1}00\}$) and the pinacoid $\{00001\}$ [55]. Steurer and Cervellino ranked the 16 strongest reflections of d -AlNiCo according to the scattering factors [56] allowing to draw the ideal shape of a decagonal quasicrystal as shown in figure 1.11.

The stability of quasicrystals revolves around the relative roles of energy and entropy. The energetic mechanism postulates that interactions among the tiles favour a unique quasiperiodic ground state. The entropy mechanism states there is no unique quasiperiodic state but quasiperiodicity in the long-range order is a property of "random tiling". According to Dieter and Veit the energy mechanism argues in favour of growth getting in the way of perfection whereas the entropy view-point argues the opposite; growth may be fundamental in providing a pathway to the entropically stabilised state [58]. In their paper, they describe a theoretical model that show that the maximum entropy state of a random tiling quasicrystal is accessible through growth alone. The extremely slow kinetics of attachment in the growth direction perpendicular to the 10-fold axis is considered in the growth protocol [59].

AlNiCo exhibits a number of different decagonal phases depending on the exact composition and temperature [48]. The different phases are summarised in the

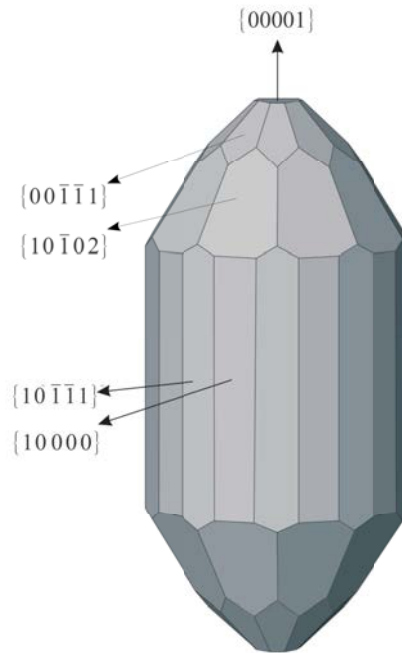


Figure 1.11: Ideal shape of a decagonal AlNiCo showing the decagonal dipyramids $\{00\bar{1}\bar{1}1\}$ and $\{10\bar{1}02\}$, the decagonal prisms $\{10000\}$ and $\{10\bar{1}00\}$ and the pinacoid $\{00001\}$. Figure reprinted from [57].

phase diagram in figure 1.12. There are many different quasicrystalline phases in this diagram referring to different structural varieties [61, 62]. Edagawa *et al* reported weak diffraction spots upon the annealing of $\text{Al}_{70}\text{Ni}_{15}\text{Co}_{15}$ situated at the centres of pentagons [62]. Upon annealing, these superlattice peaks start losing intensities at 750°C . At 850°C one set of superlattice peaks reaches 40% of the initial intensity while the other one disappears completely. It shows that there are two independent order parameters in this system. The former set of superlattice spots are called the S1 spots while the latter that disappears completely are called the S2 spots [7]. The type I superstructure displays both S1 and S2 reflections, the type II superstructure displays a ring-like zone of low diffraction intensities and reflections at the position of half-integer indices [63]. $5f$ and $5f_{HT}$ are 1D periodic 5-fold states with a superstructure for the latter. Finally other structure varieties are referred to as the Co and Ni rich phase [64, 65]. The phases differ in their tilings. The structure of S1-state, type-I superstructure, type-II superstructure and $5f_{HT}$ phases show diffraction patterns with so-called superlattice reflections. On the other hand, the Ni-rich and Co-rich phases without superlattice reflection are formed by a pentagonal quasiperiodic arrangement of large atomic clusters with a decagonal section of 3.2 nm in diameter,

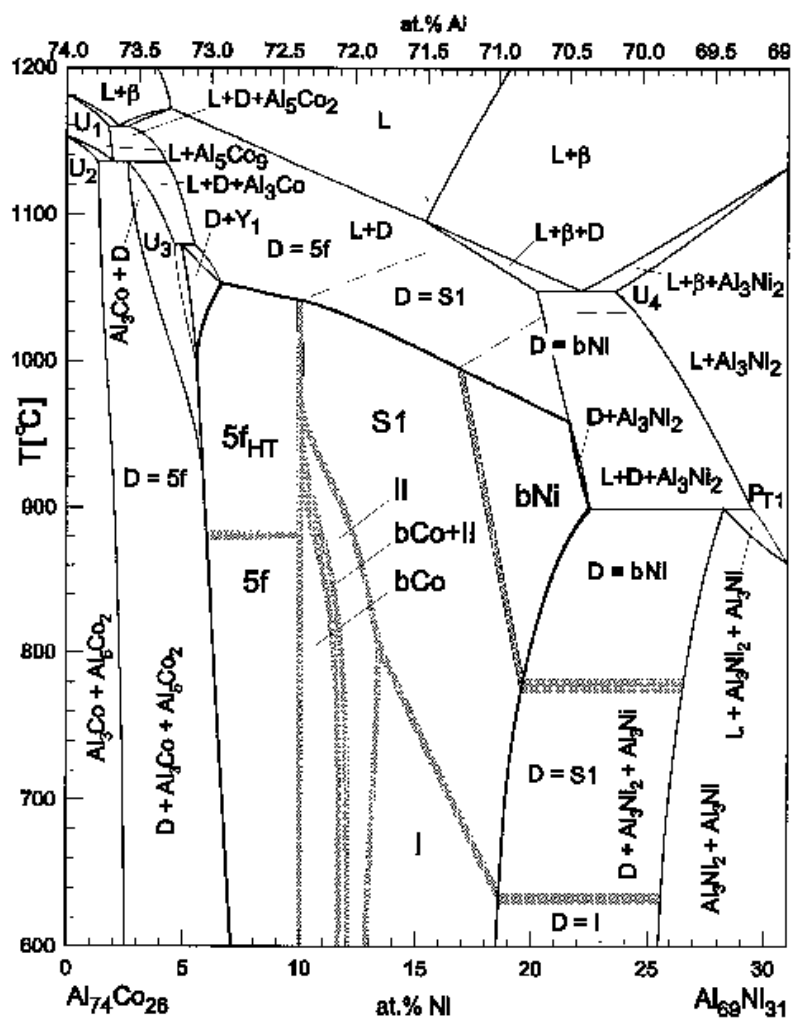


Figure 1.12: Temperature against composition section along the composition line $\text{Al}_{74}\text{Co}_{26}\text{-Al}_{69}\text{Ni}_{31}$. This composition line is the maximum extension of the stability region of the decagonal phase. Abbreviations: L, liquid; D, decagonal phase in general. Figure reprinted from [60].

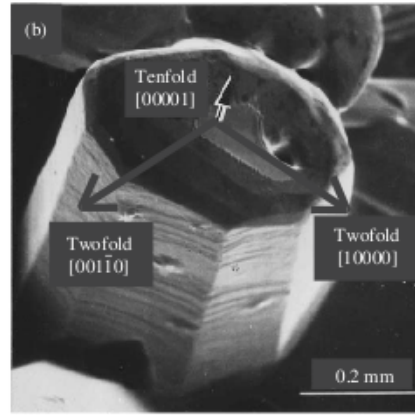


Figure 1.13: SEM image of a *d*-AlNiCo single grain showing the different high symmetry axes. Figure reprinted from [48].

which is τ times as large as the atomic clusters in the other phases [66]. All phases share some common characteristics. The interplanar distance along the periodic axis is approximately 2 \AA [67, 68]. The structure can be described by columnar clusters of 20 \AA diameter with a pentagonal symmetry within each plane [69] as shown in figure 1.13.

Decagonal quasicrystals consist of quasiperiodic atomic layers stacked according to different sequences. The structure can be described in terms of columnar clusters parallel to the ten-fold axis [8]. The columnar cluster model can be described as a three-dimensional extension of a two-dimensional Penrose tiling. The atoms are arranged analogously to the rhombic Penrose tiles and the interactions connecting clusters are comparable to the Penrose matching rules. The clusters have pentagonal symmetry, and are rotated at each plan by 36° .

It was widely accepted that two types of clusters were necessary to force quasiperiodicity, but Steinhardt *et al* [70] have proposed a new model for the quasicrystalline structure of $\text{Al}_{72}\text{Ni}_{20}\text{Co}_8$ using a single repeating "quasi-unit-cell". Instead of the two incommensurate lengths from the two different tile shapes, quasiperiodicity can be obtained by allowing the nearest-neighbour distances between clusters to overlap as shown in figure 1.14. An overlapping means that unlike a periodic unit cell, the clusters can share atoms. To determine the atomic structure, one must determine the atomic distribution within the decagonal tile. Steinhardt *et al* have proposed the atomic structure shown in figure 1.15.a. Because of its high structural quality, AlNiCo allows the complete identification of atomic positions. Image 1.15.b shows an HAADF image (HAADF imaging mode is discussed in section 4.9) of a

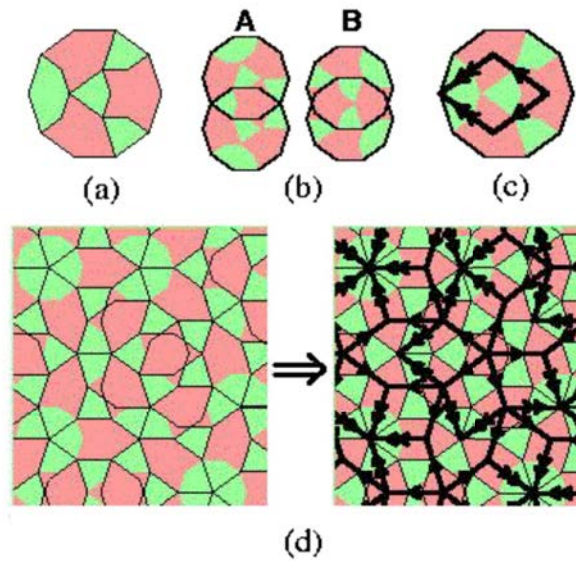


Figure 1.14: A quasiperiodic tiling can be forced using marked decagons (a). Two decagons are allowed to overlap if shaded regions match. Two overlapped regions lead to two possibilities, small (A-type) or large (B-type). Inscribing a decagon with an obtuse rhombus (c), a Penrose tiling appears from the overlapped decagons. Figure reprinted from [70].

AlNiCo sample showing atom positions. On top of the TEM image (figure 1.15.a) is superposed the atomic model introduced above (figure 1.14). The resulting structure provides a better fit than previous models including Penrose tiling.

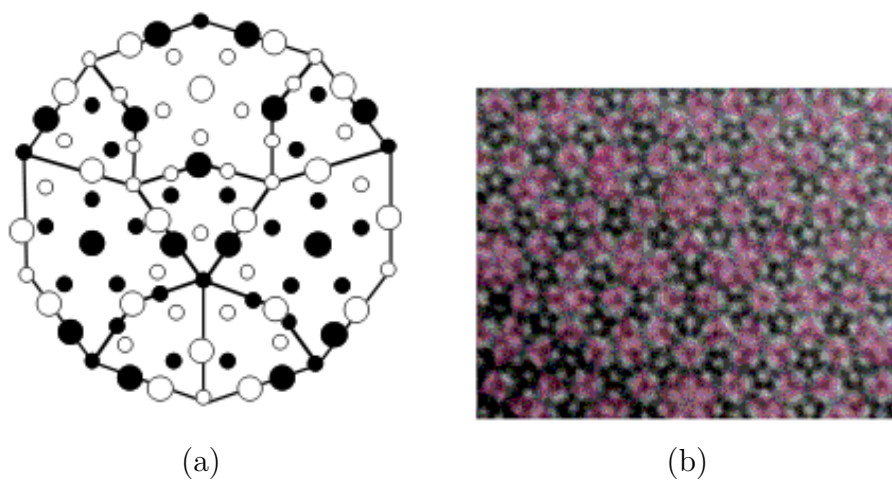


Figure 1.15: (a) candidate model for the atomic decoration of the decagonal quasi-unit-cell. Large circles are Ni and Co and small circles are Al. Solid and open circles are layers at $c = 0$ and $c = 1/2$ along the periodic c -axis. After [9] and reference therein. (b) superposition of a perfect decagon tiling placed over the HAADF image of Al-Ni-Co. Figures reprinted from [70].

1.5.3 Icosahedral quasicrystals

Quasicrystals with icosahedral diffraction symmetry are called icosahedral quasicrystals. In 1986, the first stable icosahedral quasicrystal was discovered in the system AlCuLi [71, 72]. Their structures are quasiperiodic in three dimensions and they are therefore referred to as 3D quasicrystals. There are no 3D quasicrystals known with symmetry other than icosahedral.

The 3D analogue to the pentagon is the icosahedron. It is characterised by 5-fold, 3-fold, and 2-fold rotational symmetries. This symmetry can be visualised directly on the SEM image of an as-grown single-grain as shown in figure 1.16 or as in figure 1.17 with the electron diffraction patterns of an AlPdMn showing quasiperiodic reflection arrays in three orientations. In 3D, 5-fold rotations are fulfilled

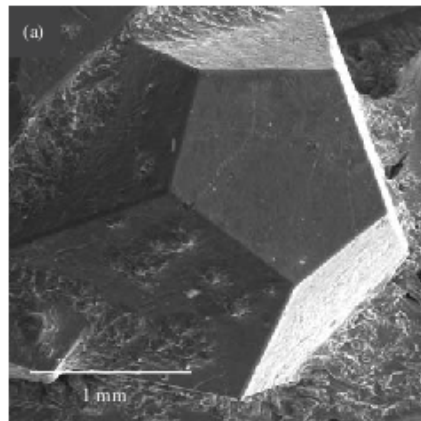


Figure 1.16: SEM images of a *i*-AlPdRe single grain showing the different high symmetry axes. Figure reprinted from [48].

with a regular icosahedron defined by six of the vectors from centres to vertex and consequently at least a 6D space is required to accommodate a periodic lattice with icosahedral symmetry. The rotational symmetry of an icosahedron is 6 five-fold axes, 10 three-fold axes (from center to triangular faces), 15 two-fold axes (from center to middle edges).

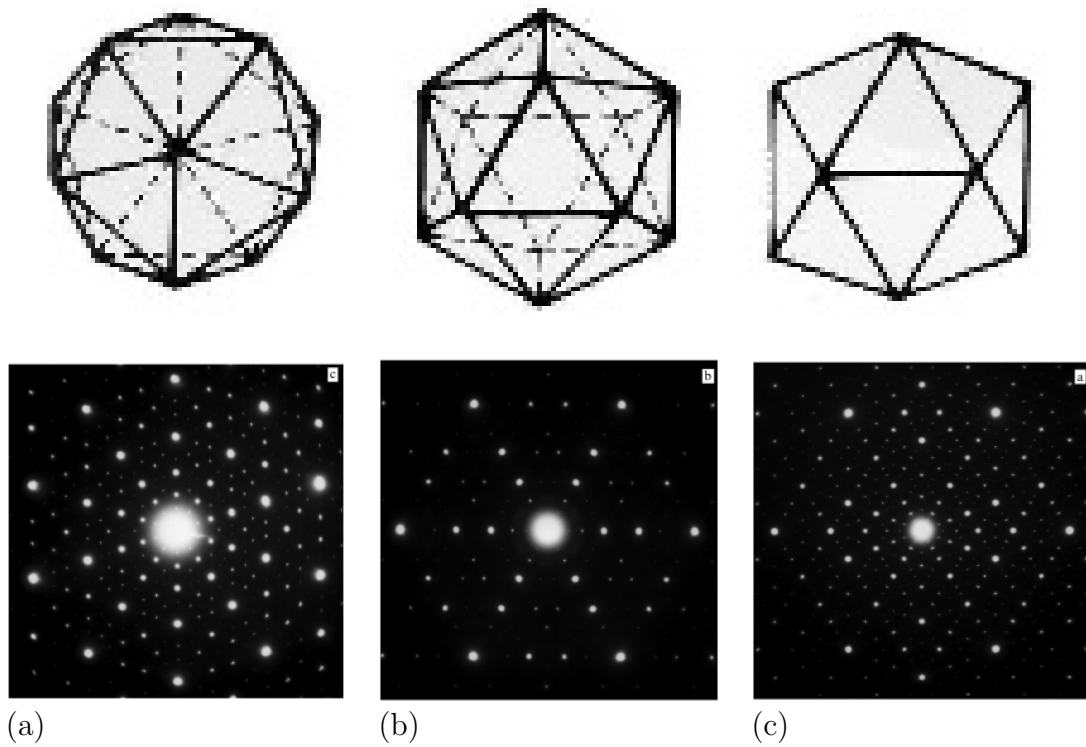


Figure 1.17: Top, an icosahedron viewed along its (a) 5-fold, (b) 3-fold, and (c) 2-fold symmetry axis. Bottom, corresponding diffraction pattern of above symmetry from an $i\text{-Al}_{69.5}\text{Pd}_{21}\text{Mn}_{9.5}$ quasicrystal. Figure reprinted from [73].

Chapter 2 : Quasicrystal Thin Films

In the thin film limit, a quasicrystal substrate can induce its own ordering to an overlayer. If one can form a truly 2D structure, then the overlayer could be of a single element whereas, in the bulk, quasicrystals require a combination of at least two elements. Quasicrystals in this new form could be used to extend the understanding of the relationship between quasiperiodicity and the resulting physical properties independently of the complex chemistry. Such overlayers could also be attractive for the study of electronic and dynamic phenomena in 2D.

In this chapter we will discuss the state of the art of the surface science of quasicrystals, including oxidation effects, surface preparation and quasicrystal thin film growth modes.

2.1 Oxidised surfaces

Passivation by an oxide layer is common among Al-rich quasicrystals as it is generally for Al alloys. Thiel *et al* exposed an AlCuFe quasicrystal to air at room temperature after sputter-annealing in UHV [8]. The sample was analysed with X-ray photoemission spectroscopy (XPS) (section 4.6) and X-ray induced Auger electron spectra (XAES), showing Al-induced oxidation only. The oxide depth of *i*-AlPdMn is 22-29 Å as estimated by XPS techniques [74] and 23 Å with X-ray reflectivity and diffuse scattering techniques [22]. Humidity causes the film to be larger since in vacuum pure oxygen at room temperature generates an oxide film of 4-8 Å thick on *i*-AlCuFe [22].

2.2 Topography and surface preparation

In order to produce atomically flat surfaces, the sputter-annealing method has been found to be more efficient than *in-situ* cleavage. The latter forms aggregate of clusters at the surface of *i*-AlPdMn for example, which result in a very rough surface as analysed by Ebert *et al* with STM [75] and shown in figure 2.1. In contrast,

sputter-annealing cycles generate atomically flat surfaces on a polished surface. A study conducted by Papadopolos *et al* also showed that 0.25 μm diamond paste yields the best surface for STM experiments [76]. After sputtering the surface is very rough due to clusters at the surface as observed with scanning tunneling microscopy (STM) by Ledieu *et al* [77].

An STM experiment was carried out on $\text{Al}_{70}\text{Pd}_{21}\text{Mn}_9$ cleaved along either the fivefold or twofold axes within UHV [78]. Compared to a sputter-annealed surface, they observed a rough surface with an average corrugation of 10-15 Å (<1 Å for the sputter-annealed surfaces). The surface structure is made of cluster aggregates, the smallest of which are 8-10 Å in diameter, matching the size of the pseudo-Mackay icosahedron (9.6 Å) (figure 2.1). For the sputtered surface, this gives evidence that there are many intact pseudo-Mackay clusters in the surface region with other atoms filling the space between the clusters to yield a flat surface.

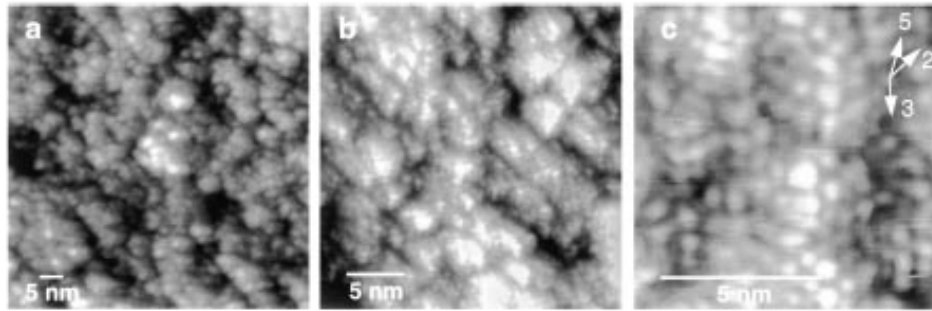


Figure 2.1: STM constant current images of the occupied density of states of an *i*-AlPdMn single crystal cleaved along a twofold plane. Arrows indicate the direction of the 2-fold, 3-fold, and 5-fold axis. Figure reprinted from [75].

The surface also depends on the thermal history of the sample growth and subsequent annealing treatments. For example, quasicrystals contain significant amounts of bulk vacancies from the growth process itself or subsequent annealing. To minimise the density of these voids the sample is annealed under UHV at high temperature for a long time to facilitate void formation at the surface which can be repolished. Ebert *et al* annealed an AlPdMn sample at 800°C for 3 months before surface preparation [79].

Sharma *et al* compiled all annealing temperatures of Al-based quasicrystals that resulted in a near-bulk composition at the surface (table 2.3) [48]. The sputter-annealing method is the best way to study the quasicrystal surface without the

Sample	Annealing temperature
<i>i</i> -AlPdMn	550 – 650°C
<i>i</i> -AlCuFe	50 – 750°C
<i>i</i> -AlCuRu	600 – 750°C
<i>i</i> -AgInYb	350 – 400°C
<i>d</i> -AlNiCo	700 – 900°C
<i>d</i> -AlCuCo	700°C
ξ' -AlPdMn	550 – 580°C

Table 2.3: Optimum temperature of different quasicrystals and approximant to obtain near-bulk composition [48].

oxide influence and with the possibility to prepare a new surface repetitively. This method can, however, create chemical and physical disruptions. In the case of the quasicrystals, chemical disruption is critical since the phase stability range spans only a few percent in the atomic concentration. Chemical changes at the surface can occur in two ways: preferential removing of light elements by sputtering and preferential evaporation of a particular metal upon annealing. Sputtering induced phase change has been observed in *i*-AlCuFe [80] and *d*-AlNiCo [81]. High temperature annealing induced phase transitions were reported by Naumovic on the fivefold surface of *i*-AlPdMn [82]. The transition from cubic to quasicrystalline has been observed with RHEED by Barrow *et al* and is illustrated in figure 2.2. The sputtered surface can be annealed in order to regain the bulk composition and quasicrystalline order.

STM has been widely used to characterise the structural arrangement of these aperiodic surfaces. On the Al₇₀Pd₂₁Mn₉ surface and by connecting the points of high contrast, one will see a Penrose like tiling made of rhombuses, pentagonal stars, regular pentagons and crowns. Within a terrace, characteristic motifs have been identified and called "dark stars", "white flowers", and "rings" (figure 2.3). The latter is terrace-dependent, varying with the annealing condition and not present in figure 2.3.

2.2.1 Surface science of *d*-AlNiCo: 10-fold surface

Reciprocal and real space techniques have been used to analyse the 10-fold *d*-AlNiCo surface. Sharma *et al* used spot-profile analysis low energy electron diffraction (SPA-LEED) to study the tenfold (00001) surface of *d*-Al_{71.8}Ni_{14.8}Co_{13.4} of the type-I superstructure. The diffraction pattern spots are dense and can be indexed using the surface projected basis vector introduced in section 1.5.2 suggesting that

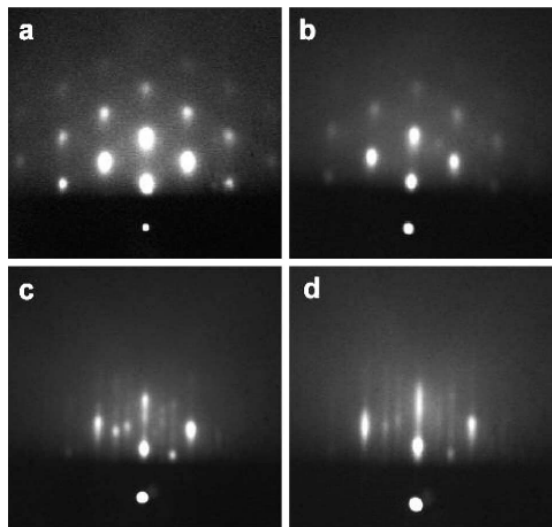


Figure 2.2: RHEED patterns of AlCuFe after (a) sputtering, (b) annealing at 570K, (c) annealing at 670K, and (d) annealing at 770K showing cubic structure after sputtering and recovery of the quasicrystalline surface. Figure reprinted from [80].

the surface corresponds to a bulk truncation without surface reconstruction. A similar conclusion was drawn on the Co-rich phase using dynamical LEED analysis and STM [64].

Using ABAB stacking with A and B rotated by 36° with the initial atoms' coordinates of the Ni-rich phase of an X-ray diffraction study [83], the authors found that the outermost layer spacing is contracted by 10% relative to the bulk inter-layer spacing while the next layer is expanded by 5%. According to the authors, the relaxation is of the kind as observed in relatively open metal surfaces. It is in general a reaction to the charge smoothing present in metallic surfaces. An atomic resolution STM image of AlNiCo in the 10-fold plane is shown in figure 2.4.a and after Fourier filtering in 2.4.b. STM images were acquired from large terraces showing protrusions of atomic dimensions and the pentagonal and decagonal groupings of these features [64].

2.2.2 Surface science of *d*-AlNiCo: 2-fold surface

As discussed previously in section 1.5.2, the 2-fold surface can either be in the (10000) or (001 $\bar{1}$ 0) directions. The latter is sometime referred as the non-equilibrium 2-fold surface. Sharma *et al* used helium atom scattering to study the non-equilibrium 2-fold surface. This surface develops facets in the $\langle 10000 \rangle$

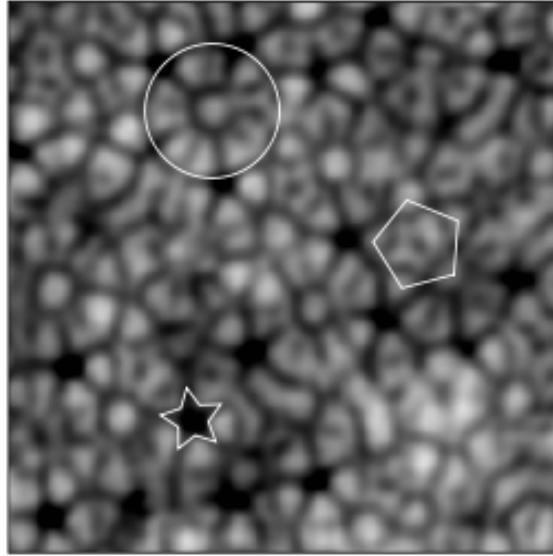


Figure 2.3: 8 nm x 8 nm STM image of Al₇₀Pd₂₁Mn₉ surface where a regular pentagon, a "dark star" and a "white flower" are outlined. Figure reprinted from [68].

direction indicating a lower surface energy of the (10000) plane [84].

2.3 Thin film growth modes

Molecular beam epitaxy (MBE) forms layers in diverse phases as discussed in section 4.4. The layer growth is accomplished through a nucleation and an atomic relationship between the two phases involved. The phases are namely epilayer, over-layer or adsorbate and substrate, respectively.

The term epitaxy refers to the growth of one layer in a particular crystallographic orientation imposed on the deposit layer by its relationship with the underlying substrate layer. An epitaxial growth system is characterised by the two parallel contact planes of the two crystal structures and by the parallel crystallographic directions within these planes. Homoepitaxial growth refers to the case where the two adjacent phases are isochemical. In this case, the lattice match induces a favourable wetting resulting in layer development [85]. In heteroepitaxial growth, deposit materials are different from the substrate. The crystallographic mismatch between the species generates interactions between adatoms and substrate, namely a strain in the over-layer to generate particular growth modes [86].

In the next sections we will discuss the different growth modes and the state of the art in thin film growth on quasicrystals. Another section will introduce the

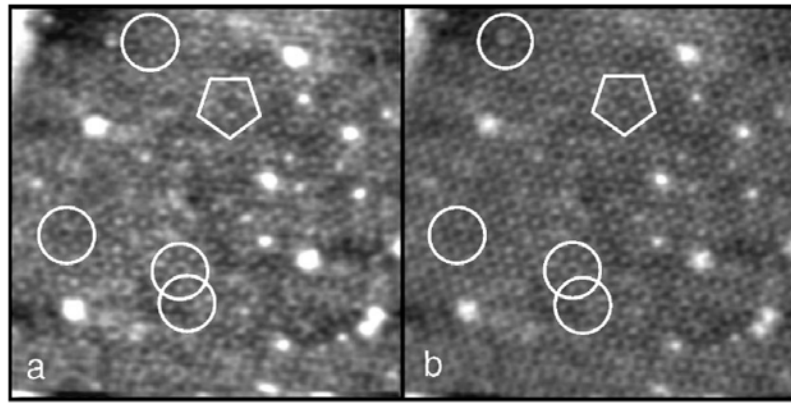


Figure 2.4: (a) $180 \times 180 \text{ nm}^2$ STM image from AlNiCo and (b) after Fourier filtering. Tunneling conditions are: -1.00 V , current 1 nA . Circles and pentagons identify features in the image. Figure reprinted from [64].

crystal-quasicrystal epitaxy which exists in a limited number of orientational relationships.

2.3.1 Lattice registration

When the wetting of the adsorbate is favourable, the subsequent growth characteristic depends mostly on the comparative structure of substrate and adsorbate. That is to say, layer-by-layer growth occurs when the mismatch between film and substrate is small. This condition is sometimes fulfilled with a structural modification of the adsorbate as hcp or fcc on the system Co/Cu(001) and Co/Fe(001) [87] or body centred tetragonal with the system Cu/Pd(001) [88].

In 1958, Ernst Bauer introduced a classification of epitaxial growth modes based on thermodynamic considerations. Three main modes are distinguished:

- Islands or Volmer-Weber (VW): Film atoms are more strongly bound to each other than to the substrate leading to direct growth of three-dimensional islands (fig.2.5a).
- Layer-by-layer or Frank-van der Merve (FM): The film atoms are more strongly bound to the substrate than each other. Two-dimensional growth takes place since each layer is fully completed before the next layer starts to grow (fig.2.5b).
- Layer-plus-island or Stransky-Krastanov (SK): An intermediate case between FM and VW. The growth of islands takes place after complete formation of

one or more layers (fig.2.5c) [89].

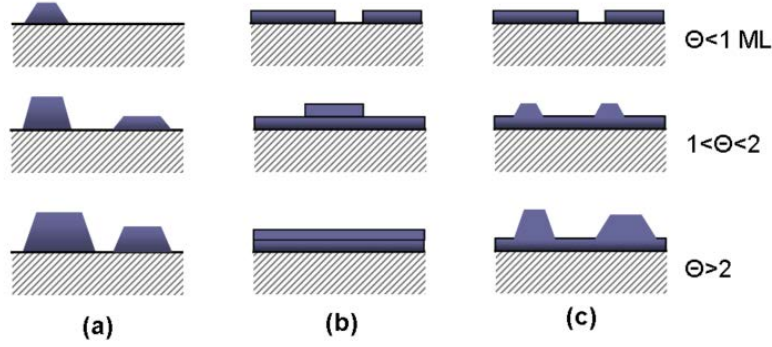


Figure 2.5: Schematic representation of the three growth modes as a function of the coverage θ in monolayer (ML) units. (a) Volmer-Weber; (b) Frank-van der Merwe; (c) Stranski-Krastanov growth modes.

The previous qualitative description of the growth modes originates from a balance between the surface free energy of the deposit γ_d , of the substrate γ_s , and of the interface free energy γ_{int} [85]. Because epitaxial growth is intrinsically a non-equilibrium process controlled by both kinetics and thermodynamics, the morphology may deviate more or less from the thermodynamic depiction [90].

If we deposit a material onto a substrate, we get island growth if

$$\gamma_s < \gamma_d + \gamma_{int}. \quad (2.1)$$

The energy minimisation requires a reduction of the area covered by the deposit (figure 2.5.a). For layer growth, the area covered by the deposit is maximised

$$\gamma_s > \gamma_d + \gamma_{int}. \quad (2.2)$$

The deposit will grow smoothly, one atomic layer at a time (figure 2.5.b). If there is a slight misfit, a film can grow to a certain thickness and then develops into islands to release the strain (figure 2.5.c).

2.3.2 Origin and consequences of stress in the heteroepitaxial layer

At the initial stage of epitaxial growth, stress at the interface influences the growth process. Stresses in a film are introduced with lattice misfit, different thermal

expansion of the two phases or chemical reaction when the intermetallic compound formed is coherent to the film but has a slight lattice misfit [91]. They may also originate from defects at the interface and segregation of the substrate atoms in the film [92].

Stress induced by lattice mismatch

In heteroepitaxy the growth process depends on whether the epilayer is coherent or incoherent with the substrate. If the overlayer is incoherent with its substrate, then the layer adopts a in-plane lattice constant that minimise its free energy. In the other case, if the epilayer is coherent with the substrate, energy minimisation is achieved by adopting the lattice constant of the substrate.

Stress induced by thermal expansion

To illustrate thermal expansion we take the example of lead (Pb) deposited on silicon (Si). The coefficients of thermal expansion of Pb and Si are $29.5 \times 10^{-6}/^{\circ}\text{C}$ and $2.6 \times 10^{-6}/^{\circ}\text{C}$, respectively. When the system is cooled down to the temperature where Pb becomes superconducting (4.2K), the net change in linear dimension is 0.86%. Pb tries to shrink but Si restricts it doing so, hence the Pb film is under tension. Upon heating to room temperature, Pb tends to expand but again is restricted by Si, hence Pb is under compression upon heating. Since room temperature is half its melting point temperature, atomic diffusion is substantial and Pb releases its compressive stress by atomic diffusion to finally generate hillocks [91].

2.3.3 Stranski-Krastanov: a 2D to 3D phase transition

The driving force for the formation of islands is the reduction of the total energy of the strained epilayer system. Two-dimensional structures can relax only in the direction perpendicular to the surface. With formation of three-dimensional islands, the strain can be relieved more efficiently within and around the islands. To illustrate the changes in the total energy of a mismatched system during constant deposition rate, Samuelson *et al* introduced a three regions diagram [93]. As shown qualitatively in figure 2.6, region A is the 2D growth, B is the 2D to 3D transition, and C is the ripening of islands.

At the beginning of the deposition, the system evolves in a layer-by-layer growth

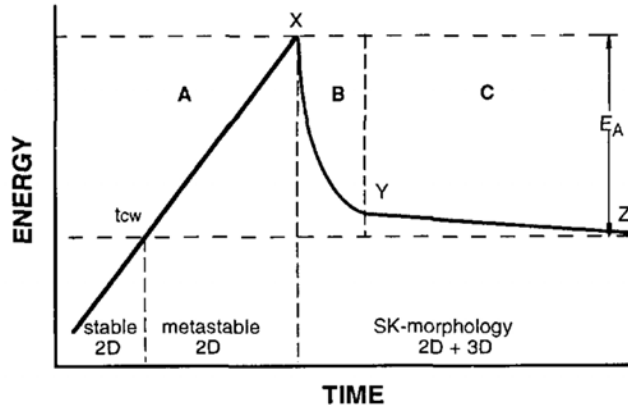


Figure 2.6: Schematic of the total energy versus time for the 2D-3D morphology transition. t_{cw} is the critical wetting layer, E_A is the barrier for formation of 3D islands and X is the point where a pure strain-induced transition becomes possible (no thermal activation). The ripening process occurs between Y and Z. Figure reprinted from [93].

mode which leads to a perfect wetting of the substrate. The accumulated elastic strain energy increases linearly with the deposited volume. Above t_{cw} in image 2.6, the system is potentially ready to undergo a transition towards a Stranski-Krastanov morphology. At the morphological phase transition, period B, 3D islands grow rapidly by consuming accumulated material in the supercritically thick wetting layer. The growth process is initiated by growth and nucleation as discussed above. The activation energy for the nucleation process is $E_A - E_E$ with E_E and E_A , the excess energy in the metastable 2D layer and the transition barrier, respectively. In region C mobile material is consumed. A slow transfer of material towards equilibrium comes from the energy difference between islands favoring large islands (coarsening).

A metastable layer with a critical thickness of 6 ML was observed in the system Ge/Si(100) in a reflection high-energy electron diffraction (RHEED) experiment [94, 95] and metastable layers of up to 7 monolayer thickness by scanning transmission electron microscopy (STEM) [96] on the same system.

2.4 Quasicrystal thin film growth modes

In the next sections we will discuss the thin film growth mode on quasicrystals. The film can adopt its own crystallographic structure but if the latter is oriented

along the high-symmetry axis of the quasicrystal, the growth mode is referred to as rotationally epitaxial. Some films have been observed to adopt a quasicrystal structure, but this example of epitaxial growth has been observed only in the sub-monolayer or monolayer range. Finally, the epilayer is incapable of wetting the substrate adopting its own crystallographic structure through islands growth mode or Volmer-Weber mode. Several experiments have been carried out using different elements as an epilayer. Intermixing may occur with the consequent formation of an alloyed species. The results are diverse without showing any correlation from one element to another. Using review article [97,98], typical experiments will be briefly introduced with an emphasis on multi-layer deposition.

2.4.1 Rotational epitaxial growth

In this section we will be discussing the different structures adopted by atomic species after deposition on quasicrystal surfaces. If multiple orientations of the adsorbate lattice occur with a common relation to a high-symmetry axis in the substrate surface mesh, the growth is referred to as rotational epitaxy [99–101]. In the special case where the adsorbate structure is identical to the substrate, the growth is pseudomorphic. Epitaxial match is the desired growth mode to achieve a quasiperiodic film made of a single element, which so far has only been observed for structure at the monolayer regime.

In the rotational epitaxial growth mode, the film is composed of crystalline structure of the bulk adsorbate aligned to a high-symmetry axis of the quasicrystalline surface. In the next sections, we will introduce experiments where this growth mode was observed element by element upon deposition on quasicrystal.

Group 3A: Al

The first vacuum-deposited epitaxial films was reported by Bolliger *et al* with Al on the 5-fold *i*-AlPdMn surface [100,102]. The authors used LEED and secondary electron imaging (SEI) to analyse a 20 Å thick layer on the substrate. The substrate was kept at room temperature during deposition in order to prevent Al diffusion to the film. They observed stronger signal after the layer deposition due to the large number of scattering planes from periodic domains. It was discovered that Al nanocrystals grow in the face-centered cubic structure in five different sets of domains composing the film. Their [111] axes are aligned parallel to one of five

3-fold symmetry axes of the substrate. When deposited on *d*-AlNiCo [103], Al also grows in rotational epitaxial structures.

Transition metal: Ag

No Al-based crystals were reported to alloy with Ag. Ag was deposited on the 5-fold AlPdMn at room-temperature at a thickness larger than 10 ML. The surface was analysed with STM. The epilayer forms a very rough film with needle-like islands indicating a large value of the interfacial free energy [104, 105]. However, the orientation of Ag(111) nanocrystals was determined by the substrate. The nanocrystals are hexagons and grow in five orientations reflecting the symmetry of the underlying substrate up to a thickness of 100 Å .

Transition metal: Au

10 ML Au deposited on the 10-fold Al₇₂Ni₁₂Co₁₆ surface at room temperature develops a multiply twinned AuAl₂ crystalline overlayer with the help of In as a surfactant and following annealing [106, 107]. Au combines with Al from the substrate to form a layer of randomly oriented AuAl domains. After annealing, the layer transforms into AuAl₂ with fcc domains oriented with the (110) plane parallel to the surface. Without surfactant, Au grows in polycrystalline films even after annealing. The action of In as a surfactant confirms that surface energy considerations apply for quasicrystalline surfaces as well.

Shimoda *et al* deposited Au on the 5-fold surface of *i*-AlPdMn [108]. Deposition at room temperature of 7 ML of Au leads to the formation of a Au-Al alloy without evidence of ordered structure. Annealing to 325°C induces Al diffusion into the film, producing AuAl₂ alloys with still no indication of structures. Even with a previous deposition of 0.5 ML layer of In, no crystallisation of the adlayer was observed.

Transition metal: Pt

Pt thin films deposited on the clean 10-fold AlNiCo were observed with RHEED and XPS [109]. When Pt is deposited at room temperature on the 10-fold surface, the film is polycrystalline and does not evolve after subsequent annealing. Using In as a surfactant, the film is still polycrystalline after deposition but develops into large epitaxial twinned PtAl₂ crystals after annealing to 490 K. Each domain has a (110)-oriented surface and azimuthal directions correspond to one of the 10 equivalent

2-fold axes of the substrate.

Transition metal: Cu

Ledieu *et al* reported STM and LEED results of Cu films grown on the 5-fold surface of *i*-AlPdMn deposited at 308 K [110,111]. At a coverage below 1 ML, islands were observed which were isotropic in shape with height measured at $1.9 \pm 0.1 \text{ \AA}$. At 5.5 ML a new LEED pattern generated by the Cu structure is observed. An STM image is shown in figure 2.7.a illustrating that the film comprises five domain orientations with visible stripes. These stripes have their origins in topographical ripples at the surface. The rows have separations of $S=4.5 \pm 0.2 \text{ \AA}$ and $L=7.3 \pm 0.3 \text{ \AA}$, whose ratio equals the golden mean τ within experimental error (figure 2.7.c). The structure is an arrangement of 1D features aligned along the five principal directions. Cu is the only element presents in the film as monitored by Auger spectroscopy. As the coverage was increased, this row structure was preserved but islands became progressively smaller and eventually generated incomplete layers. The LEED pattern starts to degrade at 20 ML and vanishes at 25 ML.

Ferromagnetic transition metal: Fe

Fe thin films were deposited on the 5-fold AlPdMn surface at room temperature and analysed with STM, LEED, and Auger electron spectroscopy (AES) [112] and at 340 K with LEED, SEI, and AES [113]. Both experiments display the same growth mode. In the first experiment, Wearing *et al* grew films up to about 3 ML and layer-by-layer growth was observed by islands coalescence. No LEED pattern was observed which indicated that the layers were disordered. The AES results ruled out intermixing. Above this coverage, there is a transition to a multilayer island growth mode. The islands are rotated by 72° and have a bcc(110) structure.

Fe deposited at room temperature on 10-fold *d*-AlNiCo creates intermixed layers in an initial layer-by-layer fashion as observed by STM, LEED, and AES [114]. The absence of clear LEED patterns indicates that these layers are disordered. At a coverage of 9 ML, nanosized multilayer islands are observed in five domains pointing along the five high symmetry directions.

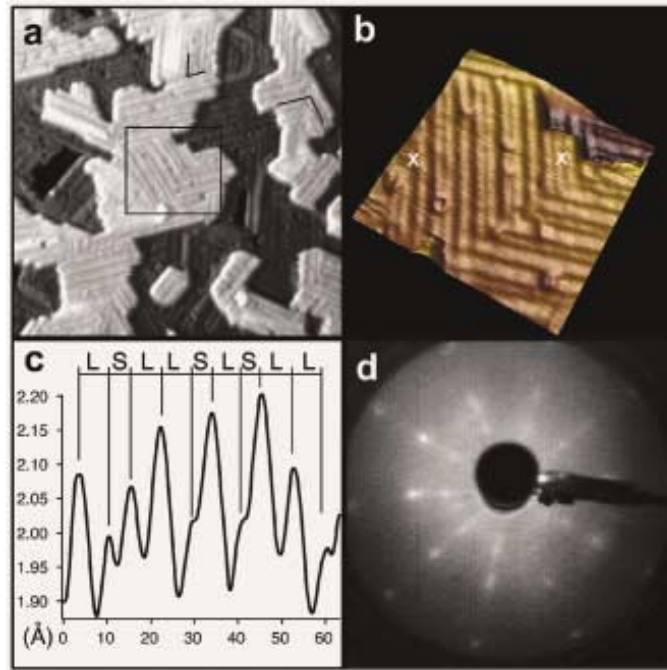


Figure 2.7: (a) $400 \times 400 \text{ \AA}^2$ STM image of the fivefold surface of Al-Pd-Mn after deposition of 5.5 ML of Cu. (b) $100 \times 100 \text{ \AA}^2$ detail from (a). (c) profile image between the points marked as crosses in (b). (d) LEED pattern of this phase at a beam energy of 50 eV. Figure reprinted from [110].

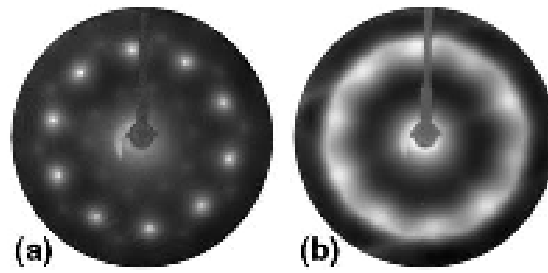


Figure 2.8: LEED patterns obtained at an electron energy of 115 eV after (a) 1.9 ML and (b) 19 ML Ni evaporation on 5-fold AlPdMn surface. Figure reprinted from [115].

Ferromagnetic transition metal: Ni

Weisskopf *et al* have deposited Ni on 5-fold *i*-AlPdMn at room temperature [115]. After deposition of a 1 ML thick Ni layer, additional spots were observed with LEED. Ni intermixes with the substrate surface at the initial stage of growth followed by Al migration to grow a structurally modified icosahedral AlPdMn region due to a modified chemical composition. Assuming that these spots are generated by a multi-twinned structures, the authors found the distances between parallel atomic rows to be approximately 0.230, 0.282, and 0.400 nm. These values point to five cubic domains exposing their (110) faces perpendicular to the surface normal and azimuthally rotated by $2\pi/5$ with respect to each other. The spot pattern gradually degrades into a Ni overlayer as thick as 19 ML (figure 2.8).

Ferromagnetic transition metal: Co

Row-like structures very similar to those observed already for Cu on AlPdMn [111] were obtained for Co deposited on 5-fold *i*-AlPdMn after analysis with STM, LEED, and AES [116]. On these systems, Co forms an initial complete layer upon which smaller domains in a pseudomorphic row structure take shape. These domains are made of Fibonacci spaced rows with periodic lattice parameter along the rows of 2.5 ± 0.1 Å. Better ordered structures were found for Co deposited on 10-fold *d*-AlNiCo compared with Cu since the smallest lattice parameter of Co matches the smaller characteristic distances.

2.4.2 Epitaxial growth

Sb and Bi

The first single element pseudomorphic growth was reported by Franke *et al* with Sb and Bi monolayers deposited on the 10-fold AlNiCo and the 5-fold AlPdMn [117]. With the substrates hold at high temperature, Sb and Bi films grow pseudomorphically on the surface with long-range quasicrystalline order.

Group 5A: As

Franke *et al* observed a faceting at the surface of decagonal AlNiCo after deposition of As at high temperature. The faceting promotes the growth of AlAs islands on the facets. Since the islands adopt only one orientation, this system is seen as epitaxial rather than rotational epitaxial. Arsenic adsorbed on the 10-fold surface of *d*-AlNiCo leads to an epitaxially intermixed AlAs(111) film [118].

Transition metal: Pb

Pb has been deposited at room-temperature on 5-fold AlPdMn [119], 10-fold AlNiCo [120], or 5-fold AlCuFe [99] with thin film studies carried out with STM, LEED, or XPS. In these experiments, no more than one complete monolayer has been found to grow epitaxially. It is still not clear why the sticking coefficient drops so sharply after completion of the pseudomorphic layer.

2.4.3 Volmer-Weber growth

Lanthanides: Gd

Gd deposited at room temperature and analysed by STM did not show any wetting when deposited on the *i*-AlPdMn surface. Nanocrystals develop with increasing coverage without the formation of a flat atomic layer. Gd deposited on 5-fold *i*-AlPdMn develops into a film through the formation of three-dimensional clusters without any indication of ordering [121].

2.5 Quasicrystal-crystal epitaxy

The relationship between quasicrystalline and crystalline structures has been an active field of research. It was established in 1985 that Ar ion bombardment at

room temperature transforms the quasicrystalline surface into a crystalline cubic structure [122]. The crystalline structure has a specific orientation relationship with respect to the quasicrystalline substrate. As discussed in section 2.4.1, there is a fair amount of experimental data for orientational/epitaxial relationships between quasicrystalline and conventional crystalline materials (ie AuAl_2 and PtAl_2 on d - AlNiCo with (110) surface plane aligned along the symmetry axis [106,109]).

A coherent overgrowth of crystal material Y on crystal X is likely to happen if a plane of Y can lie down in such a way that a large fraction of the Y atoms can be made to coincide with the site of X atoms. A large density of these coincidences will induce a low interface energy (coincidence site lattice). This atomistic approach relies on a real-space structural model for the quasicrystal system which may not be readily available or if available not necessarily correct. Moreover, this model lacks interfacial energy considerations, or the long-range fitting for the superimposed structure since misfit dislocations and interface relaxations are ignored.

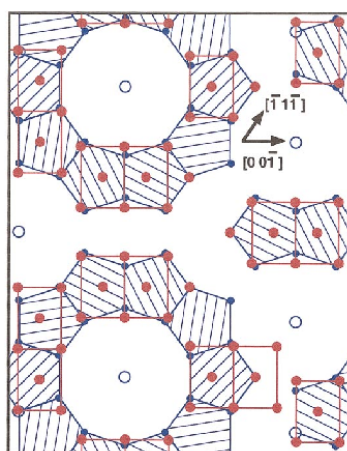


Figure 2.9: Structural model of the interface between the pentagonal surface of $i\text{-Al}_{70}\text{Pd}_{20}\text{Mn}_{10}$ (blue) and the (110) surface of bcc structural units (red). Figure reprinted from [123].

Zurkirch *et al* presented the orientational relationship between $d\text{-AlNiCo}$ and its bcc phase upon sputtering [123]. The [110] bcc axis is oriented parallel to the 10-fold symmetry direction. Using the atomic model suggested for AlNiCo [124] with the orientation chosen to match the experimental result, they found a satisfactory agreement between the cubic phase and most of the Al and transition metals. The small mismatch between the two phases was inferred to be caused by the lack of long-range ordered crystalline surface layer.

Shimoda *et al*, in an attempt to grow pseudomorphic Au overlayer thin films,

formed AuAl_2 with the (110) surface oriented to the 10-fold surface [106]. The unit cell of AuAl_2 is of the CaF_2 type with a small mismatch to the pentagonal units of the quasicrystal phase.

The correspondence between the icosahedral structure of $\text{Al}_{70}\text{Pd}_{20}\text{Mn}_{10}$ and its corresponding bcc phase upon ion bombardment was studied by Bolliger *et al* [125]. The interface model is shown in figure 2.9, the coincidence site lattice has a small mismatch between the β and the quasicrystalline lattice of 0.3%. In the system $\text{Al}-i\text{-AlPdMn}$, also introduced in section 2.4.1, Al nanocrystals were found to grow with their [111] axes aligned parallel to the threefold axes of the substrate at 37.37° away from the surface normal [100, 102]. This growth mode has no symmetry facets

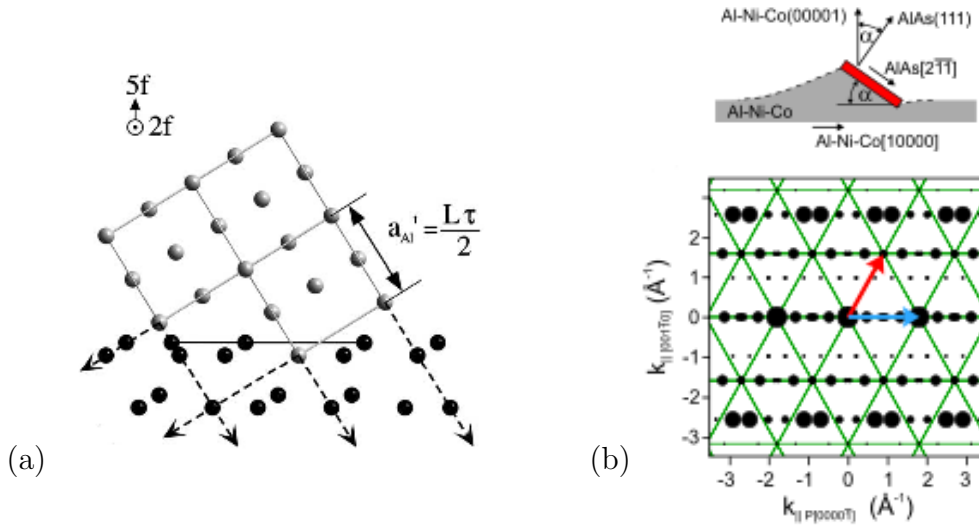


Figure 2.10: (a) Side view of the interface configuration for Al nanocrystallite on the 5-fold surface of AlPdMn. The Al lattice in gray has its [100] direction of the fcc lattice coinciding the 2-fold direction of the surface, reprinted from [102]. (b) Top, sketch of the in-plane orientation of the strained AlAs(111) film onto the faceted substrate with $\alpha = (35.27 \pm 0.15)^\circ$. (b) Bottom, AlNiCo (10 $\bar{2}$ 24) interface plane (black) superposed to the mesh of the AlAs(111) film, reprinted from [118]

parallel to the substrate surface (figure 2.10.a). Franke *et al* observed the growth of AlAs thin films on a vicinal surface of the 10-fold AlNiCo surface. AlAs(111) grows epitaxially on AlNiCo(10 $\bar{2}$ 24) as depicted by the schematic in figure 2.10.b. Because other incommensurate strong sets of Fourier components exist, quasicrystals could mediate epitaxially incommensurate materials.

Chapter 3 : MnSb Thin Films for Spintronics

With the reduction of electrical components, the leakage current through an insulating region increases exponentially as the thickness of the insulating region decreases. Thus, the printing of nano-circuits will reach a physical limit in miniaturisation that will be overcome only with a new bottom-up technique such as molecular electronics. The spintronics is a technique that utilises the quantum properties of electrons to store information. This technique allows the creation of more efficient devices without miniaturisation or modification of the silicon-based printed technology. Some spin-based devices have already proven to be commercially viable as the GMR (giant magnetoresistance) read heads integrated in hard disks in use in computers since 2000. Other spin-based semiconductors still require technological advancements. One needs a source of spin-polarised electrons, a spin-polarised current remaining coherent over the operation period, and a tool for the manipulation and detection of the spin states. To some extent, the issue related to the coherence is solved as GaAs has shown spin polarised current remaining coherent over $4\text{ }\mu\text{m}$ [126]. Manipulation of a spin-polarised current can also be performed with a static electric field perpendicular to the current which is known as the Rashba effect [127] whereas the detection can be done using spin-valves that use spin-dependent properties of semiconductor-ferromagnetic interfaces to exploit the giant magneto-resistive effect [128]. A spin-polarised current can be generated by any ferromagnet that has a degree of spin-polarisation at the Fermi energy. Since magnetic semi-conductors does not exist, the injection of a spin-polarised current in a semi-conductor is the key problem.

Different approaches aim to achieve this goal. A first one uses a tunnel junction such as an ultra thin metal-oxide layer between the metal and the semiconductor [129, 130]. Such a device requires an epitaxial match of the three structures to avoid scattering at the interfaces but even in the case of a good match, the interface itself may not be ferromagnetic [131]. It is not possible to use a typical metal-semiconductor interface since ohmic contacts heavily dope the semiconductor surface, leading to spin-flip scattering and loss of spin polarisation [132]. Another

approach would be to dope tetrahedrally coordinated semiconductors with magnetic ions since this structure would ensure epitaxial compatibility with zinc-blende semiconductors [133]. At a critical concentration, a magnetisation arises enabling the injection of spin-polarised current. However, the Curie temperature of these materials is often below room temperature making them unsuitable for usual technological application [134].

In this chapter, we will investigate another approach, the use of ferromagnetic compounds such as the MnAs and MnSb ferromagnets or the half-metallic ferromagnet NiMnSb [135]. They offer a good epitaxial match with III-IV semiconductors forming stable and abrupt interfaces [131]. However, spin-polarisation efficiency and structural details at the interface are problems that still need to be addressed.

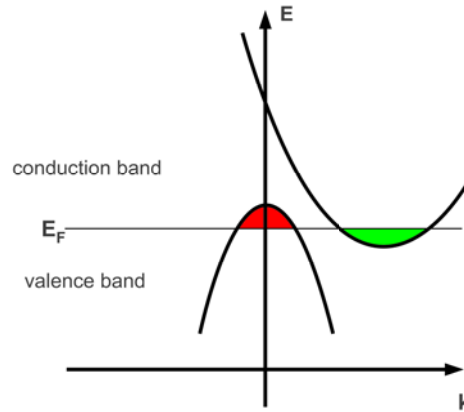


Figure 3.1: Band-structure of a semi-metal showing the slight overlapping between valence and conduction bands.

MnSb is also a semimetal. It adopts the NiAs structure and is discussed in more details in section 3.2.2. A semimetal is a material with a small overlap between the bottom of the conduction band and the top of the valence band (figure 3.1). In a semi-metal the bottom of the conduction band is situated in a different part of the momentum space than the top of the valence band. A semimetal thus has no band gap. Unlike a regular metal, semimetals have charge carriers of both types (holes and electrons), the charge carriers density is much smaller than in a proper metal. This explains why the electrical properties of semimetals are partway between those of metals and semiconductors. Antimony (Sb), arsenic (As), bismuth (Bi), α -tin (gray tin) and graphite are classic semimetals.

Figure 3.2 shows the density of states of three classes of materials [136]. Figure 3.2.a displays the density of state (DOS) for a semi-conductor. One can obtain

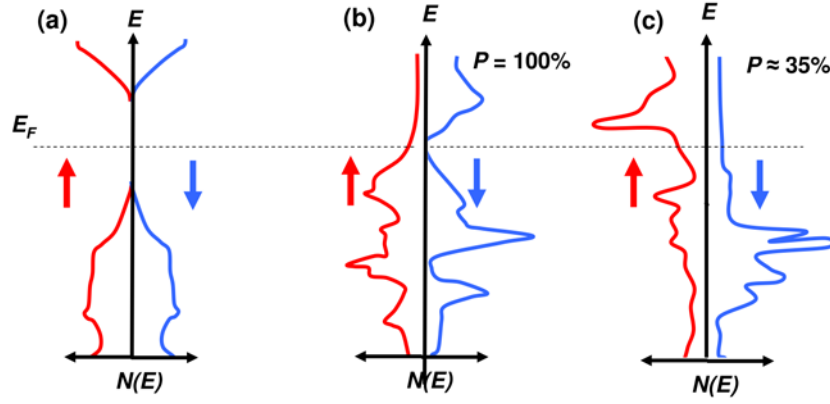


Figure 3.2: Spin-up and spin-down DOS for (a) GaAs (semiconductor), (b) NiMnSb (half-metallic ferromagnet), and (c) MnSb (ferromagnet). Figure reprinted from [136].

a spin-polarised current from a semi-conductor by excitation with circularly polarised light. Figure 3.2.b depicts the half-metallic ferromagnetic semi-heusler alloy NiMnSb. This alloy is metallic for spin-up electrons (majority spin) and semiconducting for spin-down (minority spin) resulting in a 100% spin-polarisability at the Fermi level. The third material in panel c, is a ferromagnet for which spin up and spin down DOS are different due to exchange interaction between spins [136].

MnSb has a strong potential for spintronics application. It has a Curie temperature significantly higher than room temperature (587°C) and a structure compatible with III-V(111) surfaces [136]. Since current flow is the movement of electrons close to the Fermi level, the polarisation of current P is

$$P = \frac{N_{\uparrow}(E_F) - N_{\downarrow}(E_F)}{N_{\uparrow}(E_F) + N_{\downarrow}(E_F)}. \quad (3.1)$$

The spin-polarisation for MnSb at E_F is only $\sim 35\%$ which is not particularly attractive for spintronics but demonstrates an enhanced Kerr effect after surface oxidation [137]. However, recent theoretical calculations have shown that binary pnictides such as CrSb and MnSb in the cubic and wurtzite structures would display half-metallicity [138, 139].

3.1 Magnetism and thin film magnetism

In 1831, Faraday formulated the induction principle which finally gave birth to electromagnetism. Later, a macroscopic model of the magnetic properties of free atoms or molecules (solids much later) was developed defining the paramagnetic susceptibility χ_{para} of an ensemble of N molecules of magnetic moment μ as

$$\chi_{para} = \frac{N\mu^2}{3k_B T}, \quad (3.2)$$

where k_B is the Boltzmann constant. Temperature agitation reduces the average number of aligned moments as observed experimentally by Curie and derived theoretically by Langevin. Equation 3.2 known as Curie's law describes the susceptibility of all systems in the classical limit (high temperature). Weiss introduced a microscopic theory of ferromagnetism. He postulated the existence of a molecular field which was found later to be the exchange interaction. The next major progress in the understanding of magnetism arose with contribution of quantum mechanics.

Magnetism is the result of the Pauli exclusion principle and the electron-electron repulsive coulomb term of the electronic potential. According to the Pauli principle, a symmetric orbital must be multiplied with an antisymmetric spin function, and vice versa. The tendency to form a chemical bond (formation of a symmetric molecular orbital) results through the Pauli principle automatically in an antisymmetric spin state ($s=0$, antiferromagnetic). In contrast, the Coulomb repulsion of the electrons, i.e. the tendency that they try to avoid each other by repulsion, lead to an antisymmetric orbital function of these two particles, and complementary to a symmetric spin function ($s=1$, ferromagnetic).

In a simplified atomic orbital picture, the magnetic moment is created by interaction between electrons on the same atom and the coupling between electrons on different atoms. The magnitude of the magnetic moment depends on the magnitude of the angular momentum and on the spin-imbalance between majority and minority electron bands (itinerant magnetism). The interaction changes its sign as soon as the atomic orbitals cease to overlap strongly. The orbital momentum increases and the coupling becomes ferromagnetic [140].

For the 3d transition metals the orbital moment is quenched by the strong crystal field and the magnetic moment is mostly due to the electron spin as a result of the electron band splitting with, however, a small orbital contribution responsible for the magnetocrystalline anisotropy through spin-orbit coupling [141]. The magnetism of

metallic transition metal pnictides was found to be connected to the coupling of the atomic moments through the conduction carriers in addition to superexchange via the valence band [142]. Superexchange refers to the coupling between two next-to-nearest neighbour cations through a non-magnetic anion.

3.1.1 Involved energies in ferromagnetism

The main contributions to the total energy of a ferromagnet without external fields are the **exchange energy**, the **magnetocrystalline anisotropy energy** and the **magnetostatic energy**.

The exchange interaction between electron spins at different atomic sites keep the spins aligned parallel. The **exchange interaction** is a direct consequence of Pauli's exclusion principle and hence has an electrostatic origin (not an interaction between spin magnetic moments). The exchange term is described with $E_x = -\sum J_{ij} \mathbf{S}_i \cdot \mathbf{S}_j$ with $J > 0$ for ferromagnets. Since the atomic orbitals decay exponentially as a function of distance, the exchange interaction results in a short-ranged interaction.

For itinerant materials such as MnSb, the spin-orbit interaction induces a small orbital momentum which then couples the total magnetic moments to the crystal axes [143]. The spin-orbit coupling of the electron spin to its environment, the crystal lattice, is called the **magnetocrystalline anisotropy energy** (MAE). When the spin direction is rotated from one axis to another, the rotation changes the overlap of orbits and hence the exchange interaction energy. The axis which allows the largest overlapping of orbits is the easy axis of magnetisation [144].

The difference between the energies required to magnetise the crystal in the hard and easy directions is termed the anisotropy energy. The magnetocrystalline anisotropy is specific to a given material and independent of particle shape. In cubic systems, symmetry creates multiple easy axes. In iron (Fe) and nickel (Ni), the magnetic moments align preferentially along the [100] and [111] axes, respectively [145]. High anisotropy materials have high coercivity [146].

Below 420 K, MnSb has a hexagonal close-packed structure (see section 3.1.4) and the moments are aligned along the unique axis [0001] (or c -axis). This is the easy direction as shown by the M(H) curve in figure 3.3 while the hard direction is along the c -plane. [142, 147].

Due to the coupling between electron spins and lattice, a change in the lattice constant will affect the magnetic properties. If the lattice is strained along a certain

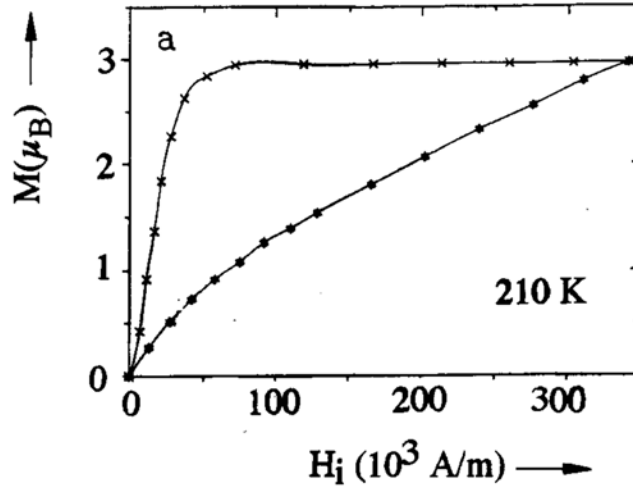


Figure 3.3: Magnetisation (M) as function of magnetic field strength (H) for MnSb along the easy and hard direction (c-axis and c-plane, respectively) at 210 K. Figure reprinted from [142].

direction, extra contributions denoted by the term **magnetoelastic anisotropy** add to the total energy [148]. Magnetoelastic anisotropy in multilayers is due to lattice mismatch between adjacent layers [149].

The third relevant energy is the **magnetostatic energy**, the local energy in a static magnetic field. This term includes dipole-dipole interaction and Zeeman term.

3.1.2 Origin of the magnetic domains in ferromagnets

The balance between exchange and magnetostatic energies is responsible for the existence of domains. The first aligns the spin in one direction but generates a huge magnetostatic energy. The latter is reduced with moments aligned on the interatomic scale but whole domains are aligned randomly [148]. In these domains, 10^{12} to 10^{18} atomic moments are aligned so that the magnetisation within the domain is almost saturated. The direction of alignment varies from domain to domain but in the absence of a magnetic field, they will align along one of the magnetic easy axes [150].

Figure 3.4 illustrates the origin of domains as a consequence of the magnetic poles formed at the surface of the crystal. The magnetic energy in configuration (A) is high while in the configuration shown in (B) the crystal is divided into two domains magnetised in opposite directions reducing the magnetostatic energy by roughly 1/2. With N domains in (C), the magnetic energy is reduced to approximately 1/ N due

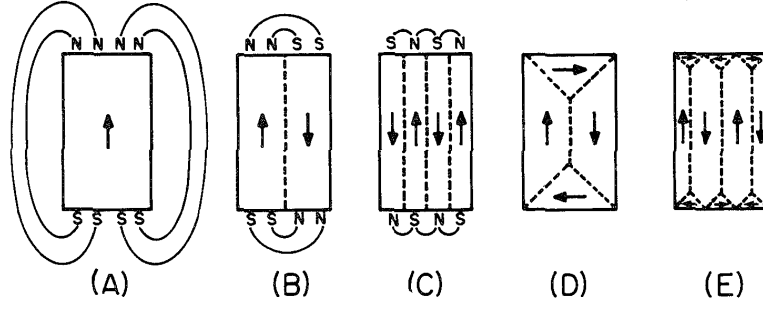


Figure 3.4: Changing in domain patterns in a ferromagnetic single crystal cross-section. Figure reprinted from [145].

to the reduced spatial extension of the field. In configurations (D) and (E), the magnetic energy is zero. Surface domains that complete the flux circuit are denoted **domains of closure** [150].

In the original Weiss theory the molecular field \mathbf{B}_e is proportional to the bulk magnetisation \mathbf{M} so that

$$\mathbf{B}_e = \alpha \mathbf{M}, \quad (3.3)$$

where α is a constant. This is a good assumption for paramagnetic materials. The magnetism in a medium surrounding a given atomic magnetic moment has same magnitude than in the bulk. A ferromagnetic material is locally inhomogeneous, due to the variation of direction in the domains. Weiss mean fields apply only within a domain. The molecular field responsible for the ordering of moments within domains is termed exchange field and expressed as

$$\mathbf{B}_e = \alpha \mathbf{M}_s, \quad (3.4)$$

where α is positive and \mathbf{M}_s is the magnetisation inside a domain. \mathbf{M}_s decreases as the temperature increases and becomes 0 at the Curie point.

The change in the moments' direction at domain boundaries is realised by transition layers in which the magnetic moments undergo a reorientation. The transition layers are commonly referred as domain walls or Bloch walls (figure 3.5). The balance between exchange energy and MAE determines the width of the domain walls. The former tries to have an abrupt transition for the spins to align in the easy axes, while the latter allow only a slight variation of the angles of adjacent spins [148]. This balance determining the domain wall width can be expressed mathematically by [151]

$$l_w = \sqrt{\frac{A}{K}}, \quad (3.5)$$

	l_{ex} (nm)	l_{w} (nm)
Fe	2.8	18
Co	3.4	5.5
Ni	9.9	51

Table 3.4: Exchange length and domain wall width of Fe, Co, and Ni at 293 K [151].

where A is the exchange stiffness and K the magnetic anisotropy constant. In a similar way we can express the exchange length [151]

$$l_{\text{ex}} = \sqrt{\frac{2A}{\mu_0 M_s^2}}, \quad (3.6)$$

where μ_0 is the permeability of the vacuum. The domain wall width is usually bigger than the exchange length as seen in table 3.4 which lists the values for the three ferromagnetic elements.

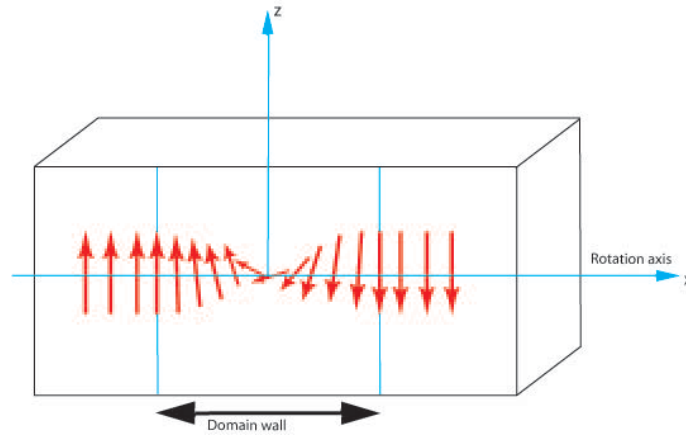


Figure 3.5: Illustration of a Bloch wall with in-plane rotation axis. The domain wall length is defined by the balance between exchange and crystalline energy.

In the particular case of a film where the Bloch wall would be wider than the thickness of the film, the surface charges would increase the energy strongly. A rotation where the magnetisation vector remains parallel to the faces of the film is energetically favorable. Such reorientations are referred to as Néel walls.

3.1.3 From macro- to microscopic systems

In thin films and particles of extremely small sizes, the strength of the exchange term (0.1 eV/atom) is much larger than those of the magnetostatic (\sim

0.1 meV/atom) and magneto anisotropy ($\sim 10 \mu\text{eV}/\text{atom}$) terms [141]. Consequently the magnetisation state is always nearly uniform. In this case, an external field induces magnetic reversal by coherent rotation of all magnetic moments. For this reason the particle can be reasonably described as a macrospin.

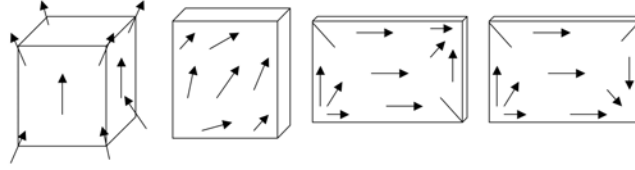


Figure 3.6: Most common single domain states. Figure reprinted from [152].

An intermediate case between the macrospin state and a macroscopic state (magnetic domains separated by domain walls) is the so-called single-domain state. It is defined by a state close to uniform magnetisation, displaying no magnetic wall or vertex (figure 3.6). The term "single domain state" must not be confused with uniform magnetisation. In single domain states, domain walls and vortices are not found at equilibrium but may occur during magnetisation reversal.

These results are summarised in figure 3.7. Exchange lengths are typically in the nanometer range and wall widths are approximately one order higher.

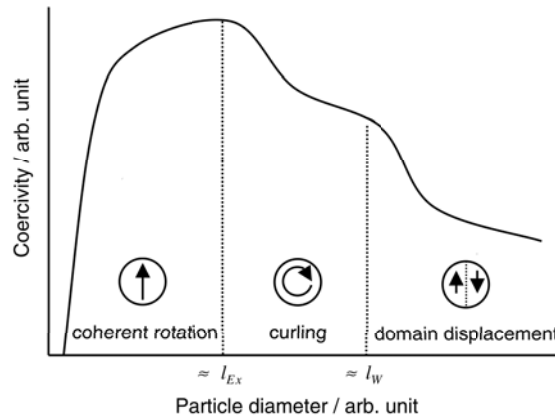


Figure 3.7: Qualitative behavior of the coercivity versus the particle diameter. Figure reprinted from [151].

3.1.4 Magnetism in thin films

Controlling growth mode via self-organisation allows the formation of low-dimensional structures. A thin film can be seen as a 2D film when the thickness is much

smaller than the exchange length. In this case, thin films are characterised by a temperature and a thickness dependent para-ferromagnetic phase transition [141]. This occurs for dimensions of the order or below 10 nm.

Before thin films could be grown experimentally, Néel foresaw that the broken symmetry of the electron band structure at surfaces or interfaces (reduced atomic coordination) would induce a correction to the magnetocrystalline anisotropy. This correction is the result of localisation and band narrowing of the atomic orbitals of the interface atoms leading to a larger DOS at the fermi level and enhanced spin imbalance between majority and minority electron bands [141]. This correction to the overall anisotropy energy is the **surface anisotropy** [152]. To a second order approximation and for hexagonal symmetry around the c -axis, the surface anisotropy E_a is given by [153, 154]

$$E_a = K_1 \sin^2 \theta + K_2 \sin^4 \theta, \quad (3.7)$$

where K_1 and K_2 are the first and the second order crystal magnetic anisotropy constant (surface anisotropy) and θ defined as the angle between c axis and magnetisation.

The second source of magnetic anisotropy after surface anisotropy in thin films is the magnetic dipolar interaction. This interaction has a long range interaction that senses the outer boundaries of the sample. The shape effect of dipolar interaction is described via an anisotropic demagnetising field \mathbf{H}_d given by

$$\mathbf{H}_d = -N\mathbf{M}_s, \quad (3.8)$$

where N is a demagnetising tensor. For a thin film, N is non-zero only for the direction perpendicular to the layer, $N^\perp = 1$. The magnetostatic energy is given by

$$E_d = -\frac{\mu_0}{2V} \int \mathbf{M}_s \cdot \mathbf{H}_d dv. \quad (3.9)$$

In equation 3.9, the anisotropy energy contribution per unit volume V is proportional to $\cos^2 \theta$ with θ the angle between c axis and magnetisation due to the vectorial product nature. The dipolar interaction favours the in-plane orientation for magnetisation [143]. Due to its long range character, the dipolar contribution to the anisotropy is shape dependent and commonly called **shape anisotropy**.

When the thickness of the ferromagnetic layer is reduced to a few monolayers, the anisotropy energy should not be treated as a continuum as in equation 3.9, but

by a discrete set of magnetic dipoles on a regular lattice. Nevertheless, for the inner layers, the average dipolar anisotropy is rather close to the value based on the continuum approach. Hence, the average dipolar anisotropy can be expressed by a volume and an interface contribution. The magnitude of the dipolar interface contribution, however, is of minor importance compared with other sources of interface anisotropy such as spin-orbit coupling [143]. Thus, the magnetic anisotropy K per unit volume of the magnetic layers with thickness d can be phenomenologically written as the sum of a volume and interface terms [143, 149]

$$K d = K_v d + 2 K_s. \quad (3.10)$$

K_v contains contributions from shape, magnetocrystalline and magneto-elastic anisotropy. K_s is interpreted as the interface or surface energy. The magnetic anisotropy is sensitive to atomic scale order, at the interface. It reflects the local symmetry felt by the magnetic atoms as shown with magnetic measurements on different substrates [137, 155, 156]. K_v favours in-plane magnetisation while the interface anisotropy K_s favours perpendicular magnetisation since they are proportional to $\cos^2 \theta$ and $\sin^2 \theta$, respectively (equation 3.7 and 3.9). It follows that at small thicknesses, the bulk contribution can be overwhelmed by the surface term so that out-of-plane magnetisation becomes energetically favourable. The total energy is then written [153, 157, 158]

$$E = A(\nabla \mathbf{m})^2 - \mathbf{H}_a \cdot \mathbf{M} + \frac{1}{2} \mu_0 M_s^2 \cos^2 \theta + K_1 \sin^2 \theta + K_2 \sin^4 \theta, \quad (3.11)$$

where $\mathbf{M} = M_s \mathbf{m}$, $|\mathbf{m}| = 1$, and \mathbf{H}_a is the applied field. The first term is the exchange energy, $\mathbf{H}_a \cdot \mathbf{M}$ the Zeeman effect term and $\frac{1}{2} \mu_0 M_s^2 \cos^2 \theta$ the dipolar interaction derived from equation 3.9.

The reversible spin reorientation transition between perpendicular and in-plane alignment arises with 6 ML-Fe overlayer deposited on Ag(100) at 380 K (since M_s varies with temperature) [159] or with Co/Pd at a thickness of 13 Å [143].

Markandeyuku *et al* observed spin reorientation by the ferromagnetic resonance (FMR) technique in MnSb single crystals [160]. They observed that the magnitude of K_1 and K_2 decreases with the increase of temperature, as does the magnetocrystalline anisotropy. K_1 and K_2 are of opposite sign and the magnitude K_2 is about one tenth of K_1 . The negative sign of K_1 at 300 K shows that the easy axis lies in the c -plane. Above 520 K the easy axis of magnetisation shifts to the c -axis (positive K_1). Above the transition temperature, both K_1 and K_2 increase to reach

a maximum, finally tending to zero as the temperature approaches T_c (587 K).

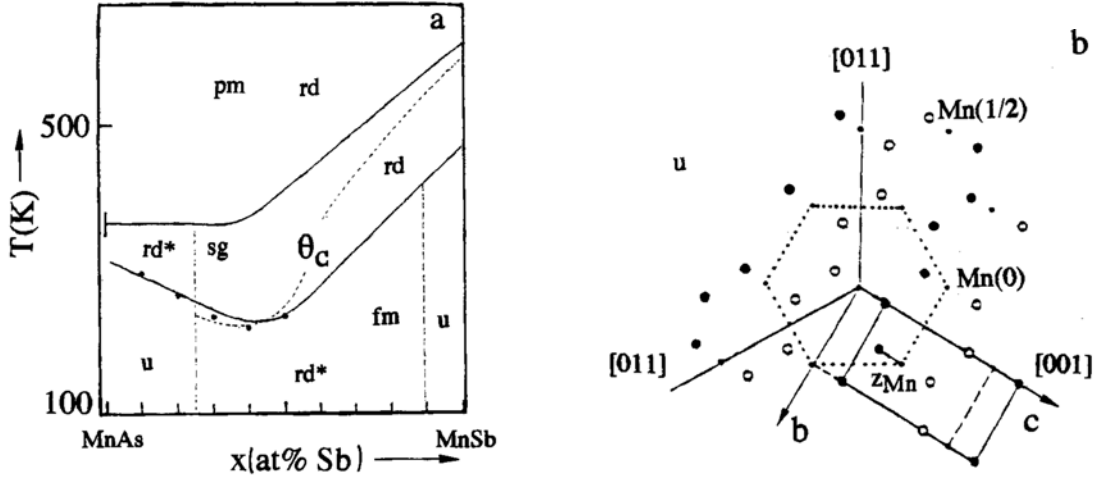


Figure 3.8: (a) Phase diagram of the MnAs-MnSb system. fm ferromagnetic order, pm paramagnetism, sg spin-glass like state, u uniaxial Mn displacements, rd random Mn displacement, rd* incomplete randomisation, dashed line fm-sg transition. θ_c paramagnetic Curie temperature. (b) Uniaxial orthorhombic distortion of a hexagonal (NiAs) lattice, projection onto the hexagonal plane. Figure reprinted from [142].

Okita *et al* in 1968 determined Curie temperatures from the temperature dependence of saturation magnetisation [154]. The graph combining the results shows a plateau at $T_c=587$ K with Mn ranging between 48% and 50.5%. After that the Curie temperature decreases linearly with Mn composition. These results differ slightly from a similar work [161] indicating the influence of the sample preparation. The authors also made measurements of the anisotropy constant of their samples. The Mn-composition drastically influences the spin-reorientation in MnSb : ≈ 80 K at 55.3%, ≈ 220 K at 52.8% and ≈ 360 K at 51.4%.

Kohnke *et al* reported two anomalies in the magnetocrystalline anisotropy [142]. Beside the zero crossing of the anisotropic constant K_1 already reported at around 520 K, they observed a spin-reorientation at 270 K. They also observed a broadening of the angular dependence $M(\theta)$ in certain temperature ranges for a high applied magnetic field. The origin of the broadening is an easy cone for which a uniaxial ferromagnet obeys $-2K_2 \leq K_1 \leq 0$ (K_1 and K_2 must have different sign). At 474 K they observed a hysteresis for the c-direction while the $M(H)$ curve is linear in the hard direction. The hysteresis appears across a large temperature range and

this suggests a structural transition (suggested also with a derived equation that determines the first spin reorientation at 270 K). The first transition is thus due to a volume thermal expansion that is the displacement order-disorder in the phase transition in the MnSb phase diagram in figure 3.8.a. The second at higher temperature comes from Mn displacements that transform the structure to an orthorhombic unit cell (figure 3.8.a). Figure 3.8.b shows how the hexagonal unit cell of the NiAs-type structure can be transformed into an orthorhombic unit cell by displacement of Mn ions in the uniaxial displacement region (458 K in figure 3.8.a).

3.1.5 Magnetic phase transition in bulk and thin films

The Curie temperature T_c can be expressed with the term α introduced in equation 3.3. Considering the magnetic phase, an applied field \mathbf{B}_a will cause a finite magnetisation and in turn will cause a finite exchange field \mathbf{B}_e . With χ_{para} the paramagnetic susceptibility, one finds [150]

$$\mu_0 \mathbf{M}_s = \chi_{para} (\mathbf{B}_a + \mathbf{B}_e). \quad (3.12)$$

With $\chi_{para} = C/T$ as given in equation 3.2 with C the Curie constant. Substituting 3.4 into 3.12, we find

$$\chi = \frac{C}{T - T_c}, \quad (3.13)$$

where $T_c = C\alpha$. Since equation 3.13 is based on a mean-field approximation, the Curie-Weiss law fails to describe many materials. Instead there is a critical behavior of the form

$$\chi \sim \frac{1}{(T - T_c)^\gamma}, \quad (3.14)$$

with the critical exponent γ . In the case $T \rightarrow T_c$ from below, one finds [150]

$$M_s \propto (T_c - T)^\beta. \quad (3.15)$$

β from equation 3.15 ranges from 1/8 to 1/2 depending on the model of calculation [153] and the anisotropy [162].

At a temperature below the Curie temperature, the correlation length describes the thickness of the interface between \uparrow and \downarrow regions [163]. As the film thickness approaches the ultrathin limit (few monolayers) and since the correlation length diverges at T_c , the correlated magnetic moments are influenced by the finite size of the specimen reducing T_c [162].

3.2 Growth on MnSb on GaAs(111)B

3.2.1 Crystallography of III-V semiconductors

III-V semiconductors are materials composed of atoms of groups III (Al, Ga, In) and V (N, P, As, Sb). III-V semiconductors adopt a zincblende crystal structure, which is a diamond structure with alternating types of atoms at different lattice sites. The GaAs structure is the result of gallium (Ga) atoms placed on one fcc lattice and arsenic (As) on the other as shown in figure 3.9.a. The lattice parameter of GaAs in the zincblende structure is 5.65 Å. On the (001) surface, the dangling bonds are aligned along $[\bar{1}10]$ while those directed towards the bulk are aligned along $[110]$ (figure 3.9.b). This convention is used for labelling the surface vectors and hence surface reconstructions. When a GaAs crystal is cleaved in the (111) direction, the surface has a plane with a single elemental specie. When the surface is Ga-terminated, the surface is referred to as (111)A and (111)B when As-terminated (figure 3.9.c).

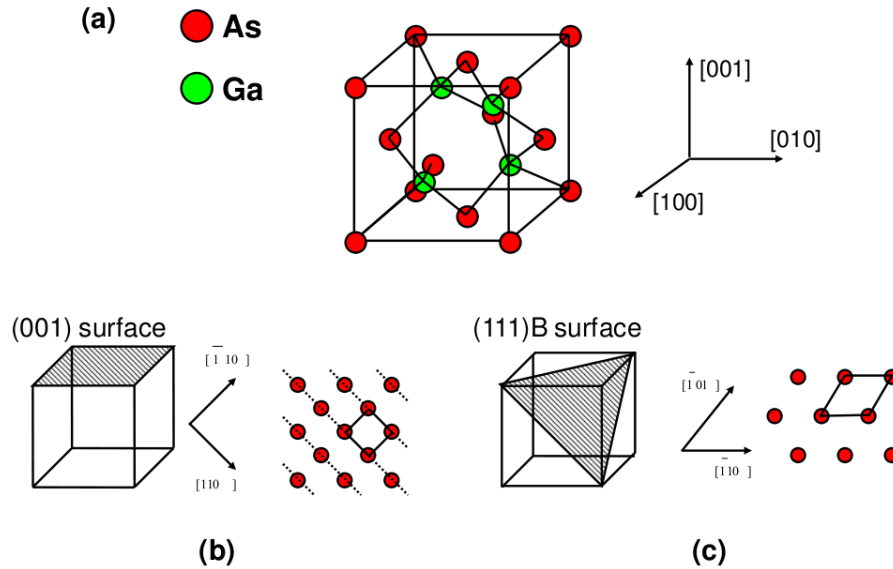


Figure 3.9: (a) GaAs crystal lattice, (b) (001) and, (c) (111)B surface.

Inspired from [136].

The surface has three back-facing bulk bonds and one dangling bond perpendicular to the surface. The (111) plane have vacancies which are related to an unrelaxed structure with (2×2) periodicity [164]. The structure relaxes to form a (2×2) reconstruction with trimer motifs [164, 165]. Due to the higher desorption rate of As over Ga, an annealed surface tends to be group III terminated [165, 166]. The modification in the surface stoichiometry with temperature and the polar surfaces

of GaAs, terminated ideally by pure Ga or As atoms, both induce a large number of surface reconstructions, one in GaAs(111)A and four in GaAs(111)B [167, 168].

3.2.2 Crystallography and surface structure of Manganese Pnictide alloys

Manganese pnictides refer to binary metallic ferromagnets containing Mn and a group V element. The most common structure is the NiAs-type also adopted by MnSb (figure 3.10). Sb atoms occupy the holes in an alternating hexagonal close-packed array (ABAC) in which A(Mn), B(Sb), C(Sb) are the different close packing positions for the hexagonal layer. In the MnSb unit cell, $(\mathbf{a}, \mathbf{b}) = 120^\circ$, $|a| = |b| = 4.128 \text{ \AA}$ and $|c| = 5.789 \text{ \AA}$ [169]. The Sb atoms occupy the sites at $(\frac{1}{3}, \frac{2}{3}, \frac{1}{4})$ and $(\frac{2}{3}, \frac{1}{3}, \frac{3}{4})$.

When deposited on GaAs(111), MnSb grows in the $\langle 0001 \rangle$ orientation. MnSb(0001) can show various surface reconstructions. The (2×2) reconstruction is the most stable and can be obtained from any other reconstruction by heating to $\sim 400^\circ\text{C}$. STM studies provide the ability to distinguish the (2×2) reconstruction from the $td(1 \times 2)$ in MnAs(0001) [170] and MnSb(0001) [171]. *td* stands for triple domains of $(n \times m)$ rotated by 120° with respect to each other.

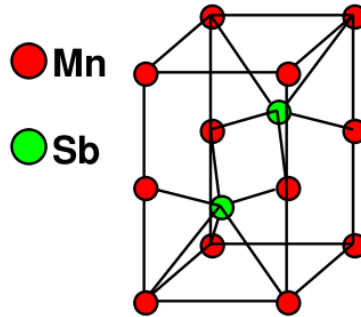


Figure 3.10: Unit cell of MnSb in the NiAs structure type.

3.2.3 Heteroepitaxial growth of MnSb on GaAs

In a growth study of MnSb/GaAs(111)B, Hatfield *et al* found the following optimal set of parameters to ensure growth of MnSb(0001) with a (2×2) RHEED pattern [136]: $T_{\text{Mn}} = 860^\circ\text{C}$, $p_{\text{Mn}} = 1 \times 10^{-7} \text{ mbar}$, $T_{\text{Sb}} = 373^\circ\text{C}$, $p_{\text{Sb}} = 8 \times 10^{-7} \text{ mbar}$,

$J_{\text{Sb/Mn}} = 8$, $T_{\text{subs}} = 400^\circ\text{C}$. T_{subs} is the GaAs substrate temperature and J is the flux ratio of Sb to Mn. The growth orientation was found to be MnSb(0001) by RHEED [171] and X-ray diffraction [136]. Experiments carried out with X-ray photoelectron spectroscopy (XPS) have reported a GaAs-like peak at the surface of a sample grown in the standard conditions described above [172]. This is attributed to Ga-Sb bonding due to Ga segregation as already reported [172]. Nevertheless, Hatfield *et al* proved their sample to be metallic by observing the valence band maximum with XPS. With a vibrating sample magnetometer (VSM) experiment, the sample was found to be ferromagnetic with a magnetic moment of $3.6 \mu_B$ per Mn atom in good agreement with bulk MnSb ($3.5 \mu_B$).

Growth monitoring by STM and measurement of the RHEED feature spacing allow the observation of the initial growth of MnSb on GaAs(111)B. Islands nucleate to form flat-topped 3D islands that coalesce with further deposition. MnSb adopts its own crystallographic structure after 1 min at a flux of $6 \pm 0.5 \text{ nm} \cdot \text{min}^{-1}$ and a transition within 3 seconds afterwards the islands coalesce relaxing the strain [136]. The micron-scale morphology of MnSb grown on GaAs depends sensitively on the growth conditions. Crystal growth with optimum conditions exhibit no strong contrast in scanning electron microscopy (SEM) (figure 3.11.i). Epilayers can also develop micron-sized mesas with flat tops separated by trenches (figure 3.11.ii). The direction of the trenches in figure 3.11.ii gives evidence of the hexagonal symmetry of MnSb(0001) crystal.

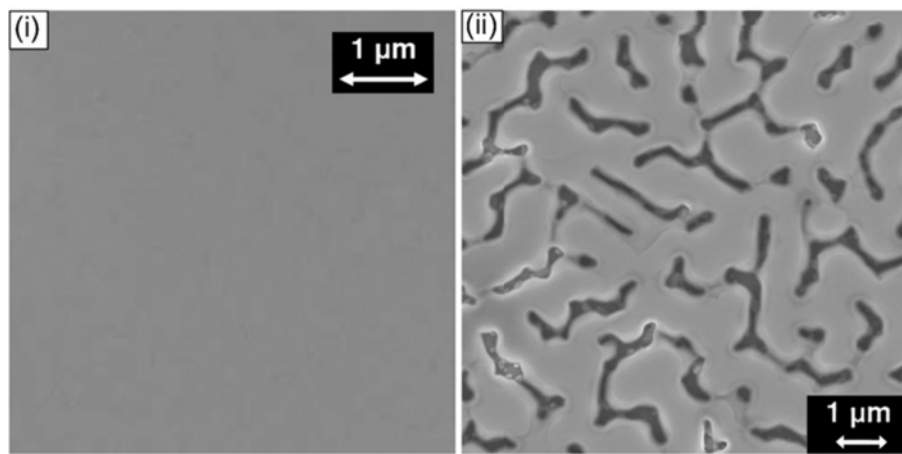


Figure 3.11: SEM Plan view of MnSb(0001) epilayers grown with $J=8$ and $T=420^\circ\text{C}$. Figure reprinted from [166].

After coalescence, the surface consists of large ($> 100\text{nm}$) atomically flat terraces separated by monolayers (c/2) and bilayers (c). In the 3D growth mode, the

total coverage is $70 \pm 5\%$ when the equivalent layer thickness L is $14 \pm 4 \text{ \AA}$ and the coverage is $97 \pm 2\%$ with L equal to $60 \pm 10 \text{ \AA}$. The average mesa heights associated with these cases are $20 \pm 5 \text{ \AA}$ and $60 \pm 10 \text{ \AA}$, respectively [136].

In this chapter, we discussed the feasibility of using a good epitaxial match to inject a spin-polarised current from a ferromagnet into a semi-conductor. The system MnSb has a spin-polarisability of 35% at the Fermi energy and has a good epitaxial match with the III-IV semi-conductor GaAs. We introduced the concept of magnetic domains in ferromagnets. They originate from a balance between the exchange and magnetostatic energies. This balance determines the width of the wall between two domains. In the thin film limit, the broken symmetry at the surface induces a correction to the magnetocrystalline energy to favour out-of-plane magnetisation. It was demonstrated that the bulk contribution can be overwhelmed by the surface contribution. The wall in this case is a rotation of the magnetisation with a rotation axis parallel to the wall plane. The Curie point of MnSb compounds varies according to the composition. After a plateau at 587 K at equi-composition, the Curie point decreases with an increase of Mn in the composition. The magnetic easy axis shifts from the c -plane to the c -axis at 520 K. When MnSb is deposited on the As-terminated GaAs(111) plane, the MnSb crystal grows in the [0001] direction. Parameters for ultimate growth conditions have been found empirically. MnSb thin films grown with these parameters show no micro-scale features that can be resolved with SEM.

Chapter 4 : Instruments

Many surface science techniques use electrons as a probe. Electrons in a certain energy range are very surface sensitive and they carry enough momentum to explore the whole Brillouin zone. They also carry a spin and are easy to generate and manipulate. Photons, in contrast to electrons, will penetrate deeply into a sample, the amount of photons scattered near the surface would be very small and would carry a small momentum.

In the next sections we will discuss the generation of electrons and their interaction with matter at different energy scale in relation with different electron microscopies. In the next sections we will introduce succinctly the scanning electron microscope (SEM), the low-energy electron microscope (LEEM), the spin-polarised LEEM (SPLEEM), the transmission electron microscope (TEM), and the scanning transmission electron microscope (STEM). The evaporators used to perform the molecular beam epitaxy experiments will also be introduced. This chapter deals with diffraction and spectroscopic techniques with the introduction of spot-profile analysis low-energy electron diffraction (SPA-LEED), electron dispersion spectroscopy (EDS), and X-ray photoelectron spectroscopy (XPS).

Finally, an introduction on electron tomography and 3D atomic reconstruction, in relation with experiments described in chapter 8, will also be succinctly introduced in this chapter.

4.1 The mean free path of electrons

The mean free path of electrons is the main reason to use electrons for surface science investigations. The collision time τ , which is the mean time between two scattering events in the Drude model, determines the mean free path of electrons λ_e [173]

$$\lambda_e = \frac{\hbar k}{m_e} \tau, \quad (4.1)$$

where \hbar is the reduced Planck's constant, k the wavenumber, and m_e the mass of electron.

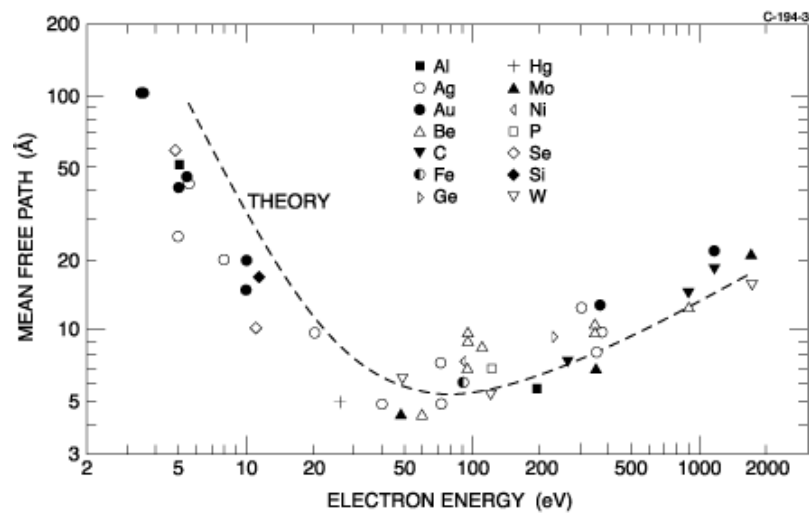


Figure 4.1: The mean free path of electrons in solid from measurement (dots) and calculation (dashed curve). Figure reprinted from [174].

The mean free path of electrons in the 0 to 2000 eV regime is plotted in figure 4.1. The data, measured from many elemental solids, scatter more or less around the calculation in dashed line since inelastic scattering of electrons in this energy range involves mostly excitation of conduction electrons whose density differs more or less from one element to the other.

The mean free path curve has a minimum at about 70 eV of around 6 Å. Any electrons observed with this kinetic energy and having left the solid without suffering a scattering event must originate from the first few atomic layers. The energy loss associated with a scattering event is large making it possible to distinguish between scattered and non-scattered electrons.

4.2 The Ewald sphere construction

LEED (and RHEED) uses elastic scattering events which are characterised by the energy of the outgoing electrons being equal to the incoming electrons. For an incident electron with wavevector \mathbf{k}_0 and scattered wavevector \mathbf{k} , the condition for constructive interference (diffraction) is given by the Laue condition

$$\mathbf{k} - \mathbf{k}_0 = \mathbf{G}, \quad (4.2)$$

where \mathbf{G} is the reciprocal lattice vector (defined in equation 1.4). Because the interactions of low-energy electrons are particularly strong only a few atomic layers are sampled. Using equation 1.4 and 4.2, the condition for interference at a 2D surface (no diffraction conditions in the direction perpendicular to the surface) is given by the following equation

$$\mathbf{k} - \mathbf{k}_0 = h\mathbf{A} + k\mathbf{B}, \quad (4.3)$$

where \mathbf{A} , \mathbf{B} are fundamental unit vectors in the reciprocal space and h, k are integers. The reciprocal lattice of a surface comprises periodically spaced rods that run perpendicular to the surface plane (figure.4.2.a). In an elastic scattering event, no energy is gained or lost. This implies the following equation

$$|\mathbf{k}| = |\mathbf{k}_0|. \quad (4.4)$$

The scattering vector $\Delta\mathbf{k} = \mathbf{k} - \mathbf{k}_0$ connects one point of a sphere with another. This sphere has a radius equal to the magnitude of the wavevector \mathbf{k} and is called

the Ewald's sphere. Any wavevector centered at the origin and terminating at an intersection between a rod and the sphere satisfies the Laue condition and represents an allowed diffraction beam, as shown in figure 4.2.b.

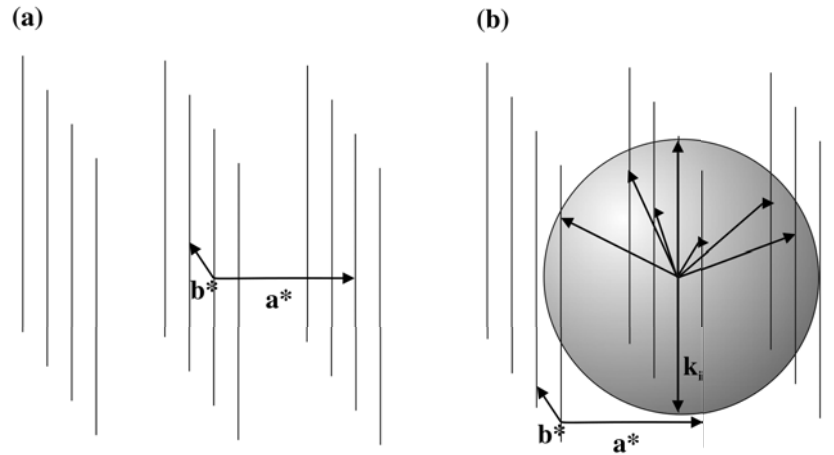


Figure 4.2: (a) Reciprocal lattice rods for a 2D periodic lattice with the unit cell vectors a^* and b^* . (b) Ewald sphere construction, allowed diffraction peaks are located at the intersection of the diffraction rods with the Ewald sphere. Figure reprinted from [175].

4.3 Electron sources and analysers

A common way to generate electrons is emission from a filament annealed by resistive heating. An anode in front of the filament eases the electron extraction. The focusing of electrons is done by placing a Wehnelt cylinder between the anode and the filament which is a negative potential with respect to the filament. However, the voltage gradient along the filament and the thermal broadening due to the required high temperature are reflected in the kinetic energy of electrons. A better design for emitting monochromatic electrons is an indirectly heated crystal which has a low work function such as Schottky emitters which provide superior performance in terms of brightness, source size and lifetime.

The Schottky emitter used at the Birmingham's lab based UHV-SEM is a $\langle 100 \rangle$ oriented tungsten crystal with facet dimensions below 100 nm and tip radius ranging from 0.4 to 0.8 μm . It is a field assisted thermionic source with the tip heated to about 1800 K and with two anodes forming a strong electric field. A reservoir of

zirconium oxide at the shank of the tip lowers the electron work function from 4.5 eV to 2.7 eV. An electrode with 300 V negative bias voltage suppresses the emission of thermal electrons from the protruding tip sides [176].

Electrons are detected with an electron multiplier. It is essentially a glass tube coated with either a resistive layer or with several sequential multiplying electrodes called dynodes. When entering the electron multiplier, a single electron induces emission of roughly 1 to 3 electrons. If an electric potential is applied between this metal plate and yet another, the emitted electrons will accelerate to the next metal plate and induce secondary emission of still more electrons. Repeated a number of times, a large shower of electrons, all collected by a metal anode at the end of the tube, will have been triggered by a single initial electron.

4.4 Molecular Beam Epitaxy

Molecular beam epitaxy (MBE) is defined as vapor deposition in UHV. With a typical flux of a few monolayers per minute (ML/min), MBE is the easiest way to grow atomically controlled multilayer structures [151]. Defects and impurities can act as nucleation sites for adsorbates and can alter the structure and properties of the film. Our quasicrystal samples were cleaned by Ar-sputtering and annealing via electron beam. The samples were as well heated via e-beam during deposition because MBE requires thermal energy to promote epitaxial film growth.

Evaporation refers to the heating of materials in order to reach a vapour pressure sufficient to achieve a flux of atoms. There are numerous types of vapour sources but they give similar results in term of crystalline quality [89].

In our experiment we deposited Al and Ni. Al was evaporated from a Knudsen cell, which is a crucible surrounded by a heater and several layers of radiation shielding. The deposition rate is extremely stable being determined by the temperature of the furnace monitored by a thermocouple. Ni which has a higher melting point is evaporated with an electron beam evaporator [89].

4.5 Imaging and spectroscopy with SEM

As we discussed above, electrons hold great advantages for surface characterisations. The resolution of microscopes depends on the wavelength of the photons or

electrons. Using electrons instead of photons drastically increases the resolution since electrons can reach sub-Angstrom wavelengths. The wavelength of a non-relativistic accelerated electron is given by the de Broglie relation

$$\lambda[\text{\AA}] = \sqrt{\frac{150.4}{E[\text{eV}]}} \quad (4.5)$$

which returns a wavelength of 0.1 Å for electrons with 10 keV kinetic energy. However, the resolution is limited by additional effects such as spherical and chromatic aberrations of the electron lenses (see section 4.9).

The scanning electron microscope (SEM) uses a deflection coil system making it a scanning rather than an imaging device. SEM uses high energy electrons typically in the energy range of 3 keV to 20 keV. Interaction of these electrons with the atomic nucleus or outer shell electrons can be either elastic or inelastic. The ionisation of the atoms in the specimen leads to secondary electron (SE), X-ray, Auger electron emission, and cathodoluminescence [177]. SE signal collection is carried out by a three component device introduced by Everhart and Thornley ("ET detector"). The device consists of a scintillator which converts the electron signal into light, a quartz or perspex light pipe which transfers the light, and a photomultiplier tube which converts the light into an electronic signal.

The interaction volume of the high energy electron beam with matter is shown in figure 4.3. Auger, SE, and backscattered electrons can escape. However, only secondary electrons with a typical energy below 50 eV are detected by using a filter. They travel a distance of about 1 nm in the near-surface region so that the lateral spatial resolution of an SEM is about 2-3 nm [177]. The Birmingham based UHV-SEM is equipped with an in-lens SE detector. Such a system produces a magnetic field at the sample surface which focuses the electrons onto the scintillator.

Electrons are ionizing radiation, capable of removing the tightly bound, inner-shell electrons from the attractive field of the nucleus. Energy dispersive spectroscopy (EDS) uses the electron beam induced X-ray whose energy is characteristics of an element. A detector converts the X-rays into voltage signals and the information is sent to a pulse processor.

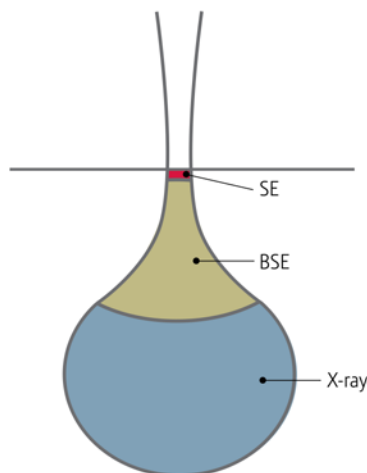


Figure 4.3: Interaction of electron beam in the keV range with matter. The ionisation of the atoms in the material leads to Auger electrons (not shown), secondary electrons (SE), backscattered electrons (BSE), and X-rays. Secondary electrons have low energies (< 50 eV) and travel a short distance in the sample (~ 1 nm). Auger are generated within a region 1 nm deep. The X-rays interaction volume is in the micrometer scale. Figure reprinted from [178].

4.6 Electron spectroscopy for chemical analysis

X-ray photoelectron spectroscopy (XPS) uses low-energy X-rays (a few keV) to induce the photoelectric effect. XPS experiments must be conducted in UHV conditions since it facilitates the transmission of the photoelectrons to the analyser but also minimizes the recontamination of cleaned sample.

The first successful recording of an XPS spectrum was made by collecting photoelectrons through a magnetic field hemisphere [179]. The positions of the smears produced on a photographic plate were characteristics of the photoelectron kinetic energy. According to the Einstein equation for the photoelectric effect, the kinetic energy E_k of the photoelectron was related to an atomic binding energy E_b by

$$E_k(e^-) = h\nu - E_b. \quad (4.6)$$

The next landmark progress in XPS was made by Kai Siegbahn in the mid 1950 by developing high-resolution beta-ray spectrometer capable of resolving previous smears into distinct peaks characteristic of a particular electron shell or to chemical bonding effects [180]. The development of quantum mechanics in the late 1920s allowed the interpretation of the intensity peaks as a quantitative measurement of

the composition of the sample's surface.

XPS is very surface sensitive, due to the attenuation of the flux of emerging photoelectrons. The X-rays penetrate a few micrometers into the sample generating photoelectrons through the irradiated volume. If produced close to the surface, the photoelectrons will escape without colliding, carrying the characteristic atomic binding energy information. The electrons produced deeper down, if they do emerge, will suffer collisions before reaching the surface. These electrons will therefore contribute to a continuous background of inelastically scattered electrons on the high-binding energy side of the photoelectron peak where they should have originally appeared.

The average distance between collisions is the inelastic mean free path (IMFP). The IMFP is a function of both the sample composition and the photoelectron kinetic energy, as shown by the well-know IMFP curve in figure 4.1. The probability $p(E)$ that a photoelectron at a depth z escapes the sample without losing energy is of the Beer-Lambert type [181]

$$p(E) = \exp \left(-\frac{z}{\lambda_e(E) \cos \theta} \right), \quad (4.7)$$

with $\lambda_e(E)$ the photoelectron inelastic mean free path at the energy E which is typically 2-5 nm, and θ the angle of the detector with respect to the normal direction of the sample surface.

In our experiments we used Al-K α X-ray (1486.6 eV) with electron detection at normal emission. The energy dispersion of the X-ray source is 0.9 eV, and the combined experimental resolution ranges between 2 and 3 eV. An X-ray spot size is typically in the millimetre range.

4.7 SPA-LEED: theory and techniques

Low energy electron diffraction is one of the first and most successful surface science techniques. The surface unit cell is experimentally accessible when the electrons wavelength is in the order of the atomic distance, which is the case for electron energies in the range of 50 to 200 eV according to equation 4.5. This technique is also non-destructive for metals. LEED and corresponding techniques (RHEED, LEEM) have been shown to be very sensitive to the presence of surface steps and others types of defects such as domain boundaries [182]. These sensitivities have different sources, some of them coming from the extra diffraction spots associated

with particular domains, others exploiting the difference between in-phase and out-of-phase scattering [183, 184].

Typical LEED optics consist of a filament that provides a nearly monoenergetic source of electrons by thermionic emission (section 4.3), electrodes to produce a narrow beam of electrons, a detector assembly that includes a set of grids for eliminating the inelastically scattered electrons, and a phosphor screen (often coupled with a charge coupled device or CCD camera for frame acquisition). LEED grids are able to remove plasmon loss electrons ($\sim 10\text{-}20$ eV) but the intensities measured include phonon scattering (~ 25 meV).

There are three types of LEED apparatus in use. In the "normal-view", a gun and a screen are mounted on a UHV flange and the pattern is viewed past the sample which therefore has to be small enough to not obscure the view. Most new systems are of the "reverse-view" type where the gun has been miniaturised and the pattern is viewed through a transmission screen and a viewport. The third and most powerful technique is where, in addition to viewing the screen, the LEED beam can be scanned over a detector using electrostatic deflectors and focusing. This technique allows spot profile analysis which is sensitive to steps and other forms of disorder at the surfaces. This instrumental technique, known as SPA-LEED, emphasises the spot-profile analysis capability.

A SPA-LEED is composed of four major parts: a fine focus electron gun, an entrance lens close to the sample, an electrostatic or magnetic deflection unit, and a small aperture in front of a single electron channel detector. Commercial SPA-LEEDs also have a screen for visual inspection of the LEED pattern. The current can be set in the range from 50 pA for high resolution to 500 nA for visual inspection. The electron beam is not focused on the sample but onto a 100-300 μm aperture in front of the channeltron detector [175].

A further important requirement is a large dynamic range for the measurement of electron intensities. With increasing transfer width, the FWHM of the central peak of the LEED spot decreases while its integral intensity stays constant resulting in a strongly enhanced peak intensity. The signal-to-noise ratio is enhanced by a factor of 200 compared to a standard 4-grid LEED optics [182]. Thus, for a well prepared Si surface, the ratio of peak to background intensity can reach 10^6 . This requires an electron detector with a dynamic range superior to 10^6 . This can be achieved by a single electron channeltron detector with a maximal count rate of more than 10^6

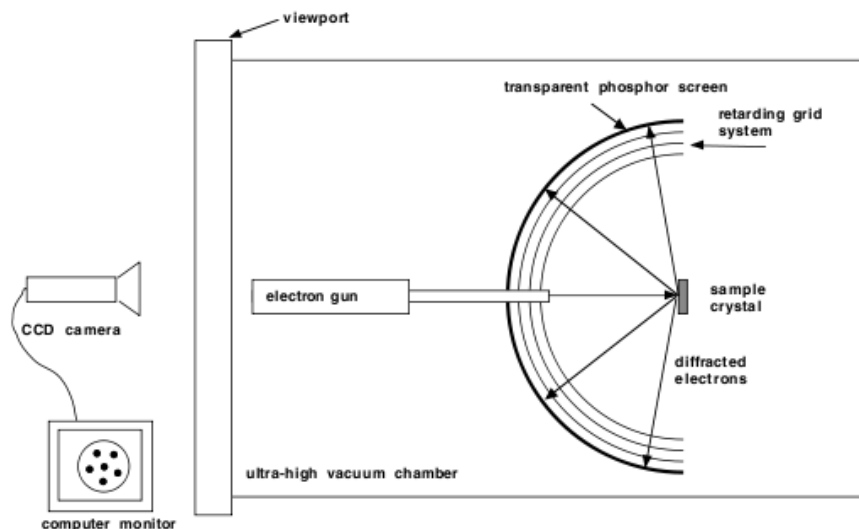


Figure 4.4: Schematic diagram of a LEED of type 2 (reverse view). The hemispherical grid system repels the electron having energies below the elastic energy and the diffracted electrons are accelerated toward the phosphor screen. The LEED can be viewed through the viewport and recorded with a CCD camera. Figure reprinted from [175].

counts/s.

A retarding field analyser reflects inelastic scattered electrons with a cut-off value of ~ 1 eV reducing the inelastic background by a factor 2 to 5 but does not discriminate electrons with phonon losses or gains.

Using a single electron detector, it is necessary to record the entire LEED pattern in the scanning mode. The SPA-LEED electrostatic deflection plates vary the angle of incidence of the electron beam at the sample position, as shown in figure 4.5. A second set of deflection plates with opposite polarity keep the electron beam position constant on the sample independent on the angle of incidence. These plates are arranged in a form of two octopoles in order to minimise field inhomogeneities in the x and y directions.

The diffracted electrons recorded by the channeltron detector follow almost the time reversed path of the incident electron due to the proximity of the detector to the electron gun. Scanning the incident angle of the electron beam results in a simultaneous variation of the angles of the diffracted electrons. This special scanning mode is sketched in figure 4.6. While the incident angle is changed, the Ewald sphere is rotated around the origin of reciprocal space (000). SPA-LEED makes

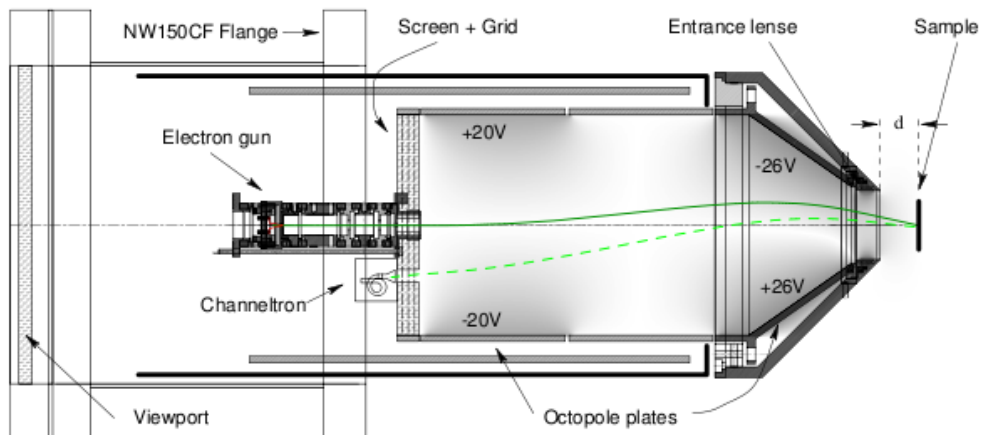


Figure 4.5: Horizontal cut through a 3rd generation SPA-LEED with conical shape showing the electron gun, the channeltron detector, the electrostatic deflection unit, the entrance lens, and the sample in a position at distance d , and the path of electrons recorded in the detector. Figure reprinted from [182].

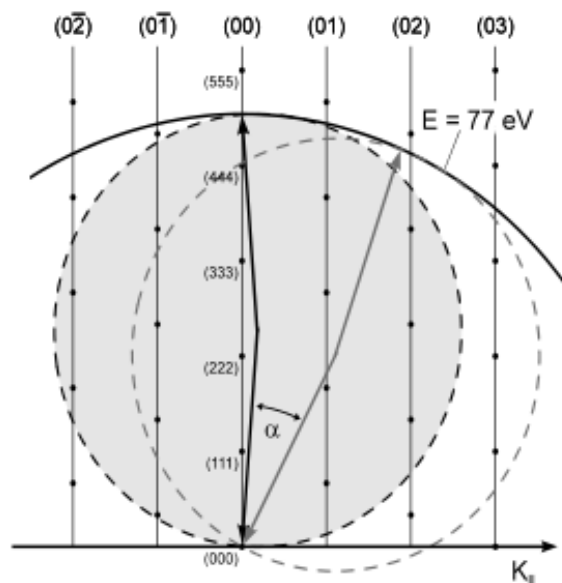


Figure 4.6: SPA-LEED diffraction geometry using internal electron gun. The relative angle between incident and final scattering vectors are kept constant. The recorded diffraction pattern is described by the envelope of the rocking Ewald sphere which is a sphere centred at the origin of the reciprocal space with a diameter twice the size of the Ewald sphere. Figure reprinted from [182].

available for measurement a larger area of reciprocal space than the 4-grid LEED at any given electron energy. The spot broadening is determined by the transfer width of the instrument which in turn defines the maximum surface area from which electrons interfere coherently. Small barrel distortions of the images are caused by non-linearities of the deflection unit. The recorded diffraction pattern can be corrected by calibration.

4.8 LEEM and SPLEEM

Low-energy electron microscopy (LEEM) images with diffracted or backscattered slow electrons. Elastically backscattered electrons used for imaging frequently have their energies smaller than 10 eV. In this energy range, their cross sections are large enough for surface imaging [183]. In contrast to scanning image acquisition, LEEM works in true imaging mode in which all pixels are acquired simultaneously from the illuminated area on the surface [184, 185]. This gives LEEM some advantages compared with other imaging techniques, such as large field of view and fast image acquisition. LEEM has a depth resolution similar to that of an STM [184] but chromatic and spherical aberrations of the cathode lenses limit the lateral resolution to about 10 nm (see section 4.8.2).

In this section, we will discuss the interactions of very low energy and slow electrons with matter in order to understand the LEEM contrast. In ferromagnetic materials, interactions depend additionally on the relative orientation of the spin of the incident electrons and electrons in the sample. The associated imaging method, spin-polarised LEEM (SPLEEM), giving magnetic information, will also be introduced.

4.8.1 Very-low-energy-electron/matter interaction

Interactions of slow electrons ($E < 10$ eV) with matter involve elastic scattering, inelastic scattering, and quasi-elastic scattering (phonon scattering and in magnetic materials, magnon scattering).

Atoms in the condensed phases cannot be described by the Born approximation which assumes static atoms in their ground states. With decreasing energy, forward scattering decreases whereas inelastic and elastic scattering become increasingly important. Elastic scattering can be calculated in the partial wave expansion.

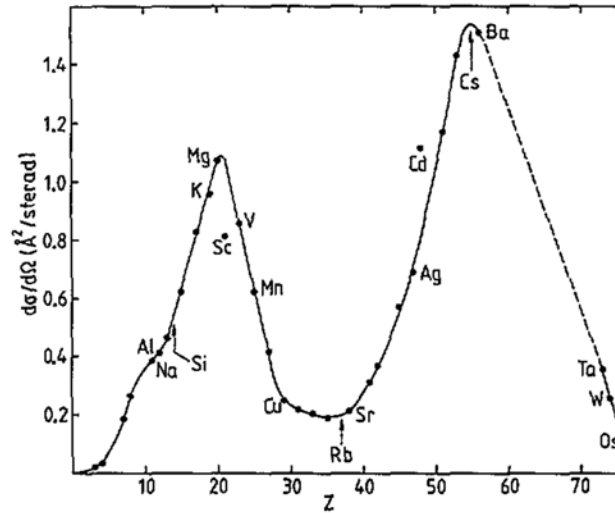


Figure 4.7: Elastic backscattering cross sections $d\sigma/d\Omega$ (178°) of free atoms as a function of nuclear charge Z for 100 eV electrons. The dashed line is a simple interpolation. Figure reprinted from [184].

In this model the scattered wave is approximated by a finite number of spherical wave [184]. Figure 4.7 shows the backscattering cross-section of free atoms calculated with relativistic Hartree-Fock-Slater potentials taking into account partial waves up to angular momentum $l=10$ [186]. Figure 4.7 illustrates that backscattering does not increase monotonically with nuclear charge. At energies below about 100 eV the truncation of the atomic potential by the neighbouring atoms in the condensed state becomes important. At lower energies still, due to charge-charge and spin-spin interactions, the scattering potential is modified between the incident and atomic electrons. Including these effects in a new model, E. Bauer found that light atoms such as hydrogen (H) may backscatter more strongly than heavy substrate atoms such as tungsten (W). Other light atoms such as Al backscatter more than W over a wide energy range [184].

In a periodic system, if we assume that the $n+1$ -electron system (n crystal electrons + one incident) does not differ significantly from the n -electron system (Koopman's theorem [187]) then 180° backscattering may be determined by the band structure $E(\mathbf{k})$ perpendicular to the surface as illustrated in figure 4.8 for the W(110) surface. The periodic distribution of the atoms produces the band structure with allowed wavevector in the energy state $E(\mathbf{k})$. Forbidden regions come from discontinuities at the Brillouin zone boundaries and by the splitting of the energy bands at band crossings. In a bandgap, as between 1 and 6 eV above the vacuum level

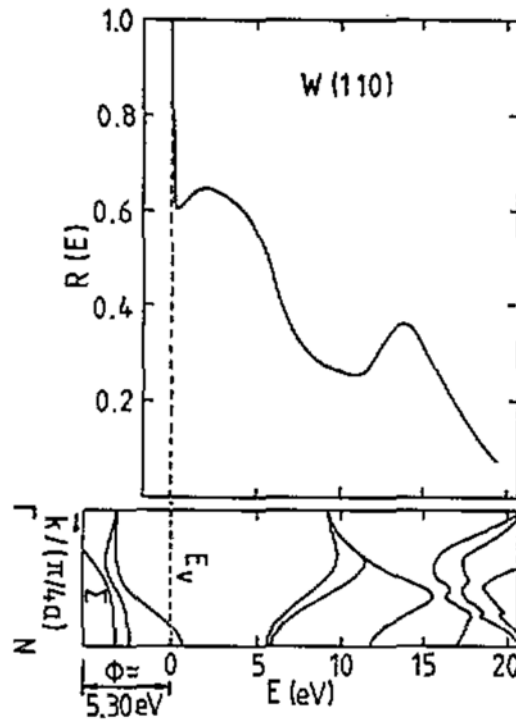


Figure 4.8: Normal incidence specular reflectivity of a W(110) surface (top) and band structure along the the surface normal (bottom). Figure reprinted from [184].

in figure 4.8, the incident electrons do not find allowed states and are consequently totally reflected. Total reflection is used in this case assuming the evanescent wave penetration, the surface states, and the momentum transfer from electron-surface phonon interaction are insignificant. Imperfections-induced scattering at surfaces are also neglected since electrons are reflected before being attenuated significantly by inelastic scattering. Backscattering and band structure cause the high reflectivity peak at 2-3 eV. The second reflectivity peak is due to the low density of states in the crystal as indicated by the steep bands. Below the vacuum energy, the energy states are filled inducing the high reflectivity peak that can be seen in figure 4.8.

Below the threshold for collective excitations, valence electron excitations (electron-hole pair creation, intra- and inter-band transitions) are the processes which determine attenuation by inelastic scattering. The high surface sensitivity of LEEM is in general the result of the strong scattering of slow electrons by inelastic scattering. Inelastic processes, which involve inner electron shells cannot take place because of insufficient energy. In contrast inelastic processes involving outer shells are near their maximum except at very low energies. The attenuation coefficients

$\mu = (\text{IMFP})^{-1}$ due to inelastic scattering and ν due to elastic backscattering of disordered Al shown in figure 4.9 were calculated using the jellium model (free electron gas embedded in a homogeneous background of equal charge). The term μ domi-

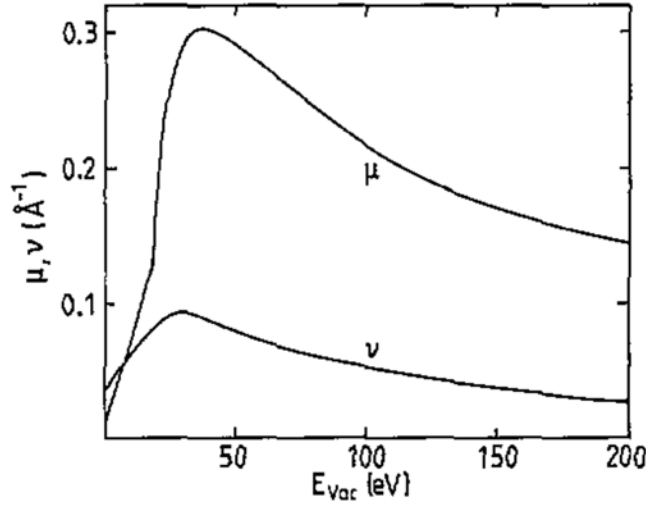


Figure 4.9: Energy dependence of the attenuation coefficients μ inelastic, and ν elastic of Al. Figure reprinted from [186].

nates ν above the threshold energy for plasmon excitations E_T ($E_T = 17.5$ eV for Al). At $E > E_T$, the sampling depth is determined mainly by inelastic attenuation with a mean free path ranging from 3 Å to 10 Å. For $E < E_T$ elastic backscattering increasingly determines the penetration depth.

In summary, at low energies backscattering is strong and depends on energy E and nuclear charge in a non-monotonic manner. The sampling depth of LEEM can be determined by inelastic and elastic backscattering depending on the band structure. Depending upon the band structure, slow electrons may be reflected from surfaces with a high reflection coefficient from the first few atomic layers or may penetrate deeply into the crystal when the incident energy can be matched to $E(k)$ states. The sampling depth may be as small as a few tenths of a nanometre around the plasmon excitation maximum in transition metals with a high density of unoccupied states above the Fermi level, or in band gaps along the \mathbf{k} direction normal to the surface. On the other hand, in insulators and free electron like metals the sampling depth may be as deep as several nanometres [183]. In many cases, tuning the energy allows one to choose the sampling depth to image a given surface and thin films.

4.8.2 LEEM optics

LEEM uses diffracted low energy electrons for imaging the real space of a surface. The electron optics of a LEEM is essentially the same as in an emission electron microscope. However, in a LEEM the specimen is the cathode of a so-called cathode lens. In these cathodes, imaging electrons are accelerated in a high electric field to an electrostatic or magnetic lens and incident electrons decelerated to the desired low energy at the specimen. These cathode lenses carry imaging information through the electromagnetic optics at high energy (15 keV) for better resolution and focusing. Surface studies with LEEM require ultra-high vacuum in all sections of the microscope since backstreaming from the illumination and imaging optics through the beam separator and cathode lens is to be avoided.

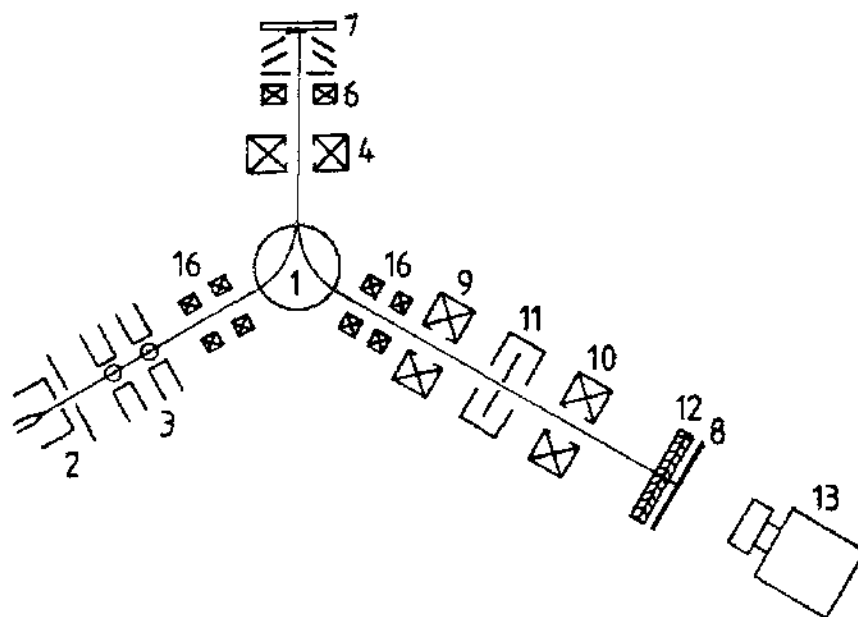


Figure 4.10: Schematic of the first LEEM instrument. Figure reprinted from [183].

A schematic of the first instrument in figure 4.10 illustrates the basic electron optical setup of a LEEM. The beam separator (1) deflects the incident beam from a field emission gun (2). The emitted electrons are focused by two condensers (3) and optionally by a collimator lens (4) into the back focal plane of the objective lens (6) onto the sample (7). If the electrons are scattered from a long-range ordered surface, they form a diffraction pattern at the focal plane of the objective lens (6) but rays of common origin meet again in the image plane to form a direct image of the surface. Changing the focal length of the first condenser allows variation of the spot

size illuminating the sample. The astigmatism of the objective lens is corrected with a magnetic stigmator (between 6 and 7). The electrons elastically reflected at the sample's surface are imaged at the center of the beam separator. The reflected electrons pass again through the sector field to reach the imaging column. The primary image in the center of the beam separator is imaged with a magnetic intermediate lens (9) and a projective lens (10) onto the detector. A pair of multichannel plates (12) enhances the image intensity on the fluorescent screen (8), allowing observation and image recording with a video camera (13) at very low beam currents. Both illumination and imaging columns are equipped with deflectors and stigmators (16). The purpose of the electrostatic filter lens (11) was to filter out secondary and inelastically scattered electrons but was later removed because it was found that the dispersive properties of the magnetic beam separator (1) were sufficient to eliminate them from the image. Varying the focal length of the intermediate lens (9) allows the imaging of either the real or reciprocal space. The combination of (9) and (10) tunes the magnification in the imaging mode.

In the past 10 years LEEM was developed further by combining it with X-ray induced photoemission electron microscopy (XPEEM), which resulted in spectroscopic photoemission and low-energy electron microscopy (SPELEEM) and in the building of instruments with aberration correction.

One of the most useful application of LEEM is the study of growth phenomena such as the interface of Cu silicide layers grown at high temperature on Si(111) observed to be isolated crystals with a variety of shapes [188]. The visualisation of monoatomic steps was one of the first successes of LEEM and studied in many systems in which the height of the steps can be extracted from the energies of maximum and zero phase contrast [184]. LEEM enlarges the understanding of phase transitions, homoepitaxy, heteroepitaxy and reactions with gases. For example, LEEM proved that the Si(111)-(7×7)↔(1×1) phase transition is of first order with a morphology and transition width which depends strongly on surface purity, pre-treatment and cooling rate [189].

4.8.3 Contrast mechanisms

Contrast in LEEM imaging has a diffraction origin in crystalline samples and backscattering origin in amorphous or fine-grained crystalline samples. In general, surfaces are heterogeneous in topography (steps, step bunches). Topographic fea-

tures distort the electric field distribution on the surface causing the usual topographic contrast. Backscattering contrast comes from a different backscattering cross-section between two elements.

Single crystalline layers with a well-defined orientation have often been studied. Flat single crystal surfaces without steps and others defects produce contrast only when regions with different crystal structures are present. If a surface presents two phases with the same normal and lateral periodicity, contrast is obtained by tilting the incident beam or shifting the aperture. An example is the Si(100) surface reconstruction with formation of dimers rotated from terraces to terraces by 90° , the two resulting domains (2×1) domains are equivalent at normal incidence. To observe contrast one shifts the aperture in the direction of one of the rows.

Another important contrast mechanism is the interference contrast on flat surfaces with height differences such as atomic steps (figure 4.11.a). Step contrast is due to destructive interference between the wave fields reflected from the adjoining terraces within the lateral coherence length. Using equation 4.5, one gets a vertical resolution of about 4 \AA with incident electrons of 10 eV energy. Nevertheless, in the absence of aberrations the reflection of slow electrons from a point source would produce an interference pattern that extends far from the step. This could make image interpretation difficult in the presence of several steps. The spherical aberration reduces the range of the interference pattern significantly and the chromatic aberration reduces it to a maximal intensity next to the step even for energy spreads as low as 0.5 eV.

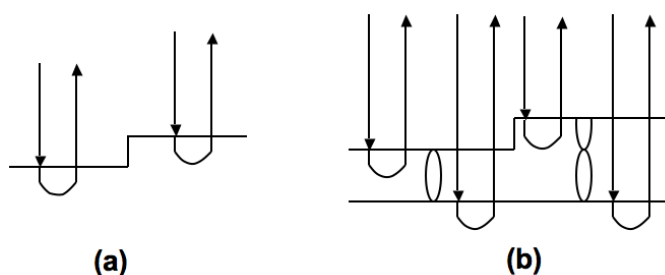


Figure 4.11: Schematic of the conditions for phase contrast in LEEM

(a) Step contrast, (b) Quantum size contrast. Inspired by [183].

A further contrast mechanism is quantum size contrast as illustrated in figure 4.11.b. Interference in this case does not require crystal periodicity. Reflected waves from the bottom surface can interfere constructively or destructively with those reflected from the top surface in a similar way to a Fabry-Perot interferometer. En-

hanced reflectivity occurs whenever $n(\lambda/2) + \phi = d$ where n is an integer, λ the wavelength of the incident electron, ϕ the phase shift, and d the film thickness. Figure 4.12 shows the contrast of two and three monolayers thick islands of Sb on Mo(001). Excluding interference phenomena, the spin-independent part of the re-

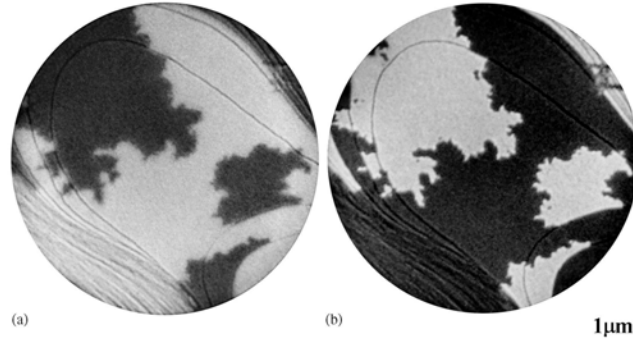


Figure 4.12: LEEM images of 2 and 3 ML Sb films on the Mo(001) surface at incident energy beam (a) 4.5 eV and (b) 5.5 eV. Figure reprinted from [190].

fectivity is determined by diffraction in the crystal. This points to a main limitation with LEEM imaging: it requires a strong preferred crystal orientation [191].

4.8.4 Spin-polarised LEEM (SPLEEM)

SPLEEM does not give structural but magnetic information. It differs from LEEM by an illumination system which produces a spin-polarised electron beam. The polarisation is achieved by illuminating a GaAs (100) surface with circular polarised light with the wavelength corresponding to the bandgap of GaAs. The surface is activated by Cs and O₂ exposure. Their negative electron affinity allows electrons from the bottom of the conduction band to escape the surface. Optical selection rules produce emitted electrons with their spins pointing up or down when excited by light of right or left helicity, respectively. Cathodes used in SPLEEM have a polarisation of 20-30% (as the one at NCEM). After extraction from the cathode, the electron beam is deflected by 90°. A magnetic rotator lens allows the polarisation \mathbf{P} to be rotated in any direction. However, in our experiments we used a direction normal to the surface and two others in preferred directions in the surface plane.

Backscattering from magnetic materials depends on the relative orientation of the spin polarisation \mathbf{P} of the incident electrons and the magnetization in the substrate \mathbf{M} . The exchange interaction is then $\mathbf{P} \cdot \mathbf{M}$. The contrast obtained depends

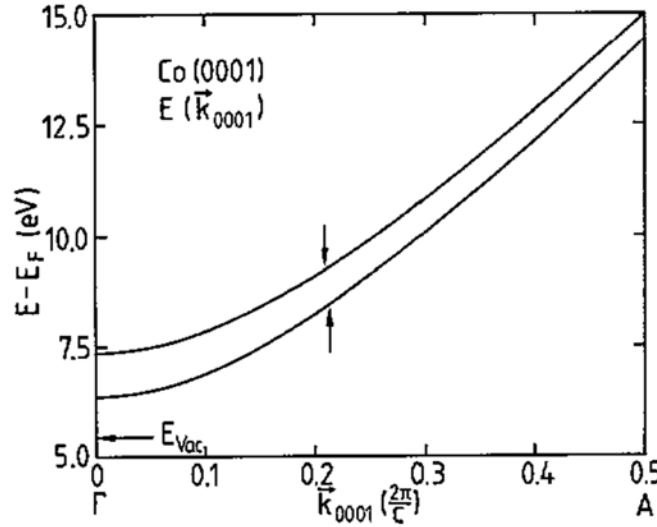


Figure 4.13: Spin-polarised band structure of Co in the [0001] direction. Figure reprinted from [184].

on beam energy not only because of the Fabry-Perot type interference (QSE) but also because the reflectivity is spin-dependent (figure 4.13). The difference between the IMFP for spin-down is shorter by a factor of up to 3 due to a higher density of unoccupied spin-down states in the crystal [191]. Between the two bands in figure 4.13, a suitable polarised electron would find allowed states and would penetrate deeply into the crystal, whereas electrons with opposite spins will be strongly reflected. This difference in reflectivity produces a magnetic contrast quantified by the following asymmetry term

$$A = P_0 \frac{(I_{\uparrow} - I_{\downarrow})}{(I_{\uparrow} + I_{\downarrow})}, \quad (4.8)$$

where the $I_{\uparrow,\downarrow}$ s are the reflected currents and P_0 is the polarisation of the incident beam. This effect is weak compared to topographic signals. To obtain a pure magnetic contrast one takes two images with opposite \mathbf{P} direction and subtracts one from the other pixel by pixel. To achieve a good signal to noise ratio with a GaAs photoemission cathode, exposures of about one second per image are needed.

4.8.5 Resolution of the SPLEEM at the NCEM

To find out the resolution of our apparatus, we measured a line profile at the step edge of a Pb-island on Si(111) (figure 4.14). By taking the value at 80% and 20% of a sharp edge we found a resolution of 48 nm. Each pixel takes the average

value of 7 pixels perpendicular to the line scan. The profile was scaled with respect to the field of view.

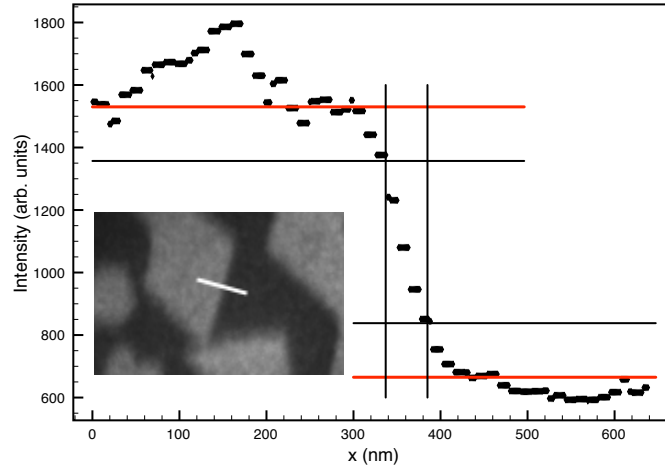


Figure 4.14: Profile analysis of a line scan across a sharp contrast giving a resolution for the SPLEEM of about 48 nm. Inset: image from which the line scan was extracted with Pb (white) on Si(111) (black).

4.8.6 Electron energy determination

The electrons are produced by a GaAs crystal heated by a voltage-induced current. The extraction of the electrons is eased by a laser beam by photoemission and a deposit of cesium that lowers the work function. The microscope user can tune a voltage U applied between the sample and the GaAs crystal. The kinetic energy of the incoming electron, E_{kin} , at the sample is then

$$E_{kin} = e(U + U_0), \quad (4.9)$$

where U_0 depends on the workfunction of the sample, the applied extracting field and the laser illumination. The value for U_0 ranges between 2 and 3 V and can be determined experimentally.

4.9 TEM and STEM

According to de Broglie's equation (equation 4.5), a transmission electron microscope (TEM) using 100 keV electrons could possibly reach a resolution of 4 pm. In fact, the resolution is limited by the electron lenses. However, recent breakthrough in TEM development namely spherical- and chromatic-aberration corrections have

allowed TEM to reach sub-angstrom resolution. Spherical and chromatic aberrations are referred as C_s and C_c , respectively. The resolution beyond the current state of the art is no longer of paramount importance.

In order to get a transmitted electron signal, the sample needs to be thin. Thin refers to electron transparency when there are enough electrons to be transmitted into the detection device. For 100 keV electrons, 1 μm aluminium alloy would be thin while steel would be thin up to several hundred nanometres.

Imaging methods in TEM utilise the information contained in the electron waves exiting from the sample to form an image. Thus, an observed image depends on the amplitude of the beam and on the phase of the electrons. Different imaging methods therefore attempt to modify the electron waves exiting the sample in a form that is useful to obtain information with regard to the sample.

The most conventional operating mode for a TEM is the bright-field imaging mode (BF) where the contrast is formed by occlusion and absorption of electrons. The atomic scattering factor is greater for heavy elements so that these atoms appear ideally as dark spots. The contrast also varies as a function of objective lens defocus and the specimen thickness. For example, the TEM may be operated at a slight defocus to enhance contrast since the sample is a weak phase object.

Higher resolution imaging (HRTEM) requires thinner samples and higher energies of incident electrons. Therefore the sample can no longer be considered to be absorbing electrons. The sample can be modelled as an object that does not change the amplitude of the incoming electron wavefunction but modifies its phase. With this technique, contrast arises from the interference in the image plane of the electron wave with itself. The images are not dependent on the number of electrons hitting the screen only. Interpretation of phase contrast images is therefore complex.

A scanning transmission electron microscope (STEM) differs from a conventional TEM as the electron beam is focused into a narrow spot scanned over the sample. The rastering of the beam across a sample allows other analysis techniques such as energy dispersive spectroscopy (EDS), electron energy loss spectroscopy (EELS), and annular dark-field imaging (ADF). These signals can be obtained simultaneously to the image allowing direct correlation between them. High-angle annular dark field scanning transmission electron microscope (HAADF-STEM) is a method of mapping the sample by collecting scattered electrons with an annular dark-field detector. This detector collects incoherent scattered electrons such as those due to

Coulomb or thermal diffuse scattering as opposed to Bragg scattering.

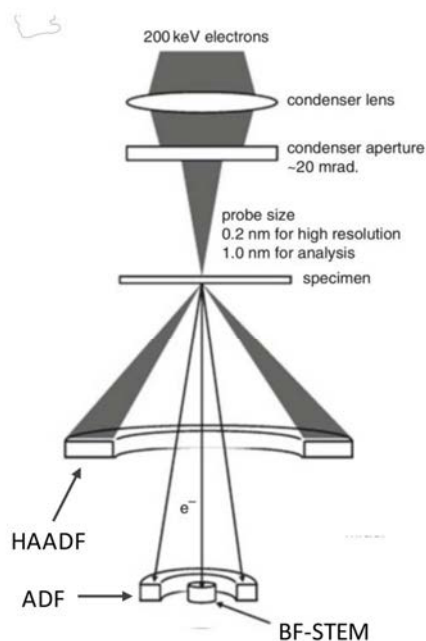


Figure 4.15: Schematic illustration of the electron microscope configuration in the HAADF-STEM mode. Adapted from [192].

Along a zone-axis orientation, the HAADF signal is approximately proportional to $Z^{1.8}$, where Z is the atomic number [193]. At large angles (50-100 mrad), the annular detector collects elastically scattered electrons with negligible phase-contrast effects. Thus, unlike HRTEM, HAADF-STEM is based on an incoherent imaging process and the contrast of the image is not reversed by defocusing or by the specimen thickness. However, HAADF-STEM intensity can vary slightly as a function of specimen thickness due to contributions from coherent and multiple scattering. The contrast is then, to a good approximation, monotonic with thickness, and is also sensitive to changes in composition. These properties make the HAADF-STEM signal ideal for tomographic application.

4.9.1 Introduction to electron tomography

Invented by biologists interested in the shapes of complex molecules, the technique of electron tomography uses a sequence of image taken at different tilts to create a 3D image. Atomic resolution images can be used to obtain a 2D projection of the specimen structure averaged along the electron propagation direction. Eluci-

dating structural and chemical variations along the depth coordinate was revealed to be quite difficult in practice. The scattering effects induced by single atoms are difficult to trace back to a particular depth position in the sample by using quantum mechanical calculations. Three-dimensional electron tomography attempts to make tomography possible at the atomic scale [194]. TEM holders allow multiple views of the same specimen by rotating the angle of the sample along an axis perpendicular to the beam. By recording multiple images at different angles, typically 1° , a set of images known as tilt series can be collected. In the phase contrast mode, this set of images can be used to get a three-dimensional representation of the sample. The technique of annular dark-field scanning transmission electron microscopy (ADF-STEM) suppresses phase and diffraction contrast, providing image intensities that vary with the projected mass-thickness of samples. ADF-STEM eliminates the edge-enhancing artefacts common in BF or HRTEM. Thus, provided that the features can be resolved, ADF-STEM can yield a reconstruction of the specimen. This technique has the drawback of probing around one cubic nanometre of material [195]. A second approach is to use the depth sectioning technique in which a sample is sliced by changing the objective lens focus. Whereas this technique still allows atomic resolution, 3D reconstruction at atomic resolution have never been reported because the depth resolution is insufficient to resolve interatomic distances along the optical axis. Another method is discrete tomography. It is a reconstruction approach that requires *a priori* knowledge of the lattice structure. Li *et al* presented a 3D structure analysis of a gold cluster from one single HAADF STEM image [196]. In their paper, Van Aert *et al* reported the 3D reconstruction of a complex crystalline nanoparticle at atomic resolution using discrete tomography by combining aberration-corrected HAADF-STEM carried out under low-voltage conditions and discrete tomography [197].

4.9.2 Electron lenses and apertures

The depth of field of a microscope is a measure of how much of a studied sample remains in focus at the same time. The term depth of focus refers to the distance over which the image can move relative to the object while remaining in focus. These properties are governed by electron lenses which intrinsically generate a non-uniform magnetic field. To improve their performances, small limiting apertures narrow the beam to at most a few micrometers across. Such apertures limit the collection angle

and allow the control of the resolution of the image formed by the lens, the depth of field and the depth of focus, the image contrast, and the angular resolution of the diffraction pattern (DP). Apertures protect the specimen from radiation of the illuminating system, they also serve for measuring or changing the beam current. These apertures cut down the intensity but increase the depth of field of the specimen and depth of focus of the images. A large depth of field is used in SEM to produce 3D-like images of the surface. It is also critical in TEM as the specimen is usually in focus from the top to the bottom surfaces at the same time. Thus users need to be careful when interpreting TEM images, TEM presents a 2D image of a 3D specimen viewed in transmission. Thus any TEM information collected (images, diffraction pattern, spectra) are averaged through the thickness of the specimen.

The electron beam current in a TEM can be as high as 0.1-1 μA which is equivalent to 10^{12} electrons passing through the specimen per second. But, at 100 keV energy, the electrons travel at about 0.5 c ($c = 3.10^8 \text{ m.s}^{-1}$), so the electrons are separated by 1.6 nm, thus there is never more than one electron in the specimen at any time. Nevertheless, electrons interfere and allow the acquisition of diffraction patterns.

The magnetic lens imperfections limit the resolution of the microscope but paradoxically help to get better depth of focus and depth of field. The main defects from these lenses are spherical aberration, chromatic aberration, and astigmatism which we will discuss in the following section.

4.9.3 Resolution, spherical and chromatic aberrations

In order to get a good signal, it is important to produce an electron beam with diameter typically less than 5 nm and until below 0.1 nm.

Spherical aberration occurs when the lens field behaves differently for off-axis rays. Electromagnetic lenses bend off-axis electrons more strongly toward the axis. As a result, a point is imaged as a disk of finite size, degrading detail discernibility (figure 4.16.a).

A way to compensate spherical aberration is to create a diverging lens that spreads out the beam off-axis such that they re-converge in a point instead of a disk. The spherical aberration correction is achieved by a highly complex, computer-controlled set of quadrupoles and hexapoles or octupoles.

It is assumed illuminating electrons are monochromatic, in fact the actual energy

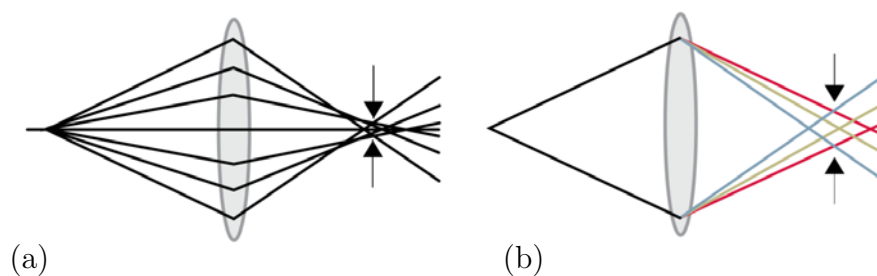


Figure 4.16: Left: by bending the rays at the outside of the lens more than those close to the axis a point object is imaged as a disk in the image plane with a minimum radius in the plane of least confusion. Right, chromatic aberration is the result of electrons with a range of energies being focused in different planes. Emerging electrons with no loss of energy are less strongly focused than those that lost energy. Adapted from [178].

spread is ~ 0.3 eV for a cold field emission gun (FEG) and ~ 1 eV for a LaB_6 gun. However, the energy spread of electron sources can be ignored compared to the whole range of energies created when having a specimen under a beam. The objective lens bends electron of lower energy more strongly and thus a point in the object plane forms a disk in the image plane (figure 4.16.b). To get around this limitation one can use very thin specimens as chromatic aberration gets worst for thick samples [193]. Since most TEM specimens are not thin enough, we have to live with C_c limitations. C_c is typically 10 times larger than C_s -limited resolution so when measuring a thick sample the performance of the TEM is 10 times worse than the specified resolution.

Astigmatism occurs when the electrons sense a non-uniform magnetic field. It can arise from a non-perfectly rounded soft iron bore, microstructural inhomogeneities, slight misalignment of the lenses, charging of contamination of the apertures which can all disturb the optics [193]. Astigmatism can be corrected using stigmators which are small octupoles that compensate the field inhomogeneities.

4.9.4 Electron optics in TEM

The TEM column can be divided into three components: the illumination system, the objective/lens stage, and the imaging system. The illumination system comprises the gun and the condenser lenses and serves to transfer the electron to the specimen. The objective and specimen stage system is the place where the various images and

diffraction patterns (DP) are created. The imaging system uses several lenses to magnify the image or the DP to focus on a viewing screen or a computer screen via a detector.

In TEM mode, the first two condenser lenses (C1, C2) are adjusted to illuminate the specimen with a parallel beam of electrons. For STEM mode and materials research dedicated TEMs, to get the desired probe size $\ll 1$ nm, the usual solution is to introduce a C3 or so-called condenser-objective (c/o) lens (figure 4.17).

If the C2 lens is focused to produce an image of the crossover at the front-local plane (see figure 4.17.a), then a parallel beam of electrons is formed by the objective lens. Parallel illumination is essential to get the sharpest selected area DPs (SADP). Users underfocus C2 in order to fill the viewing screen or strengthen C2 (less parallel) in high magnification mode to keep the illuminated area just filling the screen and illuminate less of the specimen.

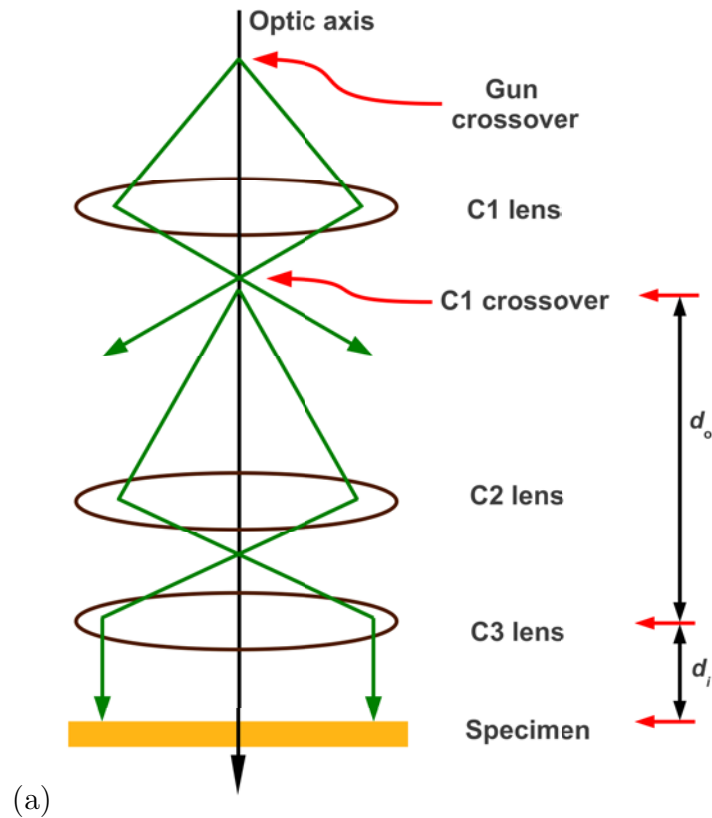


Figure 4.17: The objective focus the beam to the desired probe size. The large d_o/d_i ratio gives the maximum demagnification of the image of the gun crossover. A strong C1 lens results in a large demagnification giving a smaller beam at the specimen. A weaker lens gives a broader probe. Adapted from [193].

The objective lens takes the electrons emerging from the specimen, disperses them to create a DP in the back focal plane, and recombines them with the intermediate lens to form an image in the image plane. An SADP aperture is inserted into the image plane of the objective lens in order to obtain a parallel beam of electrons to obtain a sharp DP.

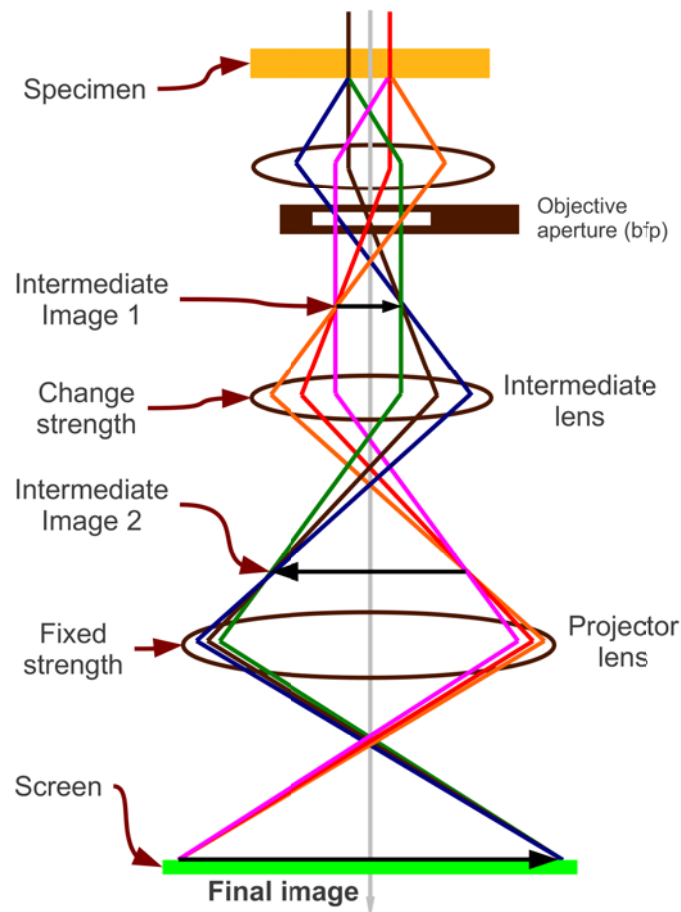


Figure 4.18: The intermediate lens selects the image plane of the objective lens as its object. This diagram is highly simplified, modern TEMs have many more lenses allowing greater flexibility in terms of magnification and focusing range both in DP and imaging mode. Adapted from [193].

To look at an image, the intermediate lens is adjusted so that its object plane is the image plane of the objective lens as shown in figure 4.18.

This chapter has introduced various material analysis techniques namely microscopy, spectroscopy, and diffraction. These techniques use either light or electrons as a probe, thus an emphasis has been made on the interaction of light and electron with matter (excitation, diffraction, interference). SEM, LEEM, TEM microscopes and the associated SPLEEM, STEM techniques have been introduced succinctly. We also studied the principles of chemical and structural analysis tool such as XPS, EDS, and SPA-LEED. These tools have been used for the experiments which will be introduced next. In chapter 5, we discuss the morphology of quasicrystals at different surface orientations with UHV-SEM. In chapter 6, we present results of quasicrystal thin film growth on 2-fold AlNiCo at different stoichiometry with XPS and SPA-LEED. In chapter 7, we explore the morphology and surface magnetism of MnSb thin films with LEEM and SPLEEM. Finally, validation experiments for a controlled etching of tungsten to be used as a base for tomography sample with TEM are presented in chapter 8.

Chapter 5 : Morphology of Various d -AlNiCo Surfaces

Most surface science studies of quasicrystals have been carried out with electron diffraction or STM techniques. In this chapter, we report surface science experiments on quasicrystals carried out with UHV scanning electron microscopy (UHV-SEM). The sample stage allows annealing, thus in this chapter we report the first observation, to our knowledge, of the intrinsic AlNiCo phase transition in *in-situ* direct space imaging. Previous studies have been carried out with LEEM, but the in-depth resolution of LEEM doesn't allow the observation of large scale structures such as islands [198]. Island formation and surface morphology change upon annealing and sputtering will be discussed in this chapter. These measurements were performed at different surface orientations of d -AlNiCo namely 2-fold, 10-fold, and a specific higher order orientation.

The quasicrystal samples have been grown by Peter Gille at the University of Munich with the Czochralski process [59]. Atomic Force Microscope (AFM) and SEM measurements were performed in our laboratory whereas Electron Dispersion Spectroscopy (EDS) studies were carried out by us at the Center for Electron Microscopy (CEM) at the University of Birmingham.

5.1 Morphology of the d -AlNiCo(10000) surface

AlNiCo is a complex alloy, as discussed in section 1.5.2. $\text{Al}_{72.2}\text{Ni}_{19.2}\text{Co}_{8.6}$ has a phase transition at about 700°C. The phase diagram 1.12 in section 1.5 doesn't point exactly in our region of interest. The quasicrystalline phases depending more on the Ni concentration than Al, we can infer the quasicrystalline phase by reading the phase diagram according the Ni concentration. However, we cannot tell with certitude if the phase transition comes from the transition type S1 towards type I or type I towards bNi.

The 2-fold $\text{Al}_{72.2}\text{Ni}_{19.2}\text{Co}_{8.6}$ surface was studied with an UHV-SEM whose sample stage allows *in-situ* annealing experiments. In this experiment, details of which are given in this chapter, the sample has been annealed several times to its high-

temperature phase.

The sample was loaded *ad-hoc* into the UHV-SEM analysis chamber. Measurements with SEM show anisotropic features with ripples pointing in one direction (figure 5.1). It has been theoretically shown that quasicrystals can grow without the need of tile-rearrangement [58]. This growth mode requires slow kinetics of attachment in the direction perpendicular to the 10-fold direction resulting in a much slower growth rate in the 2-fold direction than in the 10-fold direction [59]. Due to the anisotropy in the growth rate, we also expect the surface to display anisotropy allowing the indexing of figure 5.1.

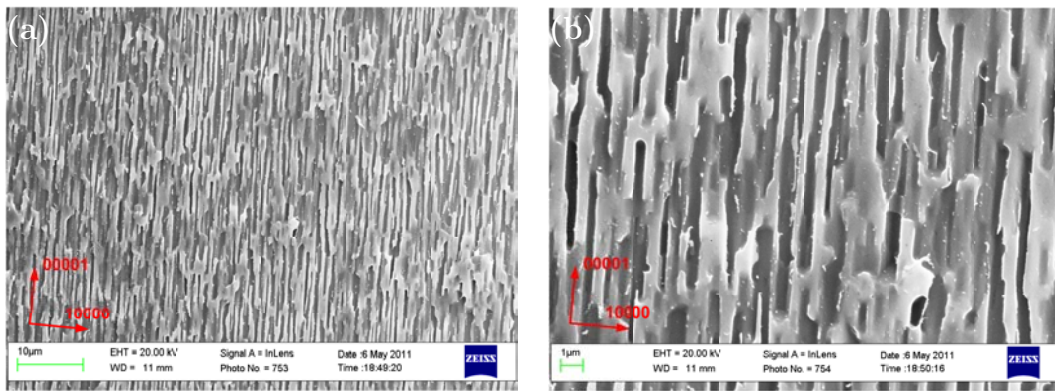


Figure 5.1: SEM images of 2-fold $\text{Al}_{72.2}\text{Ni}_{19.2}\text{Co}_{8.6}$ showing ripples along the $\langle 00001 \rangle$ direction. Electron energy: 20 keV, scale bars 10 μm and 1 μm in (a) and (b) respectively.

The sample was alternately annealed for 5 min and sputtered for 50 min followed by one additional sputter/anneal cycle of 15 min and 5 min, respectively. The sample was sputtered with Ar at a pressure of 2×10^{-5} mbar with a sample ion current of 30 μA . The annealing temperature is about 700°C and therefore above the phase transition point. After annealing three times to the high-temperature phase, we started to observe rectangular black contrast patches in the low-temperature phase in the SEM images as shown in figure 5.2.a. The sample still shows a strong anisotropy but there is now a strong contrast in the secondary electron signal that we did not observe initially (figure 5.1). The images in figure 5.1 show roughness in the surface morphology whereas the features appearing in figure 5.2.a are beyond topography as described later in this chapter. Due to the lower SEM signal coming from these regions, the features will be referred as black features.

In figure 5.2, the sample was taken out of UHV and reintroduced without any subsequent treatment. The oxidation induces a size reduction of the black features

and aggregation of matter in the form of islands as can be seen in figure 5.2.b.

The next section will answer questions raised by the appearance of these features, how they form and what their origin is. We will also discuss the changes in the island morphology upon annealing to the high-temperature phase.

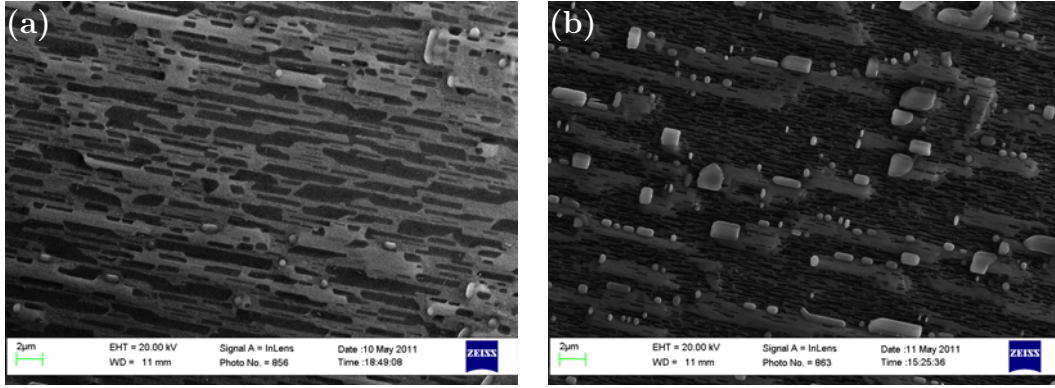


Figure 5.2: SEM images of 2-fold $\text{Al}_{72.2}\text{Ni}_{19.2}\text{Co}_{8.6}$ after annealing three times above its phase transition. (a) The surface exhibits black elongated features along $\langle 00001 \rangle$. (b) After exposure to air, patches have shrunk and matter has aggregated into islands. Electron energy 20 keV, scale bars 2 μm .

5.1.1 Island morphology on d -AlNiCo(10000) surface

To study the evolution of the islands we performed an annealing experiment. Figure 5.3 depicts a phase transition sequence starting with annealing above the high-temperature phase, at 730°C, (5.3.a-5.3.d) and cooled down below the phase transition (5.3.e-5.3.h). In the low-temperature regime, one can see rod-shaped and circular islands (figure 5.3.a). These same islands develop into faceted islands above the phase transition (figure 5.3.c). The islands have rod-like shapes with sharp edges. These islands facet whereas we might have expected the islands to adopt a shape without sharp edges since a spherical shape lowers the surface energy in the limit of very high temperatures [199]. This observation indicates a strong anisotropy in the surface energy of the islands and indicates as well that the structural quality of these islands is close to single crystallinity. The faceting can still be observed, in a lower extend, in the low-temperature phase as shown in figure 5.3.a. In this same annealing sequence, it can be seen that the islands grow and shrink. Material is transferred from substrate to islands as the sample reaches the phase transition

temperature. Both the growth and the faceting of the islands may be driven by phase transition induced changes in the surface stoichiometry or in the chemical potential of *d*-AlNiCo.

Figure 5.4.a is a zoom-in image of an island from figure 5.3.c. This island displays 5 facets on its top view. The facet edges were aligned with the edges of a decagon (figure 5.4.b) showing the quasicrystalline nature of this island. Some other islands with quasicrystalline symmetry can be seen in figure 5.3. The island in figure 5.5.a shows faceting originating from both (10000) and (001 $\bar{1}$ 0) 2-fold surfaces can be seen. In other islands, the symmetry cannot be resolved unambiguously (figure 5.5.b).

The islands were analysed by EDS with an analytical SEM. The sample transfer into this instrument involved exposing the sample to air. The electron energy of the beam was 12 keV. Interaction of electrons with matter at this energy generates X-rays originating from a volume on the order of 100 nm³ which is the resolution of this measurement (see section 4.5). We performed an EDS experiment on a typical island (figure 5.6). AFM analysis discussed later in this section gave a typical island height of 1 μ m. The volume from which X-rays originate is very small compared to the size of the island so the EDS signal from these islands does not have any significant contribution from the substrate. The atomic composition of the islands averaged from four measurements is Al_{72.6}Ni_{15.8}Co_{11.6}. Compared with the bulk composition, Al_{72.2}Ni_{19.2}Co_{8.6}, we found that the islands are Co rich and Ni deficient. Although the atomic composition of the island shifts consequently compared to the substrate, the island composition still lies in the quasicrystalline phase as informed by the phase diagram 1.12 in section 1.5 by reading the diagram at 16% Ni.

5.1.2 Topography of *d*-AlNiCo(10000) surface

In order to explore the origin of the SEM contrast referred above as black features, we used EDS to obtain chemical information. We observed a change in the chemical composition between the black features and the surrounding surface area as shown in figure 5.7. The red crosses in the SEM image are the points at which we performed the EDS measurements. We extracted the atomic composition of Al, Ni, and Co at the surface for each scan at the points along the red line. Compared to the expected bulk value, the dark patches are richer in Co and Ni but contain less Al compared to the surface. The alloy composition of the dark patches is Al₆₈Ni₂₀Co₁₂ as determined by the averaged composition of five scans in this region (figure 5.7) with a standard

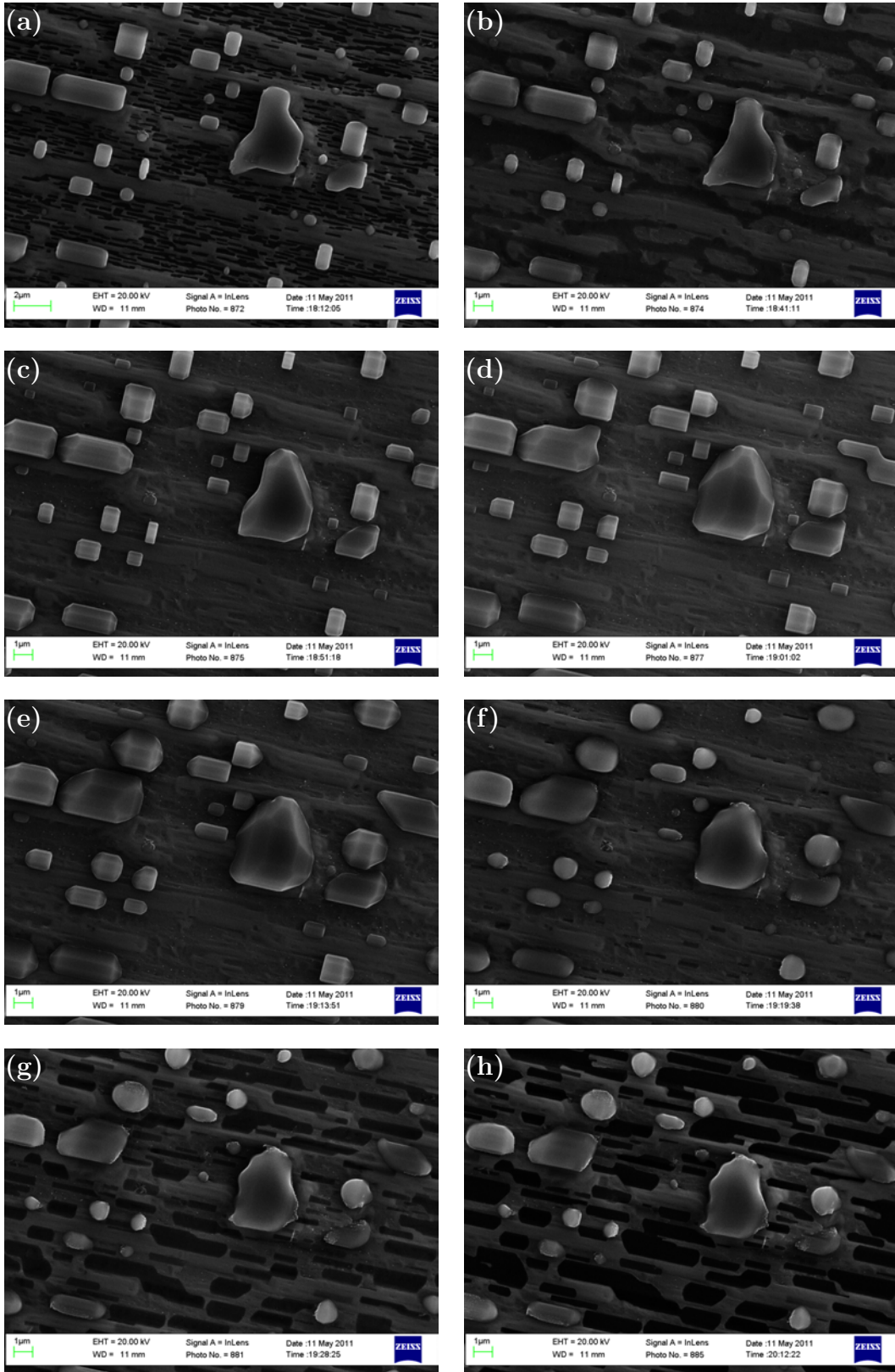


Figure 5.3: *In-situ* SEM annealing sequence of $2f\text{-Al}_{72.2}\text{Ni}_{19.2}\text{Co}_{8.6}$. The sample was heated in steps to the high-temperature phase (a-d) and subsequently cooled down to the low-temperature phase (e-f). The temperature ranges from approximately 500°C in the low temperature regime to 730°C at the maximum. Electron energy 20 keV, scale bars 1 μm .

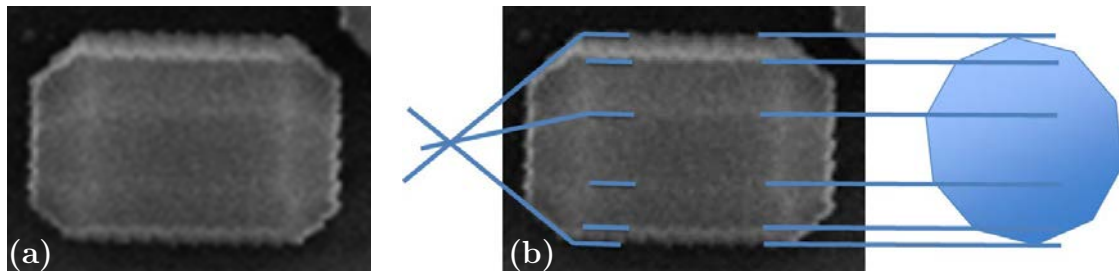


Figure 5.4: (a) zoom-in of an island from figure 5.3.c showing faceting. (b) The edges can be superimposed by the projection of decagon vertices indicating the quasicrystalline nature of the island. Island length: 1.6 μm .

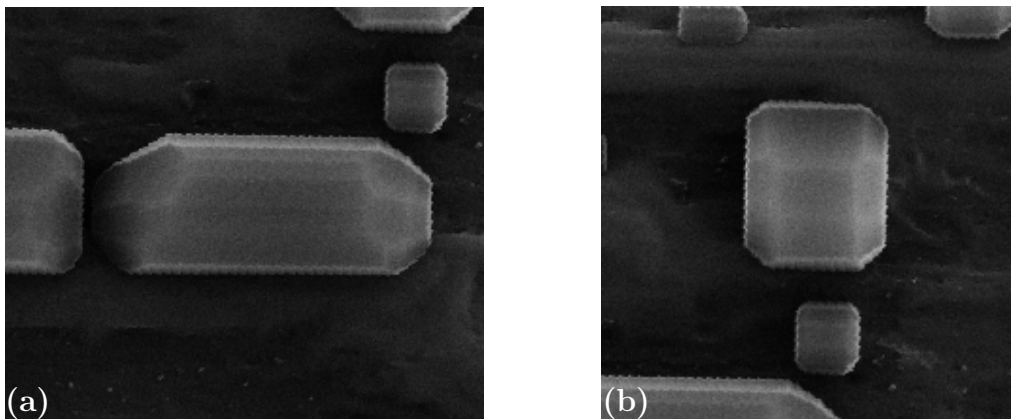
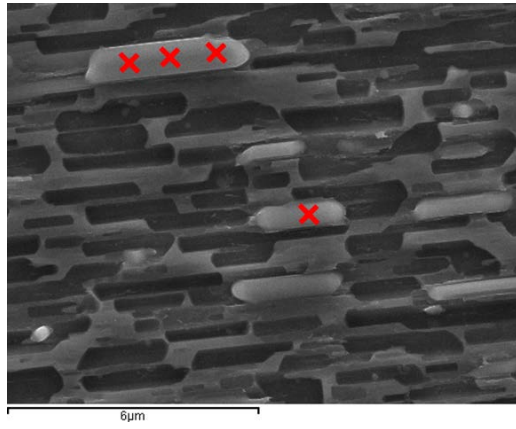


Figure 5.5: (a) zoom-in over an island showing faceting from both (10000) and (001 $\bar{1}$ 0) 2-fold surfaces. (b) island showing non resolved symmetry. Island lengths: (a) 4 μm , (b) 1.6 μm .



atomic composition of bulk

Al	Ni	Co
72.2	19.2	8.6

average atomic composition of islands

Al	Ni	Co
72.6	15.8	11.6

Figure 5.6: (a) SEM image of 2-fold $\text{Al}_{72.2}\text{Ni}_{19.2}\text{Co}_{8.6}$ after annealing 8 times and exposure to air. According to EDS analysis, the island is Co-rich and Ni-rich in a smaller extend. The data to determine atomic composition of islands comes from four spectra taken at red cross positions.

distribution of 0.15%. The Co concentration is substantially higher in the black features with a relative increase of 20%.

According to the phase diagram 1.12 in section 1.5, both the surface and the islands lie in the decagonal S1 phase. If the contrast was only chemical related, then the features would actually appear brighter with SEM because they are richer in heavy elements. Thus the contrast is either due to the topography or from the local workfunction. To resolve the topography we used Atomic Force Microscope (AFM). Figure 5.8.a and 5.8.b are contact mode AFM images of the 2-fold AlNiCo quasicrystal in a representative area. Figure 5.8.b is a zoom of the highlighted area in figure 5.8.a. A profile line scan performed over a typical island (figure 5.8.c) gives a height of 1 μm for a width of 2 μm . Figure 5.8.d is a line scan along two patches. The black features have a typical depth that ranges between 200 and 300 nm whereas the width of these patches ranges between 1 and 2 μm .

Using AFM and EDS measurements, we have resolved both the topography and chemical composition of the black features. Both lie in the decagonal S1 phase. The black features are richer in heavy elements. The topography of the black features studied with AFM have been established as hollows 200 to 300 nm deep.

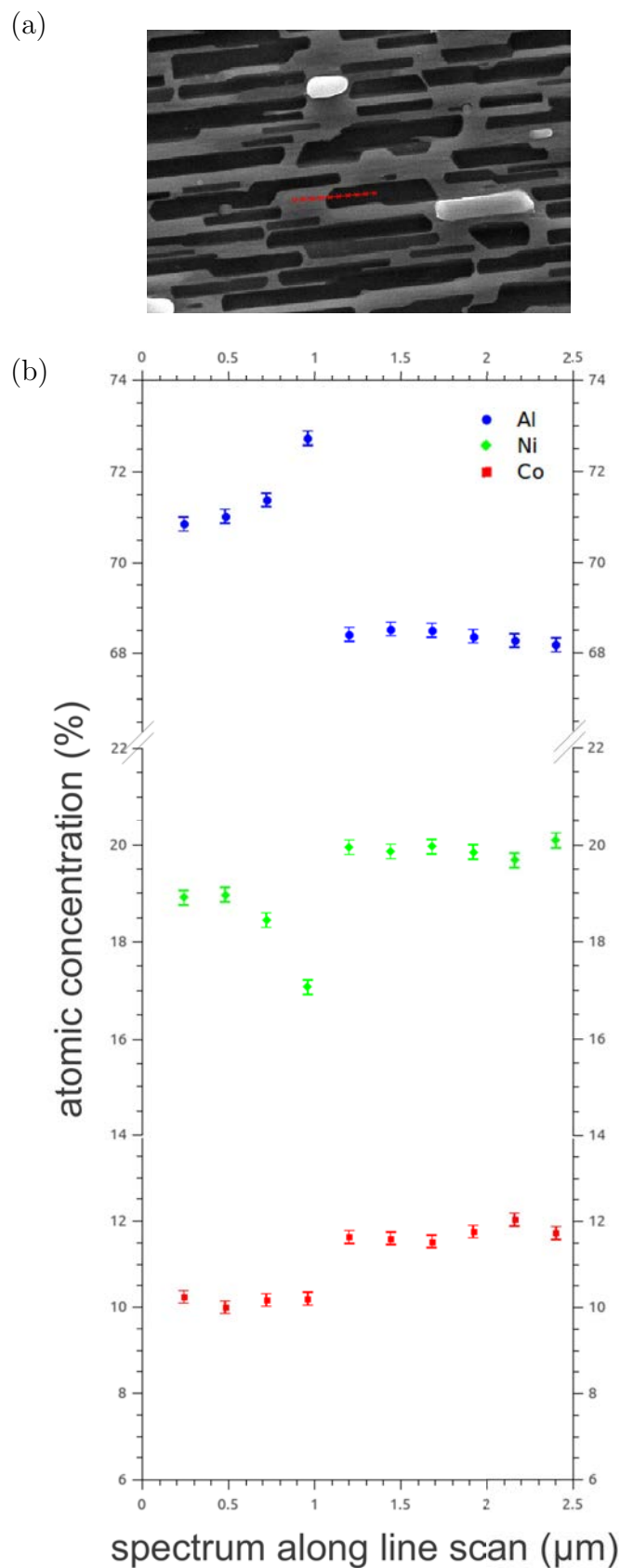
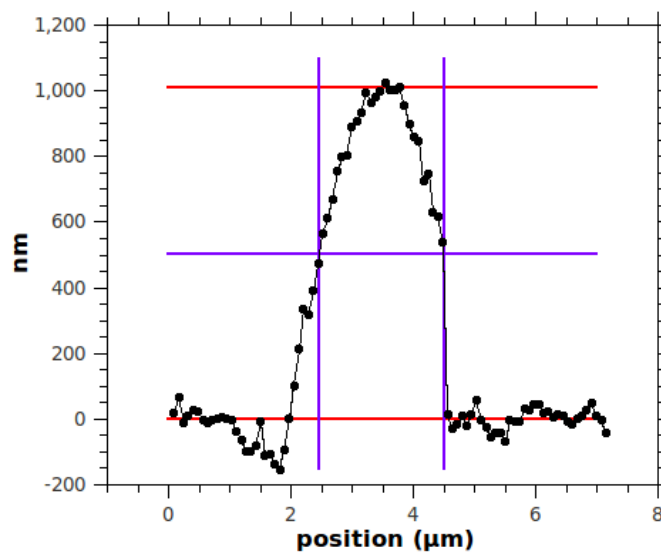
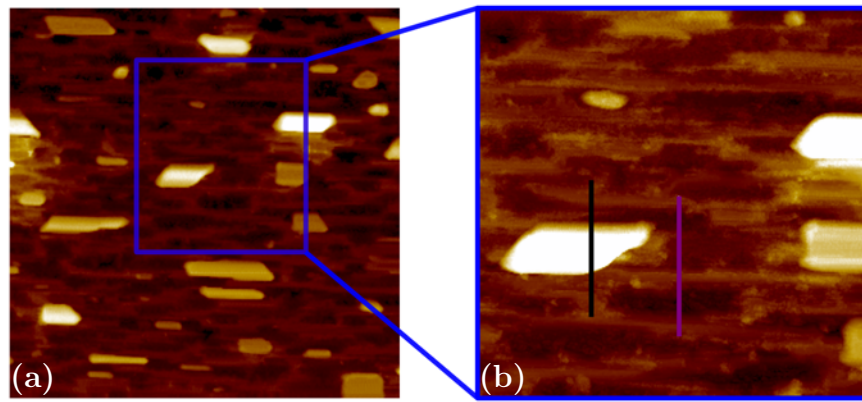
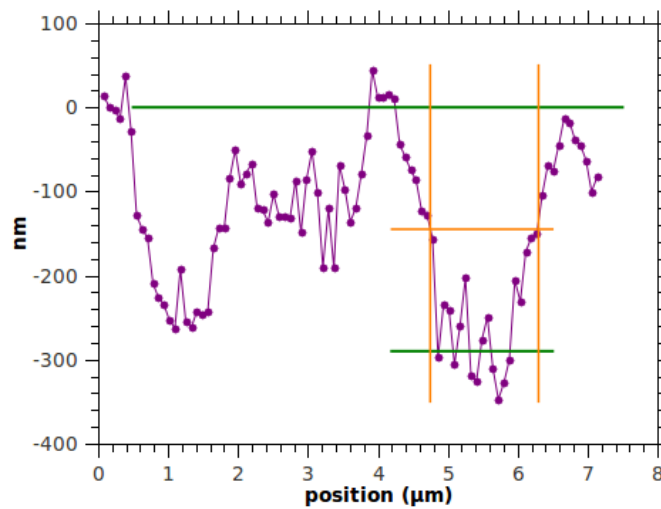


Figure 5.7: (a) SEM image of 2-fold $\text{Al}_{72.2}\text{Ni}_{19.2}\text{Co}_{8.6}$ after having been annealed 8 times to the phase transition and exposed to air for transfer. (b) EDS results of the atomic concentration of Al, Ni, and Co given in percent for 10 spectra at the points indicated in (a) from left to right.



(c)



(d)

Figure 5.8: (a) $50\,\mu\text{m} \times 50\,\mu\text{m}$ contact mode AFM image and (b) $20\,\mu\text{m} \times 20\,\mu\text{m}$ AFM image of the highlighted area in (a). (c) line scan across a typical island. (d) line scan across an SEM dark patch.

5.1.3 Growth study of the black features

In this section, we will investigate the growth behaviour of the features that appear when cooling down from the high-temperature phase. Megastructures, such as the one shown in figure 5.9, have been observed to develop at the surface of the 2-fold AlNiCo quasicrystal. These structures aggregate material. The areas at the vicinity of these structures are island free (figure 5.10). In one of these areas, the surface morphology was observed after the 5th, 6th, 7th, and 8th annealing step above the phase transition without any additional sputtering treatment (figure 5.10). After the sixth annealing the surface morphology shows a stabilisation in the size of the features in the low-temperature phase (figure 5.10.c and 5.10.d).

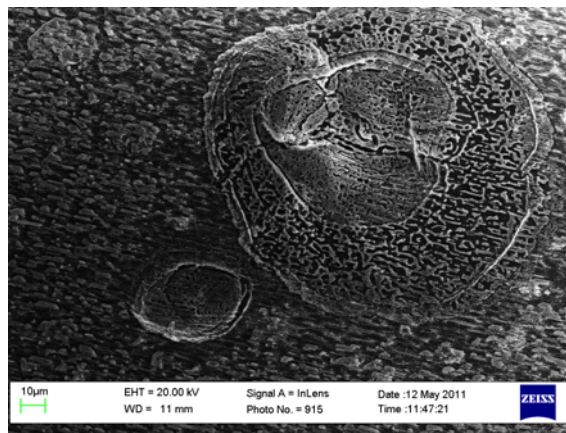


Figure 5.9: 100 μ m large structures developping at the 2-fold AlNiCo surface after several annealing treatments. Electron energy 20 keV, scale bar 10 μ m.

Using SEM we observed the phase transition in the 7th annealing step. The sequence is shown in figure 5.11 starting at high temperature (figure 5.11.a) and as the sample is cooled down to the low-temperature phase (figure 5.11.h). At the top-right corner, one can see the edge of a large structure similar to the one shown in figure 5.9.

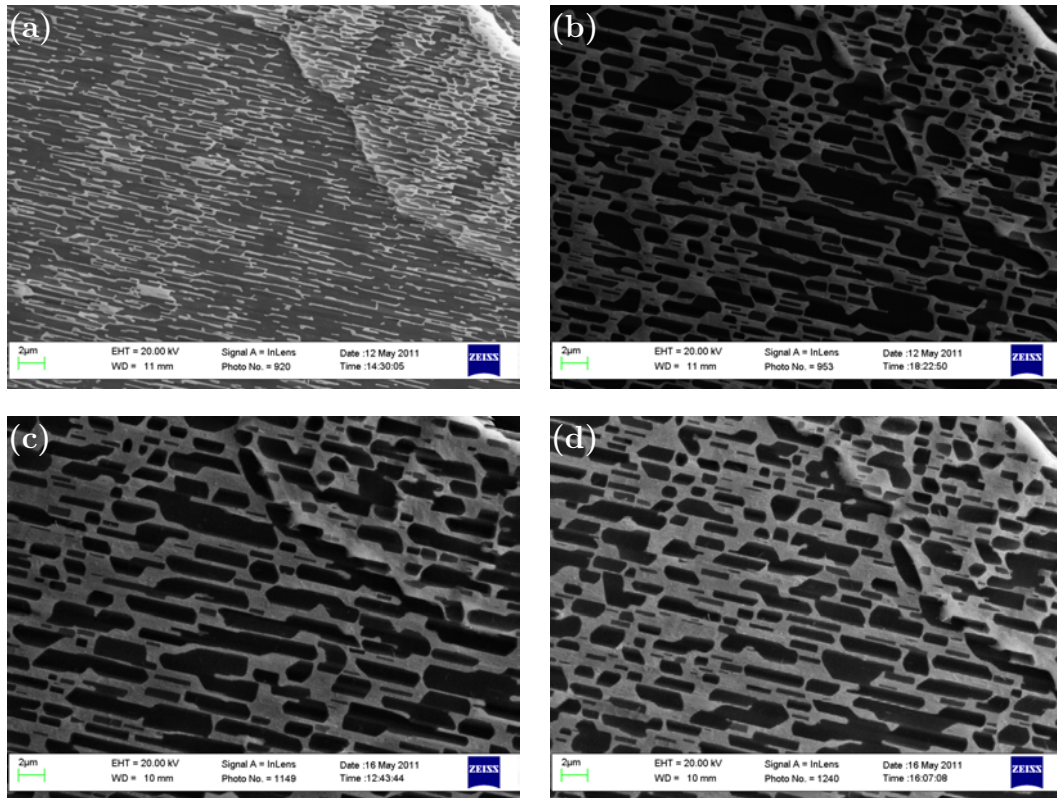


Figure 5.10: SEM images of 2-fold $\text{Al}_{72.2}\text{Ni}_{19.2}\text{Co}_{8.6}$ after annealing (a) five times, (b) six times, (c) seven times, (d) eight times above its phase transition. The surface shows some stabilisation in its morphology after the sixth transition. Electron energy 20 keV, scale bars 2 μm .

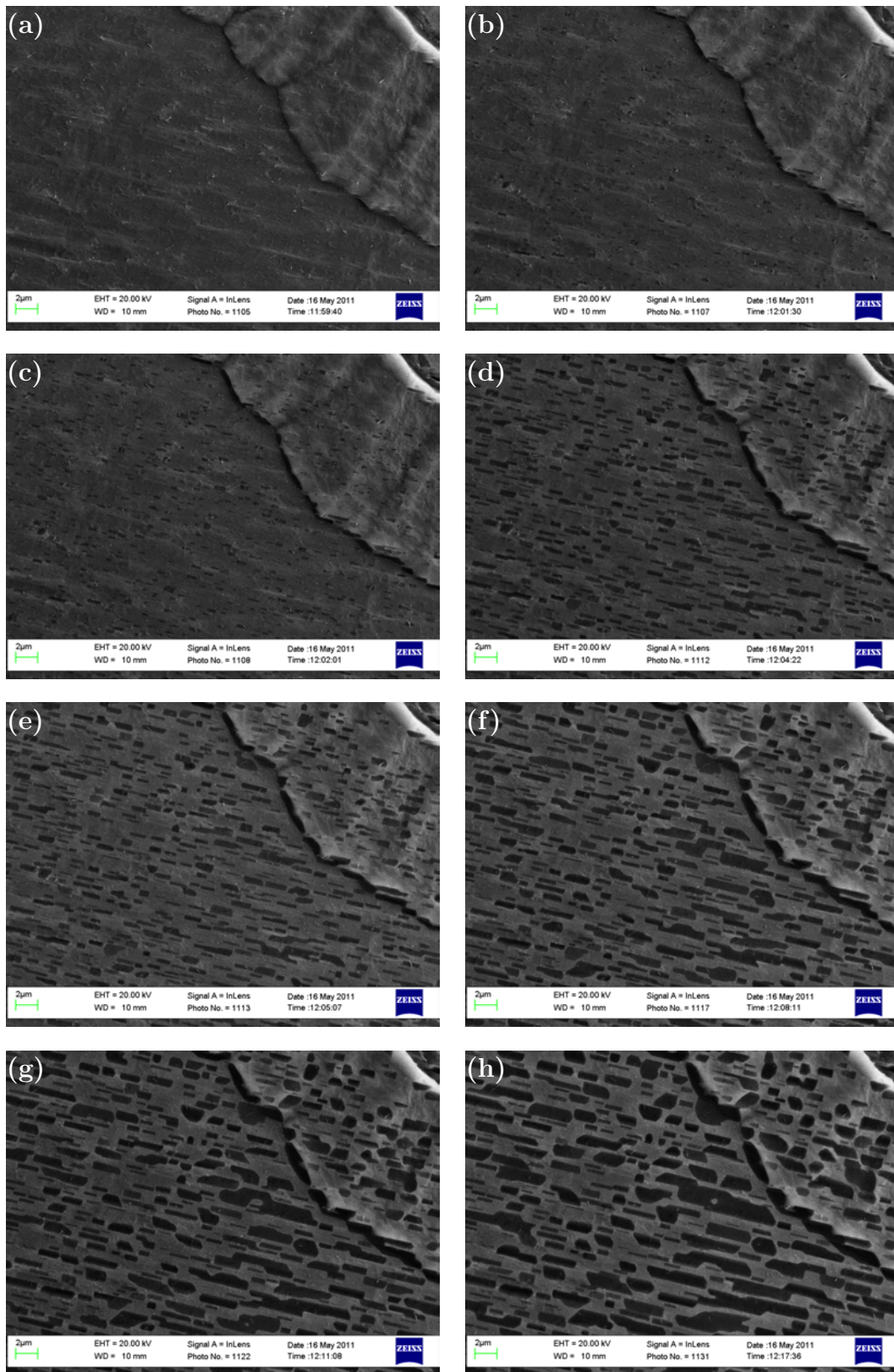


Figure 5.11: SEM images of the sample crossing the phase transition at 700°C from high temperature (a) to room temperature (h) in an island free area. At high temperature the surface is smooth whereas features with sharp SEM contrast develop below the phase transition. Electron energy 20 keV, scale bars 2 μm .

In the frames in figure 5.11, it can be seen that the features are elongated rectangles aligned along a preferred direction. These features grow and coalesce so that the original rectangular shapes develop into larger, non regular, polygonal shapes. These features appear randomly over the surface after each annealing as it can be seen by comparing figure 5.10.c with figure 5.10.d.

Examining the figure 5.11, it seems that the features coalesce instead of following a Ostwald ripening-like growth mode. In order to support this statement, we analysed quantitatively the frames from the phase transition shown in figure 5.11. The particles were fitted with the tool "Analyze Particles" in ImageJ. In order to use this tool, the frames were converted to 8-bit images. The images were rotated so that the features are aligned horizontally and finally the frames were smoothed. The fitting requires a 8-bit value to make the distinction between particles and background. The values were calculated individually according to the overall brightness of the images. The background level increases with sample temperature due to the light from the glowing filament and sample. The appearance of an image also depends on the sensitivity of the detector that can be adjusted by the operator. Figure 5.12 displays two typical images after the particle analysis.

Features in the yellow area in frame 1113 (figure 5.12.a) were tracked along four frames. Through these frames the features grow and eventually coalesce. In this analysis we want to show that the particles do not shrink, or disappear to rule out Ostwald ripening-like growth. The feature analysis tool is unable to identify particles smaller than 50 pixels reliably, which corresponds to a surface of $\pm 0.029 \mu\text{m}^2$. This value was used as an error for the measurement of particle areas. Features smaller than 150 pixels were discarded from the analysis.

The graph in figure 5.13.c shows the binned size difference of features in frames 1116 (figure 5.13.b) and 1113 (figure 5.13.a) against the particle size in frame 1113. This analysis shows that, within the accuracy of our measurement, the particles do not shrink. A close inspection of the features in the different frames showed that the features grow in steps in contrast to a continuous growth mode.

In the histogram in figure 5.14, one can see the size distribution of the features inside the yellow area in frame 1113 (figure 5.12.a) and frame 1122 (figure 5.12.b). The maximum size of $1.5 \mu\text{m}^2$ in frame 1113 reaches $2.7 \mu\text{m}^2$ in frame 1122 with the average size increasing from $0.30 \mu\text{m}^2$ to $0.63 \mu\text{m}^2$.

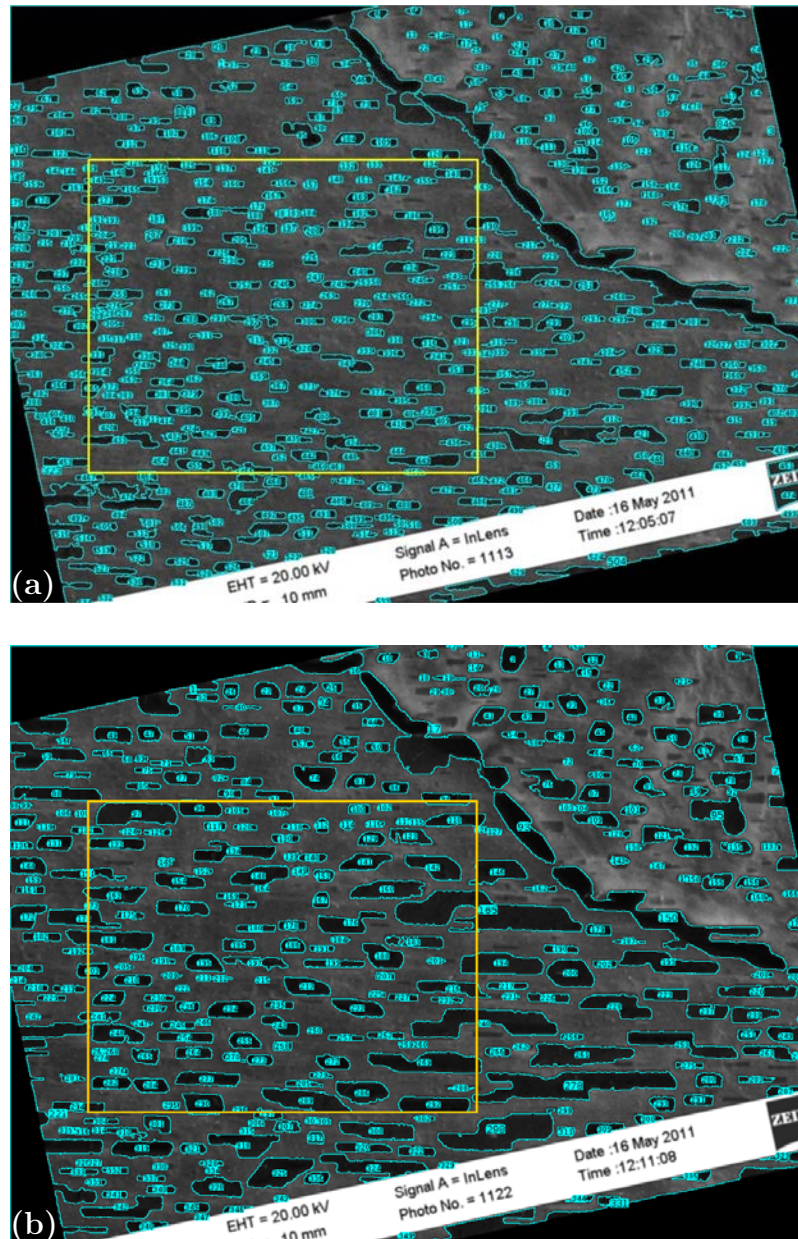


Figure 5.12: Images from the phase transition sequence were converted to 8-bit, rotated, smoothed. Frame 1113 (a) and frame 1122 (b), figure 5.11.e and figure 5.11.g respectively, after fitting the particles with the "Analyze Particles" tool in in ImageJ.

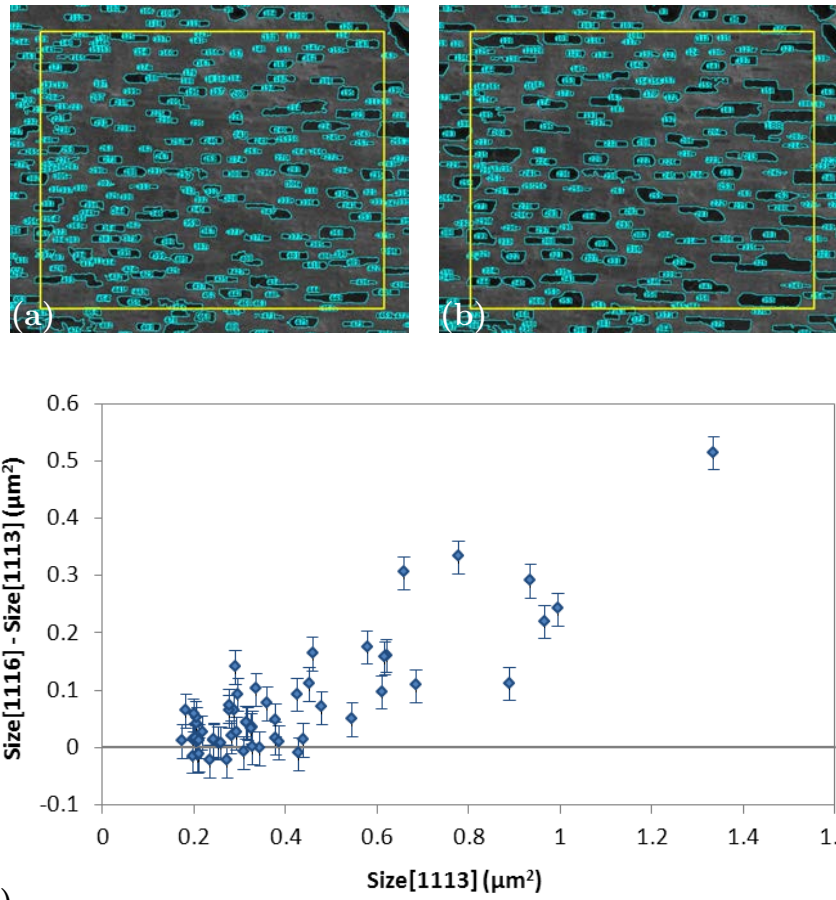


Figure 5.13: Particles in yellow area were analysed from frames 1113 (a) to frame 1116 (b). (c) Plot of the size of particles in frame 1113 vs the size difference of particles in frame 1116 and frame 1113. Coalescence events and small particles were discarded from the analysis.

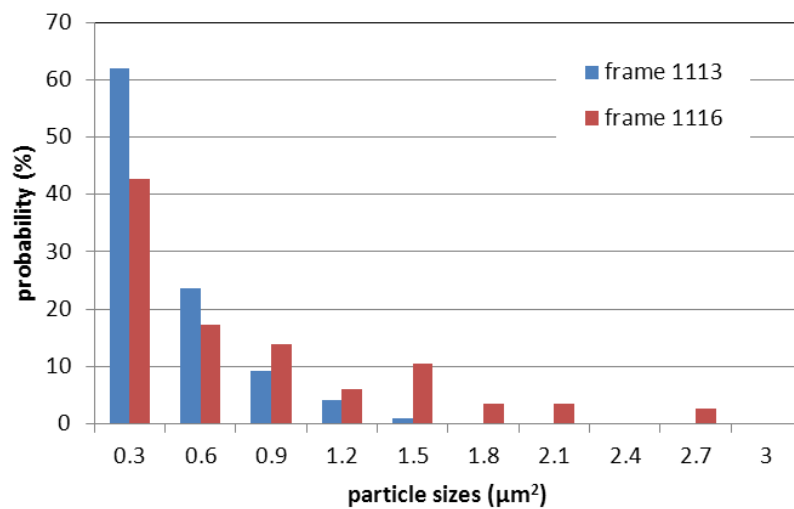


Figure 5.14: Size probability distributions of features in yellow area in frame 1113 (figure 5.11.a) and frame 1116 (figure 5.11.b).

This section discusses SEM observations of the 2-fold *d*-AlNiCo surface. After an anneal/sputter cleaning procedure and annealing the quasicrystal to the high-temperature phase, we observed significant morphology changes. We observed square-shaped islands which grow in the high-temperature phase. Interestingly, these islands exhibit facets at high-temperature. Some of these islands have been found to have a 10-fold geometry at high temperature. Chemical composition measurements carried out by EDS have shown that the islands are still in the quasicrystalline region in the phase diagram.

After cooling the quasicrystal from its high-temperature phase, we observed the appearance of rectangular and elongated black features. With an AFM and EDS analysis, these features were found to be 300 nm deep hollows with a Ni- and Co-rich composition. The lower secondary-electron signal does not come from the chemical composition since the chemical composition of these features is shifted towards more heavy elements (Ni and Co). Furthermore, the lower signal does not come from a shadowing effect due to the topography because the contrast is not gradual and the features are many times larger (2-3 μm) than they are deep (0.2-0.3 μm). The lower SEM signal may come from a different workfunction of these structures. In island free areas, as well as between the islands, we have observed qualitatively and quantitatively the growth mode of the features during the formation in the phase transition. The features grow continuously and coalesce to form bigger polygonal features.

5.2 Morphology of the $d\text{-AlNiCo}(10\bar{2}\bar{2}4)$ surface

$d\text{-AlNiCo}(10\bar{2}\bar{2}4)$ is a decagonal quasicrystal sample with a surface orientation tilted by 35° with respect to the 10-fold axis as shown in figure 5.15.b. This particular orientation is of interest because it can provide an epitaxial match to a film of periodic crystal structure [200]. The sample was repolished using P1200 emery paper (average grain size $15\ \mu\text{m}$) and $1\ \mu\text{m}$ diamond paste. After annealing at 750°C , we observed a smoothing of the surface. Cooling down the sample to the low-temperature phase, we observed nano-pillars appearing at the surface, such as the ones shown in figure 5.15.a. Looking at the large pillars in figure 5.15.a, one can see that the pillar grows keeping the same perimeter shape from bottom to top and does not adopt an energetically favourable shape such as round or symmetrically faceted pillars. The pillars were imaged along the surface normal and appear clearly tilted. d -quasicrystals' building units are decagonal pillars that grow preferentially in the direction aligned with the 10-fold direction (figure 1.13, section 1.5.2) [58,59]. Since we know the 10-fold direction points at an angle of 35° from the surface normal, it can be reasonably assumed that the pillars are tilted along the 10-fold direction.

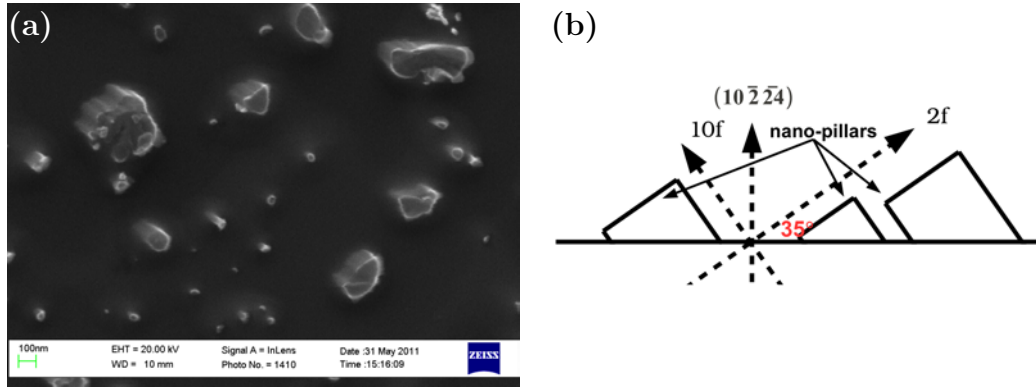


Figure 5.15: (a) Structures of the miscut $d\text{-AlNiCo}(10\bar{2}\bar{2}4)$ appear at the surface after cooling the sample from the phase transition. Electron energy 20 keV, scale bars 100 nm. (b) $d\text{-AlNiCo}(10\bar{2}\bar{2}4)$ is a direction tilted by 35° with respect to the 10-fold surface. Nano-pillars observed after annealing the sample above the phase transition grow along the 10-fold direction.

In the experiment described above the sample was repolished and oxidised. In order to know if the nanopillar growth would occur also on a clean surface, the sample was cleaned by three anneal/sputter cycles, 5 min each step, with a sputter current

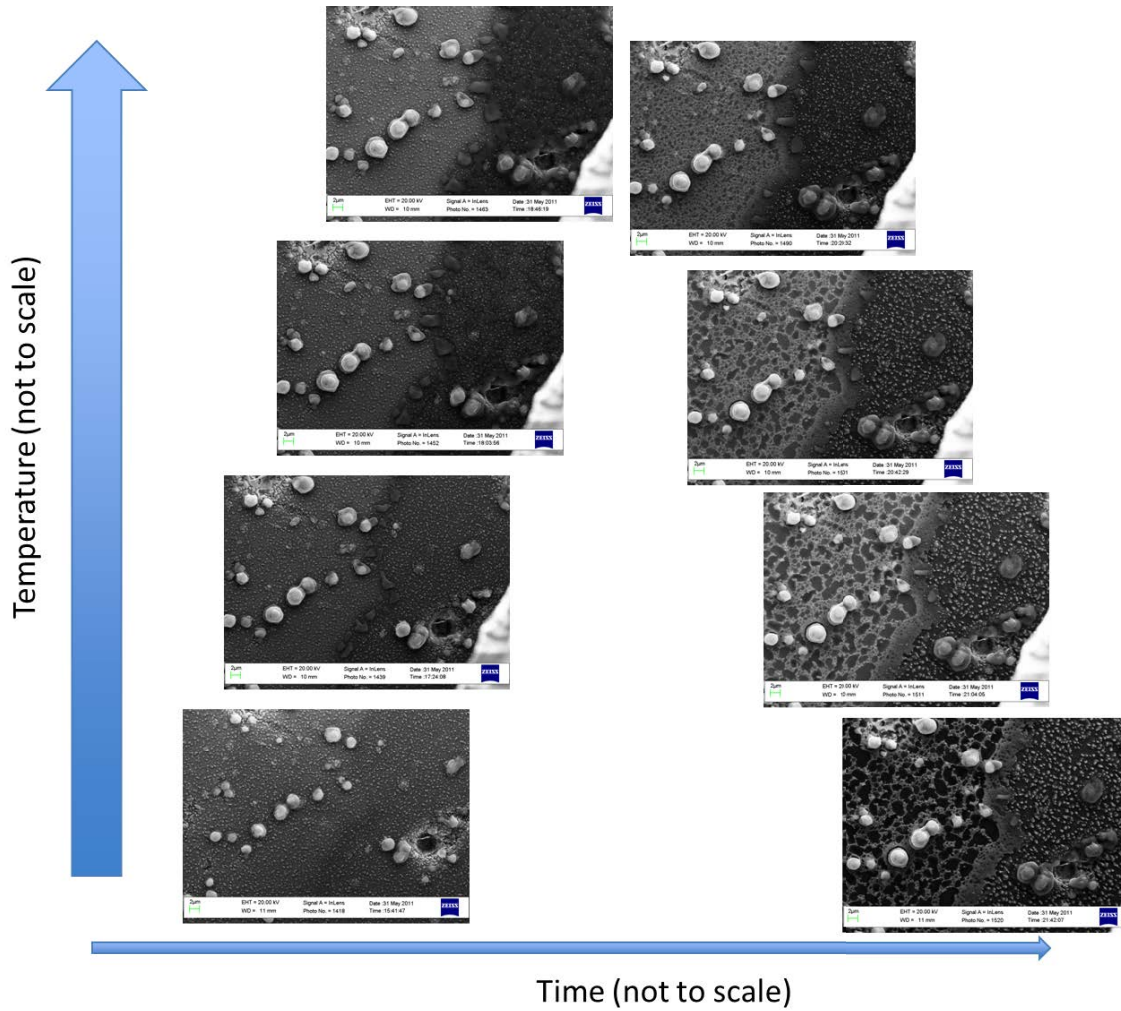


Figure 5.16: SEM images showing d -AlNiCo(102̄24) during annealing (left) and subsequent cooling (right) from the low-temperature (bottom) to the high-temperature (top) phase. The sputtering induces different contrast and surface morphology on the sputtered and non-sputtered areas. See text for explanation. Electron energy 20 keV, scale bars 2 μm .

of $12\mu\text{A}$, $15\mu\text{A}$, and $5\mu\text{A}$ respectively and annealing at 650°C as measured with a pyrometer. In order to screen the light from the sample stage filament and non-imaged regions of the sample, a home-made shield was mounted on the sample holder preserving, as a side effect, some part of the surface from sputtering. Figure 5.16 shows the surface after sputtering at different stages of annealing (left) and cooling (right) from the low-temperature (bottom) to the high-temperature phase (top). One can see a different contrast in the sputtered and non-sputtered area inside a same image. The sputtered area is on the left-hand side and appears brighter. Upon annealing, islands start to grow preferentially at the interface of the two areas. Such islands are indicated by red arrows in figure 5.17.

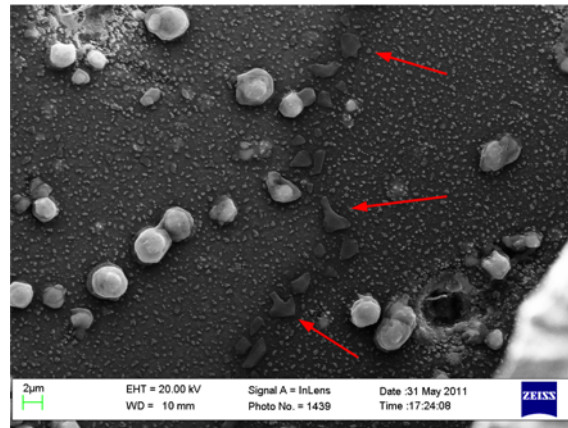


Figure 5.17: Upon annealing, islands start to grow preferentially at the interface of the sputtered and non-sputtered areas as indicated by red arrows. Electron energy 20 keV, scale bar $2\mu\text{m}$.

The annealing related morphology changes are very different on sputtered and non-sputtered areas highlighting the importance of surface preparation in surface science of quasicrystals. Features appear on both the sputtered and non-sputtered area. On the sputtered area (bright side on images), one can see features at the surface which are similar to the ones observed on the 2-fold surface although they are not elongated. When the sample is annealed to the high-temperature phase, the features disappear and the surface smoothens (not shown). In contrast, the non-sputtered area shows the nano-pillars as described above and shown in figure 5.18.

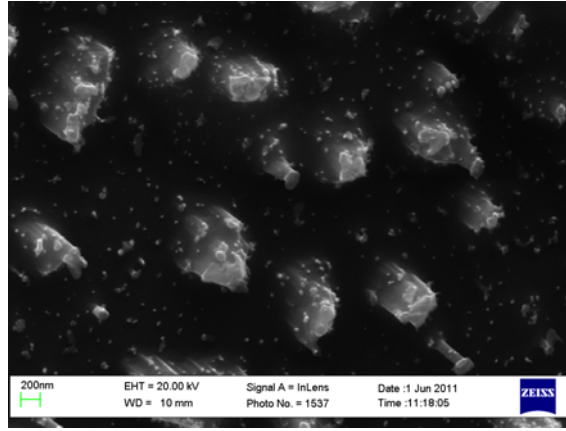


Figure 5.18: Zoom-in image of figure 5.17 on the non-sputtered area demonstrating nano-pillars growth during cooling from the high-temperature phase.

5.3 Morphology of the d -AlNiCo(00001) surface

10-fold d -Al_{72.2}Ni_{19.2}Co_{8.6} has been polished and annealed at 700°C. An annealing experiment performed with UHV-SEM did not reveal the presence of phase-transition related features, such as black and white contrast (figure 5.19). However, we did observe out-of-phase materials as shown in figure 5.19.b-c.

In contrast to the 2-fold surface, the bulk phase transition does not induce reversible surface morphology changes observable by SEM. This experiment highlights the stability of the quasiperiodic plane compared to the periodic one.

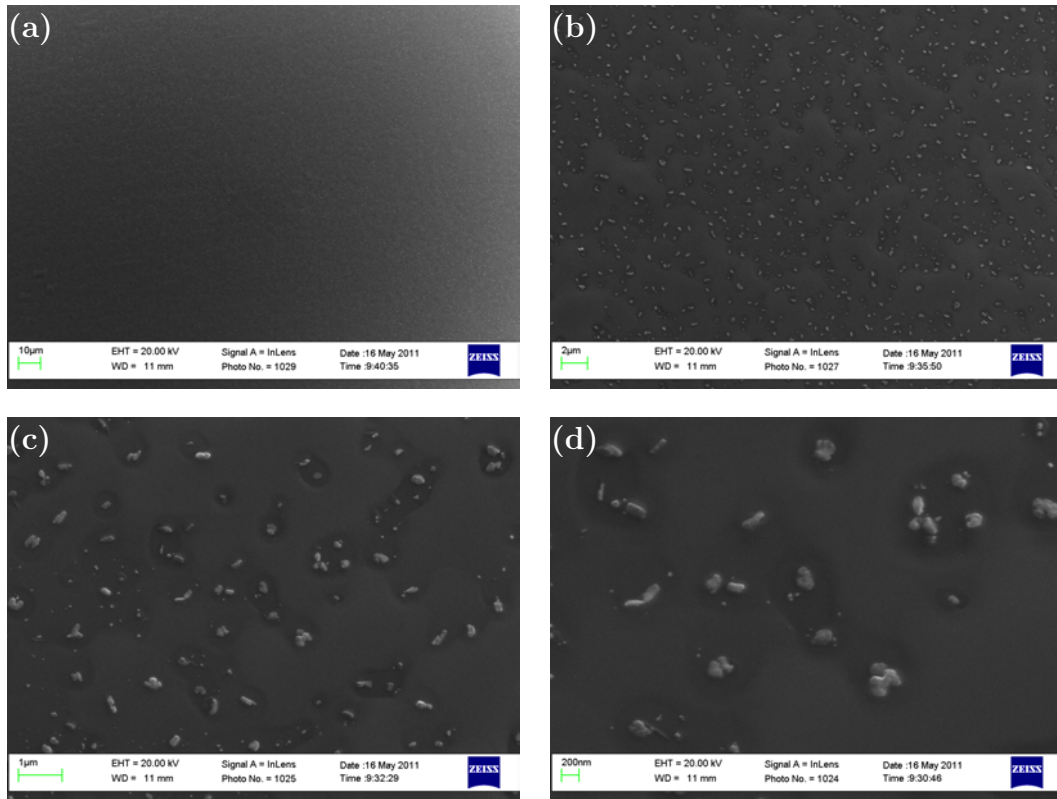


Figure 5.19: SEM images of 10-fold $\text{Al}_{72.2}\text{Ni}_{19.2}\text{Co}_{8.6}$ after annealing to 750°C showing the stability of the 10-fold surface.

Electron energy 20 keV, scale bars: 10 μm , 2 μm , 1 μm , 200 nm.

5.4 Summary

In this chapter we presented morphological studies of AlNiCo samples with different surface orientations. We related the effects of sputtering and annealing to the high-temperature phase. To our knowledge, direct space observation of a quasicrystal phase transition has never been reported with so much detail. Other qualitative experiments of quasicrystal surfaces have been conducted with LEEM. However, this technique does not allow to image large height topographical features, for example.

On the 2-fold surface, after the sample was cooled- down from the high-temperature phase, SEM revealed rectangular and elongated black features as well as the growth of rod-shaped and circular islands. These islands grow in the high-temperature phase and interestingly the islands facet at high temperature. The faceting of some islands have been identified as 10-fold symmetry. Faceting related to the $(001\bar{1}0)$ surface has also been observed. The features were analysed with EDS, although they appear black, these features are richer in heavy elements. Studied by AFM, we found that the features are 300 nm deep depressions. The morphology of these features cannot be responsible for any screening of the secondary electrons signal and point instead toward a different workfunction of these features. In an island free area, a study of their dynamic growth has shown that these features coalesce in contrast to a Ostwald ripening-like growth mode.

On the high index surface, d -AlNiCo($10\bar{2}\bar{2}4$), we observed the occurrence of nanopillars on a non-sputtered surface after cooling the sample down from the high temperature phase. These pillars grow in the kinetically favoured 10-fold direction and indeed appear tilted in the SEM images. On the sputtered surface, we observed features similar to the ones observed on the 2-fold surface.

Although we observe quite a rich behaviour of the 2-fold and the $(10\bar{2}\bar{2}4)$ surface regarding phase transition related features or islands growth, the 10-fold surface appears extremely stable.

Chapter 6 : AlNi Thin Film Growth on 2-fold AlNiCo

The influence of quasiperiodicity on the physical properties is a question not fully resolved. Although stable binary quasicrystals exist such as those in the alloy cadmium-ytterbium (Cd-Yb) system [201], they are not compatible with vacuum systems. Thus, experiments on stable quasicrystals are performed with ternary alloys and investigations of their properties would be simplified with reduced chemical complexity. Obtaining such structures can be achieved with MBE where an epilayer would adopt a substrate's structure up to a certain thickness depending on the interface strain energy between the two phases. Various experiments were reported using different elements. Single element epilayer quasicrystal thin films were observed only in the monolayer or sub-monolayer regime (section 2.3).

In this chapter we report successful growth of binary alloy AlNi thin films with quasicrystalline structure using 2f-AlNiCo as a growth template. To our knowledge, there are no reports on the stabilisation of quasicrystal binary alloy films on quasicrystal surfaces. These experiments establish the basis for an understanding of binary alloy film growth with the ultimate goal of growing quasicrystalline AlCu films. Cu as opposed to Ni has its *d*-band removed from the Fermi energy and would allow band-mapping measurements of a free electron like in the Fermi region of a quasicrystal. The system AlNi on 2-fold AlNiCo was chosen because the epilayer and substrate were both likely to contribute to successful results. AlNi has a chemical composition close to the substrate's one and the 2-fold surface has a large corrugation to lock the epilayer in the substrate structure. Furthermore, the 2-fold surface displays a strong LEED signal compared to the 10-fold surface.

In order to promote the growth of a quasicrystalline thin film, we want to deposit Al and Ni in such a ratio that the Al amount in the AlNi film is close to the bulk value in $\text{Al}_{72.2}\text{Ni}_{19.2}\text{Co}_{8.6}$, that is to say $\text{Al}_{72}\text{Ni}_{28}$. As discussed in section 2.3, epitaxial growth requires thermal energy. However, we need to use the smallest possible annealing temperature in order to limit diffusion of Co from the substrate into the film.

The experiments were performed at the Freie Universität Berlin as part of a collaboration with Professor Katharina Franke and Professor José Ignacio Pascual's groups. The thin films were grown *in-situ* in UHV conditions at a base pressure in the 10^{-10} mbar range. The crystallographic structure was explored with spot profile analysis low energy electron diffraction (SPA-LEED) and the thin-film chemical stoichiometry was measured by X-ray photoelectron spectroscopy (XPS).

6.1 Calibration

We calibrated the dependence of the sample's temperature on heating power using pyrometric data from an experiment using highly oriented pyrolytic graphite (HOPG). For e-beam heating, the power is the product of the applied voltage and the electron current hitting the sample. Experimental points are displayed in figure 6.1 in watt along the temperature in degree °C. We fit these data points with the Stefan's law to achieve a calibration function. According to Stefan's law, the power radiated per unit surface area of a black body is proportional to the fourth power of the black body's absolute temperature

$$j = A \epsilon \sigma T^4, \quad (6.1)$$

where j is the emissive power, A the object's surface area, ϵ the emissivity, σ the Stefan's constant, and T the temperature in Kelvin. We used HOPG instead of AlNiCo because AlNiCo's phase transitions and surface roughness impact on the emissivity. Based on the physics

$$P = a (T^4 - T_{RT}^4) \quad (6.2)$$

is a suitable parametrisation. We can rearrange this equation to get the temperature as a function of power

$$T = (P/a + T_{RT}^4)^{1/4}. \quad (6.3)$$

Assuming 0.98 for the emissivity in the temperature measurement [202], we find $a = 2.23 \times 10^{-11} \text{ W} \cdot \text{K}^{-4}$. Using equation 6.3, we obtain the temperature according to the applied power with a standard deviation σ_T of $\pm 6^\circ\text{C}$. However, the uncertainty when deriving the temperature of a different sample on the same holder will be larger and we use an estimate of $\pm 20^\circ\text{C}$ for such a case.

In chapter 5, we observed hollow depressions on the 2-fold surface after sputtering and annealing to the high-temperature phase (approximately 700°C). For the

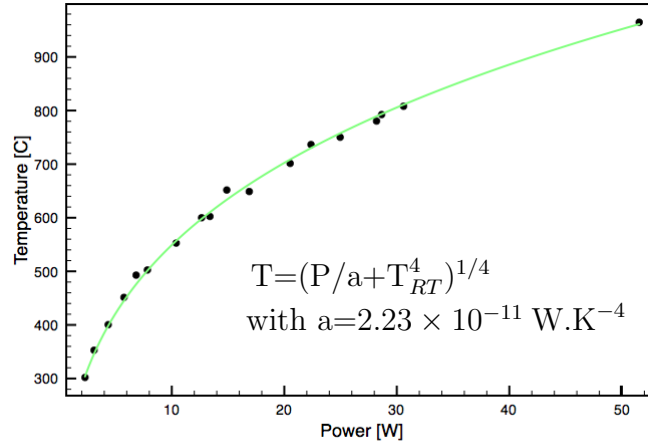


Figure 6.1: Measured temperature of an HOPG sample as a function of the applied power. The power is the product of the voltage and the emission current hitting the sample. Solid line: Fit using Stefan's law.

experiments described in this chapter, we are not interested in annealing the sample to the high-temperature phase as this involves surface modification. Thus, annealing for the cleaning procedure was done at the top end of the low-temperature phase at 650°C. However, during the initial surface preparation the sample has been annealed to the high-temperature phase and it is very likely that the surface contains topographic features. The sample was illuminated by an Al X-ray source ($\hbar\omega = 1486$ eV) whose spot-size is in the millimetre range. The angle of illumination is 45° with respect to the surface normal and photoelectrons were detected in normal emission. Thus, according to equation 4.7, the probability of a photoelectron with an energy E and generated at a depth z to escape the sample without losing energy is

$$p(E) = \exp\left(-\frac{z}{\lambda_e(E)}\right), \quad (6.4)$$

with $\lambda_e(E)$ the inelastic mean free path of electrons at energy E .

The intended composition of the AlNi thin film is $\text{Al}_{72}\text{Ni}_{28}$. This replaces the Co in the bulk composition by Ni and keeps the Al fraction the same. In order to obtain this ratio, one would calibrate two evaporators and deposit Al and Ni in a flux ratio of about 2:1. The Al evaporator is of the Knudsen cell type (section 4.4). This type of evaporator is very stable since the flux depends on the temperature of the crucible which can be accurately controlled. We calibrated the deposition rate (DR) of the evaporator by recording substrate derived Ni peak heights. Depositing Al at room temperature on 2-fold $d\text{-Al}_{72.2}\text{Ni}_{19.2}\text{Co}_{8.6}$ and taking XPS measurements of the Ni2p signal after every 5 minutes of deposition, we obtained the plot shown in figure 6.2.

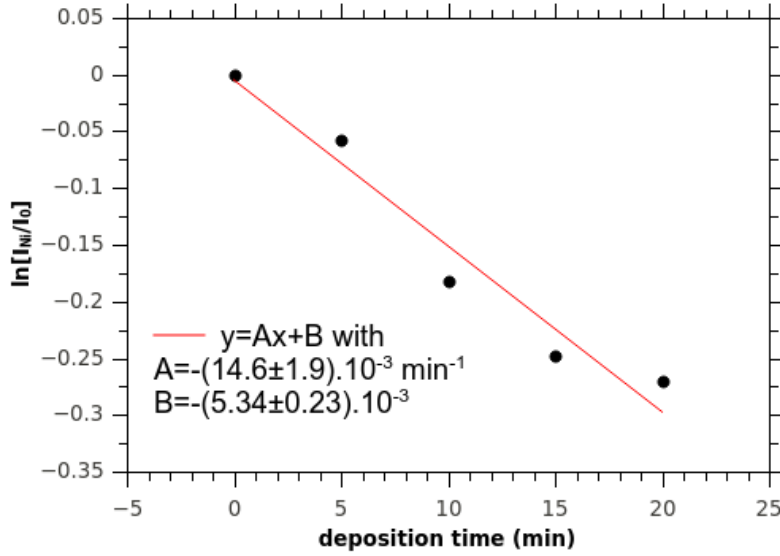


Figure 6.2: Logarithm of the normalised Ni2p_{3/2} signal for 4 cumulative depositions of Al for 5 minutes each. The Ni signal was normalised to the start peak height I_0 before deposition. The slope of the curve is $A = -(14.6 \pm 1.9) \times 10^{-3} \text{ min}^{-1}$ and is used to determine the deposition rate of the Al evaporator.

The plot in figure 6.2 indicates the covering of Ni by Al and can be used to determine the deposition rate using the following equation

$$\text{DR(Al)} = -\text{IMFP}(\text{Ni}2\text{p}_{3/2}) \times A, \text{ with } A = \frac{d \left(\ln \left[I_{\text{Ni}2\text{p}_{3/2}}(t) / I_0 \right] \right)}{dt}, \quad (6.5)$$

with $\text{IMFP}(\text{Ni}2\text{p}_{3/2})$ the universal mean free path of electrons at the energy of the Ni2p_{3/2} peak, and A the slope at which the Ni signal decreases upon Al deposition in min^{-1} . With $\text{IMFP}(705\text{eV}) = 11.1 \pm 1.5 \text{ \AA}$, and $A = -(14.6 \pm 1.9) \times 10^{-3} \text{ min}^{-1}$ (figure 6.2), we find that the Al evaporator has a deposition rate of $0.16 \pm 0.03 \text{ \AA} \cdot \text{min}^{-1}$ at our chosen operating temperature of 1060°C .

However, the e-beam evaporator used for Ni deposition is far less stable and it is difficult to determine its deposition rate quantitatively. Ni is evaporated from a rod that is heated to its melting temperature at one end for evaporation. The change of the droplet shape and its distance to the filament contributes to a non-stable flux.

6.2 Clean surface of 2-fold *d*-AlNiCo

This chapter characterises the 2-fold surface after the cleaning procedure by introducing the XPS spectrum and the diffraction pattern of the surface before deposition.

2-fold *d*-Al_{72.2}Ni_{19.2}Co_{8.6} was cleaned by two sputter/annealing cycles for 50 min, 5 min, 35 min, and 5 min for each operation. The sample was sputtered with Ar at 1.1×10^{-4} mbar with a sputtering voltage of 3 kV and an emission current of 20 mA. To recover the surface after sputtering, the sample was annealed at 650 ± 20 °C. In the thin film growth experiments we evaporated materials for 60 mins at a substrate temperature of 370 ± 20 °C. In order to compare the clean surface with the epilayer surface, we have annealed the clean surface at 370 ± 20 °C for 60 min before taking XPS and SPA-LEED measurements. A SPA-LEED image was recorded with an electron energy of 100 eV as shown in figure 6.3.a. Data inside the yellow area were averaged into a profile scan which is displayed in figure 6.3.b showing the characteristic diffraction pattern of the quasicrystalline 2-fold surface. SPA-LEED distorts the diffraction pattern (section 4.7). The line scan was calibrated in such a way that the peaks are in their expected positions and related to each other by the golden mean ratio τ (section 1.2.3). The curve used to convert the actual values of 5 peaks to their expected positions is a third order polynom, $A + Bx + Cx^2 + Dx^3$, with $A = 0.402 \text{ \AA}^{-1}$, $B = 1.031$, $C = 0.029 \text{ \AA}$, and $D = 0.021 \text{ \AA}^2$. The calibration curve is shown in the inset of the profile scan in figure 6.3.b.

An overview XPS spectrum of the clean 2-fold *d*-AlNiCo surface is displayed in figure 6.4. In addition to core level and Auger lines from Al, Ni, and Co, we observe tantalum (Ta) lines from the plates clamping the sample. Figure 6.5 depicts energy regions of interest used in this chapter. That is to say Al2s, Al2p, Ni2p, Ni3p, and Co2p peaks. For deposition experiments we estimate the composition of the film by comparing peak heights of the different elements to the clean surface ones. The heights of Ni2p and Al2s were determined with an error of 50 and 100 counts per second (cps) for the background and peak signal, respectively. The peak heights of Ni2p and Al2s from the clean surface are 3860 ± 112 cps and 1640 ± 112 cps, respectively.

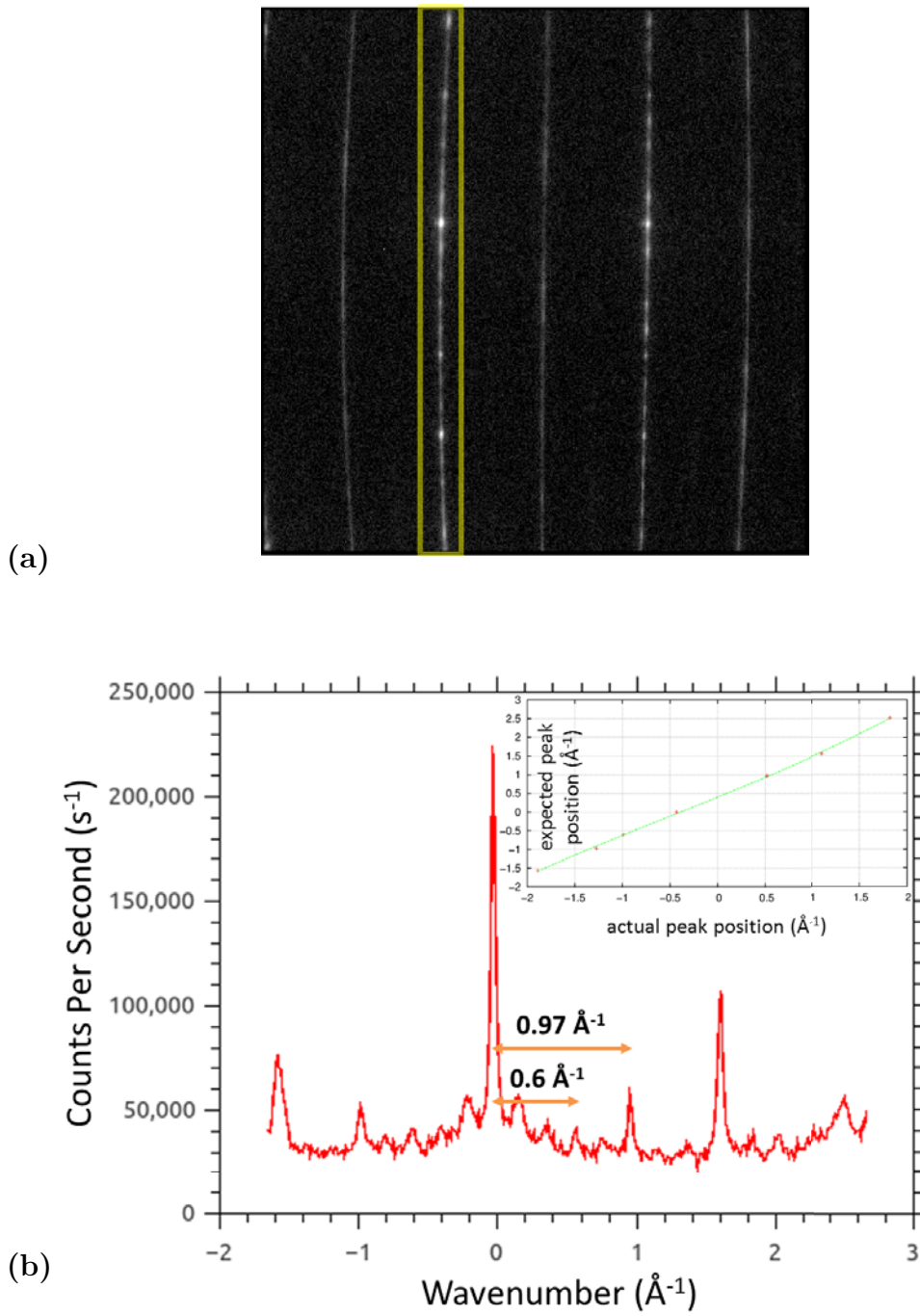


Figure 6.3: (a) $4 \text{ \AA}^{-1} \times 4 \text{ \AA}^{-1}$ SPA-LEED image of $d\text{-Al}_{72.2}\text{Ni}_{19.2}\text{Co}_{8.6}(10000)$ after cleaning (sputter/annealing) and additional annealing at $370 \pm 20^\circ\text{C}$ for 60 min. Electron energy: 100 eV. (b) Calibrated profile line scan from the yellow area in (a). Inset, polynomial of degree 3 used to calibrate the line scan.

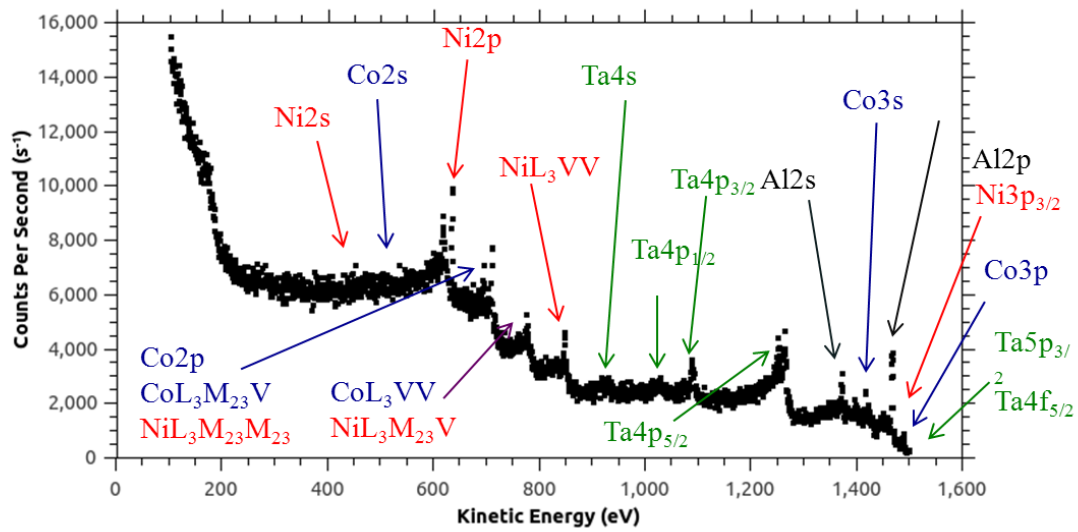
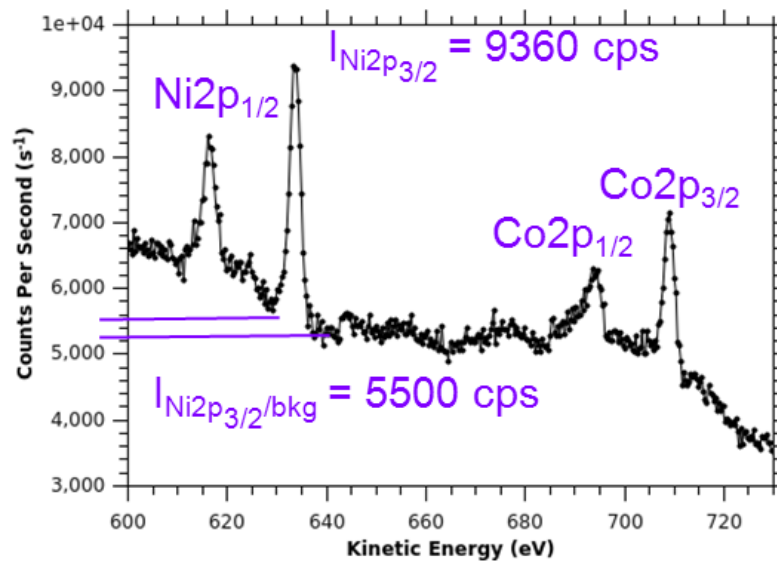
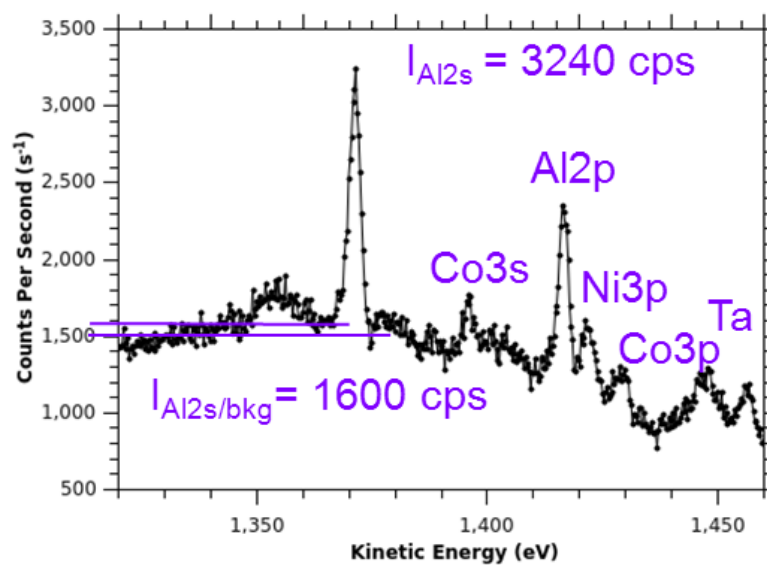


Figure 6.4: Overview spectrum of clean d -Al_{72.2}Ni_{19.2}Co_{8.6}(10000) with Al, Ni, Co, Ta core level and Auger peaks identified.



(a)



(b)

Figure 6.5: XPS spectrum of clean $\text{Al}_{72.2}\text{Ni}_{19.2}\text{Co}_{8.6}$ (10000) showing signals of interest namely (a) Ni2p and Co2p (b) Al2s, Al2p, and Ni3p. The background subtracted Ni2p and Al2s peak heights from the clean surface are 3860 cps and 1640 cps, respectively.

6.3 Ni deposition on 2-fold *d*-AlNiCo

In this experiment we deposited Ni only, without Al co-deposition, on the 2-fold surface. This experiment aims to explore whether AlNi thin films can be grown relying only on the large Al interdiffusion rate and a sufficiently low sample temperature to prevent Co interdiffusion into the film. Ni was deposited for 60 min with the substrate temperature held at $370 \pm 20^\circ\text{C}$. Before deposition, the sample was cleaned by two sputter/annealing cycles of 50 min, 5 min, 35 min, and 5 min respectively with a sputter voltage of 3 kV and annealing at $650 \pm 20^\circ\text{C}$.

The XPS spectrum in figure 6.6 shows the disappearance of the Co2p peak and a large enhancement of the Ni2p and Ni3p signals after Ni deposition. From this measurement we can conclude that Co does not appreciably diffuse into the deposited film while Al interdiffuses to the extent that the Al signal in figure 6.6 has not decreased. According to the XPS spectra, a continuous film covers the substrate's surface since the Co signal has vanished. The IMFP of the Co2p peak's photoelectrons is about 14 \AA , thus we expect the film to be at least 14 \AA thick.

We determined the stoichiometry of the film with XPS by comparing the ratio of the heights of the Ni2p (figure 6.5.a) and the Al2s (figure 6.5.b) peaks in both the thin film and the clean surface. In order to estimate the composition of the film, we will assume that the XPS signal from the annealed clean surface reflects the composition of a bulk truncated sample and that the film is homogeneous in its composition. The first assumption may not completely reflect the reality but as the surface is in the quasicrystalline phase it does not deviate much from the bulk composition. Regarding the second assumption, Al intermixes from below so it is very likely that the thin film is not homogeneous. Although the absolute results must be used carefully, the results obtained by this model still allow the comparison between experiments. Thus, the atomic ratio in the epilayer thin film is estimated using the following equation

$$\left(\frac{c_{\text{Ni}}}{c_{\text{Al}}}\right)_{\text{film}} = \left(\frac{c_{\text{Ni}}}{c_{\text{Al}}}\right)_{\text{substrate}} \times \left(\frac{h_{\text{Ni}2\text{p}_{3/2}}}{h_{\text{Al}2\text{s}}}\right)_{\text{substrate}}^{-1} \times \left(\frac{h_{\text{Ni}2\text{p}_{3/2}}}{h_{\text{Al}2\text{s}}}\right)_{\text{film}}, \quad (6.6)$$

with

$$\left(\frac{c_{\text{Ni}}}{c_{\text{Al}}}\right)_{\text{substrate}} = 0.27, \quad (6.7)$$

$$\left(\frac{h_{\text{Ni}2\text{p}_{3/2}}}{h_{\text{Al}2\text{s}}}\right)_{\text{substrate}} = 2.35 \pm 0.10, \quad (6.8)$$

and $\left(\frac{h_{\text{Ni}2\text{p}_{3/2}}}{h_{\text{Al}2\text{s}}}\right)_{\text{film}}$ derived from XPS measurement of the thin film.

The heights of Al2s and Ni2p were determined with an error of 50 and 100 counts per second (cps) for the background and peak signal, respectively. The peak heights of Al2s and Ni2p derived from XPS spectra in figure 6.6 are 1380 ± 112 cps and 10310 ± 112 cps, respectively. Using equation 6.6 with

$$\left(\frac{h_{\text{Ni}2\text{p}_{3/2}}}{h_{\text{Al}2\text{s}}}\right)_{\text{film}} = 7.47 \pm 0.29 \quad (6.9)$$

we obtain the following stoichiometry for the thin film

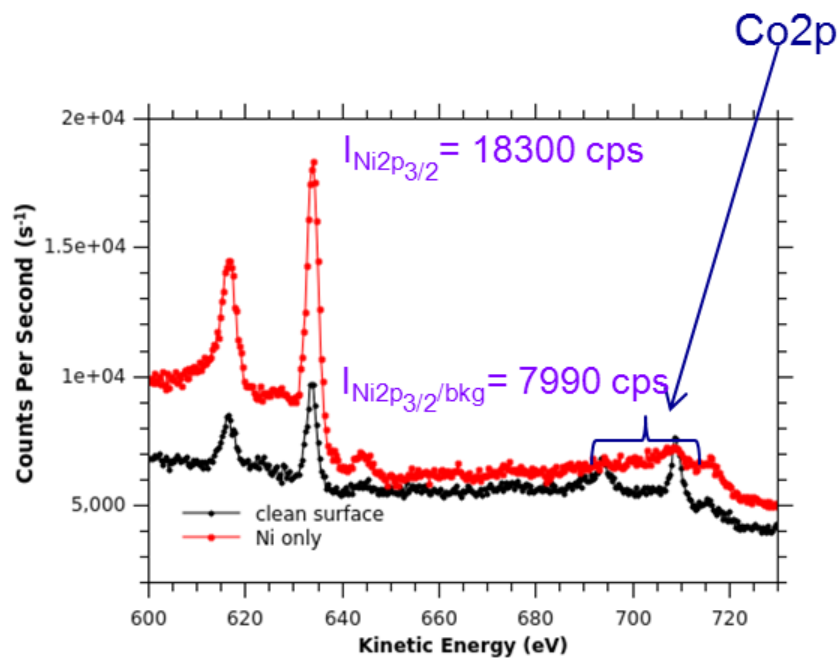
$$\left(\frac{c_{\text{Ni}}}{c_{\text{Al}}}\right)_{\text{film}} = 0.84 \pm 0.04 \quad (6.10)$$

or,

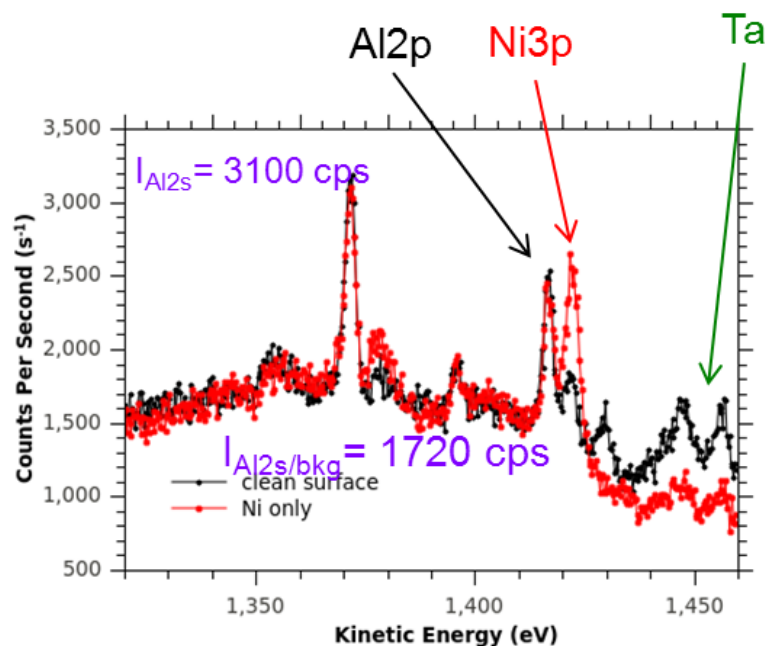
$$\left(\frac{c_{\text{Ni}}}{c_{\text{Al}} + c_{\text{Ni}}}\right)_{\text{film}} = 0.46 \pm 0.02 \quad (6.11)$$

In contrast to Co, this last result indicates a large diffusion of Al into the film. The crystallographic structure of the thin film was analysed with SPA-LEED. The diffraction pattern shows a quasicrystalline 2-fold pattern demonstrating that we have grown an ordered binary alloy AlNi thin film in a quasicrystalline structure (figure 6.7). However, a closer observation reveals dim additional diffraction spots which are not quasicrystal related. The origin of these spots has not been clearly identified. Because the Co2p peak is completely covered, it can be concluded that the film is at least 14 \AA thick according to the IMFP of photoelectrons at Co2p peak energy. The quasicrystalline pattern was acquired with 100 eV energy electrons. The IMFP of electrons at this energy is about 7 \AA which is a factor 2 smaller than the lower bound estimate of the film thickness which is 14 \AA . Thus, according to equation 6.4, the quasicrystal-related peaks observed originate from the thin film.

In this experiment the substrate provides half of the atoms present in the film. Al diffuses into the film in order to stabilise the quasicrystalline phase. Nevertheless, the Ni atomic ratio c_{Ni} in the film is far from 0.28 which is the value for an Al concentration identical to that in quasicrystals. In the next experiment we have co-deposited Ni and Al in order to rebalance the film composition towards this limit.



(a)



(b)

Figure 6.6: XPS spectrum in Ni area (a) and in Al area (b) on clean surface (black) and after Ni deposition (red). The background subtracted peak heights of Al2s and Ni2p are $1380 \pm 112 \text{ cps}$ and $10310 \pm 112 \text{ cps}$, respectively and are used to determine the thin film composition. See text for details.

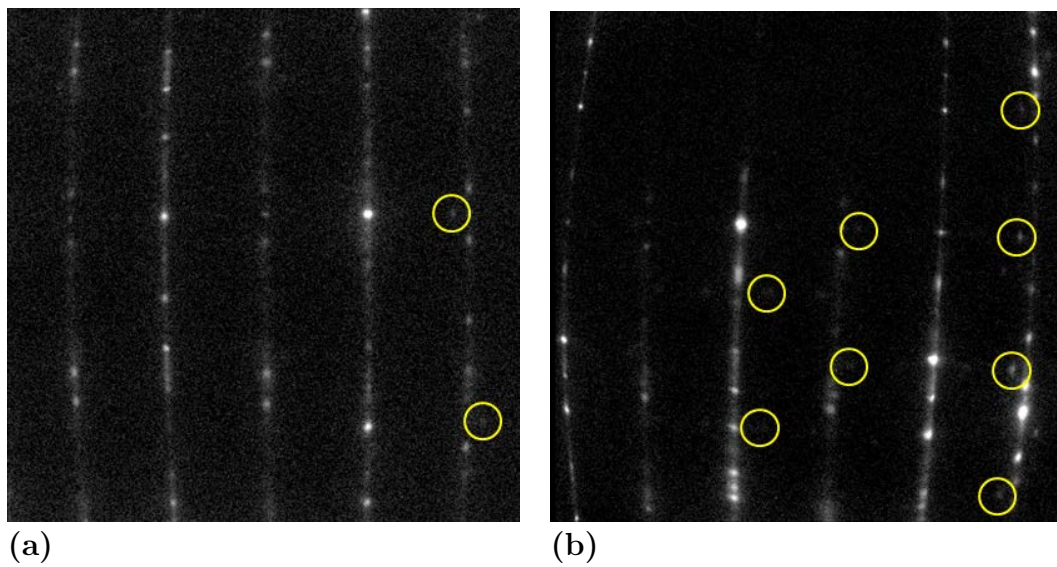


Figure 6.7: $4 \text{ \AA}^{-1} \times 4 \text{ \AA}^{-1}$ SPA-LEED image of $\text{Al}_{54}\text{Ni}_{46}$ without further annealing. (a) Electron energy: 100 eV. (b) Electron energy: 60 eV. Yellow circles highlight diffraction spots not related to a quasicrystalline structure.

6.4 Al/Ni co-deposition on 2-fold *d*-AlNiCo

In order to get an Al concentration closer to that found in Al-based quasicrystals of about 70%, we deposited Al and Ni simultaneously. The sample was cleaned by two sputter/annealing cycles of 30 min, 5 min, 30 min, and 5 min respectively with a sputtering voltage of 3 kV and temperature annealing of 650 ± 20 °C. Al and Ni were deposited simultaneously for 40 min at a substrate temperature of 370 ± 20 °C. The stoichiometry and atomic structure were measured after every 20 minutes. The XPS spectra of the clean surface and those after the first two depositions are shown in figure 6.8 where the Co signal at 710 eV decreases gradually with each deposition step (figure 6.8.a). After the first 20 minutes deposition, we observed with SPA-LEED the diffraction pattern shown in figure 6.9.a. The pattern is still 2-fold but the spots are spaced regularly along what used to be the quasicrystal line direction. The AlNi has adopted a crystallographic structure that matches the quasicrystal one. Figure 6.9.b. shows the plot profiles extracted from the diffraction pattern in figure 6.9.a. The plot profile of the thin film's diffraction pattern is in green and is superposed with the substrate's one in red. The spacing between spots is 0.196 \AA^{-1} . The unit cell adopted by the AlNi alloy, highlighted in figure 6.9.a, has a perpendicular base with a dimension of $32 \text{ \AA} \times 4 \text{ \AA}$.

AlNi alloys adopt different structures in bulk depending on their stoichiometry. These structures are summarised in table 6.5. Following the indications given by SPA-LEED, we know that the unit cell is orthorhombic, ruling out Al_3Ni . The lattice constant is about 4 \AA making AlNi an impossible candidate ($\sim 2.8 \text{ \AA}$). From the three structures left, Al_3Ni_5 and AlNi_3 are inconceivable since by evaporating only Ni we obtained a binary alloy with about 50:50 stoichiometry. What remains is Al_3Ni_2 whose unit cell is 4.04 \AA which is also included 8 times in 32 \AA . Al_3Ni_2 is the most likely candidate. The $32 \text{ \AA} \times 4 \text{ \AA}$ unit cell is an 8×1 superstructure of the tetragonal Al_3Ni_2 structure type.

Looking at the profile line scan of the thin film's diffraction pattern in green in figure 6.9.b, the fourth peak from the left at -1 \AA^{-1} appears sharper than the other periodic related peaks. According to the attenuation of the Co2p signal, the thin film is approximately 3.1 nm. The film depth is smaller than the depth sensitivity of our measurement. Thus, the diffraction pattern in figure 6.9.b displays both thin film and substrate information. To explore the structural quality of the thin film in both the periodic and quasiperiodic directions profile line scans, from quasiperiodic-

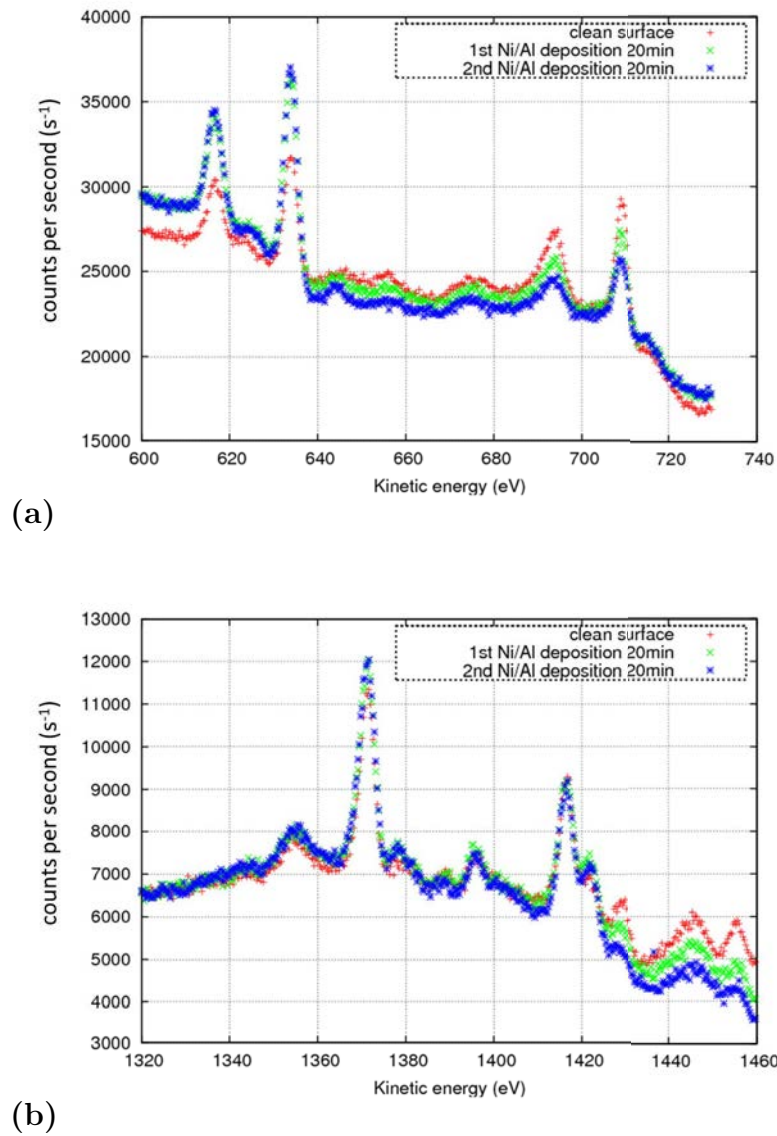


Figure 6.8: XPS spectra showing Ni and Co peaks (a) and Al peak (b) on clean surface (red), 20 min Al/Ni co-deposition (green), and another 20 min (blue).

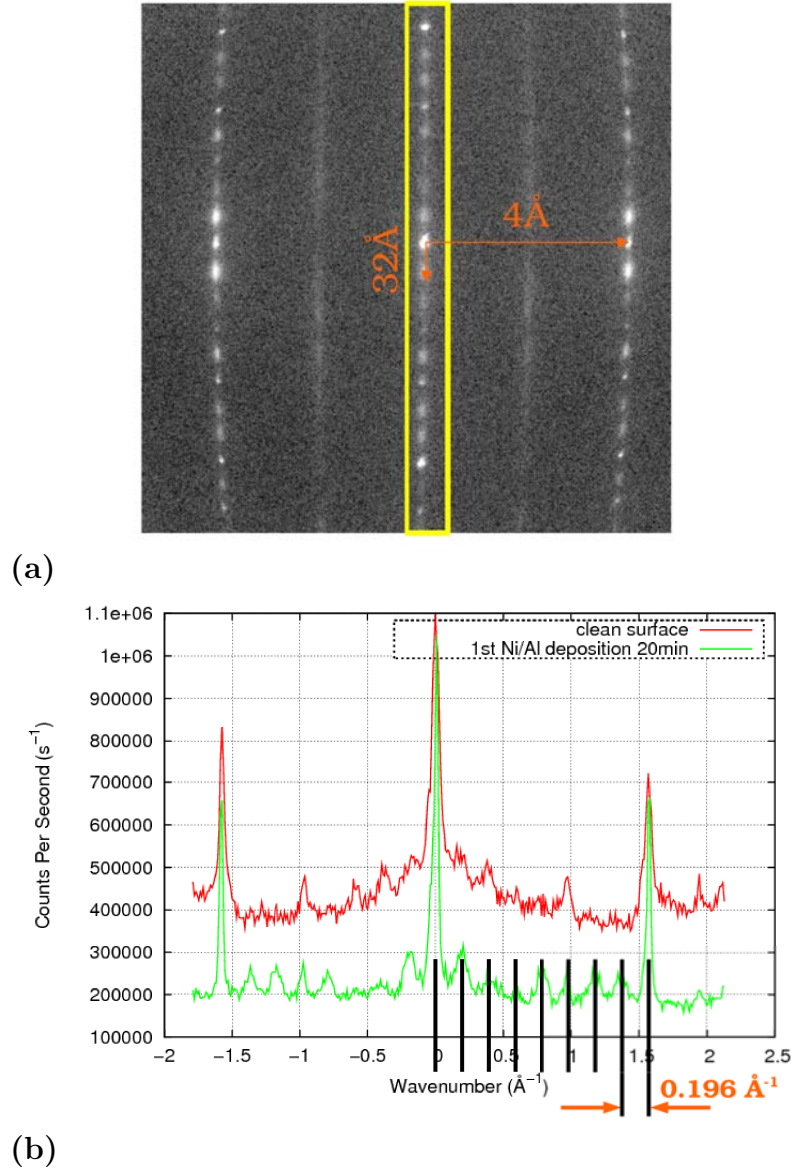


Figure 6.9: (a) $4 \text{\AA}^{-1} \times 4 \text{\AA}^{-1}$ SPA-LEED image of the quasicrystal after the first 20 min deposition without further annealing. Electron energy: 100 eV. The diffraction pattern shows regularly spaced spots along the quasicrystalline direction. The pattern still has a 2-fold symmetry but the AlNi alloy adopts a crystallographic structure with a unit cell of $32 \text{\AA} \times 4 \text{\AA}$. (b) Recalibrated line scan from the yellow area in (a) according to the expected peak position values.

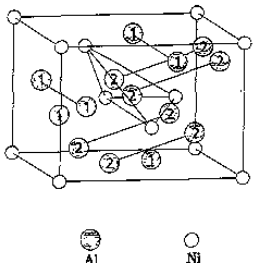
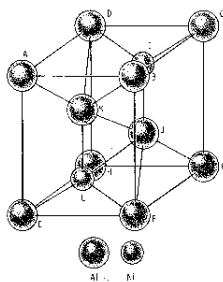
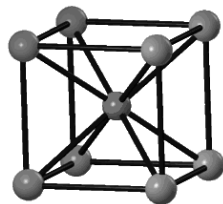
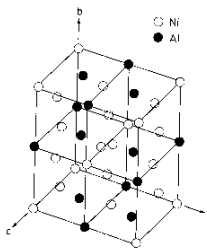
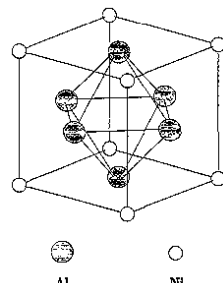
Al_3Ni [203]		<p>BaS_3-type (DO_{20}) orthorhombic</p> <p>$\alpha \neq \beta \neq \gamma$ $a = 6.6 \text{ \AA}$ $b = 7.3 \text{ \AA}$ $c = 4.8 \text{ \AA}$</p>
Al_3Ni_2 [204]		<p>Al_3Ni_2-type tetragonal</p> <p>$\alpha = \beta = \gamma = 90^\circ$ $a = b \approx 4.04 \text{ \AA}$ $c \approx 4.9 \text{ \AA}$</p>
AlNi [204]		<p>CsCl-type cubic</p> <p>$\alpha = \beta = \gamma = 90^\circ$ $a = b = c \approx 2.8 \text{ \AA}$</p>
Al_3Ni_5 [205]		<p>$D_{2h}^{19}(\text{Cmmm})$ orthorhombic</p> <p>$\alpha = \beta = \gamma = 90^\circ$ $a = 7.47 \text{ \AA}$ $b = 6.73 \text{ \AA}$ $c = 3.73 \text{ \AA}$</p>
AlNi_3 [206]		<p>Cu_3Au-type cubic</p> <p>$\alpha = \beta = \gamma = 90^\circ$ $a = b = c \approx 3.5 \text{ \AA}$</p>

Table 6.5: The crystallographic structures of the AlNi alloy.

and periodic- related peaks, were extracted and superposed for direct comparison. A quasicrystal is a brittle material and in this respect its crystalline quality is closer to silicon than a metal. The structural quality of a film can be estimated by measuring the width of a diffraction spot. The Full-Width at Half Maximum (FWHM) of a diffraction pattern spot reflects the structural coherence of a crystal. In a simple approach, and for comparative study only, the coherence length λ will be associated with the FWHM of a diffraction spot with the following equation

$$\lambda = \frac{2\pi}{\text{FWHM}}. \quad (6.12)$$

For this analysis, we use the fifth and sixth peaks at -1 \AA and -1.2 \AA in figure 6.9.b which originate from the periodic thin film and quasiperiodic substrate, respectively. The superposition of the plot profiles of the third and fourth peaks extracted from figure 6.9 along the quasiperiodic (00001) and periodic (10000) directions are displayed in figures 6.10 and 6.11, respectively. These images, unlike others SPA-LEED images are displayed in a linear count scaling instead of logarithmic. The thin film and quasiperiodic related spots are displayed in green and red, respectively. The values for the plot profiles were averaged over 3 pixels in the direction perpendicular to the scan profile direction. The peaks have been fitted by a gaussian function to obtain the FWHM of these spots.

In the quasiperiodic direction, as shown in figure 6.10, the periodic - and quasiperiodic - related spots have an FWHM of $0.068 \pm 0.004 \text{ \AA}^{-1}$ and $0.027 \pm 0.001 \text{ \AA}^{-1}$, respectively. The periodic structure has a coherence length of $91 \pm 6 \text{ \AA}$, significantly smaller than the quasiperiodic one which is $232 \pm 10 \text{ \AA}$. Along the quasiperiodic direction the film is less coherent than the quasicrystal substrate.

We analysed the same peaks in the periodic direction as shown in figure 6.11. We found a spot width of $0.034 \pm 0.002 \text{ \AA}^{-1}$ and $0.035 \pm 0.001 \text{ \AA}^{-1}$ for the periodic and quasiperiodic related spots, respectively. The coherence lengths are $186 \pm 10 \text{ \AA}$ and $179 \pm 5 \text{ \AA}$ for the film and substrate, respectively. In this case, the difference in the structural quality between the crystalline film and quasicrystalline substrate is null within the error in the determination of the spot width.

According to the spot-profile analysis, substrate and thin film have same structural quality in the periodic direction. We observed the same coherence length because the epilayer matches the substrate according to an 1-to-1 epitaxial relation. However, the film has a poor coherence length along the quasiperiodic direction, $91 \pm 6 \text{ \AA}$, since in this direction the film is out-of-phase.

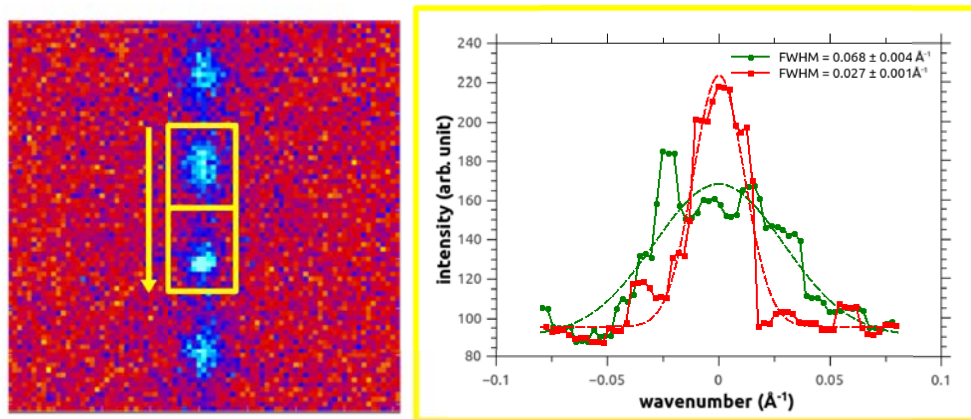


Figure 6.10: Profile line scan of quasiperiodic- (red) and periodic-related (green) peaks along the quasiperiodic direction.

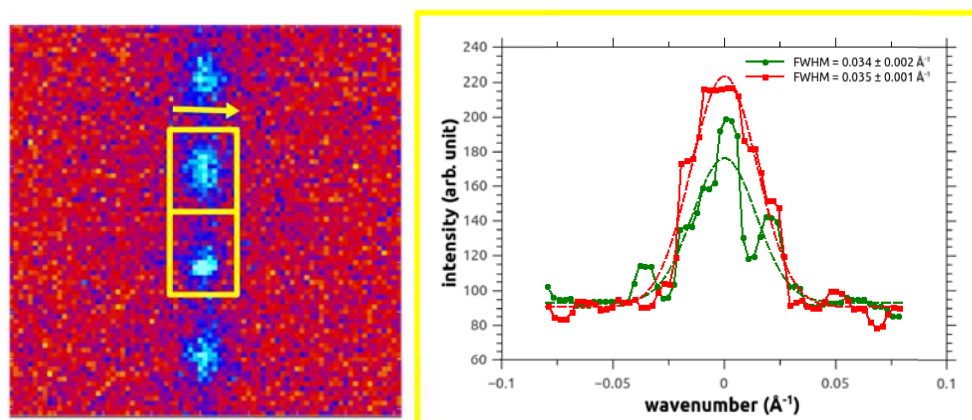


Figure 6.11: Profile line scan of quasiperiodic- (red) and periodic-related (green) peaks along the periodic direction.

After the second Al/Ni co-deposition, the periodic structure has disappeared as shown in figure 6.12. The film still being very thin as shown by the XPS data displayed in blue in graph 6.8, we cannot come to a conclusion regarding the thin film structure. The layer may be amorphous or rough and the diffraction pattern may come from the substrate. According to the attenuation of the Co signal, the film was about $\sim 7.4 \text{ \AA}$.

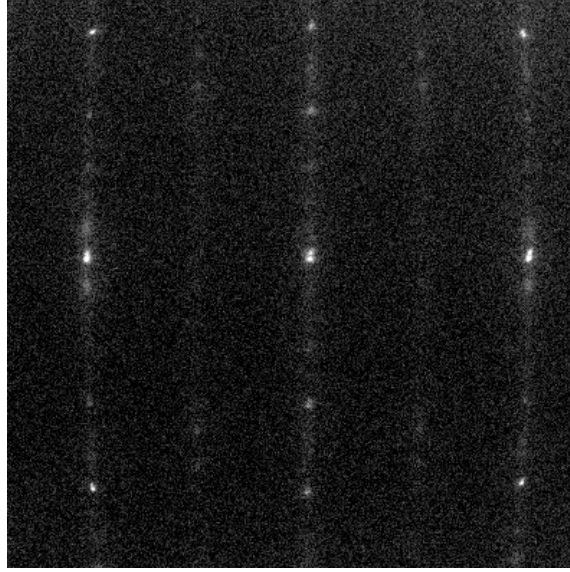


Figure 6.12: $4 \text{ \AA}^{-1} \times 4 \text{ \AA}^{-1}$ SPA-LEED image of the quasicrystal after second Al/Ni deposition without further annealing. Electron energy: 100eV. The pattern reverted to a quasicrystal structure.

6.5 Al/Ni co-deposition on 2-fold d -AlNiCo at higher Al:Ni ratio

Al/Ni deposition was carried out in a similar way as in the experiment described in section 6.4. In order to get a thin film closer to the desired $\text{Al}_{72}\text{Ni}_{28}$ composition, deposition was carried out with a higher Al flux. The deposition experiment was performed at the same temperature ($370 \pm 20^\circ\text{C}$) and with the same deposition time (60 min) as the experiment presented in section 6.3. Before deposition the sample was cleaned by two sputter/annealing cycles of 50 min, 5 min, 35 min, and 5 min respectively with a sputter voltage of 3 kV and annealing temperature of $650 \pm 20^\circ\text{C}$.

XPS measurement in figure 6.13 shows total extinction of the Co2p peak signal. According to the IMFP at the Co2p peak value, the film is thicker than 14 \AA . Since

the surface sensitivity of electrons at 100 eV is approximately 7 Å, the XPS signal of the film has no contribution from the substrate and the thin film is made only of Ni and Al elements. Figure 6.13 shows both the clean substrate (black) and thin film XPS signals. After deposition, both Ni and Al signals have increased substantially.

The crystallographic structure of the thin film was explored with SPA-LEED and is shown in figure 6.14. According to the XPS signal, the deposition of Ni and Al has not resulted in island growth since no Co signal can be seen. The film structure is either crystalline, quasicrystalline, or amorphous. Since no crystal related peaks can be observed in the diffraction pattern in figure 6.14 and the surface sensitivity of electrons at 100 eV is about 7 Å, the film cannot be amorphous, pointing instead toward a binary alloy quasicrystal thin film.

In order to determine the stoichiometry of the AlNi quasicrystal thin film, we compare the ratio of the background subtracted values of the peak heights of Al2s and Ni2p peaks as we did in section 6.3. The heights have been measured from the XPS spectra in figure 6.13. The heights of Al2s and Ni2p were determined with an error of 100 and 50 counts per second (cps) for the peak and background signal, respectively. The peak heights of Al2s and Ni2p are 1920 ± 112 cps and 8650 ± 112 cps, thus,

$$\left(\frac{h_{\text{Ni}_{2p3/2}}}{h_{\text{Al}_{2s}}} \right)_{\text{film}} = 4.50 \pm 0.13. \quad (6.13)$$

Using equation 6.6 we find

$$\left(\frac{c_{\text{Ni}}}{c_{\text{Al}}} \right)_{\text{film}} = 0.51 \pm 0.02, \quad (6.14)$$

or

$$\left(\frac{c_{\text{Ni}}}{c_{\text{Al}} + c_{\text{Ni}}} \right)_{\text{film}} = 0.34 \pm 0.01. \quad (6.15)$$

To conclude, we have successfully grown a AlNi binary alloy quasicrystalline thin film by rebalancing the composition towards an Al:Ni ratio of 2:1.

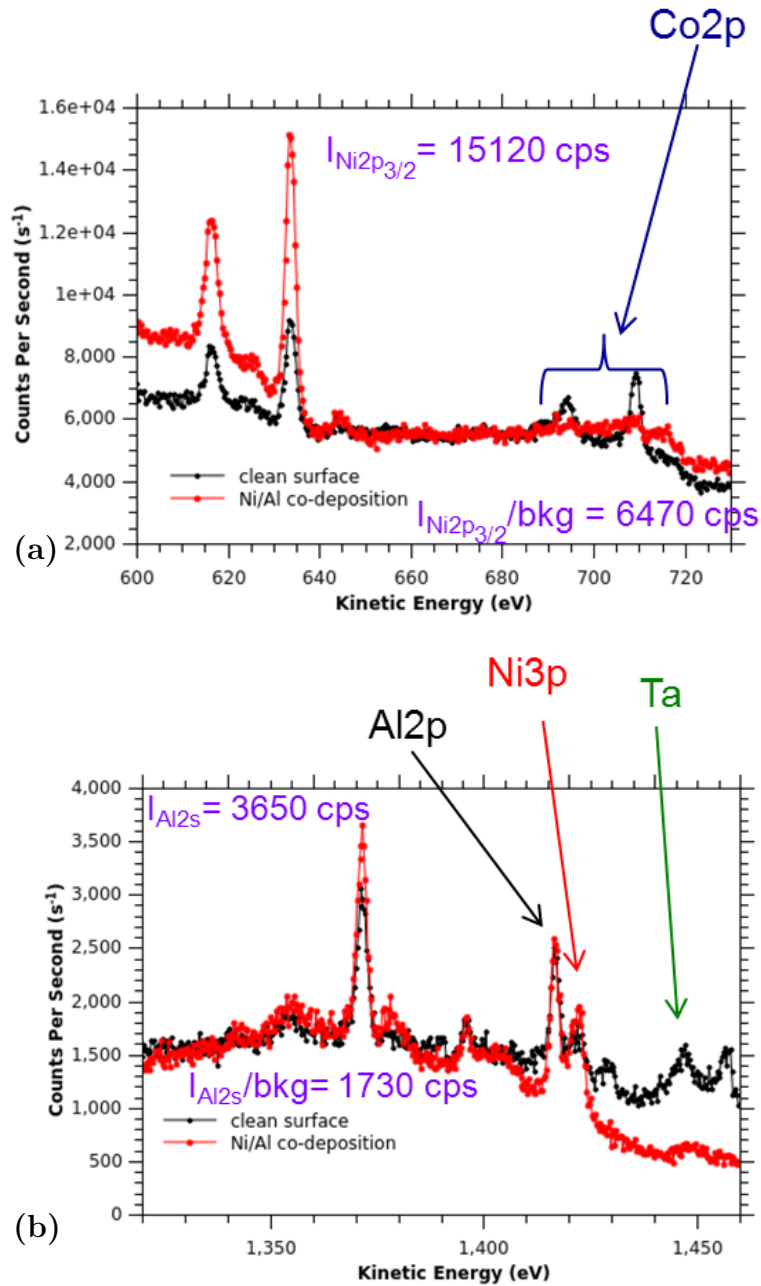


Figure 6.13: XPS spectrum in Ni area (a) and in Al area (b) on clean surface and after Al/Ni co-deposition in black and red respectively. After deposition, Ni and Al signals have significantly increased whereas the Co signal has vanished. The background subtracted peak heights of Al_{2s} and Ni_{2p} are 1920 ± 112 cps and 8650 ± 112 cps, respectively and are used to determine the thin film composition. See texts for details.

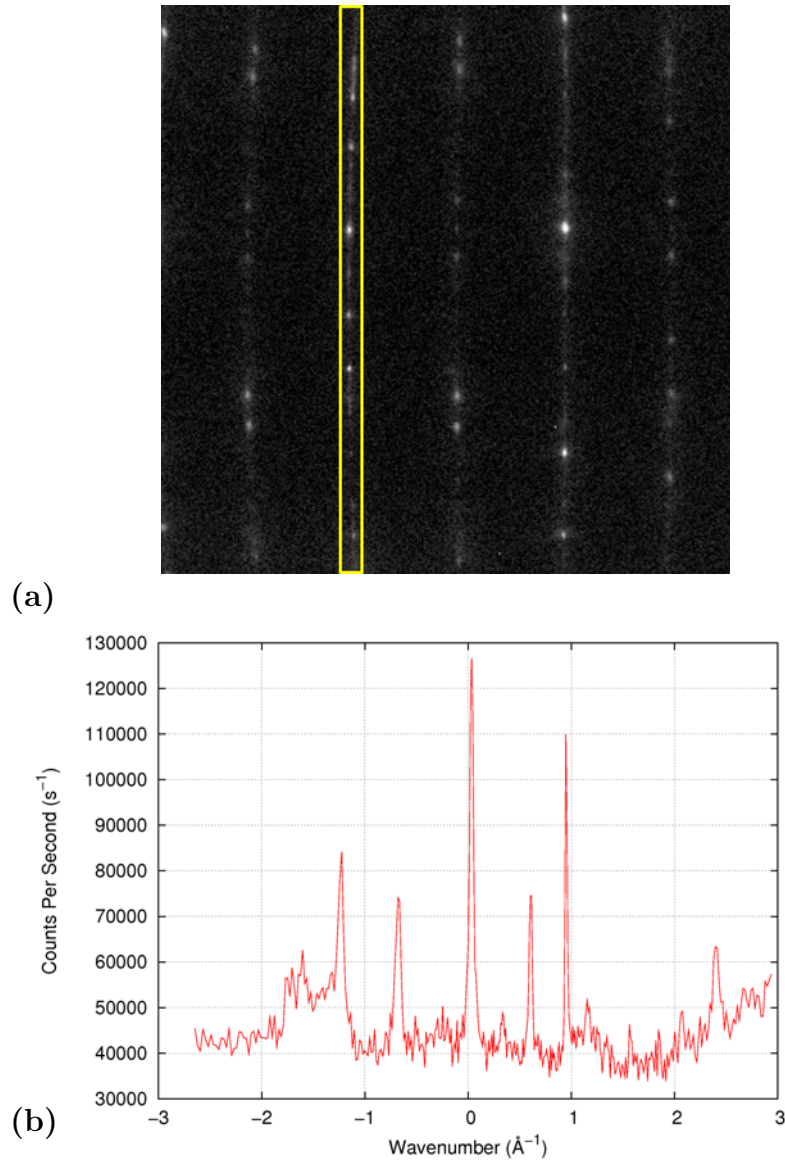


Figure 6.14: (a) $4 \text{ \AA}^{-1} \times 4 \text{ \AA}^{-1}$ SPA-LEED image of $\text{Al}_{66}\text{Ni}_{34}$ without further annealing. Electron energy: 100 eV. (b) calibrated 1D SPA-LEED image from yellow area in (a).

6.6 Summary

In this chapter, we reported experimental evidence of quasicrystal thin film growth by deposition of Ni and Al on the 2-fold surface of $d\text{-Al}_{72.2}\text{Ni}_{19.2}\text{Co}_{8.6}$. In order to get satisfactory epitaxial condition, the deposition was carried out with the sample temperature held at $370 \pm 20^\circ\text{C}$. With the simplified assumption that the epilayer doesn't intermix with the substrate, we found that AlNi thin films grow in a quasicrystal structure with an atomic percent of Ni ranging from 34 to 46 %. In the Ni-poor regime (34%), which is the closest one to the aimed composition (28%), we observed quasicrystalline film growth at a thickness larger than 14 \AA . At 40% Ni, the AlNi thin film adopted an Al_3Ni_2 structure-type, epitaxially matching the 2-fold decagonal surface. For higher film thickness at the same composition, the AlNi film turns back into a quasicrystalline structure. In the Ni-rich regime (46%), Ni deposition only yields crystalline spots. Other stoichiometries are not reachable at our growth temperature of 370°C due to interdiffusion of elements from the bulk to the film.

We analysed in detail the Al_3Ni_2 2-fold periodic thin film. Measuring the spot width of the diffraction patterns in the periodic and quasiperiodic directions, we found that the structural coherence length of the thin film is smaller than that of the substrate in the quasiperiodic direction.

A binary alloy quasicrystalline thin film has never been reported in the literature. It would be interesting to know to which thickness it can be grown while preserving a quasicrystalline structure. The d -band is removed further from the Fermi energy in Cu than Ni. Growing quasicrystalline aluminium based binary alloy with Cu instead of Ni would allow the exploration of a quasicrystal with s-p type electron bands in a large energy range around the Fermi energy.

Chapter 7 : Surface Magnetism of MnSb/GaAs(111)B

Due to their large surface-to-volume ratio, the surface magnetic anisotropy of low dimensional systems can change the magnetic easy direction and/or enhance the effective magnetic anisotropy (section 3.1). The large polarisation at the surface can be utilised to inject a spin-polarized current into non-magnetic materials [151].

Gavin Bell and co-workers have been very active in studying epitaxial growth of MnSb on GaAs(111)B (section 3.2). To exploit MnSb-based devices it is crucial to understand the temperature dependence of the spin-polarisation. Defects, disorder and magnetic inhomogeneity may prevent high spin-polarisation at the surface. Excellent single crystal films can be prepared by MBE but the native oxides are difficult to remove without affecting the stoichiometry, the morphology, or the magnetic properties.

In this chapter, we will present a SPLEEM investigation of MnSb(0001) surface magnetism and of the temperature dependence of the film morphology. The experiments were performed at the National Center for Electron Microscopy (NCEM) at the Lawrence Berkeley National Laboratory in Berkeley with the help of Dr. Andreas Schmidt and Dr. Adrian Quesada.

7.1 Description of the sample

The sample used was made by Dr. James Aldous and Dr. Gavin Bell from the Department of Physics at the University of Warwick. A GaAs(111)B substrate was degased at $\sim 420^\circ\text{C}$ for 1 hour. The degasing was followed by ion beam bombardment for 15 minutes and a final $\sim 480^\circ\text{C}$ anneal. Before deposition, the usual (1×3) pattern was observed by RHEED. The MnSb film was grown with a flux ratio J of As over Mn of about 6.5 for 20-25 minutes at the standard conditions given in section 3.2.3. The thickness of the film was estimated to be about 130 nm. After deposition, the film shows the expected (2×2) surface reconstruction. At the NCEM, to remove the few nanometer thick Mn oxide layer, the sample was dipped in HCl for 10 seconds. After a quick loading, the sample was sputtered with argon and annealed to 400°C .

7.2 Morphology change upon annealing

LEEM experiments allow us to observe morphology changes *in-situ* with a video acquisition frame rate (see section 4.8). Samples are heated by radiation from a filament and the temperature is measured with a C-type thermocouple. The sample was cleaned by sputtering as shown in figure 7.1.a and 7.1.b for two hours to remove the water induced oxide film. The LEED pattern obtained after sputtering indicates a poor quality surface (figure 7.1.c).

The electron optics of the SPLEEM from sample to projection screen is solely based on electrostatic lenses (not magnetic). Thus the images are not rotated. As the camera for LEEM and LEED are implemented in the same side, LEED and LEEM images can be directly compared in terms of sample orientation.

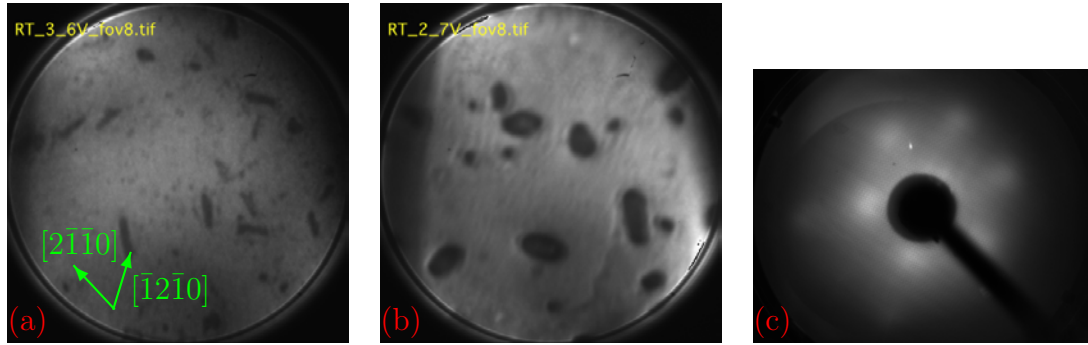


Figure 7.1: (a, b) LEEM images of MnSb/GaAs(111)B from different areas after sputtering and (c) LEED pattern. The spots in panel (c) are very broad indicating a low degree of long-range order.

We observed no changes at the surface up to about a temperature of 360°C (figure 7.2) as expected. Afterwards, we heated the sample to slightly below the

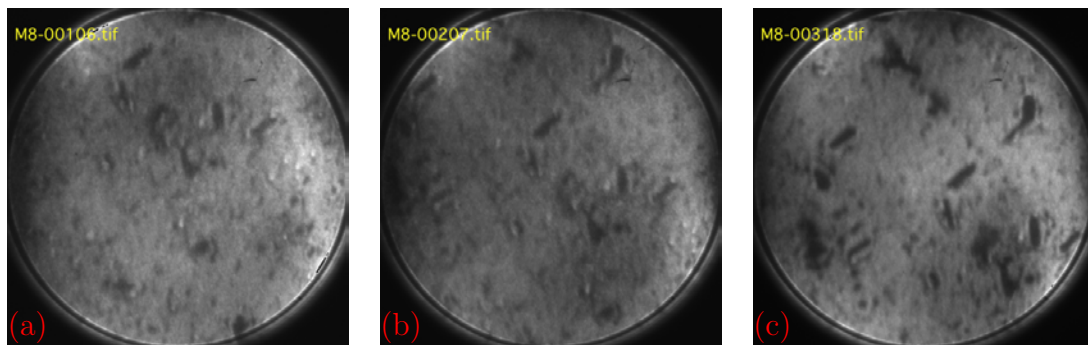


Figure 7.2: LEEM images of MnSb/GaAs(111)B at different temperatures; (a) $\sim 273^\circ\text{C}$, (b) $\sim 328^\circ\text{C}$, (c) $\sim 350^\circ\text{C}$. Sample voltage: 4.3 V, field of view: $8\ \mu\text{m}$.

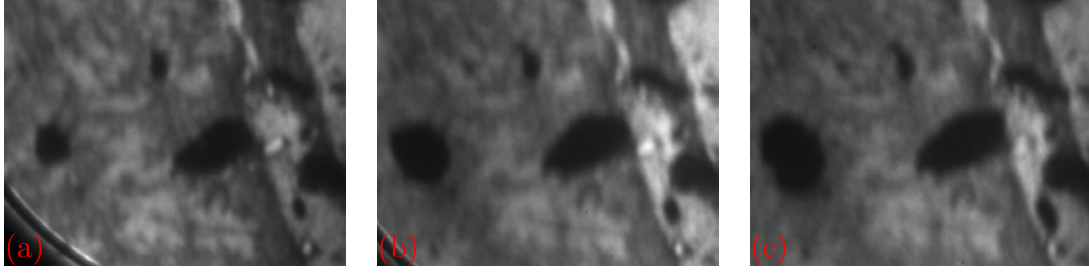


Figure 7.3: LEEM images of MnSb/GaAs(111)B at different temperatures showing the growth of a black stain: (a) 371°C, (b) 390°C, (c) 396°C. Sample voltage: 7.2 V, horizontal field of view: $\sim 4.5 \mu\text{m}$.

damage threshold. We observed the growing of a black feature as shown in figure 7.3. The surface structure of the sample was subsequently studied with LEED (figure 7.4.a). The peaks are much sharper indicating a better quality of the surface. Comparing with the Si(111)-7x7 LEED pattern (fig.7.4.b) and using equation

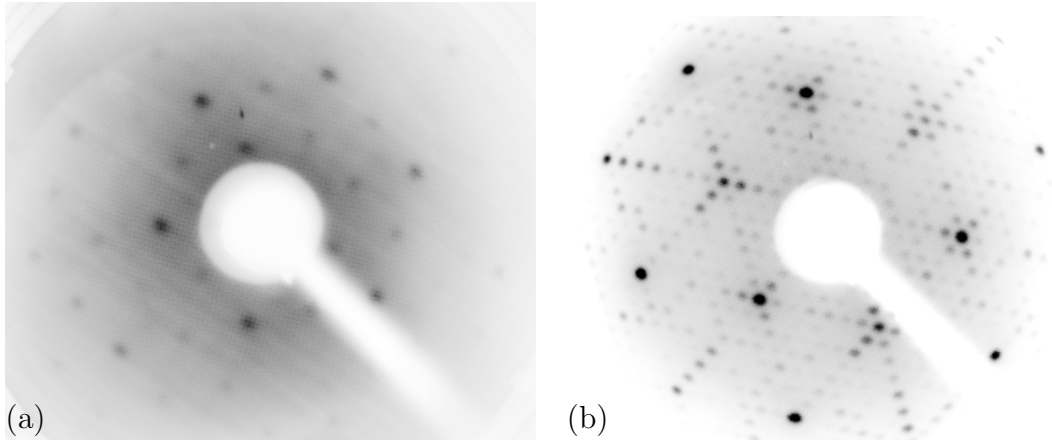


Figure 7.4: LEED pattern of the MnSb film (a) and the surface reconstructed Si(111)-(7x7) (b). The electron beam energy is 110 eV. The contrast was inverted for convenience.

1.5, one can calibrate the MnSb diffraction pattern. Because both unit cells have hexagonal geometry, we can write the following equation

$$A_{\text{Si}(111)-(7 \times 7)} = \alpha A_{\text{MnSb}}, \quad (7.1)$$

where A is the reciprocal unit cell and α is a constant. In the Si(111) plane, the length of the (1×1) unit cell is $\sqrt{2}/2$ times the lattice constant (5.43 \AA). On the

images, we measured α to be 4.55/2.4. With equation 1.5 and 7.1, we find

$$a_{MnSb} = 5.43 \times \frac{\sqrt{2}}{2} \times \frac{4.55}{2.4} = 7.3 \text{ \AA}. \quad (7.2)$$

This value is close enough to twice the side of the MnSb hexagonal unit cell $2a = 8.25 \text{ \AA}$ to indicate we had the good (2×2) pattern. A slight change in the distance between the video camera and the sample may have induced the discrepancy.

7.3 SPLEEM contrast of MnSb/GaAs(111)B at different energies

Modulating the spin direction θ , a preliminary experiment (not shown) shows no contrast for out of plane magnetisation $\theta=0^\circ$ at room temperature. This is consistent with the previous discussion in section 3.1.4. For the following experiments and unless specified differently θ will always be 90° . Images in figures 7.5 show a LEEM image and its SPLEEM related image. The sample has defects but the magnetic image does not show any influence of them on the magnetic domain structure.

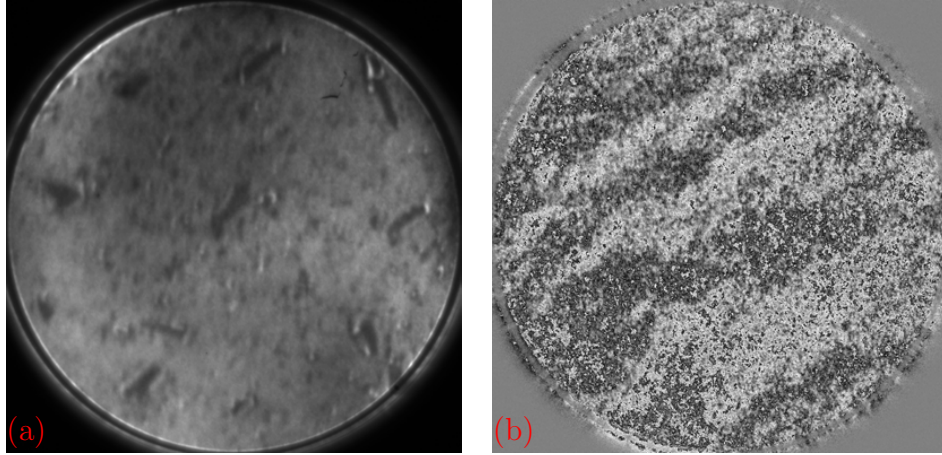


Figure 7.5: (a) LEEM image (spin-down), (b) related SPLEEM image with sample voltage of 4.5 V. Field of view: $8 \mu\text{m}$.

For the subsequent analysis, we recalculate the SPLEEM image in order to compensate for a possible drift between spin-up and spin-down images due to the required long integration time (a few seconds). The SPLEEM recalculation also allows us to scale the grey contrast.

The drift correction was performed by introducing a quality factor defined as below

$$Q(\Delta i, \Delta j) = \frac{\sum_{(i,j) \in \mathcal{A}} [I_{\uparrow}(i + \Delta i, j + \Delta j) - I_{\downarrow}(i, j)]^2}{\sum_{(i,j) \in \mathcal{A}} [I_{\uparrow}(i + \Delta i, j + \Delta j) + I_{\downarrow}(i, j)]}, \quad (7.3)$$

with i and j the pixel coordinates in a fixed central window \mathcal{A} . Δ is the drift in pixels between two images. The drift Δ between two images was the one that returns the smallest quality factor. Because the brightness of two images may be slightly different, we introduced a c -factor after shift in a least-square function D before calculating the SPLEEM image

$$D = \sum_{(i,j) \in \mathcal{A}} (I_{\uparrow}(i, j) - c \times I_{\downarrow}(i, j))^2, \quad (7.4)$$

where \mathcal{A} is the area defined above. Calculating the first derivative and setting it equal to 0, the value of c that minimises D is

$$c = \frac{\langle I_{\uparrow} \times I_{\downarrow} \rangle}{\langle I_{\downarrow}^2 \rangle}. \quad (7.5)$$

Thus, we calculated the SPLEEM images with the following equation

$$I_{sp} = \frac{I_{\uparrow} - c I_{\downarrow}}{\langle I_{\uparrow} + c I_{\downarrow} \rangle}, \quad (7.6)$$

with I_{\uparrow} drift compensated. With this method, the difference between the highest and lowest pixel intensity, or data range, gives the magnetic signal ($\sim 20\%$).

Spin-up and spin-down image pairs were recorded at different beam energies. The intensity in black and white regions were analysed by extracting the average pixel intensity in the four domains (blue, green, yellow and red) as shown in the inset of figure 7.6. The magnetic contrast is the difference of averaged pixels intensity in white and black regions (yellow/red and blue/green respectively) and is shown in figure 7.6. The magnetic contrast oscillates and reaches a maximum at 4 V. In the inset of figure 7.6 one can observe the contrast reversal. A series of ten acquisitions was captured at a sample voltage of 4 V that allowed us to extract the standard deviation for this point that we also used for all others points. For the subsequent analysis on MnSb/GaAs(111)B the sample voltage was tuned to values between 4 and 4.5 V since this voltage provides the best contrast.

Image 7.7 shows the magnetic contrast of the MnSb film after annealing to 520°C.

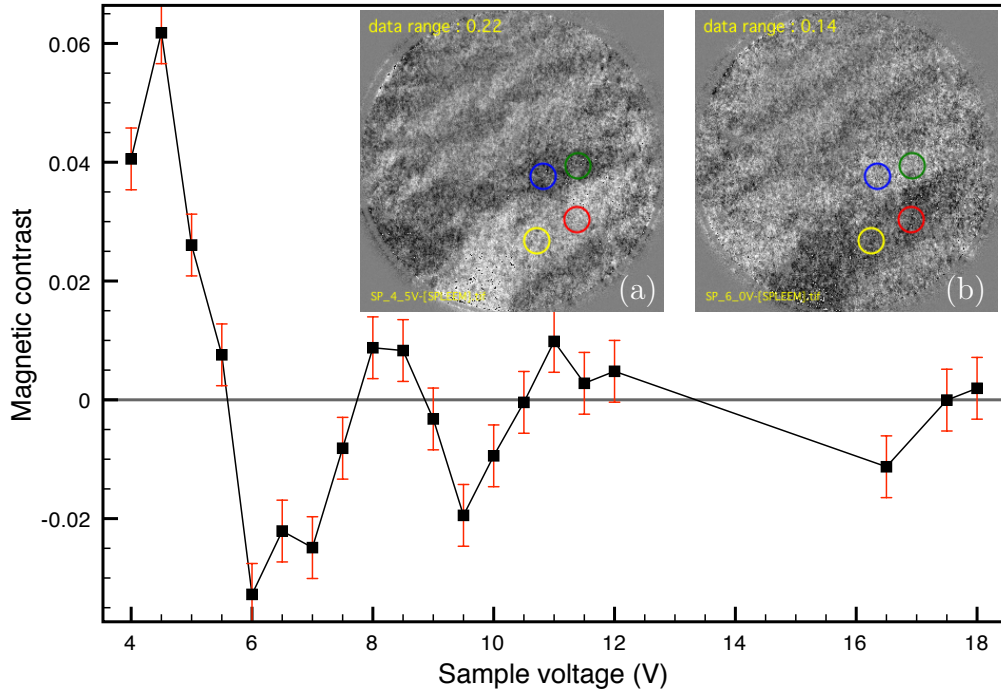


Figure 7.6: Calculated magnetic contrast for different illumination beam energy. The error bars were calculated for ten images acquired at 4 V and extrapolated to others points.

The drift was corrected, and the SPLEEM contrast was calculated locally with the following equation (no average in the denominator)

$$I_{sp} = \frac{I_{\uparrow} - cI_{\downarrow}}{I_{\uparrow} + cI_{\downarrow}}. \quad (7.7)$$

The contrast was symmetrised around the medium grey value and the contrast enhanced as it can be seen in the left-hand side contrast bar of figure 7.7. The image was acquired with an applied voltage between sample and the GaAs crystal of 4.5 eV, the actual kinetic energy of the incoming electrons is 6.2 eV.

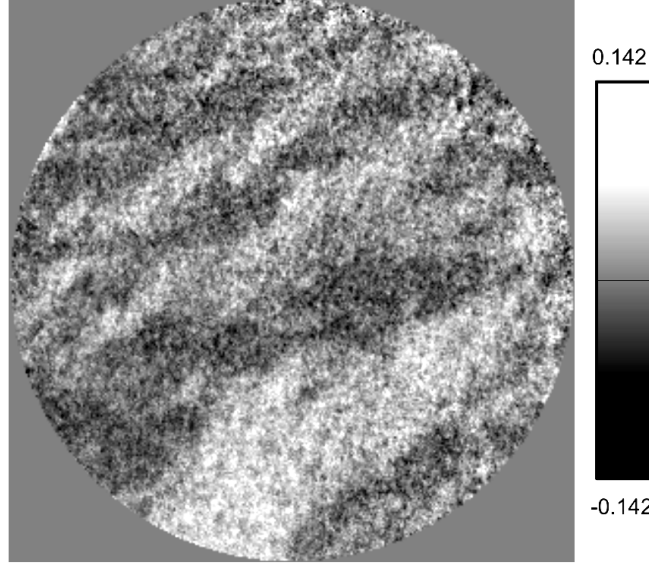


Figure 7.7: Contrast-optimised SPLEEM image of an uncapped, HCl-etched MnSb sample after UHV annealing to 520°C. The integration time is 5s with an electron beam energy of 6.2eV relative to the Fermi energy. Electron spin-polarisation is in-plane. Field-of-view: 8 μ m. [207]

7.4 Direction mapping of MnSb magnetic domains

The polarisation of the spin of the illuminating electron beam can be rotated (see section 4.8.4). With two SPLEEM frames as in figure 7.5.b acquired at two angles perpendicular at each other it is possible to measure the local magnetisation vector. We will be using the intensity values of frame 1 and 2 calculated with equation 7.7 and displayed in figure 7.8. The method consists in giving a color to a pixel according to the following equation

$$\alpha = \tan\left(\frac{I_{sp1}}{I_{sp2}}\right), \quad (7.8)$$

considering that I_{sp} can either be positive or negative, equation 7.8 can take a full set of value in 360°. The color given to each pixel is defined with the following equation

$$\begin{cases} \text{RGB}(\alpha), & \text{if } r = (I_{sp1}^2 + I_{sp2}^2)^{\frac{1}{2}} > r_{cutoff} \\ \text{black}, & \text{otherwise.} \end{cases} \quad (7.9)$$

The result of the operation using equations 7.8 and 7.9 can be seen in figure 7.9 with $\text{RGB}(\alpha)$ referring to the mapping in the inset in figure 7.9. Thus, in our analysis the color distribution does not depend on the magnitude of the intensity. The cutoff aims to reduce noise. The SPLEEM images in which the color indicates the magnetic

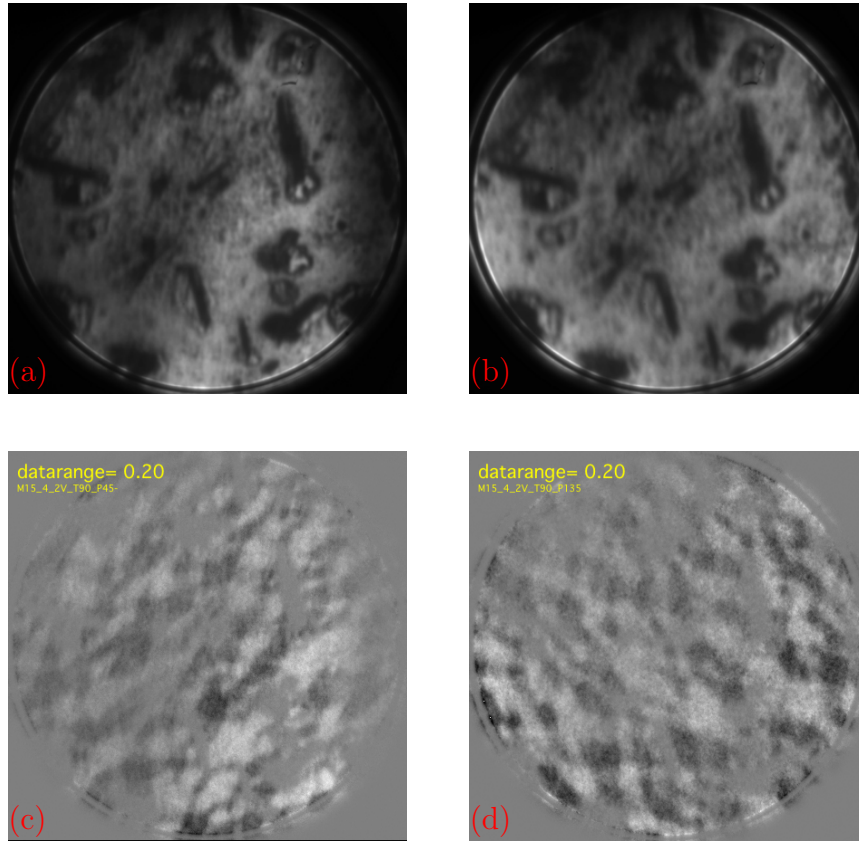


Figure 7.8: LEEM images with spin-up electron polarised in-plane at 45° (a) and 135° (b). (c) and (d) SPLEEM images calculated with (a), (b) and their spin-down counterparts. Field of view: 8 μ m.

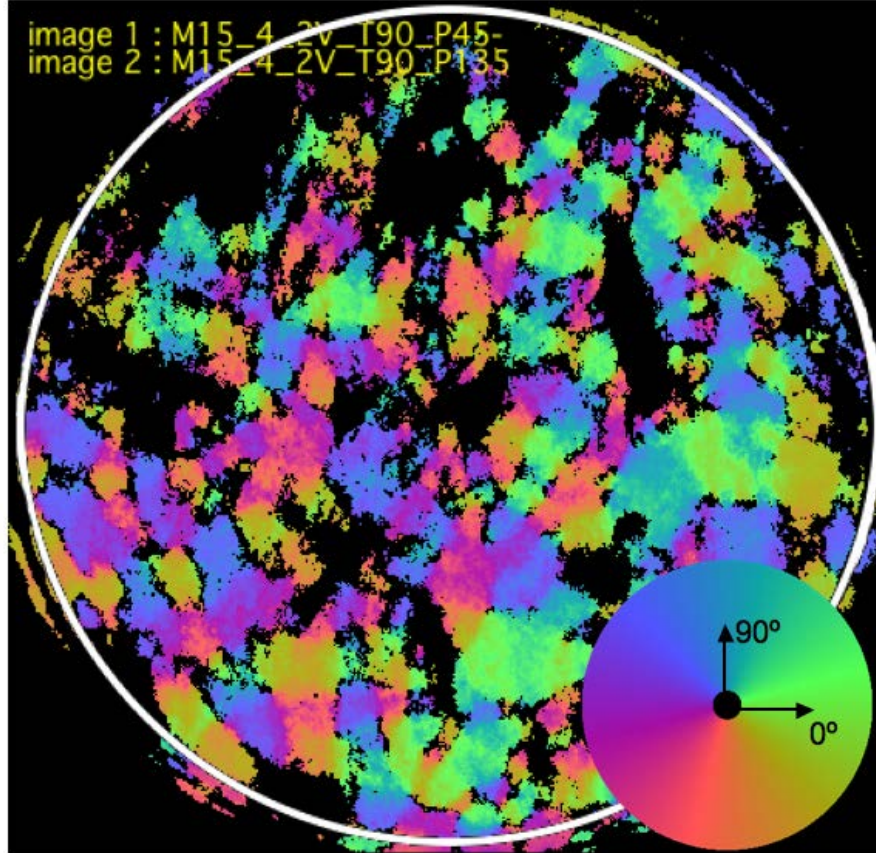


Figure 7.9: 2D-SPLEEM image in which the color indicates the spin direction in magnetic domains. The direction can be decoded with the mapping panel in the inset. This image was calculated with $r_{cutoff} = 0.015$ and the data range of both SPLEEM images is 0.2. The white circle shows the overlapping region of the SPLEEM image. Field of view: $8\mu\text{m}$.

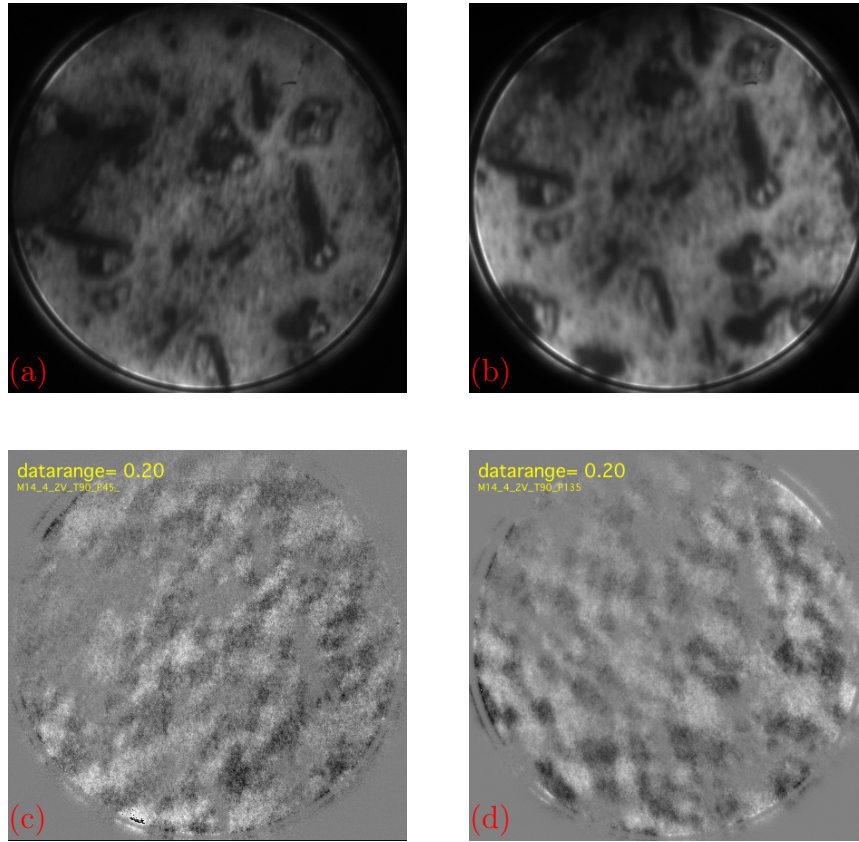


Figure 7.10: LEEM images with spin-up electron polarised in-plane at 45° (a) and 135° (b). (c) and (d) SPLEEM images calculated with (a), (b) and their spin-down counterparts. Field of view: $8\mu\text{m}$.

direction of the domains will be subsequently called 2D-SPLEEM images.

The LEEM images in figure 7.8 were taken with spin polarised at 45° and 135° . Between two sets of data, a drift was compensated. The sample was previously annealed at temperatures above the paramagnetic phase transition so the magnetic domains are randomly organised as discussed in section 3.1.2. Images in figure 7.8 present a shadow effect that degrades the quality of the 2D-SPLEEM images (figure 7.9). The magnetic signal found with the data range is about 15%. The grey scales were calculated with the same scaling number (data range) so two SPLEEM images are equivalent to generate the 2D-SPLEEM image.

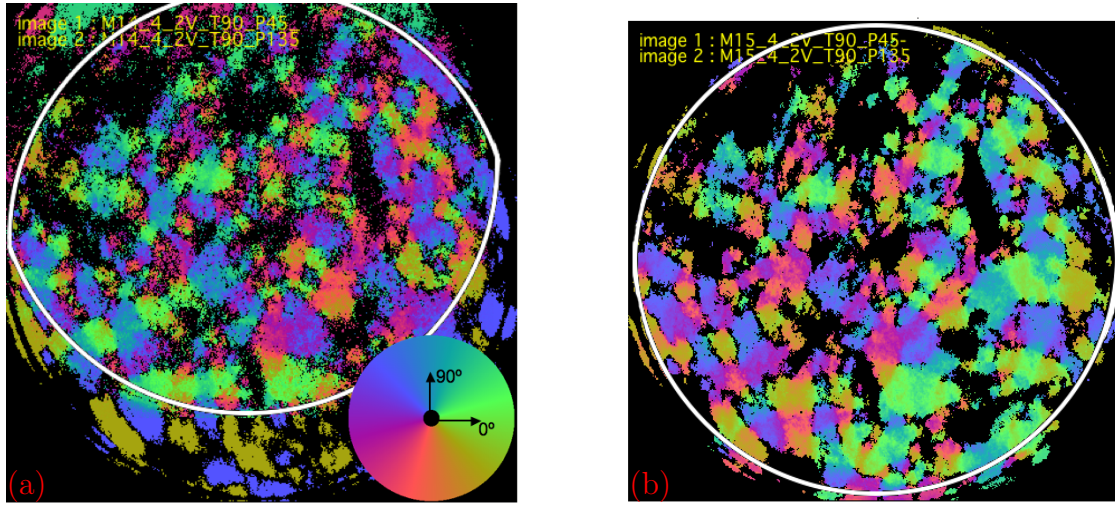


Figure 7.11: 2D-SPLEEM images calculated with SPLEEM beam polarised at 45° and 135° from two data sets from the same area. Both images were calculated with $r_{cutoff}=0.015$. The white circles show the overlapping of the SPLEEM images. Magnetic domain shapes are consistent unlike their magnetic directions due to a shadowing effect. Details given in text. Field of view: $8\mu\text{m}$.

Another set of data in the same area is shown in figure 7.10. The SPLEEM images have a shadow effect less pronounced but were acquired with a shorter integration time reducing the contrast of this set.

Again the 2D-SPLEEM image in figure 7.11 was calculated with the same scaling factor. The two images in figure 7.11 show the magnetic domains in the same area. The two images show the consistency of the analysis. The magnetic domains display same shapes and sizes (about 400 nanometers). The magnetic contrast is not homogeneous over the field of view due to a flickering of the beam polarisation. Due to an inhomogeneous illumination of the sample, I_1 or I_2 can be outweigh. This can be seen in figure 7.11.a which appears greenish on the left-hand side and reddish on the right. In the same way image 7.11.b presents inhomogeneities in the color distribution. This shadow effect is due to a normalisation by an average pixel intensity on a large area. To reduce this, we may want to normalise by a locally calculated average pixel. In these images it is possible to see closure domain relations. A good example is shown in figure 7.12 where the domains organise themselves to minimise the magnetostatic energy. Furthermore, when generating the final 2D-SPLEEM images we calculated the angles by simple superposition of two images without further correction. In other words, we assume that the beam has the same

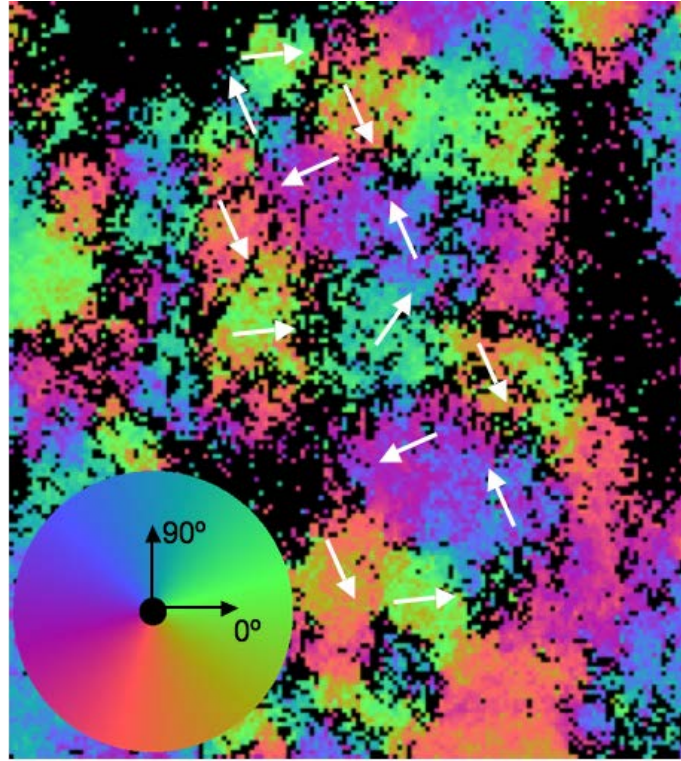


Figure 7.12: Zoomed image of figure 7.11.a showing closure domain relations of magnetic regions. Size of the image : $2.7 \times 3.4 \mu\text{m}$.

degree of polarisation for these image pairs. If this is not the case, it could induce a distortion in the angle distribution favouring one direction over the other.

7.5 Magnetisation changes across magnetic domain boundaries

The region in which the magnetism shifts from one direction to another is referred to as a Bloch or a Néel wall in a thin film (see section 3.1.2). The angles α and the magnetic signal r defined by the equations 7.8 and 7.9 are shown in figure 7.13 from a region in image 7.9. r drops when crossing a region between two domains which is the signature of a Bloch wall with helical rotation along the surface.

The magnetic direction change along the domains has a magnitude of 180° so it is a complete reversal. The width of the wall was estimated to be 104 nm on the magnetic signal graph. The resolution of the SPLEEM images used to calculate the 2D-SPLEEM image was measured to be 90 nm (figure 7.14) indicating that our analysis of the domain wall is limited by the instrumental resolution.

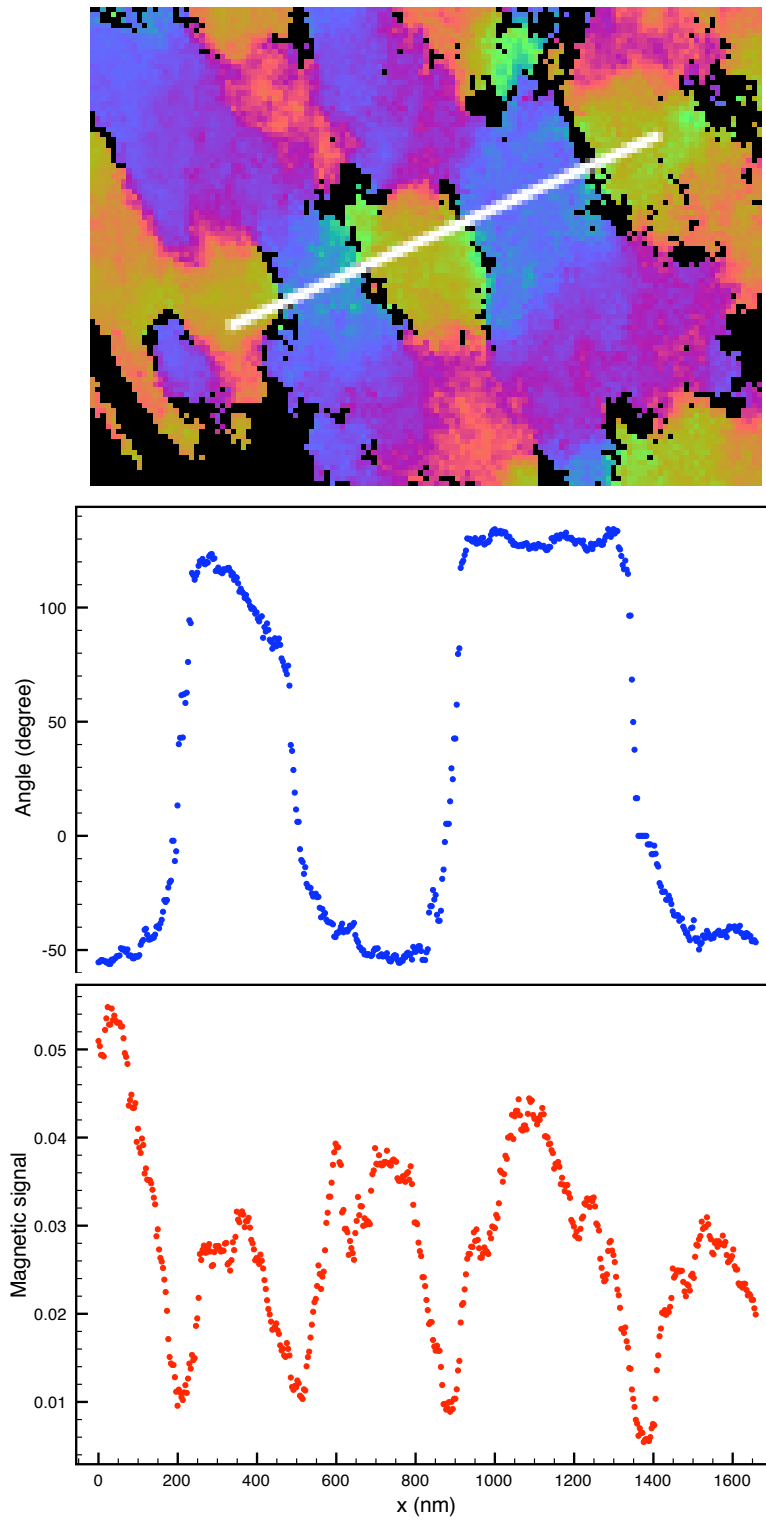


Figure 7.13: Line scan of the angle and the length r defined in equation 7.9 from figure 7.9. The decrease of the magnetic signal during magnetic rearranging is due to the helical rotation along the surface.

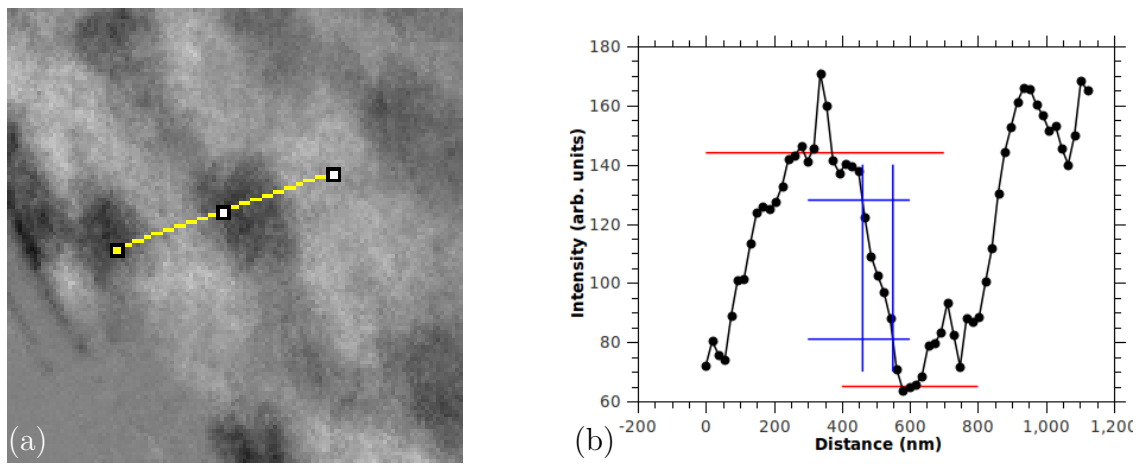


Figure 7.14: (a) Zoomed image of figure 7.10.d, (b) profile line scan along a magnetic domains showing high contrast. The resolution of the SPLEEM image was found to be approximately 90 nm using edge values of 20% and 80%.

7.6 Summary

The growth of ferromagnetic materials on a semiconductor substrate has potential applications for spintronic devices. The MnSb/GaAs(111)B system is a good candidate to be investigated since MnSb is a ferromagnetic with Curie temperature significantly above room temperature and a structure compatible with III-V(111) surfaces. In addition, MnSb has only one structural phase in the relevant temperature range for MBE.

Our most important result was the observation of magnetic contrast with the SPLEEM. With the experiments performed by SPLEEM on the MnSb/GaAs(111) sample we learned the influence of different parameters on the final quality of the SPLEEM image. Even if the morphology doesn't influence the magnetism, it is better to probe a smooth surface since the images acquired after heating show lower quality.

Our analysis procedure for SPLEEM magnetic contrast provided the measure of a physical parameter, the magnetic signal generated by the MnSb crystal under illumination of spin-polarised low energy electrons. This signal was found to be in the order of 20%. We generated images with a color scaling illustrating the domain structure. The magnetic domains observed are similar in shape and size but the process has to improve to take into account the inhomogeneity of the illuminating beam to provide more accurate values for the magnetic directions.

Other perspective work is the observation of the early magnetism of ultra thin films with in-plane/out-of-plane phase transition.

Chapter 8 : Etched Tungsten

Wires for Tomography

The development of transmission electron microscopes (TEM) has reached a point where it is now possible to obtain three dimensional atomic structures by zone-axis tomography (see section 4.9.1) to study defects and interfaces [208]. Recently, discrete tomography has been used to generate the full 3D exact atomic positions of silver nanoparticles of two to three nanometers in diameter. This method assumes prior knowledge of the particle's lattice structure and requires that the atoms fit rigidly onto that particular lattice [197]. To access more zone axes than with the "sample on grid" method, a well-established technique is the preparation by focused ion beam (FIB) of freestanding pillars 10-20 nm in diameter. However, in FIB the layers are damaged by the ion beam making discrete tomography impossible. To overcome this limit, efforts now concentrate on nano-milling (sputtering) but this technique unfortunately damages alloys due to the preferential removal of elements during sputtering. To our knowledge, no 3D reconstruction at atomic resolution has been reported using nanomilling.

In this chapter, we explore a new technique that uses an atomically flat terrace of an etched tungsten wire as the base for the sample. It is known from literature that single crystalline grains in tungsten wires have an infinite number of orientations with however the [110] direction preferentially aligned parallel to the wire axis [209]. W(110) is a close-packed surface widely used in surface science as a universal substrate. W(110) is thermally stable and the intermixing with an epilayer is almost non-existent. The average grain size can be enhanced by recrystallisation of the wire by annealing to high-temperature in vacuum. Annealing a wire after etching generates a terrace at the apex. Using a 3-5 nm (110) tungsten terrace as a base for tomography has potential benefits. We could use normal surface science technique such as sputtering and MBE to generate high quality tomography samples. After the sample preparation, one could look at the system *in-situ* without exposition to air with a high vacuum STEM (SuperSTEM, Daresbury) or, if sample preparation and measurement are done in two different systems, bismuth (Bi), sulphur (S) or arsenic (As) can be deposited on the tip as a protective layer. These elements can

be evaporated from the sample at moderate low temperature without perturbing the sample's structure.

When using the TEAM I microscope at the NCEM, this tomography technique requires mounting the tip on a puck. In order to fit in the TEM puck, the tip cannot be longer than 1 mm. Because of the low dimensions involved, we decided to perform the experiments with 0.25 mm tungsten wire for its mechanical stability. As they cannot be broken and cut by etching easily, we also performed experiments using 0.1 mm tungsten wire. If 0.25 mm W wires are used, they need to be recrystallised so they become brittle and easy to brake. Recrystallisation is achieved by resistive heating. This experiment also requires etching at well-defined positions. In this context, we developed a device to prepare tips in an automated and controlled way. This device and other designs to crystallise the wires or to heat and hold the tip for MBE deposition will be presented in the next section. This section is followed by preliminary results. These experiments were carried out at the National Center for Electron Microscopy at Berkeley as part of a collaboration with Dr Peter Ercius.

8.1 Introduction to the controlled etching device

We designed an etching device to control the etching process as shown in figure 8.1. A high-density polyethylene (HDPE) disk with 6 compartments was made at the workshop. Two are filled with potassium hydroxide (KOH) solution and the four others with distilled water. We chose HDPE because it has no or little reaction with KOH. We designed the disk with grooves so the compartments can be emptied by tipping the disk without mixing the compartments' contents. Initial cleaning and thinning of the tungsten wire are carried out in the first KOH compartment whereas final etching utilises a second one. Rinsing is achieved through the use of four water compartments, allowing to keep high purity water. A photo of the disk is shown in figure 8.2.

The tungsten wire is mounted on a tip holder above the disk. The tip stage is made of a non-conductive material to allow application of an etching voltage of 10 V. The KOH solution's top level is detected when the tip makes contact with the solution and is used as a reference position in the etching process.

To rotate the disk and approach the tip to the etching solution in a controllable way, the disk and tip-holder are activated circularly and linearly by two step motors

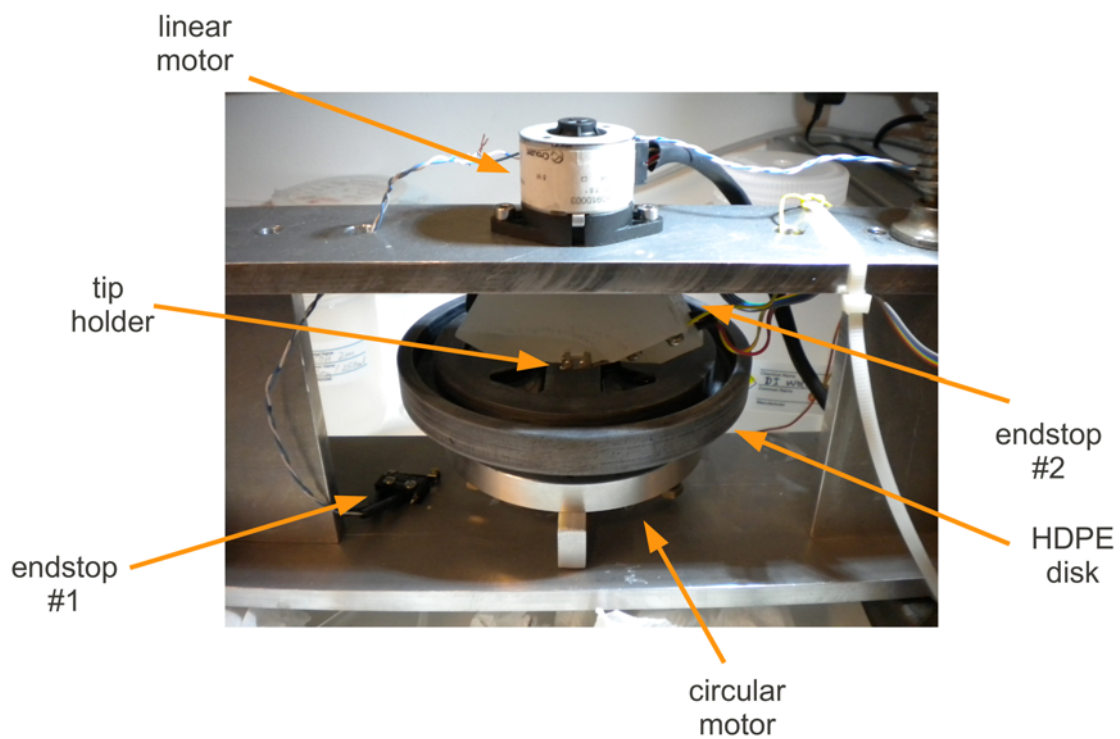


Figure 8.1: Wire-etching device. Details are given in the main text.



Figure 8.2: High-density polyethylene disk designed with 6 compartments, 2 for etching and 4 for rinsing. This picture depicts the etching compartments, the groove for pouring out liquids, and the etching counter electrodes (immersed tungsten loops).

(figure 8.1). To reset the position of the disk and the tip-holder we integrated two end-stop switches on the device (figure 8.1). After cut-etching of the wire, the etching current is stopped abruptly by an electronic circuit. The two motor drivers are controlled by a Labview program via a NI USB-6008 data acquisition card.

In order to recrystallise tungsten wires in a reproducible way, we used the custom-made flange-mounted device shown in figure 8.3. The device is made of copper for good heat conduction. The wire is clamped between two pieces of copper in a groove and the wire is annealed by resistive heating. The length over which the wire is annealed is kept at 2 cm during experiments since optimum time and current parameters were optimised empirically. We typically use 10 A for an annealing time of 4 minutes.

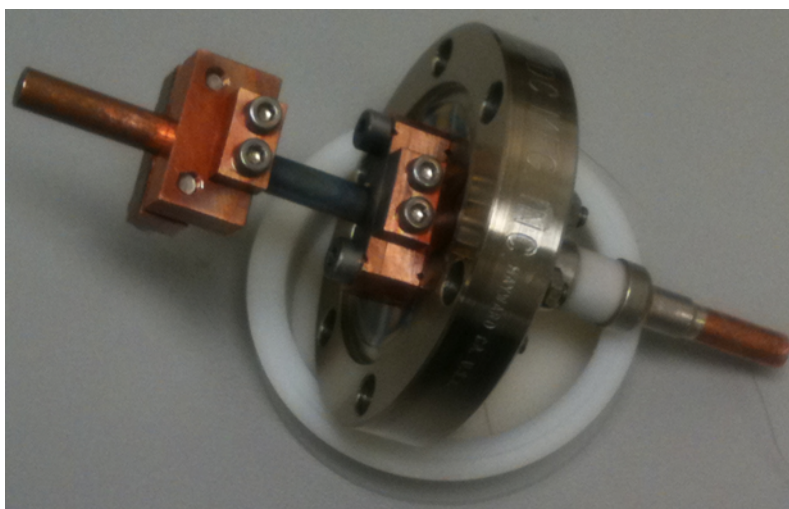


Figure 8.3: Device for annealing wire in UHV allowing tungsten for wire recrystallisation.

After etching the required tip, we want to deposit gold on the terrace in order to obtain nanoclusters. For this, we designed the device shown in figure 8.4. To hold the tip firmly, we used tungsten wires to apply a mechanical pressure on the tip. A zoom-in of figure 8.4 is shown in figure 8.5 with the tungsten wire highlighted with red and yellow lines. The tip is clamped pointing upward between the long wire and the two smalls. These same wires also allow for annealing during MBE deposition by resistive heating.



Figure 8.4: Device to clamp and anneal tips for MBE deposition.

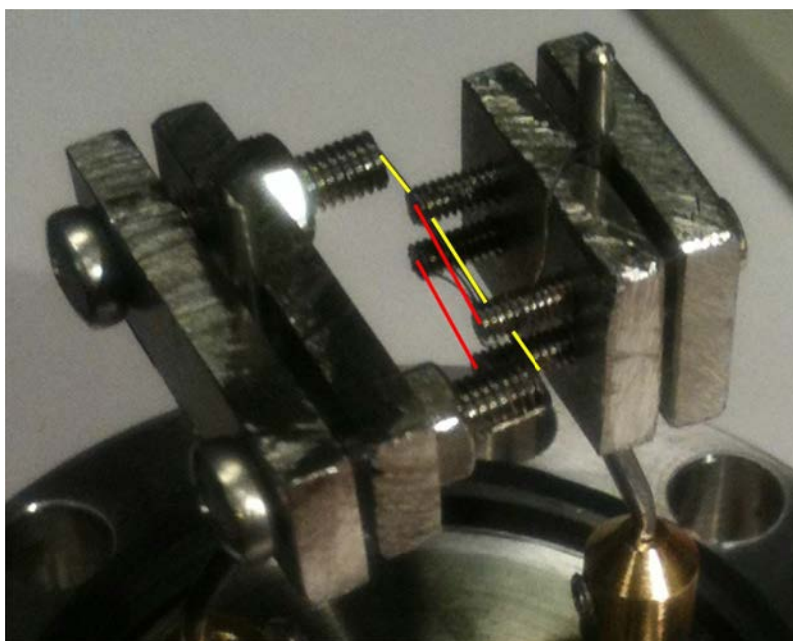


Figure 8.5: The tip is clamped by a mechanical pressure applied by three tungsten wires highlighted for illustrative purpose.

8.2 Results

As mentioned previously, recrystallised tungsten wire has the double advantage of rendering the wire brittle for easier cutting and aligning the crystal structure along the $\langle 110 \rangle$ direction. The macroscopic tip shape and grain size after *in-situ* annealing of a tip has been observed with UHV-SEM as shown in figure 8.6. The characteristic length scale of the grain is $1.5 \mu\text{m}$.

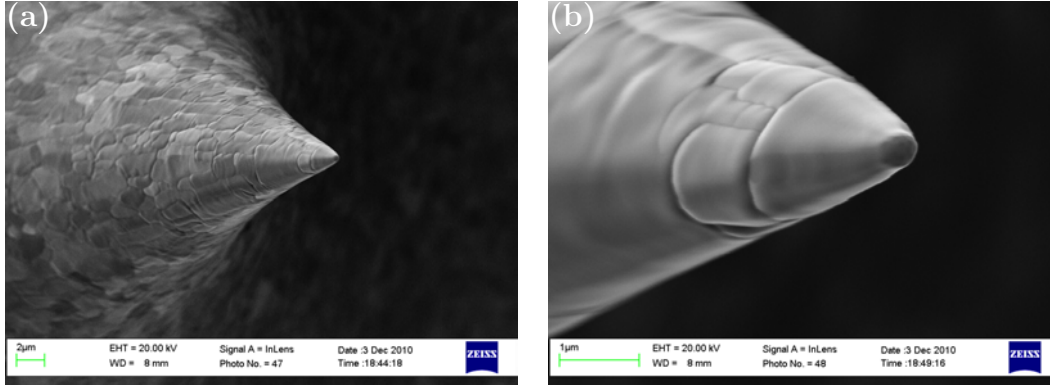


Figure 8.6: Grain structure of a post-etch annealed wire revealed by UHV-SEM. Electron energy 20 keV, scale bars $2 \mu\text{m}$ (a) and $1 \mu\text{m}$ (b).

Figure 8.7 displays SEM images of a recrystallised tungsten wire revealing facets and a flat-topped terrace at the apex of the tip. Bismuth melts at low temperature and has a high surface energy so it forms islands when deposited on metals. Furthermore Bi doesn't alloy with tungsten and can be removed fully by evaporation at a relatively low temperature. Bi has been evaporated on the tip as a feasibility experiment. After deposition, the tip was annealed to promote cluster growth (figure 8.7.d). On this image one can see bismuth on one side as the evaporation has been done sideways. The clusters typically have a diameter of 50 nm and the terrace at the apex has a diameter of 200 nm, which is much too large for an electron tomography application.

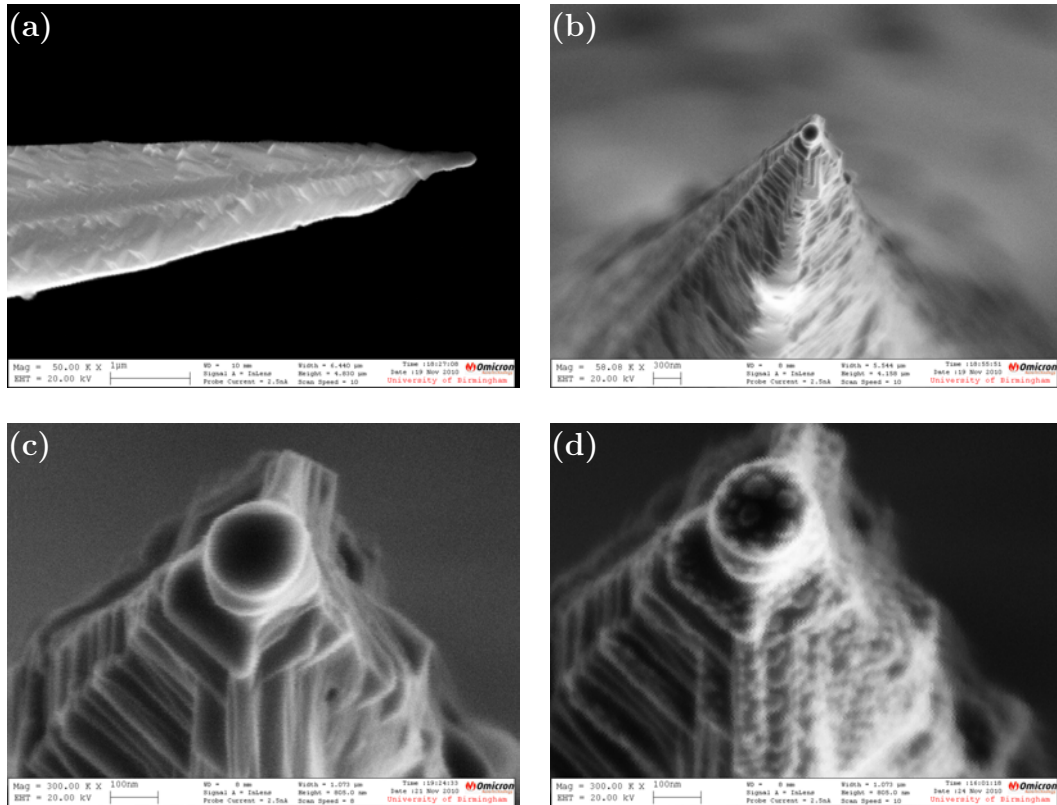


Figure 8.7: Recrystallised tungsten wire showing a flat terrace at the apex. (d) Bi evaporated on clean tungsten tip and annealed to form clusters imaged with UHV-SEM. 20 keV, scale bars 1 μ m (a), 300 nm (b), 100 nm (c), and 100 nm (d).

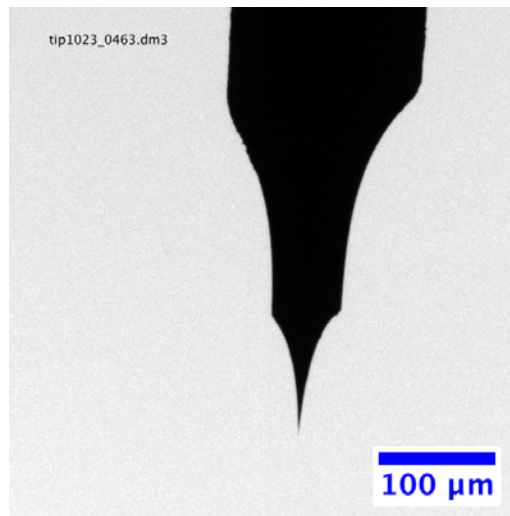


Figure 8.8: Tip etching at controlled height with the automated tip etching device.

The device discussed in section 8.1 allows for the control of the tip etching. Figure 8.8 shows a 0.25 mm wire after controlled etching. The wire was thinned for easier wire breaking. The tip was then pulled-up and final etching was carried out on the thinned section of the wire.

The tips we obtained from the etching device were often surrounded by a layer as shown in figure 8.9.a. Figure 8.9.b is a high magnification of the same tip showing the polycrystalline nature of the layer. EDS measurements performed at the NCEM did not show any evidence of contamination. Instead, the measurement pointed toward a potassium tungsten bronze layer K_xWO_3 with x equal to or less than 1 [210,211]. We tried to remove this layer through plasma etching and post-etching dipping into KOH solution, yet without success. However, we found that a rapid etching drastically limits the contamination. Fast etching was carried out with an on/off etching current with a duty ratio of 50% and a cycle time of 3 seconds. A tip etched using this method can be seen in figure 8.10. The apex is fully crystallised with a radius of 2.5 nm. K_xWO_3 layer can be seen in the upper part of the figure but there is not a discernible oxide layer at the apex. Nevertheless, most of the tips made this way were quite blunt with a tip radius ranging between 100 and 150 nm.

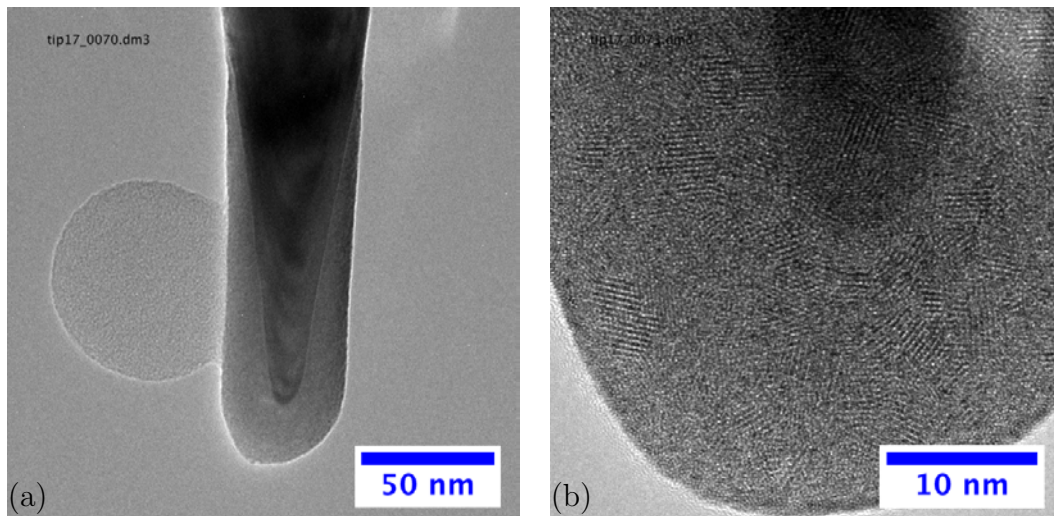


Figure 8.9: 0.25 mm recrystallised tungsten wire showing large contamination after etching procedure. The tip is also very blunt. Bluntness and contamination have been largely observed with a standard etching procedure.

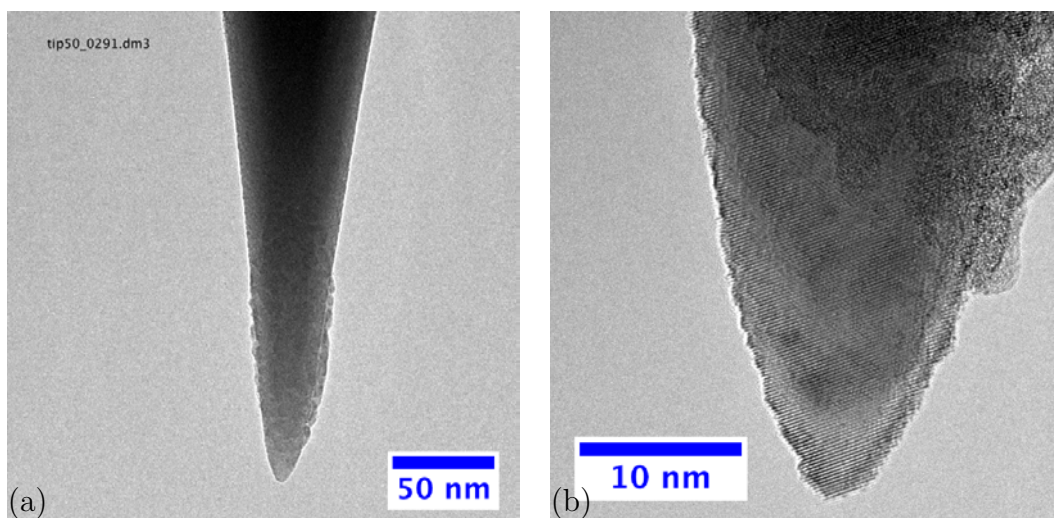


Figure 8.10: 0.25 mm recrystallised tungsten wire with no contamination. Etching procedure were carried out with a 3 seconds duty cycle current.

We also routinely made sharp tips using non-recrystallised 0.1 mm tungsten wire. Tips made from 0.1 mm tungsten wires were used to reduce the etching time. Figure 8.11 shows two successful tips etched using 0.1 mm wire. The radius of curvature for these tips is 1 nm.

We deposited gold on a tip made of 0.25 mm tungsten wire recrystallised in high vacuum (HV) environment and etched in a continuous mode (no 3 seconds etching cycles, no post-dipping). TEM measurements on this system can be seen in figure 8.12. Bronze contamination can be seen at the side of the tip in figure 8.12 in the top-left panel. Magnified images allow us to consider the size distribution of the Au-clusters grown on the excessive material. Most Au-clusters have a size smaller than 10 nm. In panels (c) and (d) in figure 8.12, one can see an individual cluster at the apex of the tip, thus demonstrating that we are able to achieve this ideal sample geometry for STEM tomography.

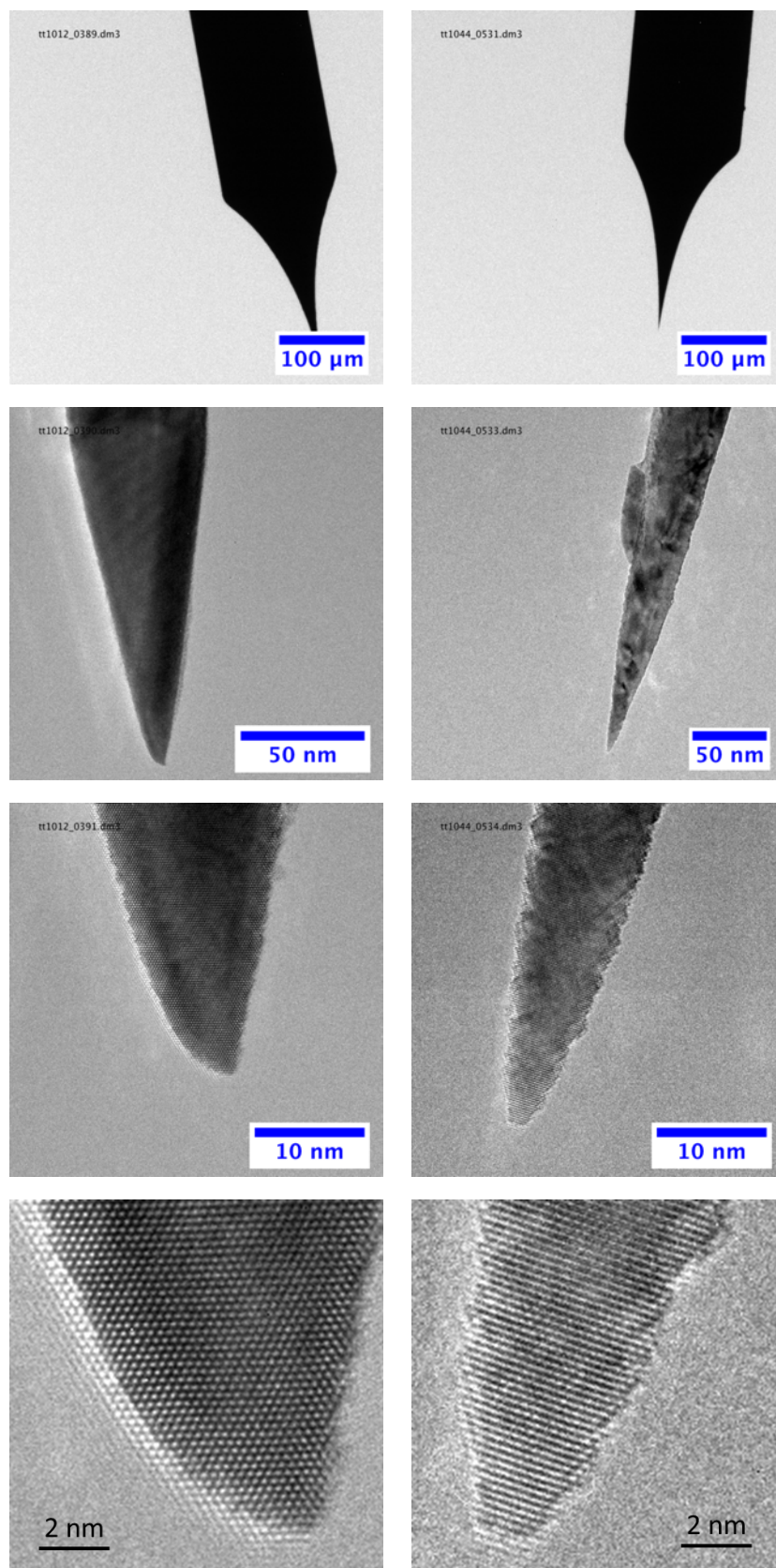


Figure 8.11: Two tips, left and right respectively, obtained with 3 seconds duty cycle etching using 0.1 mm non-recrystallised wire.

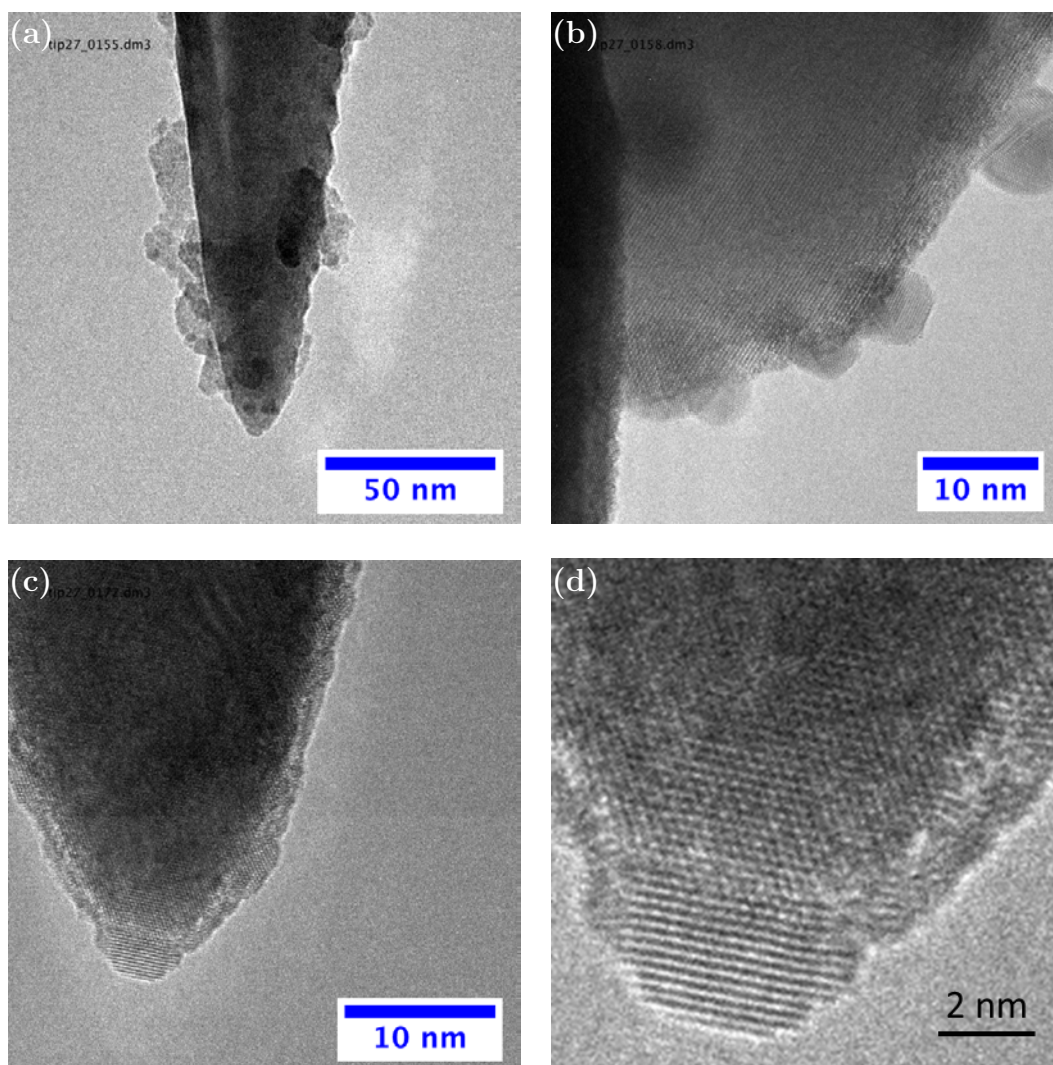


Figure 8.12: This tip is etched from 0.25 mm recrystallised tungsten wire. Gold was deposited on the annealed tip. Panel (a) shows the tip after deposition and additional annealing to promote cluster growth. Panel (b) is a magnified image of gold clusters deposited on top of bronze contamination. Panel (c) shows a 5 nm single gold cluster at the apex of the tip and panel (d) is a zoom-in image of the figure in panel (c).

Summary

In this chapter, we introduced a new technique that uses tungsten tips as a tomography sample platform. We presented the equipment and methodology developed for this purpose. Several devices were designed to etch the wire in a controllable way, to recrystallise the wire, and to clamp the tip for MBE deposition. The methodology was mainly focused on getting atomically sharp tips and avoiding tungsten bronze layers. We obtained sharp and clean tips by quick cut etching procedure. Fast etching process can be done by etching in an on/off mode or by using 0.1 mm wires. The etching device has allowed for good macroscopic control of the tip shape. We achieved tips with radius of curvature in the nanometre scale. We deposited gold cluster at the apex of an atomically sharp tip.

However, we found no benefit in having the possibility to move between reservoirs or rinsing the tip quickly. The containers turned out to be very small and needed frequent refilling. Furthermore, this device requires the use of plastic instead of glass to hold the etching solution.

With these experiments carried out at the NCEM, we gained insight allowing us to improve the etching device and the methodology. A new design for the etching device involves two beakers and a loop for etching. The loop allows cutting at any given position and control position is operated by a longer range step motor.

Conclusion and Perspectives

This thesis focused on projects related to thin film and surface science. We presented studies of the surface morphology of MnSb thin films and *d*-AlNiCo at different surface orientations conducted with LEEM and SEM, respectively. These experiments were performed in a UHV environment allowing the *in-situ* study of annealing effects and cleaning procedures. The topography and stoichiometry of AlNiCo have been analysed with AFM and EDS. This thesis also reported experimental results of the epitaxial growth of AlNi thin films on 2-fold *d*-AlNiCo. The obtained thin films were characterised chemically and structurally by XPS and SPA-LEED, respectively. This thesis comprises as well experiments on a project that uses etched tip as a base for electron tomography samples. This part focused on technical aspects such as the different designs involved to make atomically flat-topped tips in a reproducible way. Metal deposition and following annealing was employed to demonstrate the feasibility of growing metallic clusters on these tips.

Impact of annealing on the morphology of various *d*-AlNiCo surfaces

Quasicrystals have intrinsic interesting properties such as low friction and good corrosion resistance. They are also interesting for potential technological applications for example in coating materials, or in catalysis [9, 48]. Both of these applications are surface related showing that quasicrystal surfaces are significant for technological applications. With UHV-SEM we have analysed the impact of annealing on the surface morphology of *d*-AlNiCo samples with (10000), (00001), and (10 $\bar{2}$ 24) surface orientations. *d*-Al_{72.2}Ni_{19.2}Co_{8.6} has a phase transition at approximately 700°C. We observed different surface rearrangements for the different orientations upon cooling from the phase transition point. In the 2-fold sample, the rearrangement materialises with the appearance of nearly perfect 300 nm deep elongated rectangle-shaped features. In SEM images, these features appear darker than the surrounding surface areas. However their composition is rich in heavy elements which should translate into a stronger SEM signal. Ruling out any geometric screening, the lower

signal may originate from a different workfunction of these features. According to EDS measurements, the chemical composition of these so-called dark features still lies in the quasicrystalline phase field. Cooling the quasicrystal from the phase transition point, an SEM experiment shows the growth of the features. They eventually coalesce to yield polygon-shaped features. A quantitative analysis of the feature sizes from SEM frames taken at different times in the cooling sequence showed that none of the individual features shrank, thus ruling out an Ostwald ripening process.

An annealing-experiment on an area presenting sputtered and non-sputtered areas showed two distinct surface morphology behaviours. On the sputtered area, and after annealing the quasicrystal to the phase transition, we observed features that we have associated to the dark features on the 2-fold surface. On the other hand, on the same sample but on a non-sputtered area, we observed nano-pillar growth. This experiment showed the importance of the surface preparation in quasicrystals. The nano-pillars grow in the 10-fold direction, i.e. tilted by 35° . These particular surface features have their origin in the dynamic growth rate of decagonal quasicrystals which is favourable in the 10-fold direction. We didn't observe any phase transition related surface rearrangement in the 10-fold surface, demonstrating its enhanced stability.

We observed islands on the 2-fold surface. When annealed above 700°C , they grow and facet. This observation is remarkable as we expect metallic islands to adopt rounder shapes at higher temperatures to lower their surface free energy. This process is reversible. When cooled, the islands lose their facets and shrink. In the high temperature phase, the faceting of some islands has been identified as having a 5-fold symmetry. The quasicrystalline nature of the islands is supported by EDS experiments that confirm that the islands' stoichiometry lies in the quasicrystalline phase field.

AlNi thin film growth on $\text{Al}_{72.2}\text{Ni}_{19.2}\text{Co}_{8.6}$ (10000)

Using a quasicrystal as a growth template provides an avenue to force a thin film to adopt a quasiperiodic structure even if this structure is not stable in the bulk. Such a structure could be usefully for the understanding of quasiperiodicity and its associated physical properties. Single elements don't form quasicrystalline thin films beyond one monolayer [117].

In this thesis we reported the successful growth of a binary quasicrystal alloy thin film with a thickness larger than 14 Å. The intended stoichiometry is the one for which the Ni concentration replaces both the Co and Ni in the bulk quasicrystal, that is to say $\text{Al}_{72}\text{Ni}_{28}$. The films were grown at a substrate temperature held at $370 \pm 20^\circ\text{C}$. The films' compositions were inferred in the limit of the homogeneous layer model. The thin films were grown with an Ni atomic concentration ranging from 34 to 46%. In the Ni-poor regime, that is to say 34%, we observed a flawless quasicrystalline structure.

At 40% Ni concentration, the AlNi thin film adopts the crystalline Al_3Ni_2 structure matching the 2-fold substrate structure epitaxially with a 8×1 superstructure. With further deposition, the film was restored into a quasicrystalline structure. The diffraction pattern of the periodic Al_3Ni_2 thin film were analysed in detail. Spot widths of thin film (periodic) and substrate (quasiperiodic) related peaks were analysed in both the periodic ([00001]) and quasiperiodic direction ([10000]). In the periodic direction the thin film exhibits a structural quality as good as in the quasicrystal substrate (1-to-1 epitaxial relation). In contrast, the thin film's structure is degraded along the quasicrystal direction as indicated by a coherence length two times smaller.

In the Ni-rich regime (46% atomic concentration) we still observed the signature of a quasicrystalline structure in the LEED pattern. However, we also observed crystallographic related spots. Due to interdiffusion of Al into the film at our chosen growth temperature, it was not possible to achieve a Ni atomic concentration in the film richer than 46%.

It would be interesting to know how thick a film can be grown keeping a quasicrystalline structure. The films we discussed in this thesis were thick enough to determine the film stoichiometry with XPS. Using synchrotron radiation, one can determine a thin film's electronic band structure. An AlCu quasicrystal thin film would allow measurements of *s-p* derived states close to E_F since Cu has its *d*-band significantly removed from the Fermi energy. Finally, growing films at lower temperature would allow the study of a wider range of thin film stoichiometry and increase our understanding of AlNi thin film growth modes.

MnSb thin film on GaAs(111)B

The growth of ferromagnetic materials on a semiconductor substrate has potential applications for spintronic devices such as the injection of a spin-polarised current into non-magnetic materials. The MnSb/GaAs(111)B system is a good candidate to be investigated since MnSb is a ferromagnet with Curie temperature significantly above room temperature and a structure compatible with III-V(111) semiconductor surfaces. Furthermore, recent theoretical calculations have shown that MnSb in the wurtzite structure would display half-metallicity.

With LEEM, we observed annealing related surface morphology changes with a film degradation at approximately 400°C as observed previously [136]. With spin-polarised low energy electrons as a probe, we obtained magnetic information of the film surface. We found no influence of the surface morphology on the magnetism. Our analysis procedure for SPLEEM magnetic contrast provided a measurement of the magnetic signal strength. This signal was found to be in the order of 20%. We generated color-coded images to determine the spin orientation in the magnetic domains. Comparing two color-coded images from two data sets, we obtained consistent results in terms of magnetic domain shapes and sizes. The process can be improved to take into account the instability of the illuminating beam in order to obtain more detailed analysis. Using the magnetic signal we were able to establish an upper bound for the domain wall width of 90 nm which is the resolution of the experiment.

An interesting follow-up on this project could be the observation of the early magnetism of ultra thin MnSb films to observe the in-plane/out-of-plane phase transition.

Etched tungsten wires for tomography

In this thesis we discussed the development of a method that uses recrystallised tungsten wires as a base for tomography samples for 3D atomic reconstruction. This new technique will allow the use of surface science techniques such as MBE or sputtering. This project requires the preparation of tips with flat-topped apex at the nanometre scale. With this aim, we developed a device to etch the tip at controlled positions (thinning) and in different etching modes (on/off current). Etched tips often showed large contamination whose origin has been established as tungsten

bronze. Contamination issues were limited by a fast etching using either thinner wire or by etching employing an on/off current mode.

Using a combination of devices to crystallise the tungsten wires, etch the tips, and anneal these latter for MBE deposition, we successfully demonstrated the feasibility to grow metallic clusters on these tips for atomic resolution tomography.

Bibliography

- [1] D. Shechtman, I. Blech, D. Gratias, and J.W. Cahn. Metallic phase with long-range orientational order and no translationnal symmetry. *Phys. Rev. Lett.*, 53(20):1951, Nov 1984.
- [2] D. Levine and P.J. Steinhardt. Quasicrystals: A new class of ordered structures. *Phys. Rev. Lett.*, 53(26):2477–2480, Dec 1984.
- [3] M. Senechal. *Introduction to the mathematics of quasicrystals*. Harcourt Brace Jovanovitch, 1989.
- [4] W. Steurer and S. Deloudi. *Crystallography of Quasicrystals*. Springer Series in Materials Science, 2009.
- [5] M. Senechal. *Quasicrystals and geometry*. Cambridge university press, 1995.
- [6] C. Janot. *Quasicrystals: a primer 2nd ed*. Oxford University Press Inc., New York, 1994.
- [7] J.-B. Suck, M. Schreiber, and P. Häussler, editors. *Quasicrystals: An introduction to structure, physical properties and applications*. Springer-Verlag Heidelberg, 2002.
- [8] Z.M. Stadnik, editor. *Physical properties of Quasicrystals*. New York: Springer, 1999.
- [9] R. McGrath, J. LeDieu, E.J. Cox, and R. Diehl. Quasicrystal surfaces: structure and potential as templates. *J. Phys.: Condens. Matter*, 14:119–144, 2002.
- [10] B. Grünbaum and G.C. Shephard. *Tilings and Patterns*. San Francisco: Freeman, 1987.
- [11] R. Penrose. Role of aesthetics in pure and applied research. *Bulletin of the Institute of Mathematics and its Applications*, 1974.
- [12] N.G. de Bruijn. Algebraic theory of penrose’s non-periodic tiling of the plane. *Ned. Akadem. Wetensch. Proc. Ser. A*, 84:38–66, 1981.
- [13] B. Grünbaum and G.C. Shephard, editors. *Tilings and Patterns*. Freeman & Co, New York, 1985.
- [14] K. Chattopadhyay, S. Lele, S. Ranganathan, G.N. Subbanna, and N. Thangaraj. Electron microscopy of quasicrystals and related structures. *Current science*, 54(18):895–903, 1985.
- [15] L.A. Bendersky. Quasicrystal with one-dimensional translational symmetry and a tenfold rotation axis. *Phys. Rev. Lett.*, 55(14):1461–1463, 1985.
- [16] N. Wang, H. Chen, and K. H. Kuo. Two-dimensional quasicrystal with eightfold rotational symmetry. *Phys. Rev. Lett.*, 59(9):1010–1013, Aug 1987.
- [17] T. Ishimasa, H.-U. Nissen, and Y. Fukano. New ordered state between crystalline and amorphous in Ni – Cr particles. *Phys. Rev. Lett.*, 55(5):511–513, Jul 1985.
- [18] P.A. Bancel. Phason-induced transformations of icosahedral AlCuFe. *Philos. Mag. Letter*, 67(1):43–49, Jan 1993.

- [19] P. Donnadieu. The deviations of the $\text{Al}_6\text{Li}_3\text{Cu}$ quasicrystal from icosahedral symmetry - a reminiscence of a cubic-crystal. *Journal de physique I*, 4(5):791–799, May 1994.
- [20] H. Selke, U. Vogg, and R.L. Ryder. New quasiperiodic phase in $\text{Al}_{85}\text{Cr}_{15}$. *Phys. Stat. Sol. (a)*, 141(1):31–41, Jan 16 1994.
- [21] L.X. He, X.Z. Li, Z. Zhang, and K.H. Kuo. One-dimensional quasicrystal in rapidly solidified alloys. *Phys. Rev. Lett.*, 61(9):1116–1118, Aug 1988.
- [22] P.A. Thiel. *Physical properties of Quasicrystals*. New York: Springer, 1999.
- [23] N. Wang, H. Chen, and K.H. Kuo. Two-dimensional quasicrystal with eightfold rotational symmetry. *Phys. Rev. Lett.*, 59:1010–1013, Aug 1987.
- [24] Y. Yoshida and Y. Taniguchi. Disordered twin boundary regions in long-period tetragonal BiMn films. *Phil. Mag. Lett.*, 63(3):127–132, Mar 1991.
- [25] V. Elser and C.L. Henley. Crystal and quasicrystal structures in Al-Mn-Si alloys. *Phys. Rev. Lett.*, 55:2883–2886, Dec 1985.
- [26] A.P. Tsai, A. Inoue, and T. Masumoto. Preparation of a new Al-Cu-Fe quasicrystal with large grain sizes by rapid solidification. *J. Mater. Sci. Lett.*, 6(12):1403–1405, DEC 1987.
- [27] A.P. Tsai, A. Inoue, and T. Masumoto. Stable decagonal Al-Co-Ni and Al-Co-Cu quasicrystals. *Mater. Trans. JIM*, 30:463, 1989.
- [28] U. Lemmerz, B. Grushko, C. Freiburg, and M. Jansen. Study of decagonal quasicrystalline phase formation in the Al-Ni-Fe alloy system. *Philos. Mag. Letter*, 69(3):141–146, Mar 1994.
- [29] W. Sun and K. Hiraga. Formation and structures of decagonal quasicrystals in the Al-Ni-Ru . *Mater. Sci. Eng. A*, 294(SI):147–151, DEC 15 2000. 7th International Conference on Quasicrystals (ICQ7), Univ Stuttgart, Stuttgart, Germany, sep 20-24, 1999.
- [30] S. Ritsch, C. Beeli, H.-U. Nissen, T. Gödecke, M. Scheffer, and R. Lück. Highly perfect decagonal Al-Co-Ni quasicrystals. *Philos. Mag. Letter*, 74(2):99–106, Aug 1996.
- [31] P.A. Bancel and P.A. Heiney. Icosahedral aluminum–transition-metal alloys. *Phys. Rev. B*, 33(12):7917–7922, Jun 1986.
- [32] J. Friedel and F.C. Dénoyer. The quasi-crystal AlLiCu , a hume-rothery alloy. *Comptes rendus de l'académie des sciences serie II*, 305(3):171–174, Jun 21 1987.
- [33] T. Fujiwara. Electronic structure in the Al-Mn alloy crystalline analog of quasicrystals. *Phys. Rev. BB*, 40(2):942–946, Jul 1989.
- [34] F. S. Pierce, Q. Guo, and S.J. Poon. Enhanced insulatorlike electron transport behavior of thermally tuned quasicrystalline states of Al-Pd-Re alloys. *Phys. Rev. Lett.*, 73:2220–2223, Oct 1994.
- [35] T. Klein, C. Berger, D. Mayou, and F. Cyrot-Lackmann. Proximity of a metal-insulator transition in icosahedral phases of high structural quality. *Phys. Rev. Lett.*, 66:2907–2910, Jun 1991.

- [36] S. Takeuchi. Physical properties of quasicrystals - an experimental review. In Kuo, KH and Takeuchi, S, editor, *Quasicrystals and imperfectly ordered crystals*, volume 150 of *Mater. Sci. Forum*, pages 35–51, 1994.
- [37] A.P. Tsai, A. Inoue, and T. Masumoto. Chemical order in an AlPdMn icosahedral quasicrystal. *Philos. Mag. Letter*, 62(2):95–100, Aug 1990.
- [38] H. Akiyama, Y. Honda, T. Hashimoto, K. Edagawa, and S. Takeuchi. Toward insulating quasicrystalline alloy in AlPdRe icosahedral phase. *Jpn. J. Appl. Phys.*, 32(7b):L1003–L1004, 1993.
- [39] Y. Honda, K. Edagawa, A. Yoshioka, T. Hashimoto, and S. Takeuchi. AlPdRe icosahedral quasicrystals and their low electrical conductivities. *Jpn. J. Appl. Phys.*, 33(9A):4929–4935, 1994.
- [40] F.S. Pierce, S.J. Poon, and Q. Guo. Electron localization in metallic quasicrystals. *Science*, 261(5122):737–739, Aug 6 1993.
- [41] M. Zurkirch, A. Atrei, M. Hochstrasser, M. Erbudak, and A.R. Kortan. XPS and EELS study of a quasicrystalline Al₇₀Pd₂₀Mn₁₀. *Journal of electron spectroscopy and related phenomena*, 77(3):233–240, APR 30 1996.
- [42] E. Belin-Ferré, Z. Dankhazi, V. Fournée, A. Sadoc, C. Berger, H. Müller, and H. Kirchmayr. Electronic distributions and pseudo-gap in quasicrystalline decagonal Al₆₅Cu₁₅Co₂₀ and Al₇₀Co₁₅Ni₁₅ alloys. *J. Phys.: Condens. Matter*, 8(34):6213–6228, Aug 19 1996.
- [43] G. Trambly de Laissardière, D. Nguyen-Manh, and D. Mayou. Electronic structure of complex hume-rothery phases and quasicrystals in transition metal aluminides. *Progress in Materials Science*, 50(6):679–788, Aug 2005.
- [44] D. Gratias, Y. Calvayrac, J. Devaud-Rzepski, F. Faudot, M. Harmelin, A. Quivy, and P.A. Bancel. The phase-diagram and structures of the ternary AlCuFe system in the vicinity of the icosahedral region. *Journal of non-crystalline solids*, 153:482–488, Feb 1993.
- [45] L.X. He, Y.K. Wu, and K.H. Kuo. Decagonal quasicrystals with different periodicities along the tenfold axis in rapidly solidified Al₆₅Cu₂₀M₁₅ (m=Fe, Co, or Ni). *J. Mater. Sci. Lett.*, 7(12):1284–1286, Dec 1988.
- [46] T.J. Sato, T. Hirano, and A.P. Tsai. Single-crystal growth of the decagonal Al-Ni-Co quasicrystal. *J. Cryst. Growth.*, 191(3):545–552, Jul 1998.
- [47] K.J. Franke. *Quasicrystal surfaces: morphology, phase transitions, and epitaxy*. PhD thesis, Freie Universität Berlin, 2004.
- [48] H.R. Sharma, M. Shimoda, and A.P. Tsai. Quasicrystal surfaces: structure and growth of atomic layers. *Advances in Physics*, 56(3):403–464, 2007.
- [49] T. Shibuya, T. Hashimoto, and S. Takeuchi. Anisotropic conductivity in a decagonal quasicrystal Al₇₀Ni₁₅Co₁₅. *J. Phys. Soc. Jpn*, 59(6):1917–1920, Jun 1990.
- [50] W. Yun-Ping, Z.G. Dian-Lin, and L.F. Chen. Universality of the hall-effect anisotropy in decagonal quasicrystals. *Phys. Rev. B*, 48:10542–10545, Oct 1993.

- [51] L. Shu-yuan, W. Xue-mei, L. Li, and Z. Dian-lin. Anisotropic transport properties of a stable two-dimensional quasicrystal: $\text{Al}_{62}\text{Si}_3\text{Cu}_{20}\text{Co}_{15}$. *Phys. Rev. B*, 41:9625–9627, May 1990.
- [52] Z. Dian-lin, C. Shao-chun, W. Yun-ping, L. Li, and W. Xue-mei. Anisotropic thermal conductivity of the 2D single quasicrystals: $\text{Al}_{65}\text{Ni}_{20}\text{Co}_{15}$ and $\text{Al}_{62}\text{Si}_3\text{Cu}_{20}\text{Co}_{15}$. *Phys. Rev. Lett.*, 66:2778–2781, May 1991.
- [53] D.N. Basov, T. Timusk, F. Barakat, J. Greedan, and B. Grushko. Anisotropic optical conductivity of decagonal quasicrystals. *Phys. Rev. Lett.*, 72(12):1937–1940, Mar 21 1994.
- [54] J.Y. Park, D.F. Ogletree, M. Salmeron, R.A. Ribeiro, P.C. Canfield, C.J. Jenks, and P.A. Thiel. High frictional anisotropy of periodic and aperiodic directions on a quasicrystal surface. *Science*, 309(5739):1354–1356, Aug 26 2005.
- [55] P. Gille, G. Meisterernst, and N. Faber. Inclined net plane faceting observed at Czochralski growth of decagonal AlCoNi quasicrystals. *Journal of crystal growth*, 275(1-2):224–231, Feb 15 2005. 12th International Summer School of Crystal Growth held in Conjunction with the 14th International Conference on Crystal Growth, Grenoble, France, Aug 09-13, 2004.
- [56] W. Steurer and A. Cervellino. Quasiperiodicity in decagonal phases forced by inclined net planes? *Acta crystallographica section A*, 57(Part 3):333–340, May 2001.
- [57] G. Meisterernst, B. Bauer, and P. Gille. AlCoNi quasicrystal sphere growth experiment from a metallic solution. *Zeitschrift fur kristallographie*, 224(10):471–477, 2009.
- [58] J. Dieter and E. Veit. A model of quasicrystal growth. *Phys. Rev. Lett.*, 79:1066–1069, Aug 1997.
- [59] P. Gille, P. Dreier, M. Graeber, and T. Scholpp. Large single-grain AlCoNi quasicrystals grown by the czochralski method. *Journal of Crystal Growth*, 207(1-2):95 – 101, 1999.
- [60] S. Ritsch, C. Beeli, H.U. Nissen, M. GöDecke, M. Scheffer, and R. Lück. The existence regions of structural modifications in decagonal AlNiCo . *Philos. Mag. Letter*, 78(2):67–75, Aug 1998.
- [61] K. Edagawa, H. Sawa, and S. Takeuchi. Order-disorder transformation in an $\text{Al} - \text{Ni} - \text{Co}$ decagonal quasi-crystal. *Philos. Mag. Letter*, 69(4):227–234, Apr 1994.
- [62] K. Edagawa, M. Ichihara, K. Suzuki, and S. Takeuchi. New type of decagonal quasicrystal with superlattice order in $\text{Al} - \text{Ni} - \text{Co}$ alloy. *Philos. Mag. Letter*, 66(1):19–25, Jul 1992.
- [63] S. Ritsch, C. Beeli, H.U. Nissen, and R. Luck. 2 different superstructures of the decagonal quasi-crystal. *Philosophical magazine A-physics of condensed matter structure defects and mechanical properties*, 71(3):671–685, Mar 1995.
- [64] N. Ferralis, K. Pussi, E. J. Cox, M. Gierer, J. Ledieu, I.R. Fisher, C.J. Jenks, M. Lindroos, R. McGrath, and R.D. Diehl. Structure of the tenfold $d\text{-Al-Ni-Co}$ quasicrystal surface. *Phys. Rev. B*, 69:153404, Apr 2004.

- [65] J. Yuhara, J. Klikovits, M. Schmid, P. Varga, Y. Yokoyama, T. Shishido, and K. Soda. Atomic structure of an Al-Co-Ni decagonal quasicrystalline surface. *Phys. Rev. B*, 70:024203, Jul 2004.
- [66] K. Saitoh, K. Tsuda, M. Tanaka, K. Kaneko, and A.P. Tsai. Structural study of an $\text{Al}_{72}\text{Ni}_{20}\text{Co}_8$ decagonal quasicrystal using the high-angle annular dark-field method. *Jpn. J. Appl. Phys.*, 36(10B):L1400–L1402, Oct 15 1997.
- [67] H.R. Sharma, K.J. Franke, W. Theis, A. Riemann, S. Folsch, K.H. Rieder, and P. Gille. Investigation of the twofold decagonal $\text{Al}_{71.8}\text{Ni}_{14.8}\text{Co}_{13.4}$ surface by SPA-LEED and He diffraction. *Surface Science*, 561(2-3):121 – 126, 2004.
- [68] R. McGrath, J.A. Smerdon, H.R. Sharma, W. Theis, and J. Ledieu. The surface science of quasicrystals. *J. Phys.: Condens. Matter*, 22(8):084022, Mar 3 2010.
- [69] A. Yamamoto and S. Weber. Five-dimensional superstructure model of decagonal $\text{Al} - \text{Ni} - \text{Co}$ quasicrystals. *Phys. Rev. Lett.*, 78(23):4430–4433, Jun 1997.
- [70] P.J. Steinhardt, H.-C. Jeong, K. Saitoh, M. Tanaka, E. Abe, and A.P. Tsai. Experimental verification of the quasi-unit-cell model of quasicrystal structure. *Nature*, 396(6706):55–57, Nov 5 1998.
- [71] B. Dubost, J.M. Lang, M. Tanaka, P. Sainfort, and M. Audier. Large AlCuLi single quasi-crystals with triacontahedral solidification morphology. *Nature*, 324(6092):48–50, Nov 6 1986.
- [72] P. Sainfort, B. Dubost, and A. Dubus. Quasi-crystalline precipitation from solid-solutions of the AlLiCuMg system. *Comptes Rendues Acad. Sc. Paris*, 301(10):689–692, 1985.
- [73] Y.K. Vekilov and Chernikov. M.A. Quasicrystals. *Physics-Uspekhi*, 53(6):537–560, 2010.
- [74] S.-L. Chang, J.W. Anderegg, and P.A. Thiel. Surface oxidation of an $\text{Al} - \text{Pd} - \text{Mn}$ quasicrystal characterized by x-ray photoelectron spectroscopy. *Journal of Non-Crystalline Solids*, 195(1-2):95–101, Feb 1996.
- [75] Ph. Ebert, M. Feuerbacher, N. Tamura, M. Wollgarten, and K. Urban. Evidence for a cluster-based structure of AlPdMn single quasicrystals. *Phys. Rev. Lett.*, 77(18):3827–3830, Oct 1996.
- [76] Z. Papadopolos, G. Kasner, J. Ledieu, E.J. Cox, N.V. Richardson, Q. Chen, R.D. Diehl, T.A. Lograsso, A.R. Ross, and R. McGrath. Bulk termination of the quasicrystalline fivefold surface of $\text{Al}_{70}\text{Pd}_{21}\text{Mn}_9$. *Phys. Rev. B*, 66(18):184207, Nov 2002.
- [77] J. Ledieu, A.W. Munz, T.M. Parker, R. McGrath, R.D. Diehl, D.W. Delaney, and T.A. Lograsso. Structural study of the five-fold surface of the $\text{Al}_{70}\text{Pd}_{21}\text{Mn}_9$ quasicrystal. *Surface Science*, 433-435:666–671, 1999.
- [78] Ph. Ebert, M. Feuerbacher, N. Tamura, M. Wollgarten, and K. Urban. Evidence for a cluster-based structure of alpdmn single quasicrystals. *Phys. Rev. Lett.*, 77:3827–3830, Oct 1996.
- [79] Ph. Ebert, M. Yurechko, F. Kluge, T. Cai, B. Grushko, P. A. Thiel, and K. Urban. Surface structure of Al-Pd-Mn quasicrystals: Existence of supersaturated bulk vacancy concentrations. *Phys. Rev. B*, 67(2):024208, Jan 2003.

- [80] J.A. Barrow, V. Fournée, A.R. Ross, P.A. Thiel, M. Shimoda, and A.P. Tsai. Photoemission studies of the sputter-induced phase transformation on the Al-Cu-Fe surface. *Surface Science*, 539(1-3):54 – 62, 2003.
- [81] T. Suzuki, H. R. Sharma, T. Nishimura, M. Shimoda, Y. Yamauchi, and A.-P. Tsai. Electronic structure of the topmost tenfold surface of decagonal Al-Ni-Co quasicrystal. *Phys. Rev. B*, 72:115427, Sep 2005.
- [82] Z. Shen, M.J. Kramer, C.J. Jenks, A.I. Goldman, T. Lograsso, D. Delaney, M. Heinzig, W. Raberg, and P.A. Thiel. Crystalline surface structures induced by ion sputtering of Al-rich icosahedral quasicrystals. *Phys. Rev. B*, 58:9961–9971, Oct 1998.
- [83] W. Steurer, T. Haibach, B. Zhang, S. Kek, and R. Luck. The structure of decagonal $\text{Al}_{70}\text{Ni}_{15}\text{Co}_{15}$. *Acta crystallographica section B-structural science*, 49(Part 4):661–675, Aug 1 1993.
- [84] H.R Sharma, W. Theis, P. Gille, and K.H. Rieder. Faceting of the two-fold decagonal $\text{Al}_{71.8}\text{Ni}_{14.8}\text{Co}_{13.4}$ surface studied by He diffraction. *Surface Science*, 511(1-3):387 – 391, 2002.
- [85] T. Michely and J. Krug. *Islands, Mounds and atoms*, chapter I. Introduction. publisher, 2004.
- [86] J.W. Evans, P.A. Thiel, and M.C. Bartelt. Morphological evolution during epitaxial thin film growth: Formation of 2D islands and 3D mounds. *Surface Science Reports*, 61(1-2):1–128, 2006.
- [87] H. Li and B.P. Tonner. Direct experimental identification of the structure of ultrathin films of bcc iron and metastable bcc and fcc cobalt. *Phys. Rev. B*, 40:10241–10248, Nov 1989.
- [88] H. Li, S.C. Wu, D. Tian, J. Quinn, Y.S. Li, F. Jona, and P.M. Marcus. Epitaxial growth of body-centered-tetragonal copper. *Phys. Rev. B*, 40:5841–5844, Sep 1989.
- [89] K. Oura, V.G. Lifshits, A.A. Saranin, A.V. Zotov, and M. Katayama. *Surface science, an introduction*, chapter 1. 2003.
- [90] Teichert, C. Self-Organization of nanostructures in semiconductor heteroepitaxy. *Physics reports-review section of physics letters*, 365(5-6):335–432, Aug 2002.
- [91] K-N. Tu, J.W. Mayer, and L.C. Feldman. *Electronic thin film science, for electrical engineers and materials scientists*. MacMillan publishing company, 1992.
- [92] M.A. Herman, W. Richter, and H. Sitter. *Epitaxy, Physical principles and technical implementation*. publisher, 2004.
- [93] W. Seifert, N. Carlsson, J. Johansson, M.-E. Pistol, and L. Samuelson. In situ growth of nano-structures by metal-organic vapour phase epitaxy. *Journal of Crystal Growth*, 170(1-4):39 – 46, 1997. Metalorganic Vapour Phase Epitaxy 1996.
- [94] M. Zinke-Allmang, L.C. Feldman, and Marcia H. Grabow. Clustering on surfaces. *Surface Science Reports*, 16(8):377 – 463, 1992.
- [95] K. Miki, K. Sakamoto, and T. Sakamoto. *Mater. Res. Soc. Symp Proc*, 148:323, 1989.

- [96] M. Krishnamurthy, J.S. Drucker, and J.A. Venables. Microstructural evolution during the heteroepitaxy of Ge on vicinal Si(100). *Journal of Applied Physics*, 69(9):6461–6471, 1991.
- [97] J. A. Smerdon. The various modes of growth of metals on quasicrystals. *Journal of Physics-Condensed Matter*, 22(43):433002, Nov 3 2010.
- [98] V. Fournée and P.A. Thiel. New phenomena in epitaxial growth: solid films on quasicrystalline substrates. *Journal of Physics D-Applied Physics*, 38(6):R83–R106, MAR 21 2005.
- [99] Th. Deniozou, J. Ledieu, V. Fournée, D.M. Wu, T.A. Lograsso, H.I. Li, and R.D. Diehl. Aperiodic and modulated Pb thin films on fivefold icosahedral Al – Cu – Fe and Al(111): Tailoring the structure of Pb. *Phys. Rev. B*, 79(24):245405, Jun 2009.
- [100] B. Bolliger, V. E. Dmitrienko, M. Erbudak, R. Lüscher, H.-U. Nissen, and A. R. Kortan. Epitactic textures of fcc Al on icosahedral Al-Pd-Mn quasicrystal. *Phys. Rev. B*, 63:052203, Jan 2001.
- [101] K Pussi, M Gierer, and R D Diehl. The uniaxially aperiodic structure of a thin Cu film on fivefold *i*-Al-Pd-Mn. *Journal of Physics: Condensed Matter*, 21(47):474213, 2009.
- [102] R. Lüscher, M. Erbudak, and Y. Weisskopf. Al nanostructures on quasicrystalline Al-Pd-Mn. *Surface Science*, 569(1-3):163 – 175, 2004.
- [103] T. Flückiger, Y. Weisskopf, M. Erbudak, R. Lüscher, and A. R. Kortan. Nanoepitaxy: Size selection in self-assembled and oriented al nanocrystals grown on a quasicrystal surface. *Nano Letters*, 3(12):1717–1721, 2003.
- [104] V. Fournée, T. C. Cai, A. R. Ross, T. A. Lograsso, J. W. Evans, and P. A. Thiel. Nucleation and growth of Ag films on a quasicrystalline AlPdMn surface. *Phys. Rev. B*, 67:033406, Jan 2003.
- [105] V. Fournée, A.R. Ross, T.A. Lograsso, J.W. Evans, and P.A. Thiel. Growth of Ag thin films on complex surfaces of quasicrystals and approximant phases. *Surface Science*, 537(1-3):5 – 26, 2003.
- [106] M. Shimoda, J.Q. Guo, T.J. Sato, and A.P. Tsai. Surfactant-mediated growth of AuAl₂ film on a decagonal Al₇₂Ni₁₂Co₁₆ quasicrystal. *Surface Science*, 482-485, Part 2(0):784 – 788, 2001.
- [107] M. Shimoda, T. J. Sato, A. P. Tsai, and J. Q. Guo. Epitaxial crystalline film with pseudo-tenfold symmetry formed by Au-deposition on a decagonal Al₇₂Ni₁₂Co₁₆ quasicrystal. *Phys. Rev. B*, 62:11288–11291, Nov 2000.
- [108] T.C.Q. Noakes, P. Bailey, M. Draxler, C.F. McConville, A.R. Ross, T.A. Lograsso, L. Leung, J.A. Smerdon, and R. McGrath. Film growth arising from the deposition of au onto an *i* – AlPdMn quasicrystal: a medium energy ion scattering study. *Journal of Physics: Condensed Matter*, 18(22):5017, 2006.
- [109] M. Shimoda, T.J. Sato, A.-P. Tsai, and J.Q. Guo. Epitaxial film growth on a decagonal Al₇₂Ni₁₂Co₁₆ quasicrystal. *Surface Science*, 507-510(0):276 – 280, 2002.
- [110] J. Ledieu, J. T. Hoeft, D. E. Reid, J. A. Smerdon, R. D. Diehl, T. A. Lograsso, A. R. Ross, and R. McGrath. Pseudomorphic growth of a single element quasiperiodic ultrathin film on a quasicrystal substrate. *Phys. Rev. Lett.*, 92:135507, Apr 2004.

- [111] J. Ledieu, J. T. Hoeft, D. E. Reid, J. A. Smerdon, R. D. Diehl, N. Ferralis, T. A. Lograsso, A. R. Ross, and R. McGrath. Copper adsorption on the fivefold $\text{Al}_{70}\text{Pd}_{21}\text{Mn}_9$ quasicrystal surface. *Phys. Rev. B*, 72:035420, Jul 2005.
- [112] L.H. Wearing, J.A. Smerdon, L. Leung, T.A. Lograsso, A.R. Ross, and R. McGrath. Iron deposition on the five-fold surface of the icosahedral Al-Pd-Mn quasicrystal. *Surface Science*, 601(16):3450 – 3455, 2007.
- [113] Y. Weisskopf, R. Lüscher, and M. Erbudak. Structural modifications upon deposition of Fe on the icosahedral quasicrystal Al-Pd-Mn. *Surface Science*, 578(1-3):35 – 42, 2005.
- [114] L.H. Wearing, J.A. Smerdon, L. Leung, S.S. Dhesi, J. Ledieu, P. Bencok, I. Fisher, C.J. Jenks, and R. McGrath. Iron deposition on the tenfold surface of the $\text{Al}_{72}\text{Ni}_{11}\text{Co}_{17}$ decagonal quasicrystal. *Journal of Physics: Condensed Matter*, 20(1):015005, 2008.
- [115] Y. Weisskopf, M. Erbudak, J.-N. Longchamp, and T. Michlmayr. Ni deposition on the pentagonal surface of an icosahedral Al-Pd-Mn quasicrystal. *Surface Science*, 600(12):2594 – 2599, 2006.
- [116] J. A. Smerdon, J. Ledieu, J. T. Hoeft, D. E. Reid, L. H. Wearing, R. D. Diehl, T. A. Lograsso, A. R. Ross, and R. McGrath. Adsorption of cobalt on the tenfold surface of $d - \text{Al}_{72}\text{Ni}_{11}\text{Co}_{17}$ and on the fivefold surface of $i - \text{Al}_{70}\text{Pd}_{21}\text{Mn}_9$. *Philosophical Magazine*, 86(6-8):841–847, 2006.
- [117] K. J. Franke, H. R. Sharma, W. Theis, P. Gille, Ph. Ebert, and K. H. Rieder. Quasicrystalline epitaxial single element monolayers on icosahedral Al-Pd-Mn and decagonal Al-Ni-Co quasicrystal surfaces. *Phys. Rev. Lett.*, 89:156104, Sep 2002.
- [118] K. J. Franke, P. Gille, K.-H. Rieder, and W. Theis. Achieving epitaxy between incommensurate materials by quasicrystalline interlayers. *Phys. Rev. Lett.*, 99:036103, Jul 2007.
- [119] J. Ledieu, M. Krajčí, J. Hafner, L. Leung, L. H. Wearing, R. McGrath, T. A. Lograsso, D. Wu, and V. Fournée. Nucleation of Pb starfish clusters on the five-fold Al-Pd-Mn quasicrystal surface. *Phys. Rev. B*, 79:165430, Apr 2009.
- [120] J.A. Smerdon, L. Leung, J.K. Parle, C.J. Jenks, R. McGrath, V. Fournée, and J. Ledieu. Formation of a quasicrystalline Pb monolayer on the 10-fold surface of the decagonal Al-Ni-Co quasicrystal. *Surface Science*, 602(14):2496 – 2501, 2008.
- [121] J.A. Smerdon, L.H. Wearing, J.K. Parle, L. Leung, H.R. Sharma, J. Ledieu, and R. McGrath. Ordering of adsorbed species on quasicrystal surfaces. *Philosophical Magazine*, 88(13-15):2073–2082, 2008.
- [122] K. Urban, N. Moser, and H. Kronmüller. Phase transitions between the quasicrystalline, crystalline, and amorphous phases in Al_{14} at %Mn. *physica status solidi (a)*, 91(2):411–422, 1985.
- [123] M. Zurkirch, B. Bolliger, M. Erbudak, and A. R. Kortan. Structural transformations at the surface of the decagonal quasicrystal $\text{Al}_{70}\text{Ni}_{15}\text{Co}_{15}$. *Phys. Rev. B*, 58:14113–14116, Dec 1998.
- [124] S. E. Burkov. Structure model of the Al-Cu-Co decagonal quasicrystal. *Phys. Rev. Lett.*, 67:614–617, Jul 1991.

- [125] B. Bolliger, M. Erbudak, D. D. Vvedensky, M. Zurkirch, and A. R. Kortan. Surface structural transitions on the icosahedral quasicrystal $\text{Al}_{70}\text{Pd}_{20}\text{Mn}_{10}$. *Phys. Rev. Lett.*, 80:5369–5372, Jun 1998.
- [126] D. Hagele, M. Oestreich, W.W. Ruhle, N. Nestle, and K. Eberl. Spin transport in GaAs. *Applied Physics Letters*, 73(11):1580–1582, Sep 14 1998.
- [127] P. Gambardella and I. Mihai Miron. Current-induced spin-orbit torques. *Philosophical transactions of the royal society A-mathematical physical and engineering sciences*, 369(1948):3175–3197, Aug 13 2011.
- [128] C. Tsang, R.E. Fontana, T. Lin, D.E. Heim, V.S. Speriosu, B.A. Gurney, and M.L. Mason. Design, fabrication and testing of spin-valve read heads for high-density recording. *IEEE transactions on magnetics*, 30(6, Part 1):3801–3806, Nov 1994. 6th Joint Magnetism and Magnetic Materials-Intermag Conference, Albuquerque, NM, Jun 20-23, 1994.
- [129] E.I. Rashba. Theory of electrical spin injection: Tunnel contacts as a solution of the conductivity mismatch problem. *Phys. Rev. B*, 62:R16267–R16270, Dec 2000.
- [130] H.J. Zhu, M. Ramsteiner, H. Kostial, M. Wassermeier, H.-P. Schönherr, and K.H. Ploog. Room-temperature spin injection from Fe into GaAs. *Phys. Rev. Lett.*, 87:016601, Jun 2001.
- [131] J.D. Aldous. *Growth, Characterisation and Surface Structures of MnSb and NiSb Thin Films*. PhD thesis, University of Warwick, 2011.
- [132] S.A. Wolf, D.D. Awschalom, R.A. Buhrman, J.M. Daughton, S. von Molnár, M.L. Roukes, A.Y. Chtchelkanova, and D.M. Treger. Spintronics: A spin-based electronics vision for the future. *Science*, 294(5546):pp. 1488–1495, 2001.
- [133] Y. Ohno, D.K. Young, B. Beschoten, F. Matsukura, H. Ohno, and DD Awschalom. Electrical spin injection in a ferromagnetic semiconductor heterostructure. *Nature*, 402(6763):790–792, Dec 16 1999.
- [134] R. Fiederling, M. Keim, G. Reuscher, W. Ossau, G. Schmidt, A. Waag, and L.W. Molenkamp. Injection and detection of a spin-polarized current in a light-emitting diode. *Nature*, 402(6763):787–790, Dec 16 1999.
- [135] R.A. de Groot, F.M. Mueller, P.G. van Engen, and K.H.J. Buschow. New class of materials: Half-metallic ferromagnets. *Phys. Rev. Lett.*, 50:2024–2027, Jun 1983.
- [136] S.A. Hatfield. *Heteroepitaxial growth of MnSb on III-IV semiconductor substrates*. PhD thesis, The University of Warwick, 2006.
- [137] G.C. Han, C.K. Ong, and T.Y.F. Liew. Magnetic and magneto-optical properties of MnSb films on various substrates. *Journal of Magnetism and Magnetic Materials*, 192:233–237, 1999.
- [138] L. Kahal, A. Zaoui, and M. Ferhat. Magnetic properties of CrSb: A first-principle study. *Journal of Applied Physics*, 101(9):093912, May 1 2007.
- [139] W.H. Xie, B.G. Liu, and D.G. Pettifor. Half-metallic ferromagnetism in transition metal pnictides and chalcogenides with wurtzite structure. *Phys. Rev. B*, 68(13):134407, Oct 2003.

- [140] F.J. Himpsel, J.E. Ortega, G.J. Mankey, and R.F. Willis. Magnetic nanostructures. *Advances in Physics*, (4):511–597, 1998.
- [141] C.A.F. Vaz, J.A.C. Bland, and G. Lauhoff. Magnetism in ultrathin film structures. *Reports on Progress in Physics*, 71(5):056501 (78pp), 2008.
- [142] H.J. Kohnke, V. Dankelmann, Ch. Kleeberg, J. W. Schünemann, K. Bärner, A. Vetcher, and G.A. Govor. Anisotropic magnetization of some $\text{MnAs}_{1-x}\text{Sb}_x$ single crystals. *physica status solidi (b)*, 191(2):511–521, 1995.
- [143] M.T. Johnson, P.J.H. Bloemen, F.J.A. den Broeder, and J.J. de Vries. Magnetic anisotropy in metallic multilayers. *Reports on Progress in Physics*, 59(11):1409–1458, 1996.
- [144] T. Kaneyoshi. *Introduction to surface magnetism*. CRC Press, Inc, 1990.
- [145] D. Jiles. *Introduction to magnetism and magnetic materials*. Chapman & Hall, 1991.
- [146] D.L. Leslie-Pelecky and R.D. Rieke. Magnetic properties of nanostructured materials. *Chemistry of Materials*, 8:1770 – 1783, 1996.
- [147] G.C. Han, C.K. Ong, and T.Y.F. Liew. Magnetic and magneto-optical properties of MnSb films on various substrates. *Journal of Magnetism and Magnetic Materials*, 192(2):233 – 237, 1999.
- [148] R. Allenspach. Ultrathin films: magnetism on the microscopic scale. *Journal of Magnetism and Magnetic Materials*, 129(2-3):160 – 185, 1994.
- [149] F.J.A. den Broeder, W. Hoving, and P.J.H. Bloemen. Magnetic anisotropy of multilayers. *Journal of Magnetism and Magnetic Materials*, 93:562 – 570, 1991.
- [150] C. Kittel. *Introduction to solid state physics*. John Wiley & Sons, 1986.
- [151] Y. Shiratsuchi, M. Yamamoto, and S.D. Bader. Magnetism and surface structure of atomically controlled ultrathin metal films. *Progress in Surface Science*, 82(2-3):121 – 160, 2007.
- [152] O. Fruchart and A. Thiaville. Magnetism in reduced dimensions. *Comptes Rendus Physique*, 6(9):921 – 933, 2005. Spintronics.
- [153] C. Chappert and P. Bruno. Magnetic anisotropy in metallic ultrathin films and related experiments on cobalt films (invited). *Journal of Applied Physics*, 64(10):5736–5741, 1988.
- [154] T. Okita and Y. Makino. Crystal magnetic anisotropy and magnetization of MnSb. *Journal of the Physical Society of Japan*, 25(1):120–124, 1968.
- [155] H. Akinaga, S. Miyanishi, W. Van Roy, J. De Boeck, and G. Borghs. Influence of GaAs(001) surface termination on the in-plane magnetic anisotropies of MnSb epitaxial films. *Applied Physics Letters*, 73(22):3285–3287, 1998.
- [156] H. Meng, C.K. Ong, H.S. Lim, H.C. Fang, and Y.P. Feng. Effect of lattice mismatch strains on the structure and magnetic, magneto-optical properties of MnSb films on gaas substrate. *Journal of Magnetism and Magnetic Materials*, 213(1-2):37 – 42, 2000.
- [157] H.C. Siegmann. Surface and 2D magnetism. *Journal of Physics: Condensed Matter*, 4(44):8395–8434, 1992.

- [158] B. Hillebrands and K. Ounadjela. *Spin dynamics in confined magnetic structures I*. Springer-Verlag Berlin Heidelberg New York, 2002.
- [159] Z.Q. Qiu, J. Pearson, and S.D. Bader. Asymmetry of the spin reorientation transition in ultrathin Fe films and wedges grown on Ag(100). *Phys. Rev. Lett.*, 70(7):1006–1009, Feb 1993.
- [160] G. Markandeyulu and K.V.S. Rama Rao. Spin reorientation in MnSb single crystals by FMR. *Journal of Magnetism and Magnetic Materials*, 67(2):215 – 220, 1987.
- [161] C. Guillaud. Propriétés ferromagnétiques des alliages manganese-antimoine et manganese-arsenic. *Annales de physique*, 4(Nov-):671–703, 1949.
- [162] P. Pouloupoulos and K. Baberschke. Magnetism in thin films. *Journal of Physics: Condensed Matter*, 11(48):9495–9515, 1999.
- [163] R. Skomski. *Simple models of magnetism*. Oxford University Press, 2008.
- [164] C.B. Duke. Semiconductor surface reconstruction: The structural chemistry of two-dimensional surface compounds. *Chemical Reviews*, 96(4):1237–1260, 1996.
- [165] J.M.C. Thornton, D.A. Woolf, and P. Weightman. Reconstruction of the GaAs(111)B surface. *Applied surface science*, 123(124):115–119, 1998.
- [166] S.A. Hatfield, J.D. Aldous, and G.R. Bell. Stoichiometry, contamination and microstructure of MnSb(0001) surfaces. *Applied Surface Science*, 255(6):3567 – 3575, 2009.
- [167] K. Yang and L.J. Schowalter. Surface reconstruction phase diagram and growth on GaAs(111)B substrates by molecular beam epitaxy. *Applied Physics Letters*, 60(15):1851–1853, 1992.
- [168] D.A. Woolf, D.I. Westwood, and R.H. Williams. Surface reconstructions of GaAs(111)A and (111)B: A static surface phase study by reflection high-energy electron diffraction. *Applied Physics Letters*, 62(12):1370–1372, 1993.
- [169] H. Zhang, S.S. Kushvaha, A.T.S. Wee, and X. Wang. Morphology, surface structures, and magnetic properties of mnsb thin films and nanocrystallites grown on graphite. *Journal of Applied Physics*, 102(2):023906, 2007.
- [170] A. Ouerghi, M. Marangolo, M. Eddrief, B. B. Lipinski, V.H. Etgens, M. Lazzeri, H. Cruguel, F. Sirotti, A. Coati, and Y. Garreau. Surface reconstructions of epitaxial MnAs films grown on GaAs(111)B. *Physical Review B (Condensed Matter and Materials Physics)*, 74(15):155412, 2006.
- [171] S.A. Hatfield and G.R. Bell. Mapping the surface reconstructions of MnSb(0001) and (1 $\bar{1}$ 01). *Surface Science*, 601(23):5368 – 5377, 2007.
- [172] K. Ono, M. Shuzo, M. Oshima, and H. Akinaga. Ga segregation in MnSb epitaxial growth on GaAs(100) and (111)B substrates. *Phys. Rev. B*, 64(8):085328, Aug 2001.
- [173] P. Hofmann. Electron spectroscopy. <http://philiphofmann.net/surflec3/surflec011.html>, Sept 2012.
- [174] A. Zangwill. *Physics at Surfaces*. Cambridge University Press, 1988.

- [175] R.D. Diehl, J. Ledieu, N. Ferralis, A.W. Szmodis, and R. McGrath. Low-energy electron diffraction from quasicrystal surfaces. *Journal of Physics: Condensed Matter*, 15(3):R63, 2003.
- [176] Schottky emitter test data. 2009.
- [177] W. Zhou and Z.L. Wang. *Scanning Microscopy for nanotechnology - Techniques and applications*.
- [178] An introduction to electron microscopy. http://www.fei.com/uploadedFiles/Documents/Content/Introduction_to_EM_booklet_July_10.pdf, 2010.
- [179] P.D. Innes. On the velocity of the cathode particles emitted by various metals under the influence of rontgen rays, and its bearing on the theory of atomic disintegration. *Proceedings of the royal society of London series A*, 79(532):442–462, Aug 1907.
- [180] K Siegbahn and K Edvarson. Beta-ray spectroscopy in the precision range of $1:10^5$. *Nuclear physics*, 1(3):137, 1956.
- [181] R. Paynter. XPS Theory. http://csacs.mcgill.ca/francais/docs/CHEM634/XPS_Paynter_t.pdf, Sept 2012.
- [182] M. Horn-von Hoegen. Growth of semiconductors layers studied by spot profile analysing low energy electron diffraction. *Zeitschrift für Kristallographie*, 214:591–721, 1999.
- [183] E. Bauer. *Science of microscopy, Volume 1*. Springer, 2007.
- [184] E. Bauer. Low energy electron microscopy. *Report on Progress in Physics*, 57(9):895–938, 1994.
- [185] E. Bauer. Low energy electron microscopy of nanostructures. *physica status solidi (b)*, 192(2):375–387, 1995.
- [186] D. Gregory and M. Fink. Theoretical electron scattering amplitudes and spin polarizations: Electron energies 100 to 1500 eV Part III. Li, Na, Mg, P, K, Ca, Sc, Mn, Ga, Br, Sr, Mo, Rh, Cd, Ba, W, and Os targets. *Atomic Data and Nuclear Data Tables*, 14(1):39 – 87, 1974.
- [187] F. Seitz. *The modern theory of solids*. Mc-Graw-Hill, New-York, 1940.
- [188] M. Mundschau, E. Bauer, W. Telieps, and W. Swiech. Initial epitaxial growth of copper silicide on Si(111) studied by low-energy electron microscopy and photoemission electron microscopy. *Journal of Applied Physics*, 65(12):4747–4752, 1989.
- [189] W. Telieps and E. Bauer. Kinetics of the (7x7)-(1x1) transition on Si(111). *Berichte der bunsen - gesellschaft - physical chemistry chemical physics*, 90:197–200, 1986.
- [190] M. S. Altman, W. F. Chung, Z. Q. He, H. C. Poon, and S. Y. Tong. Quantum size effect in low energy electron diffraction of thin films. *Applied Surface Science*, 169-170:82 – 87, 2001.
- [191] E. Bauer, T. Duden, and R. Zdyb. Spin-polarized low energy electron microscopy of ferromagnetic thin films. *Journal of Physics D: Applied Physics*, 35(19):2327–2331, 2002.

- [192] S. Utsunomiya, M. Kogawa, E. Kamiishi, and R.C. Ewing. Scanning transmission electron microscopy and related techniques for research on actinide and radionuclide nanomaterials. In *Actinide Nanoparticle Research*, pages 33–62. Springer Berlin Heidelberg, 2011.
- [193] D.B. Williams and C.B. Carter. *Transmission Electron Microscopy, Part 1: Basics*. Springer, 2009.
- [194] K.W. Urban. Studying atomic structures by aberration-corrected transmission electron microscopy. *Science*, 321(5888):506–510, 2008.
- [195] I. Arslan, T.J.V. Yates, N.D. Browning, and P.A. Midgley. Embedded nanostructures revealed in three dimensions. *Science*, 309(5744):2195–2198, 2005.
- [196] Z.Y. Li, N.P. Young, M. Di Vece, S. Palomba, R.E. Palmer, A.L. Bleloch, B.C. Curley, R.L. Johnston, J. Jiang, and J. Yuan. Three-dimensional atomic-scale structure of size-selected gold nanoclusters. *Nature*, 451(7174):46–48, 2008.
- [197] S. Van Aert, K.J. Batenburg, M.D. Rossell, R. Erni, and G. Van Tendeloo. Three-dimensional atomic imaging of crystalline nanoparticles. *Nature*, 470(7334):374–377, Feb 17 2011.
- [198] Y. Sato, B. Ünal, T.A. Lograsso, P.A. Thiel, A.K. Schmid, T. Duden, N.C. Bartelt, and K.F. McCarty. Periodic step arrays on the aperiodic *i*-Al-Pd-Mn quasicrystal surface at high temperature. *Phys. Rev. B*, 81:161406, Apr 2010.
- [199] P.-G. de Gennes, F. Brochard-Wyart, and D. Quéré. *Capillarity and Wetting Phenomena: Drops, Bubbles, Pearls, Waves*. Springer Science, 2004.
- [200] K. J. Franke, P. Gille, K.-H. Rieder, and W. Theis. Achieving epitaxy between incommensurate materials by quasicrystalline interlayers. *Phys. Rev. Lett.*, 99:036103, Jul 2007.
- [201] A.P. Tsai, J.Q. Guo, E. Abe, H. Takakura, and T. Sato. Alloys: A stable binary quasicrystal. *Nature*, 408(6812):537–538, 2000.
- [202] <http://www.infrared-thermography.com/material-1.htm>, January 2012.
- [203] G. Cubiotti, E.E. Krasovskii, O.V. Slobodyan, Y.N. Kucherenko, and V. Antonov. The electronic structure of Al₃Ni. *Journal of Physics: Condensed Matter*, 7(25):4865, 1995.
- [204] A. Taylor and N.J. Doyle. Further studies on nickel-aluminium system .1. beta-NiAl and delta-Ni₂Al₃ phase fields. *Journal of Applied Crystallography*, 5(Jun):201, 1972.
- [205] P.S. Khadkikar, I.E. Locci, and K. Vedula. An investigation of the Ni₅Al₃ phase. *Journal of metals*, 39(7):A64, Jul 1987.
- [206] M. Ellner, K. Kolatschek, and B. Predel. On the partial atomic volume and the partial molar enthalpy of aluminium in some phases with Cu and Cu₃Au structures. *Journal of the less-common metals*, 170(1):171–184, Jun 15 1991.
- [207] J.D. Aldous, C.W. Burrows, I. Maskery, M.S. Brewer, T.P.A. Hase, J.A. Duffy, M.R. Lees, C. Sánchez-Hanke, T. Decoster, W. Theis, A. Quesada, A.K. Schmid, and G.R. Bell. Depth-dependent magnetism in epitaxial MnSb thin films: effects of surface passivation and cleaning. *Journal of Physics: Condensed Matter*, 24(14):146002, 2012.

- [208] J.R. Jinschek, K.J. Batenburg, H.A. Calderon, R. Kilaas, V. Radmilovic, and C. Kisielowski. 3-D reconstruction of the atomic positions in a simulated gold nanocrystal based on discrete tomography: Prospects of atomic resolution electron tomography. *Ultramicroscopy*, 108(6):589–604, May 2008.
- [209] M. Greiner and P. Kruse. Recrystallization of tungsten wire for fabrication of sharp and stable nanoprobe and field-emitter tips. *Review of Scientific Instruments*, 78(2):026104, 2007.
- [210] A. Hussain and R. Gruehn. Crystal-growth of hexagonal potassium tungsten bronze by chemical-transport. *Journal of crystal growth*, 108(3-4):831–833, Feb 1991.
- [211] A. Magneli and B. Blomberg. Contribution to the knowledge of the alkali tungsten bronzes. *Acta chemica scandinavica*, 5(3):372–378, 1951.